Synthesis and Characterization of Aerogels from Shape Controlled Metal and Semiconductor Nanocrystals

Von der Naturwissenschaftlichen Fakultät der

Gottfried Wilhelm Leibniz Universität Hannover

zur Erlangung des Grades

Doktor der Naturwissenschaften (Dr. rer. nat.)

genehmigte Dissertation

von

Suraj Naskar, M.Sc.

2017

Referentin: Dr. rer. nat. Nadja-Carola Bigall

Korreferent: Prof. Dr. rer. nat. Jürgen Caro

Korreferent: Prof. Dr. Liberato Manna

Tag der Promotion: 21.03.2017

Preface

The innovative research work presented in this thesis was conducted during my Ph.D studentship under the supervision of Dr. Nadja C. Bigall from November 2013 to January 2017 in the Institute of Physical Chemistry and Electrochemistry (PCI) at Gottfried Wilhelm Leibniz University of Hannover.

During this time I have been an active participant of "Materialien aus Überstrukturen Maßgeschneiderter Kolloidaler Nanokristallbausteine"(MÜKoN) within the framework of the project NanoMatFutur (support code 03X5525) of the federal ministry of education and research (BMBF).

The original research work presented in the thesis includes four articles (at the current state three articles are published, and the fourth is submitted) namely i) Photoluminescent aerogels from quantum wells ii) Highly porous aerogels from Pt nanocubes and nanospheres directly from organic colloidal Solution iii) Site-selective noble metal growth on CdSe nanoplatelets and iv), Synthesis of ternary and quaternary Au and Pt decorated CdSe/CdS heteronanoplatelets with controllable morphology which are written by myself as the first author. Apart from that, there are three more articles where I have contributed as co-author are published, are not included in this thesis but listed in the appendix.

In the following section, the contributions of the authors in the publications are clarified.

The first article in section 2 was written by me with kind support of my co-workers and collaboration partners. In this article, I have developed synthetic strategy to fabricate highly porous macroscopic aerogels from CdSe and CdSe/CdS nanoplatelets (NPLs). I have investigated the optical characterization of the starting building blocks and the gels by means of UV-vis and PL spectroscopy. Dr. Sara Sánchez-Paradinas from PCI helped me with the optical measurements. I have also characterized the interconnected network of the

aerogels by scanning electron microscopy (SEM). Jan F. Miethe performed the structural characterization of the gels by TEM. Nadeschda Schmidt from the Institute of inorganic chemistry (ACI) of the Leibniz University of Hanover conducted N_2 physisorption experiments to evaluate the specific surface area of the aerogels. The aerogels were also investigated with XPS in collaboration with Prof. Herbert Pfnür from FKP. Dr. Karthiga Kanthasamy from FKP, assisted me to conduct the above experiments. Prof. Peter Behrens from ACI and especially Dr. Nadja C. Bigall helped me to evaluate the findings with valuable discussions and motivated me to write the article.

The second (submitted) manuscript regarding the gelation of the shape controlled Pt nanoparticles was again written by me. I have investigated the morphologies by SEM and the surface of the aerogels by Fourier transformed infrared spectroscopy (FTIR). The structural characterization of the aerogels by means of TEM, to see the connections of the individual Pt nanoparticles was conducted by Axel Freytag. In collaboration with Dr. Angela Köckritz and Dr. Jens Deutsch, from Leibniz-Institut für Katalyse e.V. at the Universität Rostock, the catalytic activity of the Pt aerogels toward asymmetric hydrogenation was performed. Natalja Wendt from ACI measured the specific surface area of the Pt aerogels. Finally, Prof. Peter Behrens, Dr. Angela Köckritz, Dr. Jens Deutsch and particularly Dr. Nadja C. Bigall helped me to write the manuscript with valuable discussions and corrections of the work.

The third article in chapter 4.2 was written by me with the kind support of my co-workers. The new synthetic strategies of fabrication of Au decorated CdSe nanoplatelets were developed by me. I together with Anja Schlosser, who worked under my supervision in her bachelor thesis, synthesized the Pt, and Pd decorated CdSe nanoplatelets. We investigated the optical characterization of the hybrid nanoplatelets by means of UV-vis absorption, photoluminescence (PL) emission spectroscopy. Characterization of the structural

morphologies of the hybrid nanoplatelets by means of transmission electron microscopy (TEM) were investigated by Jan F. Miethe and Axel Freytag from PCI. The dark filed TEM micrographs and the high angle annular dark field-scanning TEM (HAADF-STEM) micrographs were measured by Frank Steinbach and by Appl. Prof. Armin Feldhoff from PCI. Finally, Dr. Nadja C. Bigall corrected the manuscript and included her valuable opinion to improve the quality of the manuscript.

The fourth article in section 4.3 was again written by me with kind support from my colleagues and collaboration partners. The new reaction procedures to obtain hybrid structures of Au and Pt decorated CdSe/CdS core/crown NPLs with unprecedented structural morphologies have been developed by me. The optical characterization, phase transfer of the hybrid NPLs to aqueous phase were also conducted by me. The structures were characterized by bright field TEM analysis by Axel Freytag. Andreas Wolf and Franziska Lübkemann helped me to analyze the elemental compositions of the hybrid structures by scanning transmission electron microscopy coupled with energy dispersive X-ray spectroscopy (STEM-EDXS) analysis. I employed the hybrid NPLs as catalyst for photocatalytic H_2 generation. In collaboration with Prof. Detlef W. Bahnemann from the Institute for Technical Chemistry (TCI) of the Leibniz University of Hannover, the photocatalytic activities of the hybrid particles were measured. Saher Hamid from TCI constructed the catalytic experimental setup and evaluated the data and gave me valuable opinion to write the article. I investigated the oxidation state of the noble metal domains of the hybrid nanoplatelets in collaboration with Prof. Herbert Pfnür from Institute für Festköperphysik (FKP) of the Leibniz University of Hannover. Julian Koch from FKP helped me to conduct the X-ray photoelectron spectroscopy (XPS) experiments. Dr. Dirk Dorfs from PCI and Dr. Nadja C. Bigall helped with valuable consultations, corrections and final submission of the article.

Acknowledgments

I would like to express my special gratitude and thanks to my advisor Dr. Nadja Carola Bigall, you have been a tremendous mentor for me. I would like to thank you for encouraging my research and for allowing me to grow as a research scientist. She introduced me to this fascinating field of nanoparticles chemistry, motivated with innovative ideas and helped me to gain new thoughts and to build in depth knowledge about this subject. Your advice on both research as well as on my career have been priceless.

I would also like to thank my committee members, Professor Jürgen Caro and Professor Harald Behrens for serving as my committee members even at hardship. I also want to thank you for letting my defense be an enjoyable moment, and for your brilliant comments and suggestions. I would like to thank Professor Liberato Manna from Italian Institute of Technology Genova, Italy, for being the co-referee of my thesis.

Furthermore, I would like to thank all my collaboration partners, for allowing me to conduct research experiments, encouraging me with new thoughts and enabling publications. In particular I´d like to thank Prof. Hebert Pfnür, Prof. Peter Behrens, Prof. Detlef W. Bahnemann, Dr. Angela Köckritz, Dr. Jens Deutsch, Dr. Dirk Dorfs.

I would like to thank, Appl. Prof. Dr. Armin Feldhoff and Frank Steinbach for introducing me to the scanning electron microscope. Furthermore, I would like to thank Kerstin Janze, Yvonne Gabbey-Uebbe and Kerstin Battermann for technical assistance and for purchasing chemicals.

In addition, I want to thank all the members of work groups Bigall and Dorfs, the students who have conducted their bachelor and master thesis with me for helping me throughout my whole journey inside and outside the laboratories. These members are: Anja Schlosser, Axel Freytag, Dominik Hinrichs, Jan F. Miethe, Franziska Lübkemann, Tarek Mohamed,

Abstract

Synthesis of shape controlled metal, semiconductor and combined metal-semiconductor nanoheterostructures are of high significance because of their unique optoelectronic properties as well as superior catalytic activities. The thesis represents the development of new synthetic strategies to obtain nanoparticles with advanced functionalities and the self-assembly of these nanoparticles into template free macroscopic aerogels, preserving fundamental nanoscopic functionalities. Unprecedented, structural morphologies of binary, ternary and quaternary nanoheterostructures are obtained by growing noble metal domains for example Au, Pt and Pd on quasi-2D CdSe and CdSe/CdS core/crown nanoplatelets. Variation of types and amount of metal precursors, temperature, solvent, surfactant, size and composition of the semiconductor nanoplatelets and the reaction order of the metal domain growth are found to be responsible for the different nucleation behavior of the metal domains and the final morphologies of the heterostructutres.

Furthermore, CdSe, CdSe/CdS core/crown nanoplatelets and Pt nanoparticles synthesized in organic solution are converted to porous monolithic aerogels by controlled destabilization of the colloidal solution followed by supercritical drying. The structural, morphological, optoelectronic properties of the invented hybrid nanoheterostructures and the aerogels are investigated thoroughly by microscopic and spectroscopic characterization techniques.

By virtue of charge carrier separation at the metal-semiconductor interface, the nanoheteroplatelets are promising for photocatalytic reactions. The aerogels of CdSe/CdS nanoplatelets and Pt nanocubes, exhibiting (100) as the only exposed crystal facets are suitable for facet selective catalysis reactions. The potential advantages and implication of the newly developed NPs are conducted as proof-of-principle experiments such as

asymmetric catalytic hydrogenation reactions yielding selective stereoisomer and with the generation of H_2 gas by photo-reduction of water under white light irradiation. A high emphasis is given to realize the underlying mechanisms of the reactions, and the significance of the materials is discussed with respect to the state-of-the-art of the field. Furthermore, an outlook of the present work in terms of further improvements and future possibilities to fabricate multicomponent aerogels suitable for sensor based applications is demonstrated.

Keywords: Aerogel, Nanoplatelet, Metal-semiconductor hybrid

Zusammenfassung

Die Synthese formkontrollierter Metall-, Halbleiter- und kombinierter Metall-Halbleiter-Nanoheterostrukturen ist aufgrund der einzigartigen optoelektronischen Eigenschaften und der herausragenden katalytischen Aktivitäten von sehr großer Bedeutung. Die vorliegende Dissertation behandelt die Entwicklung neuer Synthesestrategien, um gezielt Nanopartikel mit verbesserter Funktionalität herzustellen und diese mittels Selbstanordnung unter Erhalt der fundamentalen nanoskopischen Eigenschaften der Nanopartikel in templatfreie makroskopische Aerogele zu überführen. Bisher noch nicht gezeigte strukturelle Morphologien binärer, ternärer und quaternärer Nanoheterostrukturen wurden durch gezieltes Aufwachsen von Edelmetalldomänen, wie z. B. Au, Pt und Pd, auf quasi-2D CdSe und CdSe/CdS Kern/Krone Nanoplättchen erzeugt. Es wurde gezeigt, dass die Variation von Typ und Menge der eingesetzten Metallverbindung, die Reaktionstemperatur, das Lösungsmittel, die Liganden, sowie die Größe und die Zusammensetzung der Halbleiternanoplättchen und auch die Reihenfolge der Reaktionssequenz beim Aufwachsen der Metalldomänen essentielle Parameter für die Nukleation der Metalldomäne und die finale Morphologie der Heterostruktur sind.

Desweiteren wurden im organische Medium hergestellte CdSe, CdSe/CdS Kern/Krone und Pt Nanopartikel durch kontrollierte Destabilisierung und anschließender überkritischer Trocknung in poröse monolithische Aerogele überführt. Die strukturellen, morphologischen und optoelektronischen Eigenschaften der noch nie zuvor gezeigten Nanoheterostrukturen und der entsprechenden Aerogele wurden in der Tiefe mittels mikroskopischer und spektroskopischer Analysetechniken charakterisiert.

Bedingt durch die Ladungsträgerseparation am Metall-Halbleiterkontakt sind die Nanoheteroplättchen vielversprechend für eine fotokatalytische Anwendung. Aerogele bestehend aus CdSe/CdS Nanoplättchen oder aus Pt Nanowürfeln, welche ausschließlich aus exponierten (100) Facetten bestehen, sind passende Strukturen für facettenselektive katalytische Reaktionen. Die potentiellen Vorteile in der Anwendung der hier neu erzeugten Nanopartikel wurden in Vorexperimenten, wie der asymmetrischen katalytischen Hydrierungsreaktion zur Erzeugung stereoselektiver Isomere oder auch der Wasserstofferzeugung durch Fotoreduktion von Wasser unter Verwendung weißen Lichts, gezeigt. Schwerpunkt waren hierbei das Verständnis der zugrunde liegenden Reaktionsmechanismen und der Einfluss des Materials sowie die Diskussion der Ergebnisse mit Bezug auf den heutigen Stand der Forschung.

Abschließend wird ein Ausblick zur Herstellung von Mehrkomponenten-Aerogelen und deren sensorischer Anwendung aufgezeigt.

Schlagworte: Aerogel, Nanoplättchen, Metall-Halbleiter Hybride

Table of Contents

1 Introduction

1.1 Impact of Nanotechnology in Our Life

The word 'Nanotechnology' is very common these days. It is the field where one nurtures the science, engineering and technology of particles which have size in the nanometer regime, typically $1 - 100$ nm. It is a rapidly expanding field of research where the researchers have tremendous success of synthesizing various types of nanoparticles (NPs) and to take advantage of their excellent optical, electrical, thermal and catalytic properties, which could not be simply achieved from their bulk solid counterpart. Probably the most known application of the NPs is the employment of quantum dots in backlight LEDs of the televisions, which have tumulted the world due to its amazing vibrant color quality.[1] Apart from the electronics world, NPs are finding interesting applications, such as stain resistance clothings, sports equipments *e.g.*, stronger and lighter tennis rackets, bicycle, golf sticks are few items to name among many others.[2] The application of titanium oxide or zinc oxide NPs to prepare beauty or cosmetic products is well known now.[3] Nanocomposites which are lighter, stronger and much effective in terms of chemical corrosion are also employed to improve the vehicle fuel efficiency. The so called 'nanofilters' employed in cars remove almost all airborne particles from the air before it reaches the combustion chamber, further improving gas mileage. Currently, the underbody panel of the new C7 Chevrolet Corvette car is fabricated from nanocomposite carbons making the car lighter with better mileage.[4] Portable water purifiers also have nanofilters with pore diameters in the range of 20-30 nm which can remove the viruses, bacteria or hazardous substances present in the water more effectively than the resins materials previously employed for this purpose. Scientists have now prepared sensors based on NPs which are employed to detect the selective chemical

molecules in amazingly low levels *e.g.*, one molecule among one billions.[5] Research is going on to employ these nanosensors in the field of surveillances and security systems or in medical front to accurately identify particular cells or substances in the body for cancer therapy. Also nanoparticles layered nanochips have been developed recently for the detection of antigen-antibody.[6] These are few examples where nanotechnology is employed successfully to improve the existing techniques and our livelihood. More excitingly, researchers all over the world are currently paying attentions to utilize the superior properties of the advanced functionalized NPs in the greater arena of solar cells,[7] water splitting,[8] H_2 fuel production,[9-10] CO oxidation,[11] nano-medicine[12] *etc.*[13-14] Therefore, in near future we can expect even more growth of the nanotechnology in various aspects of life.

1.2 Motivation

Porous aerogels from both metal and semiconductor NPs are highly interesting, since they combine high specific surface area, plasmonic behavior, electrical conductivity, gas permeability and enhanced catalytic activity.[15-17] In general, lyogels (when pores are filled with solvent) are formed by the interconnection or coalescence of the individual NPs in solution. These lyogels can be separated from the solvent by converting them into aerogels *via* supercritical drying, which provide the opportunity to bring the colloidally derived NPs into solid state, while retaining the inherent properties of the building blocks. Aerogels are light-weight, with extremely low density (at least less than 100 times of the corresponding bulk material) and consist of pores typically in the micro (< 2 nm) to macroporous (> 50 nm) regime. Therefore, reactant molecules can easily diffuse through the pores and can avail the inner surface of the gels.[17-20] These properties have made aerogels promising for many catalytic and sensor based applications.[15, 21-22]

Synthesis of shape controlled metal and semiconductor NPs is extremely useful as it provides superior control over the nanoscopic functionalities, such as optoelectronic spectra, surface plasmon resonance, superparamagnetism, *etc*. of the corresponding materials. Moreover, different shapes of the metal NPs exhibit different crystal facets on their surface *e.g.*, cubic particles are dominant in (100), tetrahedral, octahedral, icosahedral particles are dominant in (111) facets.[23-25] In certain chemical reactions, where metal NPs are used as catalyst, it has been observed that one specific shape of the particles show better catalytic activity than the others, which is attributed to the certain crystal facets present on the NPs surface. For examples, Pt nanocubes with enriched (100) facets exhibit higher turnover frequency, than the cuboctahedra, tetraherda and nanowires when employed for the hydrogenation of both *cis* and *trans* stilbine.[26] On the contrary, in many cases, the activity of the (111) crystal facets are found to be higher than the (100) facets.[27] Also in the case of semiconductor NPs, the shape and size have strong influence on the quantum confinement properties such as absorption, photoluminescence (PL) emission *etc*. For example, spherical quantum dots have quantum confinement in 3D, while rods or wire shaped particles are 2D confined and the sheet like NPLs have quantum confinement in 1D. These shape dependent quantum confinement controls the exciton mobility and the optical properties of the II-VI metal chalcogenide semiconductors.

In the present thesis, the development of new synthetic procedures to obtain porous aerogels from quasi 2D CdSe and CdSe/CdS NPLs and from cubic and quasi-spherical Pt nanoparticles is demonstrated. Also, the synthesis of site-selective noble metal growth on quasi 2D CdSe and CdSe/CdS NPLs which can be used as the building blocks for metal-semiconductor heteroaerogels is presented. The motivation of these topics is discussed in the following paragraphs:

Semiconductor NPs with variable bandgaps are very interesting for their size dependent light absorption as well as magnetic properties. Pure or doped metal oxides *e.g.*, Fe_2O_3, TiO_2, SnO_2, MnO and II-VI metal-chalcogenides *e.g.*, CdSe, CdTe, CdS, CdSe/CdS or CdSe/ZnS of different shapes and dimensions are recognized for their applications in photovoltaic, sensing, water splitting, LEDs, drug deliveries, cancer cell treatments *etc.*[28-30] The origin of these optical properties is the quantum confinement effect. Briefly, when the size of any one dimension of the particles is smaller than the average Bohr excition radius then the energy levels of the particles can be well explained by the particle-in-a-box quantum mechanical approach. The wet-chemical synthesis of 2D and 3D quantum confined II-VI metal-chalcogenides are well documented in literature for last ~30 years. Lithographic fabrication of the 1D quantum confined systems *i.e.* quantum wells are also known in literature.[31] Although the wet-chemical synthesis of 1D quantum confined II-VI metal-chalcogenides, which is named as NPLs have been invented recently in 2008, and are comparatively new.[32] These NPLs show fascinating optoelectronic properties such as narrow emission band width, high PL quantum yield, reduced Stokes shift and ultra fast radiative lifetime, due to the strong quantum confinement in their thickness direction. By controlling the quantum confinement and composition of the NPLs, one can tune the electronic structure and the optical properties of these colloidal quantum wells. Moreover, the zinc blend NPLs exhibit (100) crystal facets throughout the large flat surface. In order to improvise these excellent properties into sensor based devices, the NPLs need to be in solid state while maintaining the above mentioned quantum confinement properties. This challenge could be solved by the preparation of aerogel superstructure from these NPLs. In earlier studies, sol-gel techniques have been found to be an efficient way to obtain a voluminous interconnected network of the particles.[19, 33-34] Usually, in sol-gel process, the gel is formed by keeping the solution in atmospheric oxygen or by adding some

destabilizing agents (such as H_2O_2) in the solution. Later the lyogel obtained is converted to solid macroscopic aerogel *via* supercritical drying

The colloidal synthesis of metal NPs in different shapes and dimensions is well known in literature.[23-24, 35] The colloidal solution of the metal NPs exhibit specific color and are finding potential applications in sensors[36], medical diagnostic[37-38] and photonic.[39] In many cases, the application of these NPs derived in liquid phase are limited, especially when surfactant free solid state of the particles are desired. Therefore, there is an inherent need to develop new synthetic strategy to convert them into solid state while maintaining their inherent nanoscopic properties.[40-42]. It is important to note here that the existing techniques of aerogel formation involve multi-step reaction procedures such as concentrating the NPs solution, phase transfer *etc*. Moreover, the gelation process can only be started when the NPs are synthesized in polar solvent or transferred to polar solution. Furthermore, there are no reports on the synthesis of aerogels from shape controlled metal nanoparticles directly from organic solution, which would be advantageous since, the interconnected network of the metal NPs will have certain crystal facets outside, suitable for facet selective catalytic reactions as mentioned above. Therefore, optimization of the existing process of aerogelation is required to circumvent the above mentioned obstacles and to assemble the NPs in a simple and cost-effective way.

The combination of both metal and the semiconductor in the same particle helps to manipulate the synergistic properties of each element in the same segment and evolve new properties which could not be simply achieved from a single component. In particular the synthesis of noble metal decorated II-VI metal-chalcogenide semiconductors such as nanorods, and nanospheres are finding applications in photocatalytic water splitting, H_2 gas generation, and organic dye degradation or as sensors for detecting chemicals.[30, 43-47]

Although, the synthesis of heterostructures by growing noble metal domains on the NPLs and their applicability in different catalytic reactions have not been investigated at the beginning of this thesis. Especially, the questions like what would be the final morphologies of the hybrid structures, the nucleation behavior of the metal domains, the optical and catalytic properties of the hybrid NPLs, have motivated us to investigate the chemistry of metal decorated NPLs. Theoretically, the NPLs have larger flat surface than the nanospheres or nanorods and therefore NPLs could be more advantageous for photocatalytic reactions. It has been shown recently, that the CdSe NPLs have higher molar extinction coefficient than the spherical quantum dots, the molar extinction coefficient increases with increasing lateral dimensions of the NPLs.[48] Hence, in terms of light absorption, the colloidal NPLs would be advantageous over the nanospheres, especially when the photocatalytic reactions are considered. Moreover, the extent of charge carrier separation in the hybrid structure depends on the final morphologies; therefore, it would be of high interest to see how the electrons and holes are spatially separated upon photo-excitation after the selective growth of noble metal domains on the NPLs. In this context, it is highly relevant to develop new approaches to synthesize metal decorated hybrid NPLs and to compare their catalytic activity with the existing hybrid materials.

Overall, the thesis is dedicated to develop and optimize the process of aerogel formation from shape controlled noble metal NPs and newly invented II-VI metal-chalcogenide NPLs, since the shape control will bring certain crystal facets all over the surface of the gels which would be suitable *e.g.*, facet selective catalytic reactions. Moreover, the gels from the semiconductor NPLs will exhibit tunable optical properties, which would be suitable for sensor based applications. The other goal is the development of metal-semiconductor heteronanoplatelets by growing noble metal domains on the CdSe and CdSe/CdS NPLs and

to investigate the morphologies, metal nucleation behavior charge carrier separation on the flat surface of the NPLs.

1.3 Nanoparticles Properties

The properties of the NPs strongly depend on their material compositions and also on the size and shape. For example colloidal solution of Au NPs appears as deep red, Ag NPs appear as deep brown. Moreover, the Au NPs melt at much lower temperature ~300°C (for 2.5 nm size whereas, the bulk gold slabs have a melting point of 1064°C.[49] There are many interesting properties of the NPs due to their high surface to volume ratio such as high rate of particle diffusion, low temperature sintering, superparamagnetism *etc.* In the following sections, the properties of the semiconductor, metal NPs and metal-semiconductor hybrid are described in details.

1.3.1 Semiconductor Nanoparticles

Quantum Confinement Effect

The word 'confinement' means to restrict the motion of the randomly moving electrons in specific energy levels, and the word 'quantum' reflects atomic realms of particles. When the size of the semiconductor material decreases, the bandgap increases and the energy levels of the system become more discrete.[50-51] In nanometer scale, the energy levels are not continuous anymore; rather discrete energy levels develop. The average distance between the electron and the hole is called exciton Bohr radius. In general, if the size of a semiconductor particle in any of its dimensions is smaller than the exciton Bohr radius, then

it can be said that the particle is quantum confined and the quantum mechanical model of a particle-in-a-box can be employed as an approximation.

The change in the bandgap energy with decreasing particle size is sketched in Figure 1. It can be seen that with decreasing size of the particles the bandgap increases *i.e.* the small particles have larger bandgaps than the big particles.
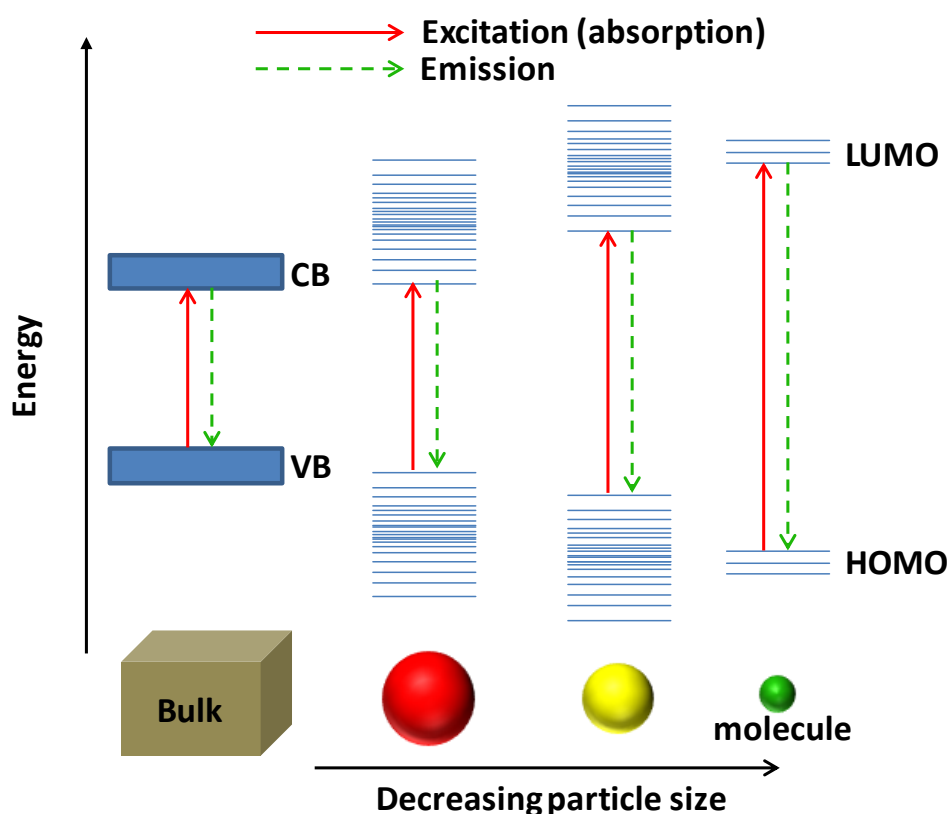

Figure 1. Schematic drawing of bandgap variation of the semiconductor materials. With the decreasing size of the particle, the bandgap increases and in molecule the bandgap become distinct. It should be noted that the changes in the conduction band (CB) and the valence band (VB) are most cases not symmetric but depend on the effective mass of the electron and the hole.

For larger particles, the bandgap become smaller and gradually approaches the value of the bulk bandgap. This so-called quantum confinement effect can be explained theoretically

considering two approaches. One is the linear combination of atomic orbital (LCAO) theory and the other one is the solid state theory. In LCAO theory n number of atomic orbitals (having same symmetry and with similar or the same energy) by linear combinations will form n number of molecular orbitals. In the case of a bulk solid material, n is very large and the bandgap of the material become constant, but in the case of NPs, this will critically depend on the particle size. This effect is referred to as size quantization effect. The other approach is the solid state theory which considers the effective-mass approximation principle. In comparison to the solid, in the NPs the charge carriers are constricted by the outer limits of the NP which is acting as potential wall (similar to the model of the particle-in-a-box approximation, the potential outside the NP is considered to be infinite). The model of effective mass approximation takes into account the fact that a crystalline solid has no constant potential, rather a periodical oscillation happen (a crystal consists of a periodic arrangement of atoms). In such cases, one cannot consider the rest masses as masses of the charge carriers; instead one should consider the so-called effective masses. Scientist Brus for the first time gave the theoretical calculation (equation 1) for the bandgap of the nano-sized semiconductors considering the effective mass approximation.[52] In this approximation an exciton (electron hole pair) is considered to be confined in a spherical volume of crystallite.

$$E_{NC} = E_g + \frac{h^2}{8R^2}\left(\frac{1}{m_e^*} + \frac{1}{m_h^*}\right) - \frac{1.8\,e^2}{4\pi\varepsilon_0\varepsilon_r R} \tag{1}$$

where, E_{NC}: Bandgap energy of the nanocrystal, E_g: Energy of the bandgap in bulk , h: Planck's constant, R: Particle size (radius of quantum dot), m_e^*: effective mass of the electron, m_h^*: effective mass of the hole, e: electron charge, ε_r: relative permittivity, ε_0: permittivity of vacuum.

Later on the electron–hole attraction is taken into account and the Brus equation is modified. The modified Brus equation can be represented as equation 2.

$$E_{NC} = E_g + \frac{h^2}{8R^2}\left(\frac{1}{m_e^*} + \frac{1}{m_h^*}\right) - \frac{1.8\,e^2}{4\pi\varepsilon_0\varepsilon_r R} - 0.248\left(E \times R_y\right) \qquad (2)$$

where, $E \times R_y$ is Rydberg energy.

Optical Transitions in Nanocrystals

Quantum confinement effects have great influence on the absorption spectra of quantum dots (QDs). An example is illustrated in Figure 2, which shows the absorption spectra of CdTe QDs of different sizes. It should be noticed that in the strong quantum confinement regime the energy spacing between the discrete levels with different quantum numbers is in the order of hundreds of meV, and therefore optical transitions between these levels can be clearly resolved in the optical absorption spectrum.[51] It can be also noticed that with decreasing size of the CdTe NPs, the absorption maximum shifts to higher energy regime. The lowest energy optical transition can be assigned to the $1S_h$ to $1S_e$ transition (where, h denotes the hole and e denotes the electron), the second transition to $1P_h$ to $1P_e$ and the third transition from $1D_h$ to $1D_e$. It is important to note that the exciton Bohr radius (a_0) provides a very convenient length scale to evaluate the impact of quantum confinement on the properties of semiconductor materials. It can be correlated that when the bandgap is more narrow, the exciton Bohr radius is larger. For example PbSe nanocrystals having *Eg* of 2.26 eV the a_0 is 46 nm while in case of CdSe with *Eg* 0.26 eV the a_0 is 4.9 nm.
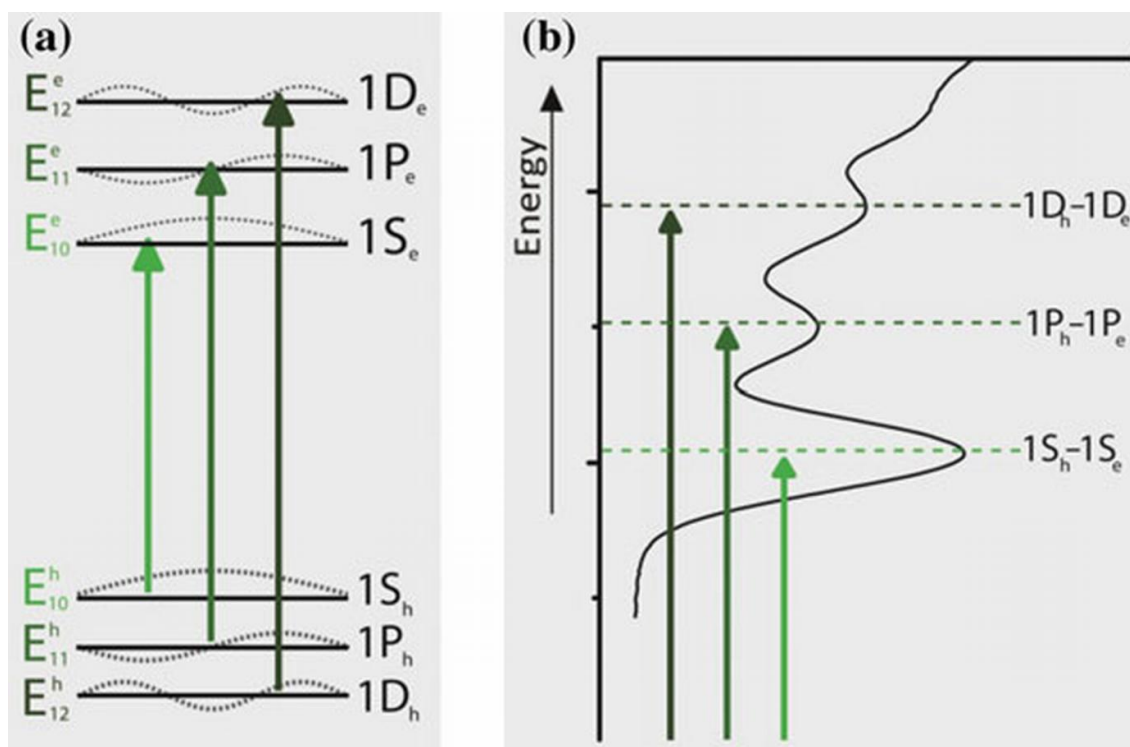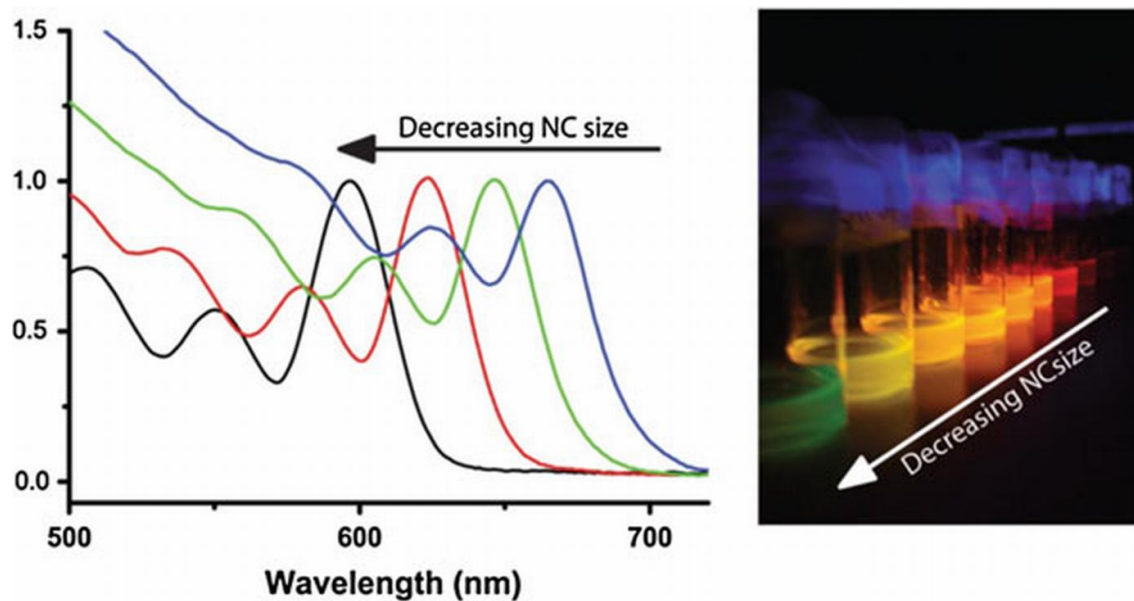
Figure 2. Upper panel absorption spectra and the photographs of the CdTe nanocrystals of different sizes. Lower pannel (a) illustrates the electronic transitions (b) assignment of the electronic transions to the respective absorption bands in relation to the energy from reference 51. Reprinted with permission from Springer.

Quantum confinement has also strong effects on PL emission of the nanocrystals.Upon photoexcitation the electrons are excited to the upper electronic states and when the electrons relaxed to ground energy state they emit energy (equivalent to the band gap) in terms of photons. The emission energy depends on crystallite size, with increasing size, the PL emission is shifted to low energy regime and vice versa.

Effects of Different Shapes

In the above discussions only spherical QDs are considered where the exciton is confined in a zero dimensional spherical potential well. However, colloidal semiconductor nanocrystals can have different (considering geometry) zerodimensional shapes *e.g.*, cubic, tetragonal, pyramidal or one dimensional *e.g.*, nanorods, nanowires and two dimensional *e.g.*, nanoplatelets, nanosheets, quantum wells *etc*. Those shapes can also acquire quantum confinement effect if the dimensions are smaller than the average exciton Bohr radius (a_0). Of course the extent of quantum confinement may varry in the different dirrections depending on the shapes and sizes. Therefore, if any two dimensions are smaller than the a_0, then the particle will experience two dimensional quantum confinement and this is generally observed in quantum rods. In the case of the NPLs the excitons are confined only in one dimension, that is in the thickness direction.[51] A schematic drawing demonstrating the energy level structures of the semiconductors with respect to the density of states is shown in Figure 3. The density of states describe the number of states that are available in a system and is essential for determining the carrier concentration and energy distribution of the carriers within a semiconductor.
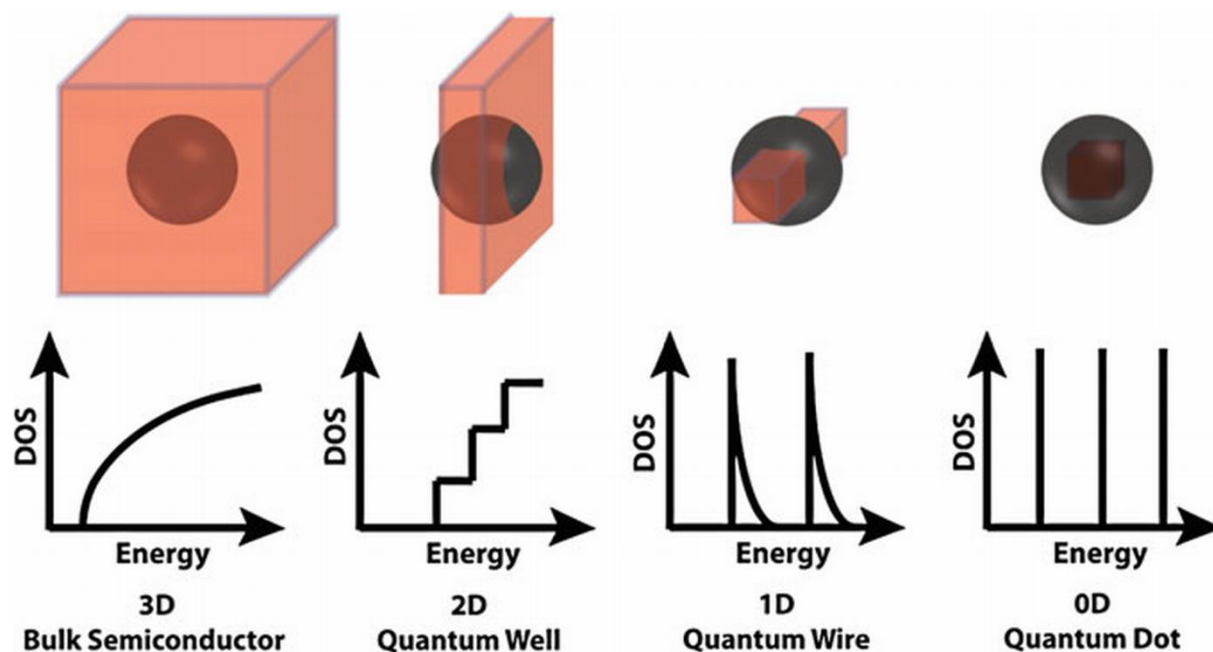
Figure 3. Schematic illustration of the density of states (DOS) with respect to energy level of semiconductor nanostructures with reduced dimensionality (3D, 2D, 1D and 0D indicate three, two, one, or zero-dimensional, respectively). The exciton Bohr diameter is represented by the sphere from reference 51. Reprinted with permission from Springer.

Cadmium Based Semiconductor Nanoparticles

Probably the most investigated metal-chalcogenide semiconductor system is CdSe, which is a n type II-VI semiconductor. Apart from CdSe; CdS, CdTe NPs are also well known in literature due to their unique optoelectronic properties.[50, 53-55] The bandgap of bulk CdSe is ~1.74 eV.[56] CdSe particles in nanometer scale shows quantum confinement properties, where the bandgap of the particles can be tuned by variation of the diameter of the particles.[56] Different shapes of the CdSe nanocrystals starting from spherical quantum dots, nanorods, nanowires, pyramids, tetrapods, octapods, to multipods are known in literature.[56-57] The optical properties of the particles also vary with shape variation. Because of their

highly tunable optical properties, CdSe NPs are highly promising material in the fields of photovoltaic, solar cell, LEDs, quantum computing, medical imaging, water splitting *etc*. The most commonly employed technique to synthesize high quality CdSe NPs is the 'hot injection method' (see section 1.4), where the NPs (capped on their surface with organic surfactant) are dispersed in organic or aqueous solution after synthesis.[54-55] The reaction parameters, such as precursors, organic ligands, temperature and reaction time have strong influence on the properties, size and shape of the CdSe NPs.[54, 58] Specific ligands are absorbed on selective facets of the nanocrystals and monitor the growth of the crystals in certain direction to obtain various shapes *e.g.*, nanorods,[59] nanowires,[60] octapods,[61] tetrapods,[62] multipods,[63] pyramids *etc.*[56]. Figure 5 represents the TEM images of the Cd based NPs of three different shapes. Suitable choice of reagents and reaction conditions could lead to very high (> 90%) PL quantum yield (PLQY, which is defined as the ratio of number of photons absorbed by the system and the number of photons emitted). The properties of CdE (E = Se, S and Te) NPs can even be modified by the growth of a shell of another material (*e.g.*, over growth of CdS or ZnS or PbS on CdSe QDs) on the previous one *via* so called 'seeded growth' technique.[57, 59] The CdSe/CdS core/shell nanospheres and nanorods are important members of this family with high application possibilities. The anisotropic layer of CdS on CdSe not only increases the PLQY of the NPs but also provides better stability and functionalities which cannot be simply observed in one material. The seeded CdSe/CdS nanorods are highly interesting for their high PLQY and suitable bandgap alignment (type I) which enables strong light absorption in the UV-vis regime and are finding interesting applications in photocatalysis.[30, 43] In the past two decades, enormous development has taken place in this arena regarding the synthesis, structural modifications, and application possibilities of these Cd based nanocrystals which is virtually unmanageable.
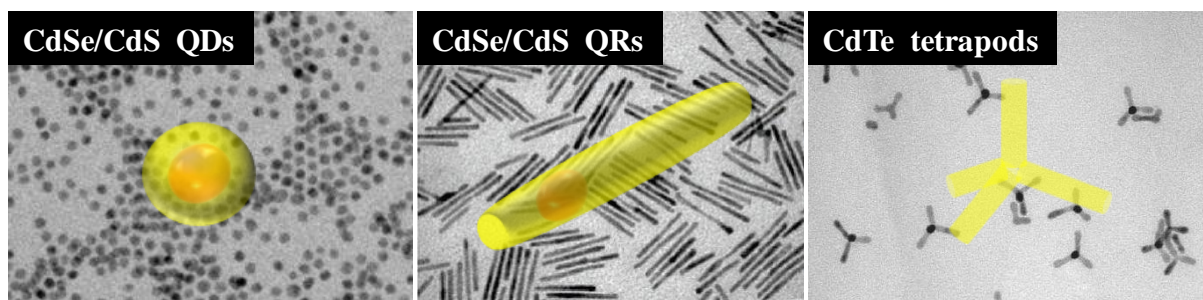
Figure 5. Different shapes of cadmium based NPs. (left) Spherical CdSe/CdS core/shell QDs (middle) CdSe/CdS core/shell nanorods, (right) CdTe tetrapods (from reference 64) having four arms. (CdTe tetrapods) Reprinted with permission from Nature publishing group.

Within the limited scope of this thesis, in-depth discussions regarding the diverse synthesis techniques, properties and applications of the cadmium based NPs are not included. For more in-depth knowledge readers are encouraged to consult the following articles (28, 54-55, 64-69).

Cadmium Based Nanoplatelets

Cadmium based nanoplatelets or nanosheets (or even sometimes called quantum wells) are the new members of this family of II-VI metal-chalcogenides, where the excitons are strongly confined in the z direction. In 2006, Hyeon and co-workers for the first time reported the synthesis of CdSe nanoribbons at much lower temperature (at 70°C) employing cadmium chloride alkylammonium complex and selenocarbamate as the precursors.[70] The nanoribbons exhibit wurtzite crystal lattice structure with a length which can reach few hundreds of nanometer, width of 10-20 nm and a uniform thickness of 1.4 nm. Due to the large lateral dimensions, the nanoribbons normally form aggregates and are not stable in colloidal solution. It was also reported that the cadmium chloride alkylammonium complex forms a lamellar structure in solution which in turn serves as a

mold for the formation of the CdSe nanoribbons. The nanoribbons with hexagonal structure grow along the [001] axis or c axis, their width is along [110] and the thickness is in the [110] direction. The crystal structure of wurtzite nanoribbons are elaborately explained in the following section. Slight variation of the synthesis parameters yields CdSe nanosheets, which are nanoribbons with a larger width ~100 nm and can be dispersed in colloidal solution.[71] The synthesis technique of Hyeon *et al.* was adopted for many other systems such as CdTe,[72] Mn^{2+} doped CdSe nanoribbons,[73] CdSe quantum belts[74] *etc*. The quantum belts are structurally similar to the nanoribbons; their first two electronic transitions are attributed to the light-hole electron and heavy-hole electron transitions as is proposed in the case of zinc blend NPLs.

In 2008, Ithurria *et al.* have reported for the first time the synthesis of zinc blend rectangular, quasi 2D CdSe NPLs, where the thickness can be controlled at atomic level.[32] Detailed synthesis procedure is described in section 4.2. In this synthesis, the lateral dimensions of the NPLs can be tuned from few nanometers to few hundreds of nanometer. The colloidal solution of the NPLs with lateral dimensions < 100 nm are stable. The thickness of the zinc blend NPLs can also be tuned in atomic levels.

The absorption spectra of the NPLs show discrete electronic transitions and very sharp PL emission. The emission peak width full width at half maximum (fwhm) measured is < 10 nm, which is much narrower than the 0D nanospheres or 1D nanorods. The Stokes shift between the first extinction peak and the emission maxima is < 10 meV, which is also never observed in the case of quantum dots or nanorods.[32] Soon after the development of CdSe NPLs, these methods were successfully adopted for other types of CdE (E = Te, S) NPLs preparation with thickness controllable over 3 to 11 monolayers.[75] The monolayer thickness of the NPLs can be distinguished by measuring UV- Vis absorption and PL

emission spectra (*e.g.*, 3 monolayer thick CdSe NPLs have sharp emission peak at 463 nm, for 4 and 5 monolayer at 513 nm and at 551 nm, respectively).[76] Very recently, the synthesis of anisotropic core/shell or core/crown NPLs are also reported by growing CdS either to the top and bottom surface of the pre-synthesized CdSe NPLs (for core/shell) or by growing only in the lateral dimensions of the NPLs, where the thickness do not alter upon CdS growth (for core/crown).[77-80]
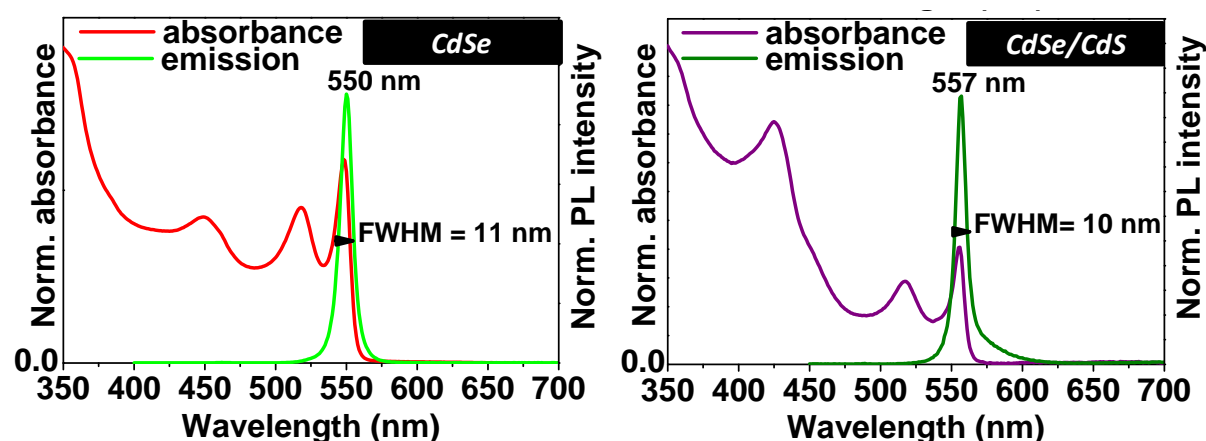

Figure 6. Optical properties of CdSe and CdSe/CdS core/crown NPLs of only 5 ML thickness. Five monolayers thick CdSe NPLs have strong emission maximum at 550 nm. After the CdS crown growth surrounding the edges if the CdSe NPLs, the emission peak shift to 557 nm. The strong absorption band offset of CdS can be seen at 430 nm. The NPLs have very sharp emission peak with fwhm 10-11 nm.

The optical properties of these NPLs are shown in Figure 6. After the growth of the CdS crown on CdSe core NPLs, the CdS absorption band appears at 430 nm and the PL emission peak is shifted only by 7 nm towards higher wavelength regime, which in turn indicate the growth of CdS only in the lateral dimensions of the core CdSe.[77] Later on cation exchange approach was utilized on CdSe/CdS NPLs for the preparation of core/shell ZnSe/ZnS and PbSe/PbS NPLs.[81] The fascinating optoelectronic properties of the NPLs have attracted tremendous attentions of the researchers and as a results in last few years

many publications have come out regarding the optimization of the synthesis conditions or the application of the NPLs in various fields such as room temperature lasing,[82-83] field effect transistors,[84] polarized light emission,[85] phonon line emission[86] and many more.[87-89] In the section below, the formation mechanism of the NPLs and the structural morphologies are discussed in details.

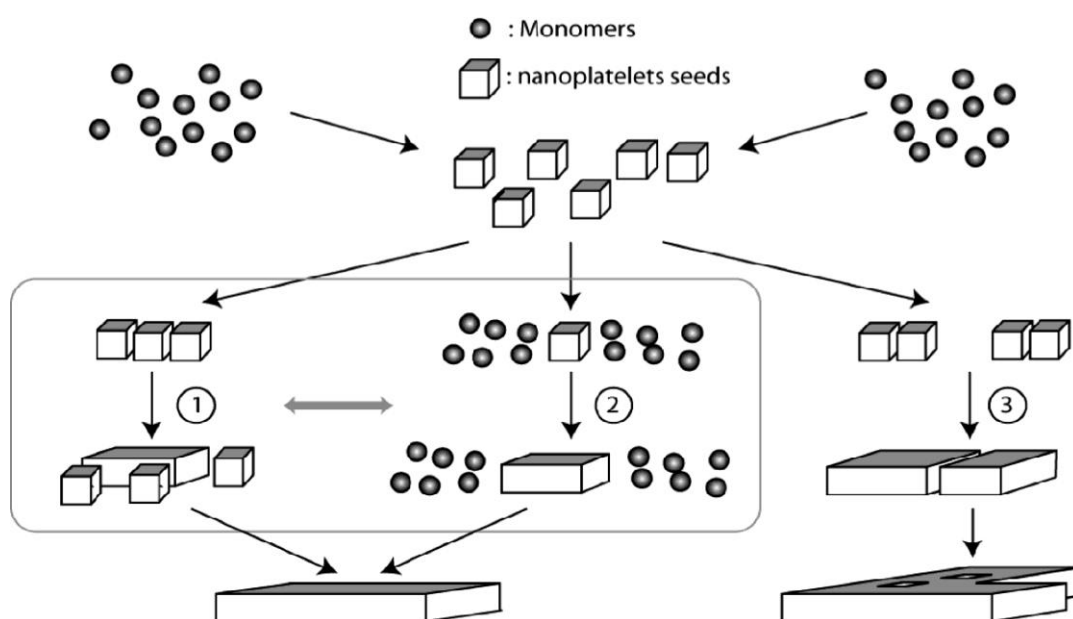## Nanoplatelet Formation Mechanism

Figure 7. Possible mechanisms for the CdSe NPLs lateral extension. The first step is the formation of the NPL seeds with dimensions < 2 nm from reaction of Cd and Se precursors. In paths 1 and 3, the lateral extension results from the self-organization of seeds that assemble only at the seed level or in patches, respectively. In path 2, the seeds form and extend laterally by continuous reaction of precursors. Photograph is reprinted with permission from 90. Copyright (2016) American Chemical Society.

The growth mechanism of the atomically thin NPLs is not yet perfectly understood. A possible mechanism, evaluated from the optical spectroscopic measurements by the Dubertret group is illustrated here in Figure 7.[90] According to their analysis, during the first

course of the reaction, after the addition of the Se precursor, small clusters of CdSe form, which in turn rapidly associate on the existing small NPLs to extend it laterally as described in path 1. It is also possible that there is a continuous reaction of the precursors (Cd and Se) to the newly formed NPLs seed to form larger rectangular sheet as shown in path 2. Third possibility is that the small NPLs clusters are formed at the expense of the NPLs seed, then these clusters associates together to form the NPLs (path 3).

Crystal Structure of the Nanoplatelets

The NPLs can acquire two types of crystal lattice structure depending on the ligands employed to stabilize the particles. For example when octylamine or oleylamine is employed as the ligand, wurtzite crystal structure results and when oleic acid is employed as the capping ligand zinc blend crystals are formed.[79, 91] It is proved with density function theory (DFT) calculations and molecular simulation that although wurtzite is the most stable polymorph of bulk CdSe, the NPLs synthesized in presence of acetate ligands, acquire zinc blend crystal lattice structure as the acetate covered surface has overall lower energy than the wurtzite ones.[92] The crystal structures of both wurtzite and zinc blend NPLs are shown below in Figure 8. The flat surface of the wurtzite NPLs is (110) which is perpendicular to the [111] axis and for zinc blend NPLs it is (100) facets which is perpendicular to the [100] axis. The (110) facets of wurtzite NPLs is composed of stoichimetric ratio of trivalent Cd and Se atoms, whereas, the (100) crystal planes of zinc blend terminate with divalent Cd atoms. The tetravalency of the Cd atoms on the surface of the wurtzite NPLs are satisfied with monodentate amines, whereas bi-dentate carboxylate ligands form chelate complex with the divalent Cd atoms present on the surface of the zinc blend NPLs.[91]
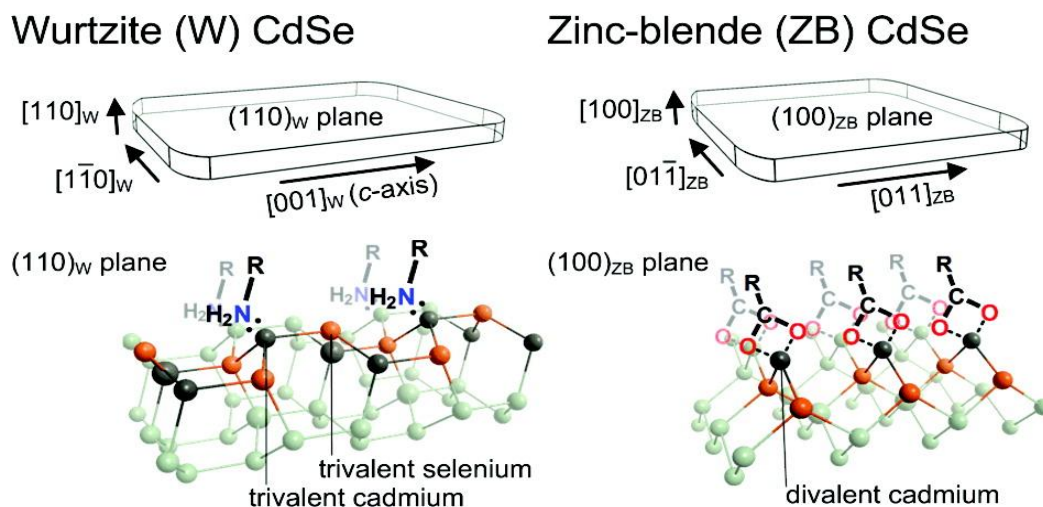
Figure 8. Crystal structure of wurtzite and zinc blend CdSe NPLs. The flat surface (110) of the wurtzite structure ends with trivalent Cd and Se atoms whereas, the flat surface (100) of the zinc blend NPLs terminates with bivalent Cd atom. Reprinted with permission from reference 91. Copyright (2012) American Chemical Society.

1.3.2 Metal Nanoparticles

Surface Plasmon Resonance

The optical properties of many metal nanostructures in the visible region are dominated by absorption and scattering due to the occurrence of localized surface plasmon resonance, which is caused by collective conduction band electron oscillation in response to the electrical field of the incident light irradiation.[93] When the frequency of the oscillation and the frequency of the light match, plasmon resonance can be excited. Particles acquiring a negative real and small positive imaginary dielectric constant are generally capable of supporting surface plasmon resonance (SPR).[94] A schematic illustration of the interaction of the metal NPs with electromagnetic waves is shown in Figure 9. In 1908, Gustav Mie[95]

found the exact solution to the Maxwell equations for the optical response of a sphere of defined size which is immersed in a homogeneous solution and subject to a plane monochromatic wave. When the size of the particle is much smaller than the wavelength of the light, the particles experience a field which is spatially constant with a time dependent phase, which is known as quasi static range.

$$\sigma_{abs}\left(\omega\right) = k \cdot 4\pi R^3 I\, m \left[\frac{\varepsilon(\omega) - \epsilon_m}{\varepsilon(\omega) + 2\epsilon_m}\right] \qquad (3)$$

$$\sigma_{sca}\left(\omega\right) = k^4 \cdot \frac{8}{3}\pi R^6 \left[\frac{\varepsilon(\omega) - \epsilon_m}{\varepsilon(\omega) + 2\epsilon_m}\right]^2 \qquad (4)$$
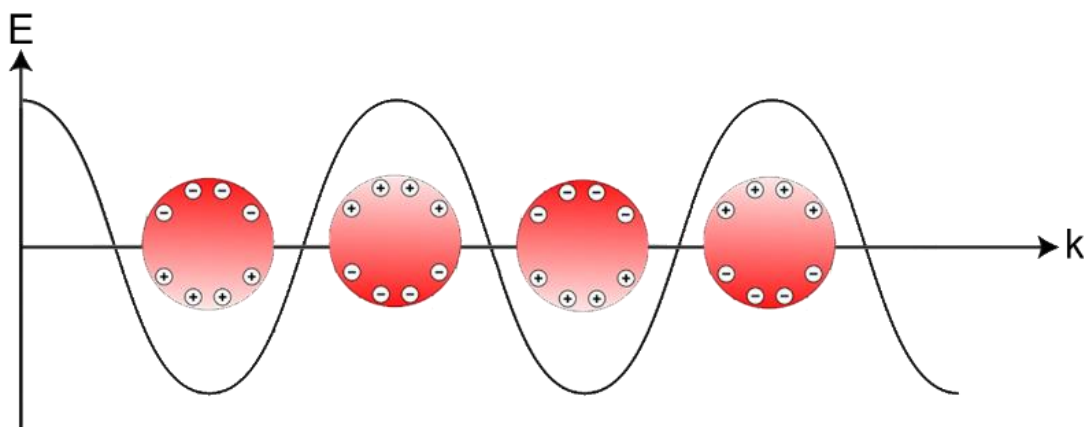
Figure 9. Light induced collective charge carrier density oscillation in metal nanoparticles. Here, the electric field is considered to be homogeneous over the particle volume, and the carriers are restricted within the surface boundary of the NPs.

Within this range the displacement of the charges in the spheres is homogeneous, yielding a dipolar charge distribution on the particle surface. This means the electromagnetic field is similar in each point of one particle and there is no deviation over the particle volume. Therefore all volume units are excited by the electromagnetic field (light) simultaneously,

which oscillates itself over the time. Within this electrostatic approximation, the absorption and scattering cross section of a spherical particle can be calculated (shown in reference 96). Where, σ_{abs} and σ_{sca} are the absorption and scattering cross section, respectively, ω is the frequency, k is the wave number, R is the radius of the sphere, ε_m dielectric constant of the solution, ε is the dielectric constant of the particle. The complete derivation of the equation 3 and 4 can be found in this reference 96. From this equation one can predict the position of the plasmon absorption for spherical metal NPs. According to this equation if $\varepsilon(\omega) = -2\varepsilon_m$, the condition for LSPR will be satisfied. This is to be noted here, that these quasi static approximation is not valid for larger particles and different shapes of the particles. Also it can be seen from these equations that in the quasi static regime no size dependence of the plasmon position exist. Additionally, the dielectric constant for the extremely small particles is not constant; it varies with the size of the particle. Hence for larger particles of different shapes and compositions, one needs to take into account lattice mismatch, polycrystalinity as well as damping effects for describing the LSPR.

Facet Selective Catalysis Reaction

Metal NPs expose low index crystal facets depending on the shapes. For example octahedral, cubic and rhombic dodecahedral nanocrystals are bound by (111), (100) and (110) low-index facets, respectively. Facet selective catalysis reactions can be appraised more accurately if there are only a single set of crystal facets available in the NPs. In Figure 10 a schematic diagram of different shapes of polyhedral bound by different crystal facets is shown. EI-Sayed and coworkers investigated the facet dependent catalytic activity of the Pt NPs with varied shapes for electron transfer reaction between hexacyanoferrate and thiosulfate.[97-99] It is proved that for this type of reactions, the tetrahedral Pt NPs containing (111) crystal facets exhibited better catalytic activity than the (100) faceted Pt nanocubes.[98]
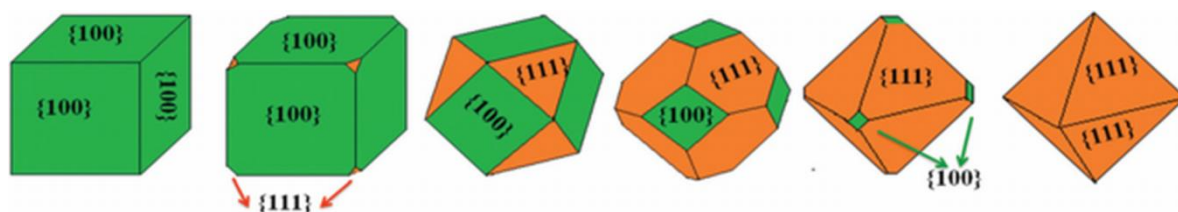
Figure 10. Schematic diagram of different shapes of polyhedral with differently bound crystal facets. Photograph is reprinted with permission from reference 100.Copyright permission (2015) Royal Society of Chemistry.

Later on Somorjai *et al.* conducted a comparative study of the catalytic activity of different shapes of Pt NPs during hydrogenation reactions. It was observed during the hydrogenation of benzene, cyclohexane was the major product when (100) facted-Pt nanocubes were employed as catalyst, but a mixture of cyclohexene and cyclohexane was obtained when Pt cuboctahedra bound by (100) and (111) facets were employed as catalyst. [101] Yeager *et al*. reported that in oxygen reduction reactions also the different shapes of Pt NPs show a decreasing order of catalytic activity in the sequence of (110) > (111) > (100).[102] Also, Pd NPs enclosed by different crystal facets are known for hydrogenation, Suzuki coupling, oxygen reduction and formic acid oxidation reactions. For selective hydrogenation of 1,3-butadine, (110) enriched Pd single crystals were found to be five times superior than the (111) facet exposed Pd.[103] These differences in catalytic activity of different facets are in general attributed to the preferential adsorption of the reactant molecules on certain type of facets. Hence, it can be concluded, that the synthesis of metal NPs bounds with certain single crystal facets are useful for facet selective catalytic reactions. More details regarding the catalytic activity of the shape controlled metal NPs, readers are encouraged to see the review reference 100.

1.3.3 Metal-Semiconductor Heterostructures

The combination of metal and the semiconductor material in the same NP generates hybrid structures where the properties of both can be manipulated in the same material. Photoexcitation of such hybrid materials causes charge carrier separation at the metal-semiconductor interface, where the holes remain at the semiconductor and the photo-excited electrons are transported to the Fermi level of the metal domains. By virtue of this charge carrier (electron-hole) separation, the hybrid materials are highly promising as catalysts for photocatalytic reactions (*e.g.,* organic dye degradation, pollutant degradation) or in photocatalytic H_2 fuel generation through water reduction reactions. [23,25,27,35] Various synthetic approaches starting from thermal reduction, photo-induced reductions to UV light assisted metal deposition are the commonly employed techniques among others which have been developed by the researcher to produce hybrid structures with different structural morphologies. In literature many possible combinations of these two components (metal and semiconductor) have been exclusively reported in the past decades. [30, 104] In earlier cases, Au, Ag, Cu and Pt metal islands were grown on semiconductor NPs such as ZnO, Fe_2O_3 or TiO_2. [105-108]. The drawbacks in these systems are the limited control over the shape and size of the semiconductors as well as the location of the metal domains. Regarding the hybrid structures of II-VI semiconductor, Banin's group for the first time in 2004 has developed synthetic strategies to grow Au domains on CdSe nanorods and tetrapods. [109-110] In this report, Au domains were found to be present selectively at the apex of the nanorods and the tetrapods. Afterwards, this route was followed for other different shapes and compositions of metal-chalcogenide. Synthetic techniques are not only limited to grow Au but also have been extended to other noble metals such as Ag, Pt, Pd, Ni, Co or even combination of two or more than two metals or semiconductors in the same segment *e.g.*,

CdSe-Au/Pt,[111-114] CdS-Au,[115-116] CdSe/CdS-Au/Pt/Pd/Co/Ag.[65, 117-119] In some cases, metal domains can be directed to grow site-selectively on the semiconductor, those structures are particularly interesting because here the holes and the electrons can be separated with a definite spatial distance which in turn reduce the chances of recombination.[120] Epitaxial growth of the metal domains on the semiconductor is useful in fabricating nanoscale devices, but the process is challenging because of the lattice mismatch between the metal and the semiconductor components. In 2010, the group of Manna has been successful to grow Au domains epitaxial on CdSe nanorods by thermal annealing using the electron beam of the TEM. Apart from the fundamental study of the optoelectronic properties of the hybrid structures, a great deal of research has also been dedicated for various promising future applications such as H_2 generation, water splitting, dye degradation, electrical transport properties.

In this context, it is to be noted that the growth of noble metal domains on newly invented quasi 2D NPLs has not been investigated before the starting of this thesis. The NPLs with large flat surface might lead to different structural morphologies and optical properties. Also, theoretically the NPLs exhibit large specific surface area and high molar absorption coefficients and hence would likely be advantageous over their nanorods or quantum dots counterpart and could lead to better photocatalytic performance. Therefore, a new synthetic technique is developed to grow noble metal domains on CdSe and CdSe/CdS NPLs and in-depth characterizations of the morphologies have been performed with TEM and TEM EDXS analysis. The results of these experiments are elaborately described in section 4.2 and 4.3.

Optical Properties of Nanoheterostructures

After the metal domain growth on the semiconductor the optical spectrum (namely absorption, emission, PL excitation) changes significantly. The spectra of the hybrid particles are not the simple sum of those of the individual components, rather it might be considered as the formation of new electronic states at the metal-semiconductor interface.[121] It was observed in the case of matchstick like core/shell hybrid structure that the coherent and incoherent interactions between the metal and the semiconductor lead to broadening and shifting of the first electronic transitions.[115] In the case of Au domain growth on CdS nanorods, the plasmon peak of Au was found to be shifted from 527 nm to 538 nm, which was explained by considering the polarizability and electrodynamics interactions between the two components (for details see reference122). In most of the cases, after the metal domain growth the absorption spectra become broader.

The fluorescence of the semiconductor system may be enhanced or quenched after the metal domain growth. The enhancement of fluorescence strongly depends on the distance between the two components, nature of the interface and also the extent of spectral overlap of the surface plasmon resonance and the emission spectra. For example CdSe/ZnS NPs when adsorbed on a Ag/SiO$_2$ core/shell structure, an enhancement of the fluorescence intensity was observed with increasing thickness of the silica shell.[123] In cases when the metal domains are in direct contact with the semiconductor, the fluorescence is drastically quenched due to the charge transfer from the semiconductor to the metal domains. This effect is observed in most of the hybrid metal-semiconductor heterostructures.

Schottky Barrier between the Metal-Semiconductor Interface

When a metal and a semiconductor domain are in contact with each other, a potential barrier appears at the interface of the two component which is known as Schottky barrier.[124] Schottky and Mott subsequently explained the mechanism of the barrier formation and also proposed a model for the calculation of the barrier height and also the shape of the barrier. Although numerous research works have been dedicated on this matter still the understanding of the metal-semiconductor junction is not complete probably due to the process dependent character of the junction. The ideal diagram for the schottky contact formation between a n type semiconductor and the metal where $\Phi m > \Phi s$ (where Φm and Φs are the work function of the metal and the semiconductor, respectively) is shown in Figure 11. The work function of the metal can be defined as the energy required, raising one electron from the Fermi level to the vacuum level. The work function of semiconductor is also defined similarly and is a variable quantity depending upon the doping of the semiconductor. According to this model the barrier generates due to the differences between the work functions of the two substances. The work function Φm has a volume contribution and a surface contribution. The parameter χ_s which is the electron affinity, defined as the energy difference between vacuum level and the lower edge of the conduction band, $\emptyset_m$ and $\emptyset_s$ are usually expressed in eV. In case of pure semiconductor there are no band bending because there are no charges at the surface of the semiconductor. While in the case of metal-semiconductor hybrid structure, after the contact is made and the equilibrium is developed, the free electron concentration near the boundary region decreases as the electrons from the semiconductor move out into the metal to create the equilibrium. Since the separation between the conduction band edge (E_c) and the Fermi level (E_f) increases with decreasing electron concentration and in thermal equilibrium the

E_f remains constant throughout, the conduction band edge E_c bends up as shown in Figure 11.

The E_c band electrons which cross over into the metal leave a positive charge of ionized donors, so the semiconductor region near the metal get depleted of mobile electrons. Therefore a positive charge is established in the semiconductor side and the electron which cross over into the metal form a thin layer of negative charge in the metal (near the Thomas Fermi screening distance from the interface ≈0.5A°). Subsequently an electric field generates from the semiconductor to the metal. As the bandgap of the semiconductor and the electron affinity do not alter upon the contact establishment, the conduction band, valence band and the vacuum level undergoes bending at the same extent.
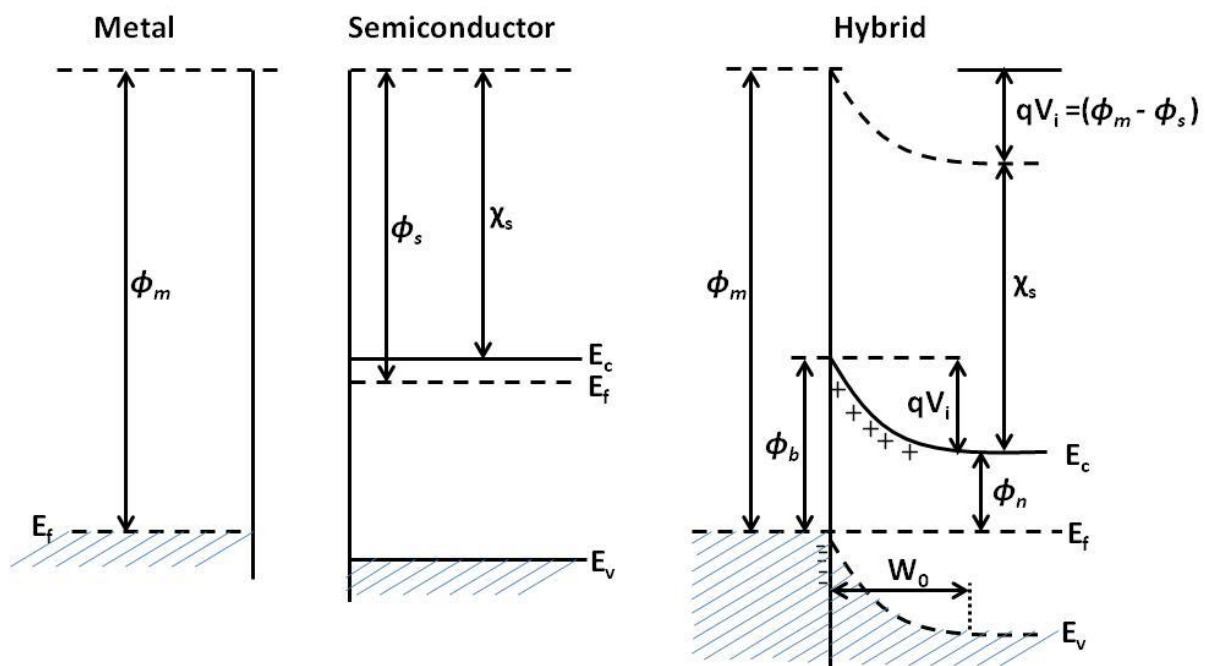

Figure 11. Electron energy band diagram of metal, semiconductor and metal-semiconductor hybrid materials forming Schottky junction.

Therefore the barrier height $\emptyset_b$ can be calculated from the difference between the $\emptyset_m$ and χ_s i.e. $\emptyset_b = \emptyset_m - \chi_s$ and as $\emptyset_s = \chi_s + \emptyset_n$, therefore $\emptyset_b = (qVi + \emptyset_n)$ where, $\emptyset_n =$

$(E_c - E_f)$ and $qV_i = (\emptyset_m - \emptyset_s)$. Where, q is electronic charge, V_i is contact potential difference or the built in potential of the junction. The foregoing discussions are only for a simple ideal contact between the n type semiconductor and metal with no net charge on the semiconductor. In practice the determination is more complicated.

The schottky barrier generates after the metal contact on the CdSe, CdS semiconductors is described by Brucker *et al.* The Schottky barrier height between the Au and CdS or CdSe and the band bending was determined by in situ C-V and I-V analysis.[125] For more information regarding this barrier formation readers are encouraged to see the references 125-126.

Photocatalytic Activity of Nanoheterostructures

The band alignment of the hybrid system can be tuned by the proper combination of the semiconductor and the metal domains to match the reduction potential of the preferred redox system. The cadmium based hybrid structures are of high significance because of their improved charge carrier separation and reduced back recombination.[30, 43, 127-128] The II-VI metal-chalcogenide nanorods with a Pt/Au/Ni tip on their apex are found to be highly promising catalyst for photocatalytic H_2 generation through photo-reduction of water.[45, 129-131] In recent reports, in certain cases, with a monochromatic light irradiation source near absolute conversion efficiency have been reported with CdSe/CdS nanorods with a single Pt tip as the catalyst.[10] The metal domains which act as a co-catalyst also have strong influence on the photocatalytic activity. For example single Pt tipped nanorods are more effective than the double tipped rods, and less number of metal domains show better efficiency.[9, 132] Not only the photocatalytic water splitting reactions but also the degradation of organic dyes has been performed using hybrid nanostructures with various compositions.[30]
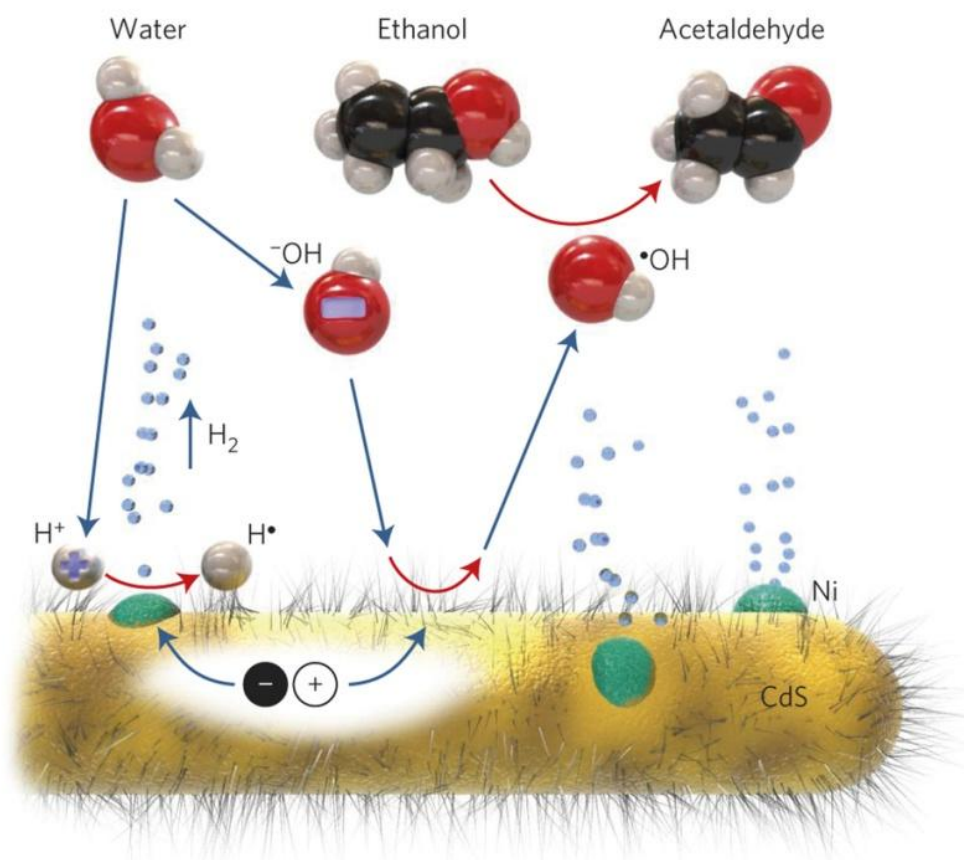
Figure 12. Schematic drawing of the photocatalytic H$_2$ generation by Ni decorated CdS nanorods. An apparent quantum efficiency of 53% was recorded. Upon photo excitation the excited electrons are transferred to the Ni domains, which further reduce H$^+$ ions to produce H$_2$ gas. Hydroxyl anion/radical serves as the redox shuttle and removes the photo-excited holes from the CdS nanorods and hence improves the efficiency. Photograph from reference 133. Reprinted with permission from Nature Publishing Group.

A schematic drawing of photocatalytic H$_2$ production by employing Ni decorated CdS nanorods is shown in Figure 12.

Therefore, metal–semiconductor hybrid nanostructures are highly important and have remained in the forefront of materials research. The growth of noble metal domains on the CdSe or CdSe/CdS NPLs which has been demonstrated later on this thesis are also subjected to the photocatalytic dye degradation as well as H_2 gas generation reactions under UV-Vis light irradiation. A compelling apparent quantum efficiency of ~19.3% is observed for the Pt decorated CdSe/CdS core/crown hybrid NPLs with a turn over frequency of ~10^5 molecules of H_2/hour/NPL. A detailed description of the reaction processes and the observed experimental data are shown in section 4.3 later in this thesis.

1.4 Synthesis of Nanoparticles

There are mainly two different approaches for the synthesis of NPs, one is the bottom up approach where NPs are formed mainly in colloidal solution by the assembly of the atoms and varying the physical forces on the nanometer scale *e.g.*, by wet chemical synthesis,[134-136] and another one is the top down approach where macroscopic objects are turned down to the nanometer scale *e.g.*, by laser ablation[34] and attrition[137] or milling.[136, 138] The top down approach has many disadvantages like the poor control over the size, the shape and the composition of the resulting NPs. A frequently employed technique to obtain high quality nanocrystals is the wet chemical synthesis where by varying the physical conditions of the reactions such as precursors, ligands, temperature pressure, reaction time *etc.* a superior control over the particles size, shape and composition can be achieved.[139]

The NPs employed in this work are synthesized by wet chemical approach or mainly using so called 'hot injection' synthesis technique.[140] In this synthesis procedure, usually, pyrolysis, thermal decomposition or chemical reduction of the organometallic reagents happens at high temperature which forms the reactive species, called monomers, whose transient oversaturation leads to the formation of nuclei. After, the addition of the 'cold'

solution, the nuclei start to grow into mature nanoparticles by the incorporation of monomers, which are still present in the reaction media.[141] The growth kinetics depends on several factors such as temperature, type of the coordinating solvent and co-surfactants *etc*. The shape control can be achieved by choosing suitable surfactants, which bind to certain crystal facets of the particles and promote directional growth.

The setup is depicted in Figure 1. Typically, the precursors *e.g.*, organometallic salts, surfactant and high boiling organic solvents are placed in a three neck round bottom flask. The middle neck of the flask is connected to the Schlenk line set up *via* a cooler, so that the environment of the reaction can be switched to argon or vacuum as desired.
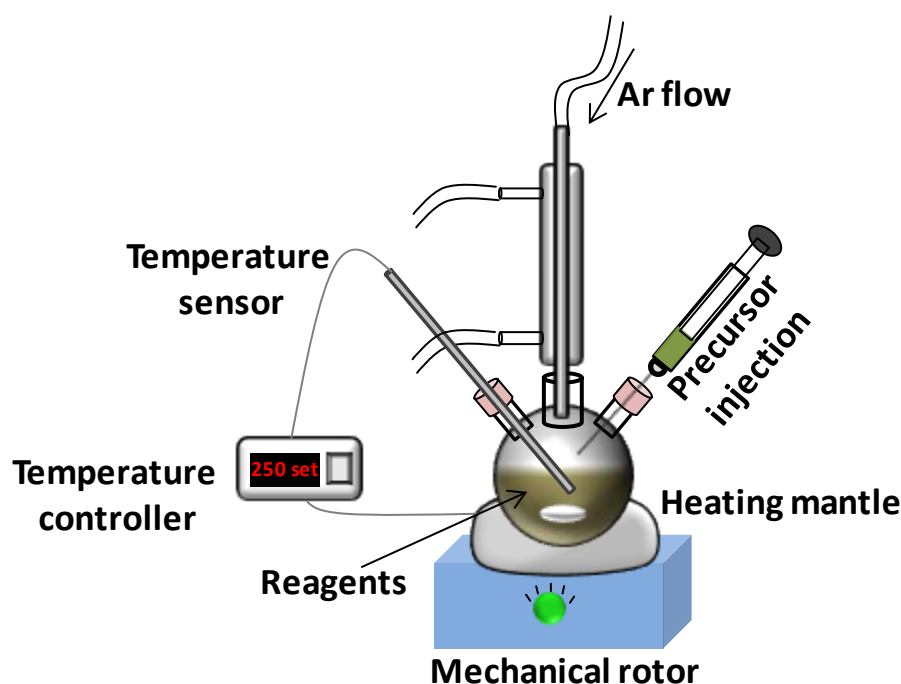

Figure 1. Experimental set up for hot injection synthesis of NPs. Precursors are placed in a round bottom flask with suitable surfactant and solvent. The temperature, pressure and the overhead environment of the reaction can be controlled precisely during the reaction.

A temperature sensor which is connected with an external temperature controller is inserted into the reaction mixture by the help of a glass finger. The round bottom flask is kept on a heating mantle and the whole set up is placed on a mechanical rotor. If needed, the precursors can be also injected during the course of the reaction. After stipulated amount of time, the reaction is stopped by lowering the temperature or by removing the heating mantle. The product obtained is then separated from other by-products and excess ligands *via* centrifugation. Afterwards, the so-produced NPs, are dispersed in the polar or non-polar solvent. The exact synthesis conditions of the NPs under consideration are described in details in the consecutive sections later on.

1.4.1 Semiconductor Nanoparticles

For semiconductors, such as Si, Ge, which involves only one element, their synthesis is usually performed by reduction of a salt of the corresponding element, with suitable reducing agents. For example Si NPs can be obtained by electrochemical reduction of bulk Si wafer using hydrofluoric acid.[142] In a typical synthesis of II-VI and III-V semiconductors, the desired cation and anion precursors are mixed in an appropriate solvent to produce the product of interest. The shape, size and composition of the final product strongly depends on various factors such as, precursor concentration, temperature, mixing rate, pH of the solution *etc.* Surfactant molecules are often employed to stabilize the NPs. These surfactants can even direct the growth along a particular crystal plane by blocking the other crystal planes (due to their adsorption on these planes) to produce shape controlled semiconductor NPs. In earlier synthesis techniques, semiconductor NPs have been synthesized in aqueous solution for example 1-thioglycerol capped CdS, where different amounts of 1-thioglycerol and H_2S were added to a solution of $Cd(ClO_4)_2.6H_2O$ in water, followed by different heat treatments.[143] Usually semiconductor NPs synthesized in

aqueous solution tend to have a high density of defects or trap states along with low overall PLQY. In recent time, synthesis of semiconductor NPs in organic solution has become popular, mainly because the synthesized particles have high quality (in terms of size and shape distributions), low density of defects and high PLQY. The II-VI metal-chalcogenide QDs, nanorods are generally synthesized in organic solution with high boiling solvents such as 1-octadecene, alkylphosphine oxides, oleylamine *etc.* using hot injection synthesis setup. At high temperature, the precursors are decomposed into corresponding atoms and then react to form the nuclei, which subsequently grow to form nanocrystals. The growth can be controlled by the co-ordinating solvent or surfactant molecules and can be monitored by measuring the UV-Vis spectra of the intermediate reaction aliquot. For example, for the synthesis of CdSe quantum dots CdO precursor is heated at 300°C in octadecene solvent, in presence of oleic acid, hexadecylamine (HDA) and trioctylphospine oxide (TOPO) as surfactants. At this high temperature, Se precursor previously prepared is injected in to this mixture.[53-54] Rapid nucleation of CdSe happens immediately after the injection and the size of the particles increases with the reaction time. Later on 'Seeded growth' approach was invented to synthesize anisotropic CdSe/CdS semiconductor NPs of different shapes. Here the CdSe is prepared by above method is employed as 'seed', on which CdS is grown by sequential addition of Cd and S precursors to obtain so-called core/shell heterostructures.[55, 57] By controlling the amount of precursor injection and variation of the surfactants the shell thickness and the growth direction can be controlled very precisely. The quasi 2D CdSe and CdSe/CdS NPLs employed in this thesis are also prepared *via* hot injection synthesis.

However, the semiconductor NPs synthesized in organic solution is not compatible for the biological applications involving aqueous environment. Therefore, to bring the QDs in aqueous solution, a number of strategies have been employed including ligand exchange, silinization or surface coating with silica. For details please see section 1.5.

Another popular approach for synthesizing semiconductor NPs is hydrothermal synthesis, which is based on reactions under high temperature and pressure and generally performed inside 'autoclaves'. For example CdTe NPs with PLQY > 10% have been synthesized in aqueous solution based on the reaction between NaHTe and $CdCl_2$.[144] However, for the hydrothermal synthesis, there are many requirements for the starting material such as the accurately known composition, as pure as possible, as homogeneous as possible and as fine as possible. For the synthesis of metal oxide semiconductors such as ZnO, TiO_2, Fe_2O_3 *etc.* hydrolysis reactions are carried out. Hydrothermal synthesis as described above is also often employed for metal oxide synthesis *via* gas phase method.[145]

A special class of semiconductor material is the doped semiconductors, where a small amount of foreign material is intentionally introduced into the host semiconductor particles to influence its properties. For doped NPs synthesis, the method is only slightly altered with the main modification that the dopant element is introduced during the synthesis.

1.4.2 Metal Nanoparticles

Chemical synthesis of metal NPs usually involves reduction of metal salts or metal ions by suitable reducing agents in liquids. The synthesis of metal NPs involves two stages, nucleation (or seed formation) and growth of the nuclei. In the second stage, the capping ligands or the surfactant play an important role in determining size and shape of the resulting metal NPs.[146] If the surfactants are weekly associated with the metal, then there will be little or no control on the size of the formed nanocrystals, which will continue to grow into large crystals or start to aggregate. However, if the surfactant is strongly associated with the metal, the size of the particles is controllable. In some reactions, the surfactants form micelle or reverse micelle and thus the size of the final NPs is

controlled.[134, 147] The employment of two or more different types of surfactants is also common in metal NPs synthesis, which helps to obtain precise control over the shape of the metal NPs. In the case of citrate or similar reducing agents, the concentration plays an important factor. The initial 'seed' concentration will be determined by the amount of reducing agents employed, which in turn determines the total number of resulting NPs. For example, with small amount of citrate, there will be less number of seeds, leading to few numbers of large particle formation, and when the concentration is high, then large number of seeds are generated and the number of particles will also be large.

Generally, as the particle size increases, the size dispersion becomes larger, which is not desirable for cases, where monodisperse particle formation is preferred. It is because nucleation and particle growth can overlap in time, the seed clusters continue to form, while the initial particles are growing. A solution to this problem can be the seed-mediated growth,[134, 148] where small seeds are formed in the first stage and in the second stage more precursors are added with weak reducing agents (*e.g.*, ascorbic acid), where the precursor ions will grow on the surface of the 'seed' and with no secondary nucleation. Seed mediated growth can be also used for controlling the shape of the metal NPs. One example is the generation of Au nanorods in presence of cetyltrimethylammonium bromide (CTAB). Here, CTAB binds to the surface radially, keeping the c-axis open, and allows growth in the axial direction.

In addition, there are synthetic routes of metal NPs synthesis in organic solvent, where the particle shapes can be controlled precisely using organic surfactants (*e.g.*, oleic acid, oleylamine *etc.*).[23, 97] Here also the growth principle is similar to that of aqueous solution and the shape and size of the particles can be varied by varying the precursor concentration, amount and types surfactants and reducing agents, respectively. In this thesis, shape

controlled Pt NPs are synthesized in organic solution by employing Pt(acac)$_2$ as the metal precursor, 1-octadecene as solvent, oleic acid and/or oleylamine as surfactant and Fe(CO)$_5$ as the reducing agents. A detail discussion on the synthesis procedure is described later in section 3.2. More information regarding the shape controlled metal NPs synthesis; readers are encouraged to see these references 97-99.

The other methods to produce metal NPs include reduction of metal ions *via* various sources of radiation *e.g.*, UV-vis light, microwave, radio frequency, sputtering, ultrasound or γ radiation.[149] It should be noted here, that the NPs synthesized in these methods usually have broad size and shape distributions.

1.4.3 Metal-Semiconductor Heteroparticles

For the synthesis of metal-semiconductor heteroparticles there are many methods in literatures, which can be in general divided into two categories, first, the components (metal and the semiconductor) are prepared separately using the above described methods and then mixed together and secondly, both metal and the semiconductor precursors are introduced simultaneously to obtain the heterostructures. For example Au, domains are grown on TiO$_2$ anatase in a ultra high vacuum chamber *via* metal vapor deposition.[150] Also Au domains were grown on Fe$_2$O$_3$ NPs at room temperature by mixing HAuCl$_4$ solution in pre-synthesized Fe$_2$O$_3$ NPs in presence of ascorbic acid as the reducing agent.[151] There are also examples of Pt domain growth on CdSe nanorods by reducing PtCl$_4$ in aqueous solution, where pH of the solution plays an important role to obtain 'nanonet' type morphologies.[112] In 2000, the work group of Banin, have reported the growth of Au domains on the apexes of CdSe rods and tetrapods. Here AuCl$_3$ precursor was dissolved in toluene solution in presence of dodecylamine and didecyl di-methylammonium bromide (DDAB) complex. At

room temperature the solution of CdSe and Au precursor were mixed under stirring conditions to obtain the hybrid structures. Ostwald ripening also plays important role to control the metal domain size, *i.e.* sometimes larger metal domains are formed at the expense of many small domains after the preliminary growth of the metal domain on the semiconductor particles. It is also shown that by choosing right parameters for the reactions, metal domains can be grown selectively at the apexes of the nanorods even in some cases Au domains can be grown epitaxialy on the CdSe nanorods.[117, 152-153]

In this thesis, new synthesis techniques are developed to obtain metal-semiconductor heterostructures by growing noble metal domains on CdSe or CdSe/CdS NPLs, for details see section 4.2 and 4.3.

1.5 Phase Transfer of Nanoparticles

Colloidal NPs synthesized in organic solution have many advantages regarding their optical and structural properties. The NPs are generally coated with hydrophobic ligands which brings stability in the colloids. However, the drawback here is the insolubility of the NPs in aqueous solution. In many cases such as biological labeling applications, water soluble NPs are desired. In order to have the synthesized NPs in aqueous solution, a phase transition from organic to aqueous solution is necessary. This is accompanied by ligand exchange reactions[154-156] or *via* encapsulation of the particles into hydrophilic (*e.g.*, silica[157-158]) or amphiphilic materials.[159] In ligand exchange reactions, the hydrophobic ligands present on the surface of the NPs are replaced with thiol based (long chain or short chain) molecules (such as 3-mercaptopropionic acid), which have in general a carboxylic acid group at one end and thiol (-SH) group at the other end. After the ligand exchange the product is usually dispersed in basic KOH solution where, the carboxylate end (-COO$^-$) interacts with water to provide the stability. The great advantage of this approach is the retention of the nanoscopic

functionalities of the NPs after the phase transition. Encapsulation of NPs with silica shell is a versatile method for phase transfer of the hydrophobic NPs. The silica coated particles are soluble in water or in buffer and have positive or negative charge depending on the surface functional group and pH of the solution.[157] Amphiphilic polymer coating technique developed by Pellegrino *et al.* also helps to make hydrophobic CoPt$_3$, Au, CdSe/ZnS and Fe$_2$O$_3$ water soluble.[159] In this case, instead of replacing the surfactant from the surface, the hydrophobic tails of the polymer interacts with the ligands and form an additional coating. The water solubility of the NPs is ensured by the hydrophilic groups present on the outer part of the polymer.[159] The reverse phase transfer *i.e.* the transfer of the particles from aqueous to organic solution is also achieved by ligand exchange (bi-dentate thiol based ligand)[160] or by employing ionic liquid.[161]

The phase transfer of the 1D and 2D cadmium based NPs such as nanorods or NPLs is recently reported by Kodanek *et al*. using short/long chain thiol and aminothiol ligands.[154] Interestingly, here the optical properties of the hydrophobic nanorods and NPLs are mostly retained in the aqueous solution after phase transfer.[154]

1.6 Aerogels

In general, 'gel' is defined as a substantially dilute cross-linked system, which exhibits no flow in the steady-state. Gels consist of 3D cross-linked network of a monomer or polymer. And by definition 'aerogel' is a synthetic porous ultra-light material derived from gel, in which the liquid component of the gel has been replaced with gas.[162] The aerogels are extremely porous, with low density and low thermal conductivity. The first aerogel is reported by Samuel Kistler in 1931 with a bet with Charles Learned to replace the existing liquid from the jellies with gas without having volume shrinkage.[163] Kistler has been able to produce opalescent and transparent silica aerogels with extremely low densities by

employing supercritical drying with liquid CO_2. In this drying process the temperature and the pressure of the autoclave, where the samples are emerged in a fluid, are raised to the supercritical conditions to avoid the direct phase transitions and thereby the fluid is converted to gas. Later the gas is released and the porous aerogels (the pores are filled with air) are collected from the chamber. The phase diagram of CO_2 is presented in Figure 13.
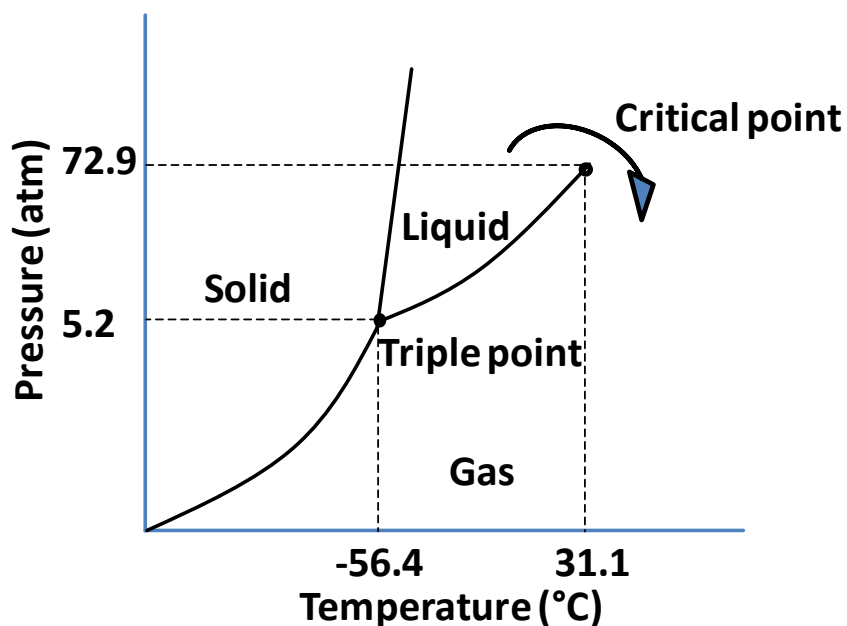

Figure 13. Phase diagram of CO_2. At critical point, the distinction between the gas and the liquid phase disappear. By increasing the temperature and pressure of the autoclave supercritical conditions (>31.1°C temperature and >72.9 atm pressures) can be reached.

The volume shrinkage is negligible with respect to the volume of the gel in liquid medium. Later this technique was successfully utilized in other systems such as alumina, chromia, tin oxide or carbon aerogels. Conventional drying of the gels under ambient conditions leads to significant volume shrinkage due to the capillary forces causing collapse of the structure.

Further investigations have been carried out regarding the improvement and applicability of the aerogels derived from this pure or doped silica, alumina or other metal oxides and from

carbon. The properties such as excellent thermal insulation, low density and transparent nature of the silica aerogels has made them an important substance for the applications in *e.g.*, Cherenkov radiators, [65] window insulation[164] even in space technology.[165]

Figure 14. Photographs of silica aerogels showing its physical properties such as i) extremely light weight, ii) optically transparent in nature iii) low thermal conductivity. Photographs are reprinted with permission from Wiley and Nature publishing group.

The silica aerogels have the advantages of extremely low density, low thermal conductivity and transparent nature, which make them promising for applications in the field *e.g.*, stardust collection, where silica aerogel acts as a filter for resisting the high velocity of the space dust and to captivate it. Silica aerogels are also employed as window insulation,[164] Cherenkov radiator, where it replaces gases under high pressure.[166] Apart from that nitrogen doped carbon aerogels are employed for oxygen reduction reactions,[21, 167] aerogels from polyurea are employed to soak oil from water.[168] Owing to their exceptional specific surface area, and very high porosity the aerogels from noble metal NPs have high application possibilities in heterogeneous catalysis, electrocatalysis, hydrogen storage and sensor systems.[17] Pd aerogels are employed for the fabrication of membrane less glucose/O_2 bio-fuel cell which are found to be more effective than the conventional catalyst.[16, 169] The semiconductor quantum dot aerogels (CdTe) are also finding applications in the field for

example biosensors, fluorescent probing.[170] CdSe aerogels have been employed as a sensor for optical detection of triethylamine.[171]

The employment of the metal-chalcogenide and noble metal aerogels in an industrial level needs further improvement regarding the stability of the system under mechanical stress. The filigree network of the NPs broke down easily under external pressure. Therefore, research focused on the durability of the aerogels is necessary. In a recent report from Eychmüller group, it has been shown that the infiltration of the metallic aerogels in a polymer matrix increases the mechanical stability of the aerogel as the pores are filled with polymer matrix[16]. Although this technique keeps the high electrical conductivity of the connected network, but the porosity of the aerogels are suppressed. Taking into account the present intensive research work going on to optimize the synthesis conditions and to improve the stability of the aerogels, it can be predicted that in near future aerogels materials will be popular in our day-to-day life.

1.6.1 Semiconductor Aerogels

Before 2002, the main focus has been given to synthesize aerogels from different metal oxides and carbon or from selective organic compounds. Stephanie L. Brock and co-workers from Wayne state university had the idea to employ the supercritical drying technique to produce aerogels from the gels of metal-chalcogenide semiconductor nanomaterials reported by Gacoin *et al*.[33, 172] They came with an exciting report of formation of highly porous, extremely light weight aerogels from various systems such as CdS, CdSe, ZnS and PbS. The aerogel monoliths had the densities of $0.07 \text{ g} \cdot \text{cm}^{-3}$ (which is only 1.4% of the bulk CdS density) and exhibited specific surface area as high as $250 \text{ m}^2 \cdot \text{g}^{-1}$ with average pore diameter ranging from 15-45 nm.[18, 173] Unlike the silica

aerogels the whole network structure was crystalline, and consisted of interconnected network of quantum dots building block which were assembled into pearl necklace-type morphology. The macroscopic monoliths of aerogels partially exhibited the quantum confinement properties of the initial NPs building blocks.
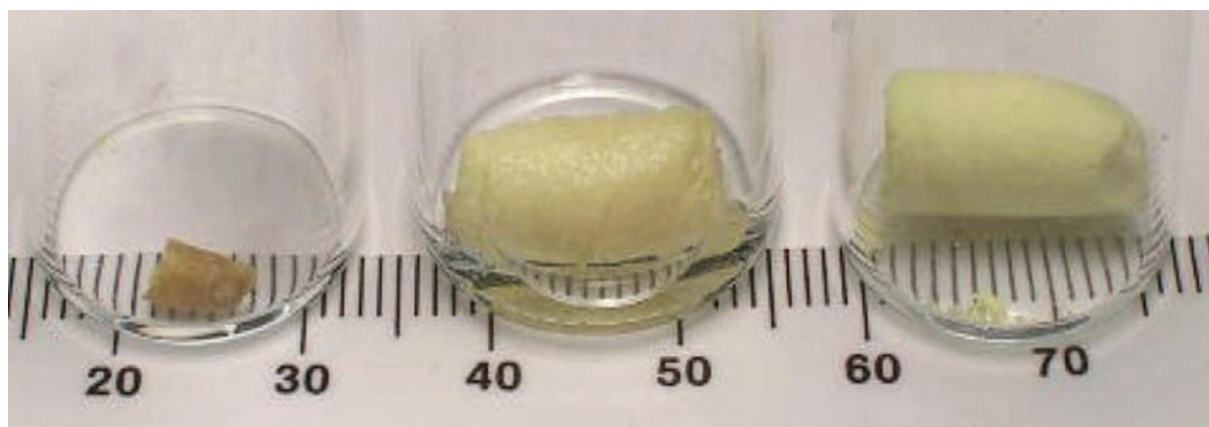

Figure 15. The first metal-chalcogenide aerogel from CdS NPs. (left) when the gel is dried under ambient conditions, (middle) monolithic CdS hydrogel and (right) monolithic CdS aerogel obtained after supercritical drying. Photograph is from reference 18. Reprinted with permission from the American Association for the Advancement of Science

The first metal-chalcogenide aerogel was obtained from CdS NPs as mentioned above.[173] Here, controlled destabilization was performed with few micro liter of diluted H_2O_2 solution to produce the hydrogel (gel in water). Later on the hydrogel was transformed to aerogel by supercritical drying with liquid CO_2. This method of fabrication of aerogels were adopted for other types of NPs such as CdTe[20], CdSe[65], CdS CdSe/ZnS *etc*.[19] In many cases the high luminescent properties of the building blocks were partially retained in the ultimate aerogels *e.g.*, CdTe and CdSe/ZnS.[174-176] Not only the spherical quantum dots but also CdSe/CdS nanorods were employed as the building blocks for the aerogel synthesis (shown in Figure 16).[177] Interestingly, here tip to tip connections of the nanorods helped to

form the porous network structure. The aerogels formed from the CdSe/CdS nanorods exhibited very high PLQY (> 29%) and ultra-long radiative lifetime (~56 ns).[177]
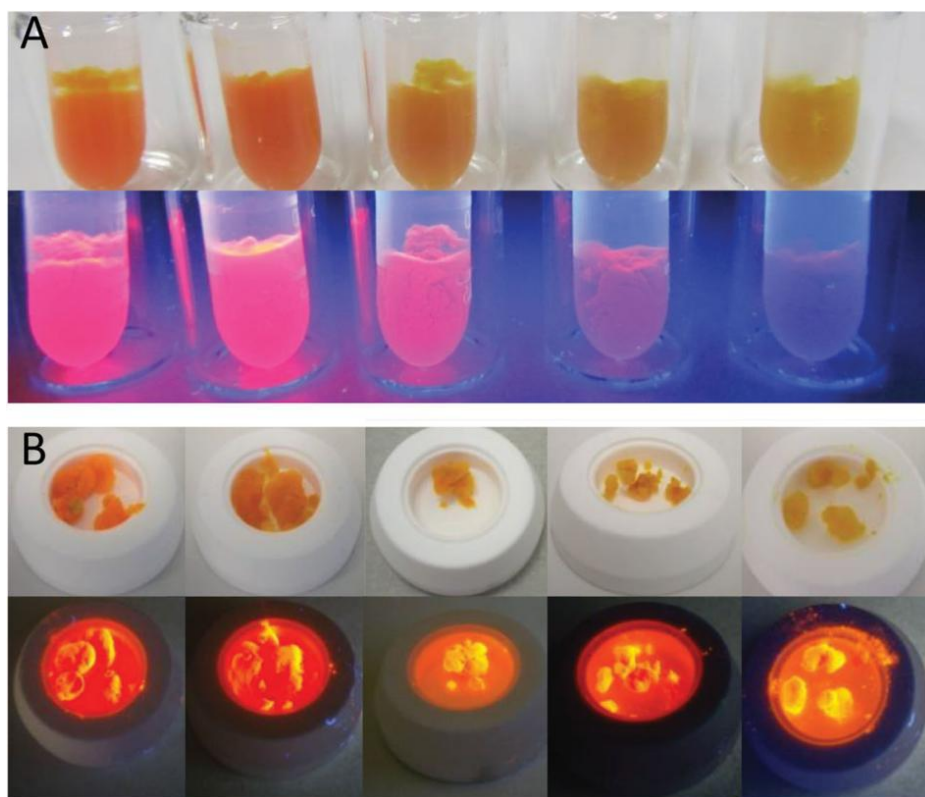

Figure 16. Photographs of (A) hydrogels and (B) aerogels from CdSe/CdS nanorods under day light (top) and under UV light (bottom) irradiation. Hydrogels are obtained after controlled destabilization of the aqueous solution by means of H_2O_2. The PLQY of the gels decreases gradually with increasing content of H_2O_2 (left to right). Photograph is from reference 177. Reprinted with permission from Wiley VCH.

At the starting of this thesis there was no report regarding the self-assembly of quasi 2D CdSe or CdSe/CdS NPLs into macroscopic porous aerogels. The NPLs have distinct optical characteristics, which cannot be achieved from quantum dots and nanorods as mentioned earlier in the section 1.3.1. Therefore, the aerogelation of these thin NPLs is highly interesting. Moreover, the NPLs exhibit solely (100) as the exposed crystal facets, hence formation of aerogels from these NPLs could lead to porous macroscopic structure with

(100) crystal facets, which would be highly suitable for facet selective catalytic reactions. Also, the questions regarding the optical properties, specific surface area, crystallographic structure, and orientation of the NPLs in the gels, exciton confinements have inspired us to study the aerogelation of the NPLs, which is presented in detail in section 2.2.

1.6.2 Metal Aerogels

The first report on the aerogel formation solely from the metal NPs is reported by Bigall *et al*. in 2009.[40] The procedure employed in this case also was similar to that developed by Brock and co-workers.[34, 173] Here, citrate stabilized colloidal solution of the noble metal Au, Ag and Pt NPs were employed as the building blocks. Hydrogels were achieved by the controlled destabilization of the system by the addition of ethanol or H_2O_2. Later the hydrogels were supercritically dried to convert them to porous aerogels. The photographs of the hydrogel and the corresponding aerogel are shown in Figure 17. The cross-linking of the individual metal NPs helps to form the porous 3D architecture. It should be noted that the surface plasmon resonance was not observed in the final aerogel morphology. Significantly, the aerogels exhibit very low densities of $0.016 \text{ g} \cdot \text{cm}^{-3}$ and specific surface areas of $\sim 48 \text{ m}^2 \cdot \text{g}^{-1}$. In comparison to the specific surface area of the metal-chalcogenides aerogels this is somewhat low. However, one has to keep in mind the high atomic weight of the noble metal elements while comparing the specific surface area. Furthermore, Eychmüller group has reported a variety of pure or mixed noble metal aerogels (such as Au, Pt, Pd, Ag or the binary and ternary combination of these elements) following the above procedure.[16-17, 21] The highest specific surface area of $\sim 92 \text{ m}^2 \cdot \text{g}^{-1}$ was obtained from beta-cyclodextrin modified Pd aerogels which show high activity toward electro oxidation of ethanol.[178] They have also reported on the synthesis of highly porous beta-cyclodextrin

modified Au aerogels *via* direct reduction of the chloroauric acid with sodium borohydride.[179]
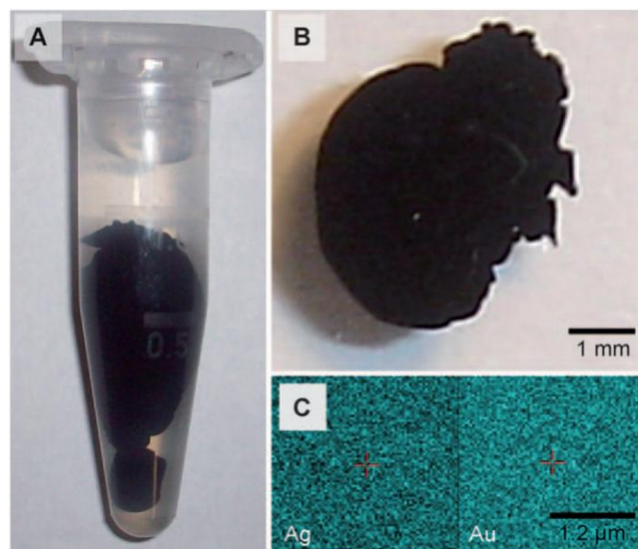

Figure 17. First noble metal (A) hydrogel and (B) aerogel made from mixture of gold and silver NPS. (C) the elemental distribution of Ag and Au in the aerogel. Photograph is from reference 40. Reprinted with permission of Wiley-VCH.

At the same time Leventis *et al*. have invented a new method for aerogel fabrication which involves process called 'nanosmelting' which is the reduction of the metal oxide to metal in presence of carbon.[180] In this technique, first the metal oxides were gelated followed by pyrolysis to reduce the metal oxides to metal aerogels. Although in this process, the specific surface area could reach as high as 410 $m^2 \cdot g^{-1}$, but the method is strictly restricted to metal oxides which are suitable for this pyrolysis reaction as well as the reduction by carbon at the end results in mixed aerogels.[180]

1.6.3 Metal-Semiconductor Aerogels

Metal-semiconductor aerogels would be beneficial as they combine the synergistic properties of both metal and the semiconductor in a solid porous geometry. Regarding the multicomponent, metal-semiconductor mixed aerogels comparatively less attention has been paid so far. In one report, Au and CdTe NPs prepared separately, are mixed in different ratios and converted to aerogels *via* supercritical drying.[182] Specifically, here the controlled destabilization was achieved by light induced oxidation of the surface thiol ligands. In the second report of multicomponent gel formation again from Au and CdTe NPs, cadmium ions were added into the mixture which formed complexes with the attached ligands and thus helped the hydrogel formation.[181-182] However, in this method the interfaces of the metal and the semiconductor cannot be controlled as well as the metal domains were present randomly on the CdTe semiconductor NPs. For superior performance in catalytic reactions, selective noble metal growth with controllable morphologies is desired for the effective separation of the charge carriers.

1.7 Aerogel Synthesis

One classical method for the production of nanostructures is the sol-gel technique, in which the NPs are formed and aggregated *via* a series of hydrolysis and condensation reactions to form a wet gel type structure.[19, 33, 69, 172] Once the wet gel is obtained, the solvent is exchanged with liquid CO_2 followed by supercritical drying to obtain porous polymeric structure which is named as aerogel. Inorganic 'sol-gel' method is well known for the synthesis of metal oxide materials (SiO_2, V_2O_5, TiO_2, *etc*.). The process involves conversion of monomers (which acts as the precursor, named as 'sol') into an integrated polymeric network (which is termed as 'gel') formation. Thereafter the gels are heated at

much higher temperature or dried at room temperature to form a so-called xerogel.[172] The oxide sol-gel process proceeds through a polymerization reaction which involves the hydrolysis of a molecular precursor followed by condensation through the formation of metal-oxide bonds. The details of the mechanism have been investigated for the silica particles and established as the model system.[183] In the case of non-oxide materials successive reactions are required to ensure the bonding between the monomers in a controlled way, thereafter similar hydrolysis and condensation processes are followed. Gacoin *et al.* have demonstrated an example with CdS NPs capped with thiol ligands which were prepared *via* inverse micelles formation and arrested precipitation.[33, 172] The gelation of these particles was observed after a long time exposure of the sol to the air under ambient conditions.[172] After the removal of the ligands the particles started to aggregate through the active sites present on the surface. As the surface of the particles was slowly activated a random coalescence of the NPs lead to aggregate formation and thus made the sol-gel transition possible. The thiolate ligands can be easily oxidized by various oxidizers such as oxygen from air, H_2O_2, sodium periodate *etc.*, which form either dithiol or sulphonate depending upon the experimental conditions. The kinetics of the gelation process and further aging of the gels were found to depend on many parameters. One of the specific parameter of the CdS gelation was the oxidized thiol fraction, which actually controls the number of the active sites on the surface.[172]

Other Fabrication Techniques

There are also reports on the fabrication of aerogels by exploiting cryogelation technique, where the aqueous solution of the NPs is subjected to freezing and subsequent freeze drying to obtain aerogels. Freytag *et al*. recently have reported a unique versatile method of aerogel fabrication which can be applied for a wide variety of materials such as metal,

metal oxide, semiconductor materials.[184] In this technique the NPs building blocks were synthesized in aqueous solution or transferred to aqueous solution *via* ligand exchange reactions. The concentrated solution of the NPs was dropped into liquid N_2 for fast freezing; subsequently the frozen object was subjected to freeze drying. It has been shown that during the fast freezing process, the NPs were highly pressed between the ice crystals, which helped to assemble them into sheet like structure. Later on the ice template was removed by sublimation process by employing freeze drying. The aerogels obtained in this method were porous, light weight and exhibit high specific surface area for catalysis reactions. Moreover, here the shape of the aerogels can be controlled as desired by using a template at the time of freezing. For more information relating the mechanism of cryogelation, readers are encouraged to consult the reference184.

Another completely different method is employed by the group of Kanatzidis who demonstrated aerogels of germanium platinum sulfide ($Ge_4Pt_2S_{9.6}$ and $Ge_4Pt_2S_{8.7}$)[185] and platinum tin selenide ($Pt_{2.1}Sn_4Se_{9.7}$, $Pt_{1.8}Sn_2Se_{5.7}$, Pt_2SnSe_4, and $Pt_{1.4}SnS_4$),[186] where clusters of sulfide and selenide when bound to metal ions *via* co-ordinative reactions, assemble into gels. These materials have high internal surface areas (up to $327\ m^2 \cdot g^{-1}$) and narrow bandgaps of 0.2-2.0 eV.[187] Although, this aerogels posses high specific surface areas and low density, the fabrication methods are complicated and based on multistep chemical reactions and purification.

However, all the above existing processes of aerogelation are only applicable to the colloidal aqueous solutions of the particles and require time consuming ultrafiltration processes for concentrating the NPs solutions before starting the gelation experiments. In practice most of the shape controlled metal NPs are synthesized in organic solution and therefore the H_2O_2 induced destabilization reaction is ineffective to remove the surface

ligands. It is known that, metal NPs with distinct facets outside are suitable for facet selective catalytic reactions. Therefore, it is of high significance to develop a new method of aerogel preparation from shape controlled NPs, directly from colloidal organic solution to circumvent the time consuming phase transfer and ultrafiltration processes. Also fabrication of 3D network of noble metal NPs with distinct facets outside would be highly advantageous for many catalytic reactions to yield selective products. Hence, to address this concern a new synthetic strategy is presented in the section 3.2, where shape controlled Pt NPs is transformed to highly porous macroscopic aerogel with only (100) as the exposed crystal facets directly from colloidal organic solution.

1.8 Reference

(1)   *http://phys.org/news/2013-01-sony-tvs-high-end-quantum-dot.html*.

(2)   Paul, D. R.; Robeson, L. M. *Polymer* **2008,** *49* (15), 3187.

(3)   Raj, S.; Jose, S.; Sumod, U. S.; Sabitha, M. *Journal of Pharmacy & Bioallied Sciences* **2012,** *4* (3), 186.

(4)
h*ttps://www.chevrolet.com/content/dam/Chevrolet/northamerica/usa/nscwebsite/en/Home/V ehicles/Cars/2014_Corvette_Coupe/Model_Overview/PDF/MY14%20Corvette%20eBrochu re_110513.pdf*.

(5)   Kong, J.; Chapline, M. G.; Dai, H. *Adv. Mater.* **2001,** *13* (18), 1384.

(6)   Endo, T.; Kerman, K.; Nagatani, N.; Hiepa, H. M.; Kim, D.-K.; Yonezawa, Y.; Nakano, K.; Tamiya, E. *Anal. Chem.* **2006,** *78* (18), 6465.

(7)   Gratzel, M. *Journal of Photochemistry and Photobiology C-Photochemistry Reviews* **2003,** *4* (2), 145.

(8)   Liao, L.; Zhang, Q.; Su, Z.; Zhao, Z.; Wang, Y.; Li, Y.; Lu, X.; Wei, D.; Feng, G.; Yu, Q.; Cai, X.; Zhao, J.; Ren, Z.; Fang, H.; Robles-Hernandez, F.; Baldelli, S.; Bao, J. *Nat Nano* **2014,** *9* (1), 69.

(9)   Amirav, L.; Alivisatos, A. P. *J. Phys. Chem. Lett.* **2010,** *1* (7), 1051.

(10)   Kalisman, P.; Nakibli, Y.; Amirav, L. *Nano Lett.* **2016**.

(11)   Xie, X. W.; Li, Y.; Liu, Z. Q.; Haruta, M.; Shen, W. J. *Nature* **2009,** *458* (7239), 746.

(12)   Salata, O. V. *Journal of Nanobiotechnology* **2004,** *2*, 3.

(13)   Gensler, R.; Gröppel, P.; Muhrer, V.; Müller, N. *Particle & Particle Systems Characterization* **2002,** *19* (5), 293.

(14)   Poizot, P.; Laruelle, S.; Grugeon, S.; Dupont, L.; Tarascon, J. M. *Nature* **2000,** *407* (6803), 496.

(15)   Liu, W.; Rodriguez, P.; Borchardt, L.; Foelske, A.; Yuan, J.; Herrmann, A.-K.; Geiger, D.; Zheng, Z.; Kaskel, S.; Gaponik, N.; Koetz, R.; Schmidt, T. J.; Eychmueller, A. *Angewandte Chemie-International Edition* **2013,** *52* (37), 9849.

(16)   Herrmann, A.-K.; Formanek, P.; Borchardt, L.; Klose, M.; Giebeler, L.; Eckert, J.; Kaskel, S.; Gaponik, N.; Eychmueller, A. *Chem. Mater.* **2014,** *26* (2), 1074.

(17)   Liu, W.; Herrmann, A.-K.; Bigall, N. C.; Rodriguez, P.; Wen, D.; Oezaslan, M.; Schmidt, T. J.; Gaponik, N.; Eychmüller, A. *Acc. Chem. Res.* **2015,** *48*, 154.

(18)   Mohanan, J. L.; Arachchige, I. U.; Brock, S. L. *Science* **2005,** *307* (5708), 397.

(19)   Arachchige, I. U.; Brock, S. L. *J. Am. Chem. Soc.* **2006,** *128* (24), 7964.

(20)   Brock, S. L.; Arachchige, I. U.; Kalebaila, K. K. *Comments Inorg. Chem.* **2006,** *27* (5-6), 103.

(21)   Herrmann, A.-K.; Liu, W.; Gaponik, N.; Bigall, N.-C.; Eychmueller, A., *Ecs Transactions*, Guldi, D. M.; Fenton, J. M.; Simonian, A., Eds. 2013; Vol. 45, pp 149.

(22)   Wen, D.; Herrmann, A.-K.; Borchardt, L.; Simon, F.; Liu, W.; Kaskel, S.; Eychmueller, A. *J. Am. Chem. Soc.* **2014,** *136* (7), 2727.

(23) Tsung, C. K.; Kuhn, J. N.; Huang, W. Y.; Aliaga, C.; Hung, L. I.; Somorjai, G. A.; Yang, P. D. *J. Am. Chem. Soc.* **2009,** *131* (16), 5816.

(24) Lee, I.; Morales, R.; Albiter, M. A.; Zaera, F. *Proceedings of the National Academy of Sciences of the United States of America* **2008,** *105* (40), 15241.

(25) Xia, Y. N.; Xiong, Y. J.; Lim, B.; Skrabalak, S. E. *Angewandte Chemie-International Edition* **2009,** *48* (1), 60.

(26) Cao, M.; Miyabayashi, K.; Shen, Z.; Ebitani, K.; Miyake, M. *J. Nanopart. Res.* **2011,** *13* (10), 5147.

(27) Yin, A.-X.; Min, X.-Q.; Zhang, Y.-W.; Yan, C.-H. *J. Am. Chem. Soc.* **2011,** *133* (11), 3816.

(28) Gaponik, N.; Hickey, S. G.; Dorfs, D.; Rogach, A. L.; Eychmüller, A. *Small* **2010,** *6* (13), 1364.

(29) Guo, S.; Zhang, G.; Wang, J. *J. Colloid Interface Sci.* **2014,** *433*, 1.

(30) Banin, U.; Ben-Shahar, Y.; Vinokurov, K. *Chem. Mater.* **2014,** *26* (1), 97.

(31) Ishikawa, E.; Fukatsu, S.; Onabe, K.; Shiraki, Y.; Ito, R., In *Science and Technology of Mesoscopic Structures*, Namba, S.; Hamaguchi, C.; Ando, T., Eds. Springer Japan: Tokyo, 1992; pp 373.

(32) Ithurria, S.; Dubertret, B. *J. Am. Chem. Soc.* **2008,** *130* (49), 16504.

(33) Gacoin, T.; Lahlil, K.; Larregaray, P.; Boilot, J. P. *The Journal of Physical Chemistry B* **2001,** *105* (42), 10228.

(34) Mohanan, J. L.; Brock, S. L. *J. Non-Cryst. Solids* **2004,** *350*, 1.

(35) Ahmadi, T. S.; Wang, Z. L.; Green, T. C.; Henglein, A.; ElSayed, M. A. *Science* **1996,** *272* (5270), 1924.

(36) Alivisatos, P. *Nat. Biotechnol.* **2004,** *22* (1), 47.

(37) Loo, C.; Lowery, A.; Halas, N.; West, J.; Drezek, R. *Nano Lett.* **2005,** *5* (4), 709.

(38) O'Neal, D. P.; Hirsch, L. R.; Halas, N. J.; Payne, J. D.; West, J. L. *Cancer Letters* **2004,** *209* (2), 171.

(39) Lu, L.; Capek, R.; Kornowski, A.; Gaponik, N.; Eychmüller, A. *Angew. Chem. Int. Ed.* **2005,** *44* (37), 5997.

(40) Bigall, N. C.; Herrmann, A. K.; Vogel, M.; Rose, M.; Simon, P.; Carrillo-Cabrera, W.; Dorfs, D.; Kaskel, S.; Gaponik, N.; Eychmuller, A. *Angew. Chem. Int. Ed.* **2009,** *48* (51), 9731.

(41) Bigall, N. C.; Eychmueller, A. *Philosophical Transactions of the Royal Society a-Mathematical Physical and Engineering Sciences* **2010,** *368* (1915), 1385.

(42) Yao, Q.; Brock, S. L. *Inorg. Chem.* **2011,** *50* (20), 9985.

(43) Dutta, S. K.; Mehetor, S. K.; Pradhan, N. *J. Phys. Chem. Lett.* **2015,** *6* (6), 936.

(44) Wang, P.; Zhang, J.; He, H. L.; Xua, X. T.; Jin, Y. D. *Nanoscale* **2014,** *6* (22), 13470.

(45) Wang, J.-J.; Li, Z.-J.; Li, X.-B.; Fan, X.-B.; Meng, Q.-Y.; Yu, S.; Li, C.-B.; Li, J.-X.; Tung, C.-H.; Wu, L.-Z. *Chemsuschem* **2014,** *7* (5), 1468.

(46) Banin, U. *Abstracts of Papers of the American Chemical Society* **2013,** *246*.

(47) Haldar, K. K.; Sinha, G.; Lahtinen, J.; Patra, A. *ACS. Appl. Mater. Int.* **2012,** *4* (11), 6266.

(48) Yeltik, A.; Delikanli, S.; Olutas, M.; Kelestemur, Y.; Guzelturk, B.; Demir, H. V. *The Journal of Physical Chemistry C* **2015,** *119* (47), 26768.

(49) Zhang, S. L., *Raman Spectroscopy and Its Application in Nanostructures*. Wiley: 2012.

(50)   Alivisatos, A. P. *Science* **1996,** *271* (5251), 933.

(51)   Koole, R.; Groeneveld, E.; Vanmaekelbergh, D.; Meijerink, A.; de Mello Donegá, C., Size Effects on Semiconductor Nanoparticles. In *Nanoparticles: Workhorses of Nanoscience*, de Mello Donegá, C., Ed. Springer Berlin Heidelberg: Berlin, Heidelberg, 2014; pp 13.

(52)   Brus, L. E. *The Journal of Chemical Physics* **1984,** *80* (9), 4403.

(53)   Murray, C. B.; Norris, D. J.; Bawendi, M. G. *J. Am. Chem. Soc.* **1993,** *115* (19), 8706.

(54)   Peng, X.; Manna, L.; Yang, W.; Wickham, J.; Scher, E.; Kadavanich, A.; Alivisatos, A. P. *Nature* **2000,** *404* (6773), 59.

(55)   Li, J. J.; Wang, Y. A.; Guo, W. Z.; Keay, J. C.; Mishima, T. D.; Johnson, M. B.; Peng, X. G. *J. Am. Chem. Soc.* **2003,** *125* (41), 12567.

(56)   Manna, L.; Scher, E. C.; Alivisatos, A. P. *J. Am. Chem. Soc.* **2000,** *122* (51), 12700.

(57)   Carbone, L.; Nobile, C.; De Giorgi, M.; Sala, F. D.; Morello, G.; Pompa, P.; Hytch, M.; Snoeck, E.; Fiore, A.; Franchini, I. R.; Nadasan, M.; Silvestre, A. F.; Chiodo, L.; Kudera, S.; Cingolani, R.; Krahne, R.; Manna, L. *Nano Lett.* **2007,** *7* (10), 2942.

(58)   Mourdikoudis, S.; Liz-Marzan, L. M. *Chem. Mater.* **2013,** *25* (9), 1465.

(59)   Talapin, D. V.; Shevchenko, E. V.; Murray, C. B.; Kornowski, A.; Förster, S.; Weller, H. *J. Am. Chem. Soc.* **2004,** *126* (40), 12984.

(60)   Xu, D. S.; Shi, X. S.; Guo, G. L.; Gui, L. L.; Tang, Y. Q. *J. Phys. Chem. B* **2000,** *104* (21), 5061.

(61)   Deka, S.; Miszta, K.; Dorfs, D.; Genovese, A.; Bertoni, G.; Manna, L. *Nano Lett.* **2010,** *10* (9), 3770.

(62)   Pang, Q.; Zhao; Cai, Y.; Nguyen, D. P.; Regnault, N.; Wang, N.; Yang; Ge; Ferreira, R.; Bastard, G.; Wang *Chem. Mater.* **2005,** *17* (21), 5263.

(63)   Yong, K. T.; Sahoo, Y.; Swihart, M. T.; Prasad, P. N. *Adv. Mater.* **2006,** *18* (15), 1978.

(64)   Manna, L.; Milliron, D. J.; Meisel, A.; Scher, E. C.; Alivisatos, A. P. *Nat. Mater.* **2003,** *2* (6), 382.

(65)   O'Sullivan, C.; Gunning, R. D.; Barrett, C. A.; Singh, A.; Ryan, K. M. *J. Mater. Chem.* **2010,** *20* (36), 7875.

(66)   Beberwyck, B. J.; Surendranath, Y.; Alivisatos, A. P. *J. Phys. Chem. C.* **2013,** *117* (39), 19759.

(67)   Liang, R.; Yan, D.; Tian, R.; Yu, X.; Shi, W.; Li, C.; Wei, M.; Evans, D. G.; Duan, X. *Chem. Mater.* **2014,** *26* (8), 2595.

(68)   Deka, S.; Miszta, K.; Dorfs, D.; Genovese, A.; Bertoni, G.; Manna, L. *Nano Lett.* **2010,** *10* (9), 3770.

(69)   Arachchige, I. U.; Brock, S. L. *Acc. Chem. Res.* **2007,** *40* (9), 801.

(70)   Joo, J.; Son, J. S.; Kwon, S. G.; Yu, J. H.; Hyeon, T. *J. Am. Chem. Soc.* **2006,** *128* (17), 5632.

(71)   Son, J. S.; Wen, X. D.; Joo, J.; Chae, J.; Baek, S. I.; Park, K.; Kim, J. H.; An, K.; Yu, J. H.; Kwon, S. G.; Choi, S. H.; Wang, Z. W.; Kim, Y. W.; Kuk, Y.; Hoffmann, R.; Hyeon, T. *Angew. Chem. Int. Ed.* **2009,** *48* (37), 6861.

(72)   Son, J. S.; Park, K.; Kwon, S. G.; Yang, J.; Choi, M. K.; Kim, J.; Yu, J. H.; Joo, J.; Hyeon, T. *Small* **2012,** *8* (15), 2394.

(73)   Yu, J. H.; Liu, X.; Kweon, K. E.; Joo, J.; Park, J.; Ko, K.-T.; Lee, D. W.; Shen, S.; Tivakornsasithorn, K.; Son, J. S.; Park, J.-H.; Kim, Y.-W.; Hwang, G. S.; Dobrowolska, M.; Furdyna, J. K.; Hyeon, T. *Nat Mater* **2010,** *9* (1), 47.

(74)   Liu, Y.-H.; Wayman, V. L.; Gibbons, P. C.; Loomis, R. A.; Buhro, W. E. *Nano Lett.* **2010,** *10* (1), 352.

(75)   Ithurria, S.; Tessier, M. D.; Mahler, B.; Lobo, R. P. S. M.; Dubertret, B.; Efros, A. L. *Nat Mater* **2011,** *10* (12), 936.

(76)   Tessier, M. D.; Javaux, C.; Maksimovic, I.; Loriette, V.; Dubertret, B. *Acs Nano* **2012,** *6* (8), 6751.

(77)   Tessier, M. D.; Spinicelli, P.; Dupont, D.; Patriarche, G.; Ithurria, S.; Dubertret, B. *Nano Lett.* **2014,** *14* (1), 207.

(78)   Pedetti, S.; Ithurria, S.; Heuclin, H.; Patriarche, G.; Dubertret, B. *J. Am. Chem. Soc.* **2014,** *136* (46), 16430.

(79)   Mahler, B.; Nadal, B.; Bouet, C.; Patriarche, G.; Dubertret, B. *J. Am. Chem. Soc.* **2012,** *134* (45), 18591.

(80)   Tessier, M. D.; Mahler, B.; Nadal, B.; Heuclin, H.; Pedetti, S.; Dubertret, B. *Nano Lett.* **2013,** *13* (7), 3321.

(81)   Bouet, C.; Laufer, D.; Mahler, B.; Nadal, B.; Heuclin, H.; Pedetti, S.; Patriarche, G.; Dubertret, B. *Chem. Mater.* **2014,** *26* (9), 3002.

(82)   Grim, J. Q.; Christodoulou, S.; Di Stasio, F.; Krahne, R.; Cingolani, R.; Manna, L.; Moreels, I. *Nature Nanotechnology* **2014,** *9* (11), 891.

(83)   She, C.; Fedin, I.; Dolzhnikov, D. S.; Demortiere, A.; Schaller, R. D.; Pelton, M.; Talapin, D. V. *Nano Lett.* **2014,** *14* (5), 2772.

(84)   Lhuillier, E.; Pedetti, S.; Ithurria, S.; Heuclin, H.; Nadal, B.; Robin, A.; Patriarche, G.; Lequeux, N.; Dubertret, B. *Acs Nano* **2014,** *8* (4), 3813.

(85)   Abecassis, B.; Tessier, M. D.; Davidson, P.; Dubertret, B. *Nano Lett.* **2014,** *14* (2), 710.

(86)   Tessier, M. D.; Biadala, L.; Bouet, C.; Ithurria, S.; Abecassis, B.; Dubertret, B. *Acs Nano* **2013,** *7* (4), 3332.

(87)   Halder, O.; Pradhani, A.; Sahoo, P. K.; Satpati, B.; Rath, S. *Appl. Phys. Lett.* **2014,** *104* (18).

(88)   Pelton, M.; Ithurria, S.; Schaller, R. D.; Dolzhnikov, D. S.; Talapin, D. V. *Nano Lett.* **2012,** *12* (12), 6158.

(89)   Lhuillier, E.; Hease, P.; Ithurria, S.; Dubertret, B. *Chem. Mater.* **2014,** *26* (15), 4514.

(90)   Ithurria, S.; Bousquet, G.; Dubertret, B. *J. Am. Chem. Soc.* **2011,** *133* (9), 3070.

(91)   Lim, S. J.; Kim, W.; Shin, S. K. *J. Am. Chem. Soc.* **2012,** *134* (18), 7576.

(92)   Koster, R. S.; Fang, C.; van Blaaderen, A.; Dijkstra, M.; van Huis, M. A. *PCCP* **2016,** *18* (32), 22021.

(93)   Noguez, C. *The Journal of Physical Chemistry C* **2007,** *111* (10), 3806.

(94)   Willets, K. A.; Duyne, R. P. V. *Annu. Rev. Phys. Chem.* **2007,** *58* (1), 267.

(95)   Mie, G. *Annalen der Physik* **1908,** *330* (3), 377.

(96)   Uwe Kreibig, M. V., *Optical Properties of Metal Clusters*. Springer-Verlag Berlin Heidelberg:, 1995; Vol. 25.

(97) Narayanan, R.; El-Sayed, M. A. *The Journal of Physical Chemistry B* **2005,** *109* (26), 12663.

(98) Narayanan, R.; El-Sayed, M. A. *Nano Lett.* **2004,** *4* (7), 1343.

(99) Narayanan, R.; El-Sayed, M. A. *The Journal of Physical Chemistry B* **2003,** *107* (45), 12416.

(100) Pal, J.; Pal, T. *Nanoscale* **2015,** *7* (34), 14159.

(101) Bratlie, K. M.; Lee, H.; Komvopoulos, K.; Yang, P.; Somorjai, G. A. *Nano Lett.* **2007,** *7* (10), 3097.

(102) Marković, N. M.; Adžić, R. R.; Cahan, B. D.; Yeager, E. B. *J. Electroanal. Chem.* **1994,** *377* (1), 249.

(103) Conrad, H.; Ertl, G.; Latta, E. E. *Surf. Sci.* **1974,** *41* (2), 435.

(104) Yang, J.; Levina, L.; Sargent, E. H.; Kelley, S. O. *J. Mater. Chem.* **2006,** *16* (41), 4025.

(105) Subramanian, V.; Wolf, E. E.; Kamat, P. V. *J. Am. Chem. Soc.* **2004,** *126* (15), 4943.

(106) Subramanian, V.; Wolf, E. E.; Kamat, P. V. *The Journal of Physical Chemistry B* **2003,** *107* (30), 7479.

(107) Hirakawa, T.; Kamat, P. V. *J. Am. Chem. Soc.* **2005,** *127* (11), 3928.

(108) Wood, A.; Giersig, M.; Mulvaney, P. *The Journal of Physical Chemistry B* **2001,** *105* (37), 8810.

(109) Mokari, T.; Rothenberg, E.; Popov, I.; Costi, R.; Banin, U. *Science* **2004,** *304* (5678), 1787.

(110) Mokari, T.; Sztrum, C. G.; Salant, A.; Rabani, E.; Banin, U. *Nat. Mater.* **2005,** *4* (11), 855.

(111) Naskar, S.; Schlosser, A.; Miethe, J. F.; Steinbach, F.; Feldhoff, A.; Bigall, N. C. *Chem. Mater.* **2015,** *27* (8), 3159.

(112) Elmalem, E.; Saunders, A. E.; Costi, R.; Salant, A.; Banin, U. *Adv. Mater.* **2008,** *20* (22), 4312.

(113) Meyns, M.; Bastus, N. G.; Cai, Y.; Kornowski, A.; Juarez, B. H.; Weller, H.; Klinke, C. *J. Mater. Chem.* **2010,** *20* (47), 10602.

(114) Meyns, M.; Willing, S.; Lehmann, H.; Klinke, C. *ACS Nano* **2015,** *9* (6), 6077.

(115) Saunders, A. E.; Popov, I.; Banin, U. *J. Phys. Chem. B* **2006,** *110* (50), 25421.

(116) Habas, S. E.; Yang, P.; Mokari, T. *J. Am. Chem. Soc.* **2008,** *130* (11), 3294.

(117) Maynadie, J.; Salant, A.; Falqui, A.; Respaud, M.; Shaviv, E.; Banin, U.; Soulantica, K.; Chaudret, B. *Angew. Chem. Int. Ed.* **2009,** *48* (10), 1814.

(118) Li, X.; Lian, J.; Lin, M.; Chan, Y. *J. Am. Chem. Soc.* **2010,** *133* (4), 672.

(119) Costi, R.; Saunders, A. E.; Banin, U. *Angew. Chem. Int. Ed.* **2010,** *49* (29), 4878.

(120) Deka, S.; Falqui, A.; Bertoni, G.; Sangregorio, C.; Poneti, G.; Morello, G.; Giorgi, M. D.; Giannini, C.; Cingolani, R.; Manna, L.; Cozzoli, P. D. *J. Am. Chem. Soc.* **2009,** *131* (35), 12817.

(121) Sitt, A.; Hadar, I.; Banin, U. *Nano Today* **2013,** *8* (5), 494.

(122) Shaviv, E.; Schubert, O.; Alves-Santos, M.; Goldoni, G.; Di Felice, R.; Vallee, F.; Del Fatti, N.; Banin, U.; Sonnichsen, C. *Acs Nano* **2011,** *5* (6), 4712.

(123) Naiki, H.; Masuhara, A.; Masuo, S.; Onodera, T.; Kasai, H.; Oikawa, H. *J. Phys. Chem. C.* **2013,** *117* (6), 2455.

(124) Sharma, B. L. *Springer* **1984**.

(125) Brucker, C. F.; Brillson, L. J.; Katnani, A. D.; Stoffel, N. G.; Margaritondo, G. *Journal of Vacuum Science & Technology* **1982,** *21* (2), 590.

(126) Mehta, R. R.; Sharma, B. S. *J. Appl. Phys.* **1973,** *44* (1), 325.

(127) Yu, X.; Shavel, A.; An, X.; Luo, Z.; Ibáñez, M.; Cabot, A. *J. Am. Chem. Soc.* **2014,** *136* (26), 9236.

(128) Sigle, D. O.; Zhang, L. W.; Ithurria, S.; Dubertret, B.; Baumberg, J. J. *J. Phys. Chem. Lett.* **2015,** *6* (7), 1099.

(129) Sung, Y.; Lim, J.; Koh, J. H.; Hill, L. J.; Min, B. K.; Pyun, J.; Char, K. *Cryst. Eng. Comm.* **2015,** *17* (44), 8423.

(130) Wu, K.; Chen, Z.; Lv, H.; Zhu, H.; Hill, C. L.; Lian, T. *J. Am. Chem. Soc.* **2014,** *136* (21), 7708.

(131) Tongying, P.; Plashnitsa, V. V.; Petchsang, N.; Vietmeyer, F.; Ferraudi, G. J.; Krylova, G.; Kuno, M. *J. Phys.Chem. Lett.* **2012,** *3* (21), 3234.

(132) Nakibli, Y.; Kalisman, P.; Amirav, L. *J. Phys. Chem. Lett.* **2015,** *6* (12), 2265.

(133) Simon, T.; Bouchonville, N.; Berr, M. J.; Vaneski, A.; Adrović, A.; Volbers, D.; Wyrwich, R.; Döblinger, M.; Susha, A. S.; Rogach, A. L.; Jäckel, F.; Stolarczyk, J. K.; Feldmann, J. *Nat. Mater.* **2014,** *13* (11), 1013.

(134) Jana, N. R.; Gearheart, L.; Murphy, C. J. *Chem. Commun.* **2001,** (7), 617.

(135) Carbone, L.; Cozzoli, P. D. *Nano Today* **2010,** *5* (5), 449.

(136) Wang, Y.; Xia, Y. *Nano Lett.* **2004,** *4* (10), 2047.

(137) Sharma, A.; Verma, N.; Sharma, A.; Deva, D.; Sankararamakrishnan, N. *Chem. Eng. Sci.* **2010,** *65* (11), 3591.

(138) Amendola, V.; Meneghetti, M. *PCCP* **2009,** *11* (20), 3805.

(139) Caldorera-Moore, M.; Guimard, N.; Shi, L.; Roy, K. *Expert opinion on drug delivery* **2010,** *7* (4), 479.

(140) de Mello Donegá, C.; Liljeroth, P.; Vanmaekelbergh, D. *Small* **2005,** *1* (12), 1152.

(141) Yin, Y.; Alivisatos, A. P. *Nature* **2005,** *437* (7059), 664.

(142) Bley, R. A.; Kauzlarich, S. M.; Davis, J. E.; Lee, H. W. H. *Chem. Mater.* **1996,** *8* (8), 1881.

(143) Vossmeyer, T.; Katsikas, L.; Giersig, M.; Popovic, I. G.; Diesner, K.; Chemseddine, A.; Eychmueller, A.; Weller, H. *The Journal of Physical Chemistry* **1994,** *98* (31), 7665.

(144) Zhang, H.; Wang, L.; Xiong, H.; Hu, L.; Yang, B.; Li, W. *Adv. Mater.* **2003,** *15* (20), 1712.

(145) Hayashi, H.; Hakuta, Y. *Materials* **2010,** *3* (7), 3794.

(146) Frens, G. *Nature-Physical Science* **1973,** *241* (105), 20.

(147) Park, J.; Joo, J.; Kwon, S. G.; Jang, Y.; Hyeon, T. *Angew. Chem. Int. Ed.* **2007,** *46* (25), 4630.

(148) Jana, N. R.; Gearheart, L.; Murphy, C. J. *The Journal of Physical Chemistry B* **2001,** *105* (19), 4065.

(149) Maillard, M.; Huang, P.; Brus, L. *Nano Lett.* **2003,** *3* (11), 1611.

(150) Cao, S.-W.; Fang, J.; Shahjamali, M. M.; Wang, Z.; Yin, Z.; Yang, Y.; Boey, F. Y. C.; Barber, J.; Loo, S. C. J.; Xue, C. *CrystEngComm* **2012,** *14* (21), 7229.

(151) Park, J. B.; Conner, S. F.; Chen, D. A. *The Journal of Physical Chemistry C* **2008,** *112* (14), 5490.

(152) Figuerola, A.; Franchini, I. R.; Fiore, A.; Mastria, R.; Falqui, A.; Bertoni, G.; Bals, S.; Van Tendeloo, G.; Kudera, S.; Cingolani, R.; Manna, L. *Adv. Mater.* **2009,** *21* (5), 550.

(153) O'Sullivan, C.; Gunning, R. D.; Barrett, C. A.; Singh, A.; Geaney, H.; Sanyal, A.; Ahmed, S.; Bala, T.; Ryan, K. M., Facet Specific Gold Tip Growth on Semiconductor Nanorods. In *State-of-the-Art Program on Compound Semiconductors 51*, Stokes, E.; Goldhahn, R.; Hunter, G.; Odwyer, C.; Ambacher, O.; Huang, J.; Kohn, E.; Overberg, M. E., Eds. 2009; Vol. 25, pp 17.

(154) Kodanek, T.; Banbela, H. M.; Naskar, S.; Adel, P.; Bigall, N. C.; Dorfs, D. *Nanoscale* **2015,** *7* (45), 19300.

(155) Dubois, F.; Mahler, B.; Dubertret, B.; Doris, E.; Mioskowski, C. *J. Am. Chem. Soc.* **2007,** *129* (3), 482.

(156) Algar, W. R.; Krull, U. J. *Chemphyschem* **2007,** *8* (4), 561.

(157) Jana, N. R.; Earhart, C.; Ying, J. Y. *Chem. Mater.* **2007,** *19* (21), 5074.

(158) Darbandi, M.; Thomann, R.; Nann, T. *Chem. Mater.* **2005,** *17* (23), 5720.

(159) Pellegrino, T.; Manna, L.; Kudera, S.; Liedl, T.; Koktysh, D.; Rogach, A. L.; Keller, S.; Rädler, J.; Natile, G.; Parak, W. J. *Nano Lett.* **2004,** *4* (4), 703.

(160) Lista, M.; Liu, D. Z.; Mulvaney, P. *Langmuir* **2014,** *30* (8), 1932.

(161) Wei, G.-T.; Yang, Z.; Lee, C.-Y.; Yang, H.-Y.; Wang, C. R. C. *J. Am. Chem. Soc.* **2004,** *126* (16), 5036.

(162) J. Alemán, A. V. C., J. He, M. Hess, K. Horie, R. G. Jones, P. Kratochvíl, I. Meisel, I. Mita, G. Moad, S. Penczek and R. F. T. Stepto *Pure Appl. Chem* **2007,** *79* (10), 1801.

(163) Kistler, S. S. *Nature* **1931,** *127*, 741.

(164) Rubin, M.; Lampert, C. M. *Solar Energy Materials* **1983,** *7* (4), 393.

(165) Randall, J. P.; Meador, M. A. B.; Jana, S. C. *ACS. Appl. Mater. Int.* **2011,** *3* (3), 613.

(166) Cantin, M.; Casse, M.; Koch, L.; Jouan, R.; Mestreau, P.; Roussel, D.; Bonnin, F.; Moutel, J.; Teichner, S. J. *Nuclear Instruments & Methods* **1974,** *118* (1), 177.

(167) Gong, K.; Du, F.; Xia, Z.; Durstock, M.; Dai, L. *Science* **2009,** *323* (5915), 760.

(168) Leventis, N.; Chidambareswarapattar, C.; Bang, A.; Sotiriou-Leventis, C. *ACS. Appl. Mater. Int.* **2014,** *6* (9), 6872.

(169) Wen, D.; Liu, W.; Herrmann, A.-K.; Eychmueller, A. *Chemistry-a European Journal* **2014,** *20* (15), 4380.

(170) Yuan, J.; Gaponik, N.; Eychmueller, A. *Chemical Sensors 10 -and- Mems/Nems 10* **2012,** *50* (12), 255.

(171) Yao, Q.; Brock, S. L. *Nanotechnology* **2010,** *21* (11), 115502.

(172) Gacoin, T.; Malier, L.; Boilot, J.-P. *Chem. Mater.* **1997,** *9* (7), 1502.

(173) Mohanan, J. L.; Brock, S. L. *Abstracts of Papers of the American Chemical Society* **2003,** *225*, U55.

(174) Gaponik, N.; Wolf, A.; Marx, R.; Lesnyak, V.; Schilling, K.; Eychmueller, A. *Adv. Mater.* **2008,** *20* (22), 4257.

(175) Arachchige, I. U.; Brock, S. L. *J. Am. Chem. Soc.* **2007,** *129* (7), 1840.

(176) Chen, H.; Lesnyak, V.; Bigall, N. C.; Gaponik, N.; Eychmueller, A. *Chem. Mater.* **2010,** *22* (7), 2309.

(177) Sánchez-Paradinas, S.; Dorfs, D.; Friebe, S.; Freytag, A.; Wolf, A.; Bigall, N. C. *Adv. Mater.* **2015,** *27* (40), 6152.

(178) Liu, W.; Herrmann, A.-K.; Geiger, D.; Borchardt, L.; Simon, F.; Kaskel, S.; Gaponik, N.; Eychmueller, A. *Angewandte Chemie-International Edition* **2012,** *51* (23), 5743.

(179) Wen, D.; Liu, W.; Haubold, D.; Zhu, C.; Oschatz, M.; Holzschuh, M.; Wolf, A.; Simon, F.; Kaskel, S.; Eychmüller, A. *ACS Nano* **2016,** *10* (2), 2559.

(180) Leventis, N.; Chandrasekaran, N.; Sotiriou-Leventis, C.; Mumtaz, A. *J. Mater. Chem.* **2009,** *19* (1), 63.

(181) Hendel, T.; Lesnyak, V.; Kuehn, L.; Herrmann, A.-K.; Bigall, N. C.; Borchardt, L.; Kaskel, S.; Gaponik, N.; Eychmueller, A. *Adv. Funct. Mater.* **2013,** *23* (15), 1903.

(182) Lesnyak, V.; Wolf, A.; Dubavik, A.; Borchardt, L.; Voitekhovich, S. V.; Gaponik, N.; Kaskel, S.; Eychmüller, A. *J. Am. Chem. Soc.* **2011,** *133* (34), 13413.

(183) Brinker, C. J. S., G. Sol-Gel Science: The Physics and; Chemistry of Sol-Gel Processing; Academic Press: London *Sol-Gel Science: The Physics and Chemistry of Sol-Gel Processing; Academic Press: London, 1990*

(184) Freytag, A.; Sánchez-Paradinas, S.; Naskar, S.; Wendt, N.; Colombo, M.; Pugliese, G.; Poppe, J.; Demirci, C.; Kretschmer, I.; Bahnemann, D. W.; Behrens, P.; Bigall, N. C. *Angew. Chem. Int. Ed.* **2015,** *DOI: 10.1002/anie.201508972*.

(185) Armatas, G. S.; Kanatzidis, M. G. *Nature* **2006,** *441* (7097), 1122.

(186) Trikalitis, P. N.; Rangan, K. K.; Kanatzidis, M. G. *J. Am. Chem. Soc.* **2002,** *124* (11), 2604.

(187) Bag, S.; Gaudette, A. F.; Bussell, M. E.; Kanatzidis, M. G. *Nat Chem* **2009,** *1* (3), 217.

2 Aerogels from Quasi 2D CdSe and CdSe/CdS Core/Crown Nanoplatelets

2.1 Summary

The newly invented colloidal NPLs of only few monolayer thickness exhibit fascinating optoelectronic properties due to very strong quantum confinement in the z direction. Self-aggregation of these NPLs in organic hexane solution by means of a little amount of ethanol addition leads to needless type geometry which emits polarized light. But the self-assembly of the NPLs into highly porous macroscopic solid state superstructure has not been investigated before. The following study presented in section 2.2, shows a new method to fabricate macroscopic 3D aerogels from the quasi 2D CdSe and CdSe/CdS core/crown NPLs. First the NPLs are synthesized in organic medium and then transferred to aqueous medium by using ligand exchange reaction. The hydrogels are obtained by controlled destabilization of the aqueous NPLs solution by means of H_2O_2 addition. The optimum gelation conditions are investigated by varying the amounts of H_2O_2 content. Thereafter, the hydrogels are converted to aerogels by supercritical drying. The optical properties of the hydrogels and the aerogels are evaluated by measuring the absorption, PL emission and PL decay time. Interestingly, the aerogels partially exhibit the quantum confinement properties of the initial colloidal NPLs. The interconnected network of the gels are investigated by means of TEM and SEM analysis, which proves that the NPLs are randomly oriented and connected edge-to-edge to form this porous structure. Moreover, the aerogels reported here have extremely low densities and very high specific surface areas in

the range of 189-219 $m^2 \cdot g^{-1}$. Furthermore, the aerogels exhibit mostly (100) as the exposed crystal facets all over the surface.

2.2 Photoluminescent Aerogels from Quantum Wells

Suraj Naskar, Jan. F. Miethe, Sara Sánchez-Paradinas, Nadeschda Schmidt, Peter Behrens,

Karthiga Kanthasamy, Herbert Pfnür, Nadja C. Bigall*

Photoluminescent Aerogels from Quantum Wells

Suraj Naskar,[†,||] Jan F. Miethe,[†,||] Sara Sánchez-Paradinas,[†,||] Nadeschda Schmidt,[‡,||] Karthiga Kanthasamy,[§,||] Peter Behrens,[‡,||] Herbert Pfnür,[§,||] and Nadja C. Bigall*[,†,||]

[†]Institute of Physical Chemistry and Electrochemistry, Leibniz Universität Hannover, Callinstraße 3A, 30167 Hannover, Germany
[‡]Institute for Inorganic Chemistry, Leibniz Universität Hannover, Callinstraße 9, 30167 Hannover, Germany
[§]Institut für Festkörperphysik, Leibniz Universität Hannover, Appelstraße 2, 30167 Hannover, Germany
[||]Laboratory for Nano and Quantum Engineering, Schneiderberg 39, 30167 Hannover, Germany

S Supporting Information

ABSTRACT: Highly porous self-supported three-dimensional aerogel monoliths are synthesized from strongly quantum confined quantum wells, namely, 5 monolayer thick CdSe and CdSe/CdS core/crown nanoplatelets. The aerogels are synthesized by hydrogelation of the aqueous quantum well solutions and subsequent supercritical drying. The aerogels are optically characterized by UV−vis absorption spectroscopy, emission spectroscopy, and photoluminescence (PL) decay analysis. Morphological and structural characterizations are achieved by transmission electron microscopy, scanning electron microscopy, and X-ray diffractometry. The macroscopic aerogels exhibit extremely low densities of 0.038 ± 0.007 g·cm^{-3} and a significantly high specific surface area of 219 m^2·g^{-1} with nearly entirely (111) as the exposed crystal facet. Moreover, the aerogels feature properties related to quantum confinement comparable to those of their original building blocks with photoluminescence quantum yields up to 10.3%.

CdSe/CdS NPLs   CdSe/CdS aerogel
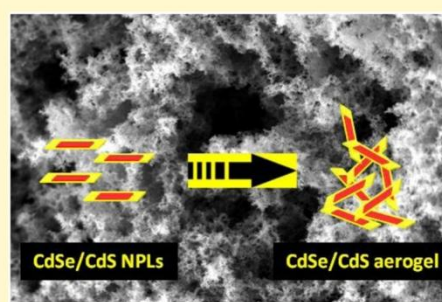
1. INTRODUCTION

Metal-chalcogenide nanoparticles, such as colloidal quantum dots, rods, tetrapods, octapods, nanowires, nanoribbons, nanoplatelets (NPLs), or nanosheets (sometimes also referred to as quantum wells), have attracted the attention of many scientists due to their interesting size and shape dependent optoelectronic properties.[1−6] By controlling the shape of the nanocrystals, the exciton (electron−hole pair) can be confined in three dimensions, e.g., in quasi-spherical crystals, in two dimensions such as in nanorods and nanowires, and in one dimension, namely, in quantum wells such as NPLs. In recent years, a variety of only few monolayer (ML) thick NPLs, core/shell NPLs, or core/crown NPLs of various compositions, such as CdSe,[4,7−10] CdSe/CdS,[5,11] CdSe/CdS/CdZnS,[12] PbSe/PbS,[6] ZnSe/ZnS,[13] and CdSe/CdTe[14] have been reported, with unique optoelectronic properties such as high photoluminescence quantum yields (PLQYs), extremely narrow emission band widths, ultrafast fluorescence decays, and reduced Stokes shifts. As for applications, electroluminescent emitters, reversible oxygen sensing, and room temperature lasing with low energy threshold have already been reported.[15−18] Furthermore, the CdSe NPLs were assembled into close-packed pile-shaped products emitting polarized light.[8] Instead, the assembly of the NPLs into self-supported, highly porous 3D bulk architectures, which would be of interest for a variety of possible applications, such as in photovoltaics, sensors for detecting chemicals, and photocatalysis, has not been reported so far.

In earlier studies, porous aerogels from quasi-spherical CdS nanoparticles were obtained by controlled destabilization of the colloidal solution.[19] Since then, research efforts have been dedicated to extend this technique to other colloidal semiconductor building blocks of various cadmium chalcogenide compounds including quasi-spherical and rod-like shapes.[20−26] Regarding possible applications, metal chalcogenide aerogels for capturing radioactive elements and enzyme encapsulated quantum dot hydrogels for the development of biosensors have already been demonstrated.[21,27] More recently, also, mixed aerogels, e.g., from Au and CdTe,[28,29] and aerogels solely from metal nanoparticles (such as Pt, Au, Ag)[30−36] have been reported. Here, we present to the best of our knowledge for the first time the assembly of fluorescent quantum wells to form self-supported highly porous, extremely lightweight, macroscopic 3D aerogels with large specific surfaces. The destabilization of the here employed anisotropic 5 ML thick CdSe and CdSe/CdS core/crown NPL building blocks in aqueous medium was achieved by hydrogen peroxide induced ligand oxidation. The impact of variable amounts of H_2O_2 on the gelation process and on the optical properties of the resulting hydrogels and aerogels is investigated. A diagram representing the synthesis steps from the pristine colloidal NPLs in hexane solution over phase transfer to aqueous

Scheme 1. Schematic Diagram of the Aerogel Formation from CdSe/CdS Core/Crown NPLs[a]
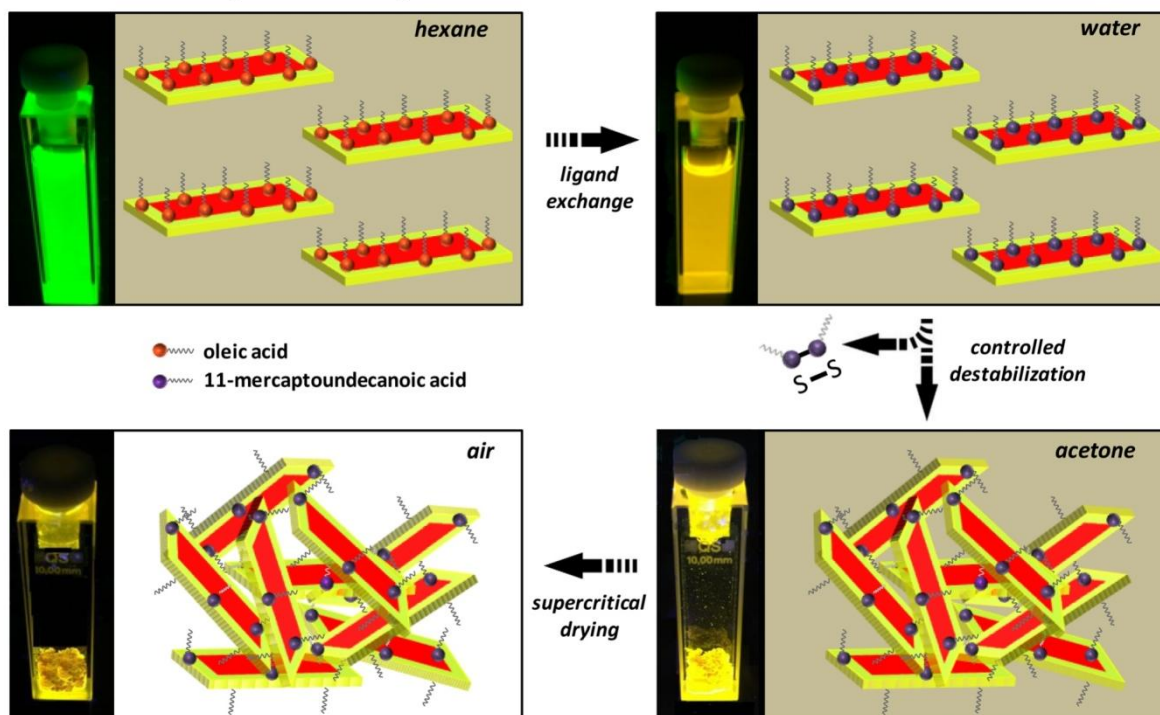
[a]First, ligand exchange is performed in order to transfer the quantum wells to aqueous solution. Controlled destabilization by means of hydrogen peroxide addition results in the formation of hydrogels, which are subsequently transferred to aerogels by supercritical drying. The photographs on the left of the schemes display the quantum wells in the respective solutions and in the gels under UV illumination.

solution, and over hydrogelation to fluorescent aerogel monoliths, is shown in Scheme 1.

The aerogels reported here exhibit intense photoluminescence and might in the future serve as an effective material for highly sensitive sensing devices. For example, Lorenzon et al.[17] have observed that CdSe based NPLs have a unique capability of photoluminescence based reversed oxygen sensing (and other gases such as CO and CO_2) attributing this property to the large specific surface of the particle increasing the probability for the creation of surface trap states which are necessary for this type of reversed gas sensing. The assembly of NPLs into a highly porous and accessible large surface superstructure (as achieved in the present work) might help making gas sensing devices from such nanoscopic building blocks, since the aerogels are self-supported in gaseous environments. The high porosity and mesoporous character of the hydrogel and aerogel materials developed in the present work might allow possible reactant molecules to access the large specific surface area, and hence, such gels are potentially also applicable for superior electrocatalytic activity.[37] A different example for possible applications, with the porous arrangement of CdSe based NPLs, was suggested by the Dubertret group[38] in their work about the employment of NPLs in electrolyte gated field effect transistors. It was found that porous arrangement leads to much higher currents due to a better chemical interface, and it was suggested that even more porous arrangements could improve this effect. Therefore, a gel-type assembly as synthesized in our present work would be of high interest also for this type of application. Moreover, aerogels of the NPLs exhibit solely (111) as the exposed crystal facet,

providing the opportunity to perform facet dependent chemical reactions on its surface. Furthermore, the here developed aerogel materials might be applicable in optical sensing, photovoltaics, and light emitting diodes (LEDs) or as a catalyst.

2. EXPERIMENTAL SECTION

Reagents. Cadmium nitrate tetrahydrate (99.999%), cadmium acetate dihydrate (98.0%), sulfur powder (>99%), sodium myristate (>99%), 11-mercaptoundecanoic acid (MUA) (95%), hydrogen peroxide (30%), 1-octadecene (90%) (ODE), oleic acid (90%), methanol (99.5%), ethanol (99.5%), n-hexane (>99%), and acetone (>99%) were purchased from Sigma-Aldrich. Selenium powder 200 meshes (99.999%), nitric acid (>69%), and hydrochloric acid (>37%) were purchased from Fluka. Indium foil, thickness of 0.1 mm, ≥99.995% trace metal basis was purchased from Sigma-Aldrich.

Synthesis of 5 ML Thick CdSe NPLs. Quasi 2D, 5 ML thick CdSe NPLs were prepared according to the procedure described in the literature with little modifications.[5,39] A total amount of 170 mg of cadmium myristate, $Cd(myr)_2$ (0.3 mM), and 14 mL of ODE was placed in a 25 mL three neck round-bottom flask. The mixture was degassed at 100 °C for 1 h at constant stirring conditions. A clear solution of cadmium myristate dissolved in ODE was obtained. Under argon flow, the temperature of the solution was raised to 250 °C. Then, 1 mL of a 0.15 mM Se solution (prepared by dispersing 12 mg of Se powder in 1 mL of ODE) was quickly injected into the mixture. Subsequently, 1 min after the selenium solution injection, a total amount of 120 mg (0.9 mM) of $Cd(OAc)_2·2H_2O$ was added to the mixture. The reaction was continued at a constant temperature of 250 °C for 10 min. Finally, 0.5 mL of oleic acid was injected into the mixture, and the reaction temperature was lowered down to room temperature by placing a water bath under the flask. The NPLs were separated from all other byproducts (mainly CdSe cubes and spheres) by adding 20 mL of a mixture of hexane/ethanol = 3:1 and

centrifuging for 15 min at 3800 g (rcf). The dark red precipitate of the CdSe NPLs was collected from the bottom of the centrifuge vial and dispersed in 2 mL of hexane.

Synthesis of 5 ML Thick CdSe/CdS Core/Crown NPLs. The growth of a CdS crown on these CdSe NPLs was performed following the modified method of Tessier et al.[5] A synthesis mixture for the growth of the CdS crown was prepared by placing 480 mg of Cd(OAc)$_2$·2H$_2$O together with 340 μL of oleic acid and 2 mL of ODE in a three neck flask. The temperature of the mixture was increased to 150 °C, and the reaction was continued for 15 min under air with constant stirring and sonication. The light gray mixture of the cadmium oleate was cooled down to room temperature, and subsequently, 3 mL of a 0.1 M sulfur precursor solution prepared previously by dissolving 19 mg of elemental S in 6 mL of ODE was added. The whole mixture was then transferred to a syringe. The entire product of the previously prepared 5 ML CdSe NPLs was placed inside a 25 mL three neck round-bottom flask with 10 mL of ODE. The temperature of the reaction flask was increased to 100 °C, and the mixture was degassed under vacuum for 30 min to remove the hexane completely. Under Ar flow, the mixture was heated up to 240 °C. The crown growth mixture (prepared previously) was continuously injected at a rate of 8 mL/h for 7.5 min by means of a syringe pump. The heating mantle was removed, and the solution was allowed to reach room temperature; after that, 15 mL of ethanol was added. The whole mixture was transferred to a centrifuge vial, and the NPLs were precipitated by centrifugation at 3800 g (rcf) for 15 min. The supernatant was discarded, and the CdSe/CdS core/crown NPLs were dispersed in 3 mL of hexane.

Phase Transfer of 5 ML Thick CdSe and CdSe/CdS NPLs. The NPLs were transferred to an aqueous medium following a procedure described by Kodanek et al.[40] Briefly, a mixture of 61 mg of MUA together with 4 mL of methanol and 0.05 g of KOH was placed in a vial and sonicated for 3 min. The entire hexane solution of the CdSe NPLs (Cd ion concentration is 25 mM as determined from AAS) synthesized above was added to the vial with the phase transfer reagent and shaken overnight. The hexane phase was removed by means of a separation funnel, and the MUA capped CdSe NPLs in the methanolic phase were precipitated by centrifugation. Afterward, the whole product was dispersed in 4 mL of a 0.1 M KOH solution. Finally, the phase transferred NPLs were washed twice with distilled water. The CdSe/CdS NPLs were transferred to aqueous medium following the same procedure as mentioned above.

Hydrogelation of the CdSe/CdS Core/Crown and CdSe NPLs. In the first set of experiments, the effect of H$_2$O$_2$ concentration on the time required for the appearance of hydrogel formation was studied. Therefore, eight, 2 mL microcentrifuge tubes were filled with 400 μL of the aqueous NPLs solution. The Cd ion concentration of the NPLs solution was kept constant at 1.77 mM. Thereafter, a series of different concentrations of H$_2$O$_2$ solutions (0.1%, 0.15%, 0.25%, 0.5%, 0.75%, 1%, 1.5% and 2%) were prepared, and 20 μL of each was added to the vials containing NPLs, which led to molar ratios of [H$_2$O$_2$]/[Cd^{2+}] = 1.2:1, 1.8:1, 3.0:1, 5.8:1, 8.7:1, 11.6:1, 17.4:1, and 23.2:1, respectively. All the sample vials were placed in an oven (already heated) at 80 °C for 2 min in order to initiate the gelation process and subsequently placed under ambient conditions in the dark. The time required for the first appearance of the hydrogel was 1.5 h for [H$_2$O$_2$]/[Cd^{2+}] = 23.2:1 (NPLs are completely bleached) and more than 14 days for [H$_2$O$_2$]/[Cd^{2+}] = 1.1:1. In the case of molar [H$_2$O$_2$]/[Cd^{2+}] ratios 1.8:1, the gelation time was approximately 1 week. In all other cases, gelation time was found to vary between 3 and 8 h. The extent of bleaching of the NPLs was found to increase with higher molar ratios of [H$_2$O$_2$]/[Cd^{2+}]. Hence, the optimum gelation condition lies between molar ratio [H$_2$O$_2$]/[Cd^{2+}] = 3.0:1 to 5.5:1, where the gelation time is 6−8 h and the NPLs are least oxidized.

In the second set of experiments, the effect of variable [H$_2$O$_2$]/[Cd^{2+}] molar ratio on the optical properties of the resulting gel was investigated following the above-mentioned optimum reaction conditions. Therefore, 5, 7, 9, 11, and 13 μL of a 0.5% H$_2$O$_2$ solution were added to each microcentrifuge tube containing 400 μL of aqueous NPLs solution (molar ratio [H$_2$O$_2$]/[Cd^{2+}] = 3.0:1, 3.7:1,

4.3:1, 4.9:1, and 5.5:1, respectively). Once the appearance of the hydrogels was observed, the supernatant solvent was exchanged with deionized water for 7 to 8 times in order to remove excess H$_2$O$_2$ and reaction byproducts from the system. Subsequently, the samples were kept at ambient conditions in the dark for 3 days (aging). Thereafter, the solvent was gradually exchanged with mixtures of 10%, 20%, 40%, and 60% (v/v) acetone in water, and finally, the samples were washed with pure acetone (7 to 8 times). In order to remove residual water, the vials were filled with dry acetone and were placed inside a desiccator with anhydrous CaCl$_2$ to avoid the contamination of moisture from air. The desiccator was evacuated until the acetone slightly boiled and left at these conditions for 8 h. The acetogels were then transferred to a supercritical drying boat in an anhydrous acetone environment. The boat was inserted in the critical point dryer chamber (E3100 from Quorum Technologies), where acetone was replaced with liquid CO$_2$. After storage in liquid CO$_2$ for 1 day, the temperature of the chamber was raised above the critical point of CO$_2$ (31.5 °C and 1100 psi), and the CO$_2$ present in the system was released as a gas. A volume shrinkage of roughly 30% to 40% was observed during the conversion of hydrogels to aerogels. The monolithic aerogels of the CdSe and CdSe/CdS core/crown NPLs were stored under ambient conditions.

Measurement of Density of the Aerogels. The aerogels are irregular in shape, which makes it difficult to estimate the exact volume. We have calculated the volume via inserting small aerogel pieces in a cylindrical vial with known inner diameter. From the filling height of the aerogel inside the vial (several measurements are taken to obtain an average height), the volume has been calculated. From the mass of the aerogel (measured with a Sartorius balance, measurement accuracy of ±0.0001 g), the density has been evaluated. We have taken into account a maximum of 20% error in the measurement.

Atomic Absorption Spectroscopy. The Cd ion concentration of the CdSe NPLs and the CdSe/CdS NPLs solution was determined by atomic absorption spectroscopy (AAS) using a Varian AA140 instrument equipped with an air/acetylene flame atomizer. The samples were prepared by digestion with aqua regia. Five standard Cd^{2+} solutions were measured to obtain a calibration curve. A 1% HNO$_3$ solution was used in order to correct the background signal.

Scanning Electron Microscopy. Scanning electron microscopy (SEM) was carried out on a JEOL JSM 6700F equipped with cold field emission gun electron source. The samples for SEM imaging were prepared by deposition of small pieces of the aerogels on adhesive carbon films.

Transmission Electron Microscopy. The morphologies of the gels were investigated by transmission electron microscopy (TEM) using a FEI Tecnai G2 F20 TMP (C_s = 2 mm, C_C = 2 mm), equipped with a 200 kV field emission gun. Micrographs were taken in bright field mode. Each sample was purified 3 to 4 times by precipitation with ethanol (CdSe NPLs and CdSe/CdS NPLs) followed by centrifugation and redispersion in hexane, prior to TEM grid preparation. Subsequently, 10 μL of the purified sample was dropcasted on a 300 mesh carbon coated copper TEM grid, purchased from Quantifoil. In the case of aqueous solution, 10 μL of the sample was dried on the TEM grid using an IR lamp for 20 min. The TEM samples of the aerogels were prepared by carefully touching the aerogels with the TEM grid.

Spectroscopic Characterization. UV−vis absorption spectra of the samples were recorded using an Agilent Cary 5000 absorption spectrophotometer. Emission spectra of the samples were recorded using a Horiba Fluoromax-4 spectrometer. The PLQYs (in absolute mode) of the samples in solution, the hydrogels, and the aerogels were measured with a Horiba-DUAL FL spectrophotometer equipped with a Quanta-φ integrating sphere (Horiba). All absorption and emission spectra of the samples were measured in a 1 cm quartz cuvette using toluene, hexane (UV−vis spectroscopy grade), water, or 0.1 M KOH as solvents. Time-correlated single photon counting (TCSPC) measurements were performed using a Fluoromax-4 combined with the Fluorohub TCSPC unit. A nanosecond pulsed LED with full width at half maxima (fwhm) around 1.2 ns was used as the excitation

source. The excitation wavelength was 368 nm for CdSe NPLs in hexane medium and 454 nm for all other samples.

X-ray Photoelectron Spectroscopy (XPS). A Leybold Heraeus XPS analyzer with Al Kα X-ray beam was used as the excitation source to analyze the surface of the aerogel. A small amount of aerogel sample was pressed onto an indium foil (~1.7 cm^2). The conductive, soft surface of the indium foil holds the sample adequately and prevents specimen charging.[21] The samples were incubated in vacuum (10^{-8} mbar) for 18 h before the measurements. All the binding energy peaks were calibrated with measured carbon 1s peak (binding energy of 284.6 eV). The raw data from XPS analysis was fitted with Gaussian/Lorentzian curve fitting using XPS 4.1 software.

Nitrogen Physisorption Measurements. Nitrogen sorption isotherms were measured at 77 K on a Quantachrome Autosorb-3 instrument. The samples were degassed under vacuum at 25 °C for 24 h before the start of the sorption measurement. Surface areas were estimated by applying the Brunauer–Emmett–Teller (BET) equation.[41] The pore size distribution was calculated using the Barrett–Joyner–Halenda (BJH) method.[42] The total pore volume was estimated using the single point method at $p/p_0 = 0.99$.

3. RESULTS AND DISCUSSION

After the NPL synthesis and prior to gelation, both CdSe NPLs and the CdSe/CdS core/crown NPLs were transferred to water following a procedure described in a previous work.[40] The TEM micrographs of the anisotropic NPLs as well as the optical characterizations, measurements from UV–vis absorbance, emission, and photoluminescence (PL) decay are shown in Figures SI-1 and SI-2 and discussed in detail in the Supporting Information. These NPLs in aqueous solution were employed as building blocks for the gel synthesis.

Prior studies reveal that hydrogels of conventional (such as dots or rods) metal chalcogenide nanoparticles are obtained by controlled destabilization of the system employing H_2O_2 or tetranitromethane as the oxidizing agents.[21,22,26,43−45] The gelation process is initiated via partial removal of the surface ligands by oxidation, which reduces repulsion between the nanoparticles and results in partial aggregation to form the gel-like network.[25,26] In the present Article, hydrogelation of the CdSe NPLs and the CdSe/CdS NPLs was achieved employing the same technique using H_2O_2 as chemical oxidizing agent. The effect of H_2O_2 amount on the CdSe/CdS (aq) NPLs gelation process was investigated by adding a defined amount of H_2O_2 in concentrations varying from 0.1% to 2%, while keeping the amount of MUA ligands and NPLs constant (see the Experimental Section). With 0.1% concentration (a molar $[H_2O_2]/[Cd^{2+}]$ ratio of 1.2:1), the initial gelation effect, i.e., a voluminous monolithic aggregation with a clear supernatant, was only observed after 2 weeks with reduced fluorescence intensity (PLQY = 4.3% ± 0.2%). For larger molar $[H_2O_2]/[Cd^{2+}]$ ratios below 3.0:1, hydrogelation also took a relatively long time (approximately 1 week). For such low hydrogen peroxide amounts probably only insufficient ligands were removed from the surface of the NPLs. Furthermore, for these low hydrogen peroxide concentrations, the hydrogels obtained exhibited low photoluminescence, and the gel consistency is not enough to enable transfer to the supercritical drying boat for further processing. In the case of higher oxidant concentrations (i.e., molar $[H_2O_2]/[Cd^{2+}]$ ratios of 11.6 to 23.2:1), a rapid gelation of the NPLs (within 1.5 h) was observed. However, with these larger amounts of H_2O_2, the emission of the wet gel was found to be completely quenched. The optimum gel formation was found to take place with molar $[H_2O_2]/[Cd^{2+}]$ ratios of 3.0:1 to 5.5:1. In these cases, also bright photoluminescence was observed. Photographs of the

hydrogels and the corresponding aerogels under daylight and upon UV light irradiation are shown in Figure 1. In this
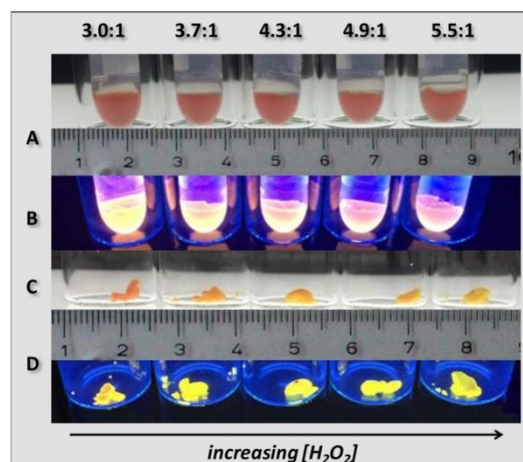

Figure 1. Photographs of the hydrogels (A and B) and aerogels (C and D) obtained from the CdSe/CdS (aq) NPLs with variable molar ratios of $[H_2O_2]/[Cd^{2+}]$ ranging from 3.0:1 to 5.5:1.(left to right, respectively). All monoliths (both hydrogels and aerogels) exhibit intense fluorescence upon irradiation with a UV lamp (wavelength of 365 nm). The hydrogel and the corresponding aerogel with $[H_2O_2]/[Cd^{2+}] = 3.0:1$ and 5.5:1 have the highest and lowest PLQY, respectively. The scale bar is in centimeters. Notably, the surfaces of the hydrogels inside the microcentrifuge tubes are curved inward which means that the volumes of the aerogel and hydrogel can not be compared directly.

parameter range, the gelation time was 6−8 h, which is slightly longer, but at the same time, there was only negligible loss of the deep orange color and fluorescence properties with respect to the original aqueous solution. The hydrogel and the corresponding aerogel with a molar $[H_2O_2]/[Cd^{2+}]$ ratio of 3.0:1 exhibited the highest photoluminescence intensities. For a further increase of hydrogen peroxide content, the photoluminescence intensity was found to decrease more and more.

As a reference experiment, the gelation of CdSe (aq) NPLs was also investigated following the same reaction conditions. We observed similar time scales for the hydrogel formation even though the photoluminescence was found to be completely quenched (a fact which is already observed for the aqueous CdSe NPL building block solutions caused by the phase transfer via ligand exchange).

In all gelation experiments, after the formation of the initial wet gel, a washing step is crucial to remove excess oxidant and soluble byproducts, e.g., disulfides.[26,44] Consecutive washing and aging allows the NPLs with their partially bare facets to come closer to each other and hence to form the stable network (as was suggested for conventional nanoparticles[25]). During the aging period, a little volume loss (around 5%) can be observed. The hydrogels obtained in this way are stable monoliths as shown in Figure 1. In order to obtain voluminous aerogels, the hydrogels were supercritically dried following Kistler's method[46] (see the Experimental Section). This method allows the network to retain its structure without any major changes since capillary forces do not occur during this drying process. The aerogels obtained after supercritical drying were monoliths of interconnected NPLs. However, it should be noted that careful handling is necessary to avoid mechanical stress and
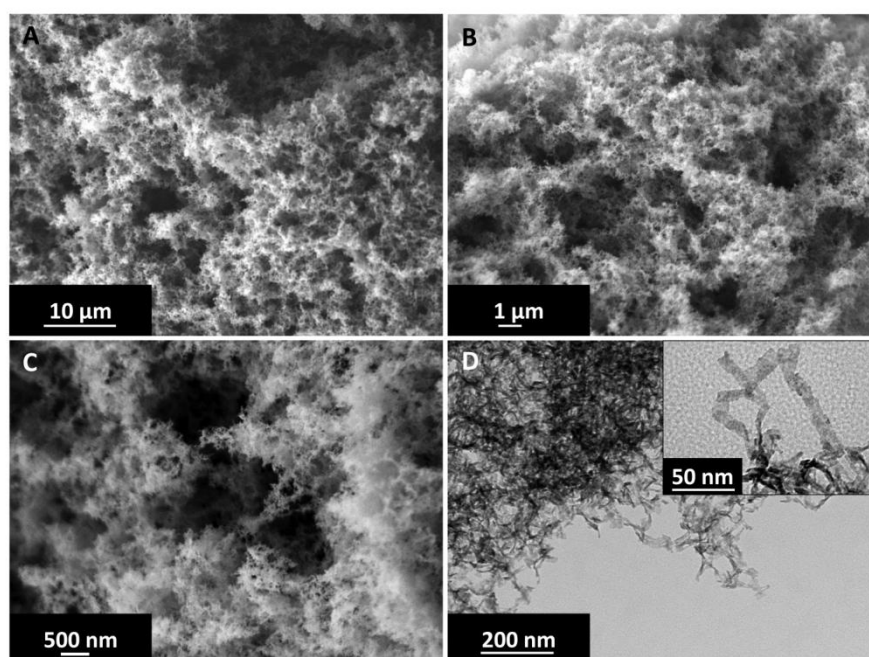
Figure 2. Morphological characterization of an aerogel. (A−C) SEM and (D) TEM micrographs of the aerogel from CdSe/CdS core/crown NPLs in different magnifications. Inset of (D) shows the orientation of the NPLs network inside the aerogel. The pore distribution ranges from mesopores (2−50 nm) to macropores (>50 nm).

electrostatic charging which might break the monoliths into smaller pieces. The resulting aerogels of CdSe/CdS core/crown NPLs are highly fluorescent (PLQY up to 10.3%, which is only slightly lower than that of the corresponding hydrogel with 12.1%). However, we observe a loss in PLQY during gelation (the PLQY of the aqueous solution is 18%). We explain the loss of PLQY as follows. The addition of H_2O_2 leads to three effects: (i) The peroxide radical can generate active $Se^{\bullet-}$ (in the case of CdSe) or $S^{\bullet-}$ and $Se^{\bullet-}$ (in the case of CdSe/CdS) at the surface of the NPLs, which in turn facilitates the formation of the interconnection of the NPLs through chalcogenide bonding.[20,22] (ii) The peroxide radical can help to generate a disulfide bonding between two MUA surface ligands, which is a soluble byproduct. When ligands desorb from the NPLs, unsaturated surface states can cause lowering of the PLQY.[20,22] (iii) An excess amount of H_2O_2 can also cause the oxidation of CdSe to form a soluble oxide species (e.g., $CdSeO_4$), which is washed out after hydrogelation by solvent exchange (see XPS measurements proving the absence of Se components other than Se^{2-} in the aerogels). This explains the dissolution of the CdSe core of the CdSe/CdS core crown NPL (which is observed by TEM by the generation of NPLs rings for higher H_2O_2 concentrations; see Figure 6). With higher oxidant concentration, the CdSe crystallites are more and more dissolved. Kinks, lattice defects, and hence unsaturated surface states are therefore created more and more. Since the PL emission of the platelets only comes from the CdSe part (for both CdSe and CdSe/CdS NPLs) due to the specific band structures of the two materials, dissolution of the CdSe also goes along with reducing the PLQY of the samples. Therefore, effects (ii) and (iii) can explain why the PLQY decreases with increasing hydrogen peroxide concentrations.

The aerogels from CdSe/CdS core/crown NPLs exhibit extremely low densities of 0.038 ± 0.007 g·cm^{-3} representing

0.8% of the density of bulk CdS (4.82 g·cm^{-3}) and 0.69% of bulk CdSe (5.816 g·cm^{-3}), respectively. Similarly, also the aerogels from CdSe NPLs exhibit low densities of 0.036 ± 0.007 g·cm^{-3} corresponding to 0.62% of the bulk CdSe. A small piece of the CdSe/CdS core/crown NPL aerogel (molar ratio $[H_2O_2/Cd^{2+}]$ = 3.0:1) was investigated by SEM to visualize the morphology of the solid structure. Figure 2A−C shows the SEM micrographs of the CdSe/CdS NPLs aerogel in different magnifications. At lower magnifications, it is evident that the aerogel superstuctures have pores in the macroporous regime (with pore size >50 nm). The higher resolution SEM micrograph also proves the presence of an enormously voluminous and branched 3D network having many pores with diameters extending from the mesoporous (2 to 50 nm) to the macroporous (>50 nm) regime. From the comparison of the lower and higher resolution SEM images, it can be derived that these aerogels consist of a fractal-type network. The SEM and TEM micrographs of the aerogels from solely CdSe (aq) NPLs also show highly porous morphology similar to the core/crown NPLs (see Figure SI-3). We have also investigated the morphology of xerogels which are obtained by drying the hydrogels under ambient conditions (see Figure SI-4). It should be noticed that the volumes of the xerogels are drastically reduced to only 1−2% of their corresponding hydrogels. This is most likely due to capillary forces, generated during the liquid evaporation process, breaking down the porous morphology to a much more compact structure.

The TEM micrographs of the aerogel from CdSe/CdS core/crown NPLs are shown in Figure 2D. In accordance with the previous observations, here also, a porous interconnected network of the NPLs is observed. Most of the CdSe/CdS NPLs are assembled in a nonordered 3D arrangement, where the NPLs coalesce in a random fashion. The NPLs are mostly bent, and sometimes, rectangular sheets with edge-to-edge con-

nections can be found. A closer look at the high resolution TEM (HRTEM) micrographs (Figure SI-5) of the gelated NPLs (through fast Fourier transformation, FFT) reveals a distance of ∼0.34 nm between the lattice planes, which accounts for the presence of (111) facets of the NPLs. Due to the extremely low thickness (∼1.5 nm) of the building blocks and rather random connections between the NPLs, by HRTEM, we are unable to find out whether the interparticle connections are crystalline-type or not. Indeed, we assume the interplatelet connections to be of noncrystalline type. The assumption of an amorphous connection is based on the outcome of a previous work on aerogels from CdSe core CdS shell nanorods,[26] in which prolonged PL lifetimes resulted from crystalline type connections, which is not the case in the present work (as shown later). If the connections between the neighboring NPLs would be crystalline-type, we would expect the possibility that excited electrons could travel to their next neighbors which would lead to a lower recombination probability and therefore a prolonged radiative lifetime.[26] In order to characterize the surface of the aerogel, whether H_2O_2 causes any surface oxidation to produce CdO or any other complex oxides, the aerogel samples (with molar $[H_2O_2]$/$[Cd^{2+}]$ = 4.9:1 and 17.4:1, respectively) are analyzed using XPS spectroscopy (Figure 3).
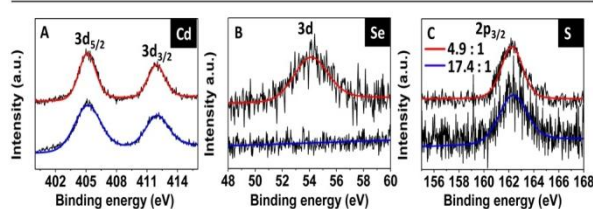
Figure 3. XPS spectra of the CdSe/CdS aerogel with molar ratios $[H_2O_2]$/$[Cd^{2+}]$ = 4.9:1 (red line) and 17.4:1 (blue line). The position of the characteristic peaks confirms the presence of Cd is in the +2 oxidation state (A) and Se and S are in the −2 oxidation state (B and C, respectively). A high amount of oxidant causes dissolution of CdSe from the center of the CdSe/CdS NPL, and hence, the intensity of binding energy peak for Se is near to noise level for the aerogel with molar $[H_2O_2]$/$[Cd^{2+}]$ = 17.4:1.

The binding energy peaks at ≈405.2 eV and at ≈412 eV can be attributed to Cd $3d_{5/2}$ and $3d_{3/2}$ doublets from CdSe, respectively. The absence of a binding energy peak ($3d_{5/2}$) near 404 eV confirms there are no CdO or other complex oxides, e.g., $CdSeO_4$, present on the surface of the aerogel.[21,48] The 3d and $2p_{3/2}$ binding energy peaks appearing at 163 eV and at 54.2 eV (Figure 3B,C) confirm the presence of sulfur and selenium in the −2 oxidation state, respectively. A very weak energy peak at ≈58 eV might be due to the presence of a tiny amount of SeO_2 that resulted due to the etching of the CdSe NPL by H_2O_2. Notably, in the case of higher oxidant concentration (molar ratio $[H_2O_2]$/$[Cd^{2+}]$ = 17.4:1), the binding energy peak from Se^{2-} is absent which confirms nearly complete dissolution of the CdSe core of the NPL under these conditions, which is consistent with the TEM micrographs shown in Figure 7. We assume that such kind of oxidized products are washed out due to their water solubility and therefore can not be determined in XPS. However, the results from optical spectra and TEM (dissolution of the CdSe domains for higher H_2O_2 concentration) are in good agreement with the missing CdSe signal in XPS.

For an overall comparison of the optical properties of the resulting hydrogels and aerogels with respect to their initial building blocks, UV−vis absorption and emission spectra were recorded. The high optical density and strong scattering behavior of the gels do not allow one to measure the optical properties in transmission mode. Therefore, absorption and emission spectra and absolute PLQY measurements were performed using an integrating sphere. A comparison of the absorption spectra of the initial oleic acid capped CdSe/CdS core/crown NPLs in hexane (CdSe/CdS (hex)), the phase transferred MUA capped CdSe/CdS core/crown NPLs in aqueous medium (CdSe/CdS (aq)), and the resulting hydrogel and aerogel (with molar ratio $[H_2O_2]$/$[Cd^{2+}]$ = 3.0:1) is shown in Figure 4A. From the absorption onset of the hydrogels and
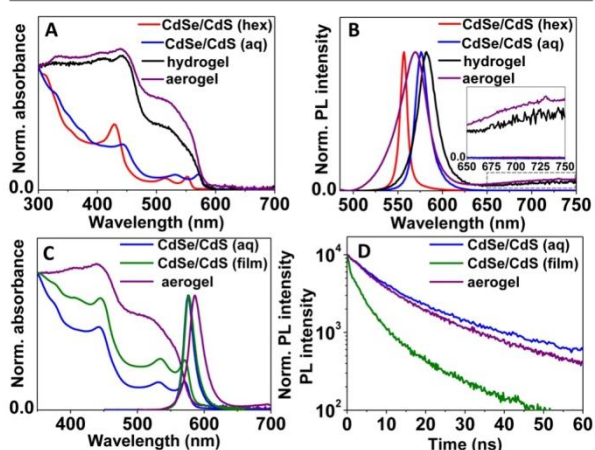

Figure 4. (A,B) Comparison of the absorption and emission spectra of the CdSe/CdS NPLs before and after gelation. Inset of (B) shows the magnification of the selected region of the spectra. (C) Comparison of the absorption and emission spectra and (D) PL decay of the CdSe/CdS NPLs in aqueous solution, as thin film and as an aerogel.

aerogels, it can be inferred that the CdS band gap is not significantly changed compared to their aqueous building blocks, which means that the quantum confinement properties are retained, even though the discrete heavy and light holes are not distinguishable and smeared out. A saturation effect in the shorter wavelength regime can be observed due to the inhomogeneity of the samples inside the cuvette, where the excitation beam can not be adjusted to only hit the sample, rather a part of the light passes beside the gels. The emission maxima of the hydrogels and aerogels, like those of the NPLs in solution (Figure 4B), can be attributed to recombination from the CdSe band edge. The emission peak of the CdSe/CdS hydrogels (black line) is 6 nm shifted toward the lower energy regime with an increased fwhm of 24 nm in comparison to the CdSe/CdS (aq) NPLs building block solution (with a fwhm of 17 nm). This effect could be due to the assembly of the CdSe/CdS NPLs, which allows energy transfer processes to occur between neighboring NPLs causing a slight shift of the emission peak to the lower energy regime.[24,26] Also, the emission peak of the hydrogels is broadened in comparison to that of the corresponding aqueous solution. In addition, for the hydrogels and aerogels, an elongated tail in the emission spectrum in the longer wavelength regime can be observed, which is attributed to trap state emission. The trap state generation could be due to partial surface dissolution of the

NPLs by peroxide radical, producing unsaturated valences on the Cd atoms present on the surface. Noticeably, there was no trap state emission of the NPL solutions observed, neither in aqueous nor in organic medium. It should also be noted that the emission maximum of the aerogel is shifted to shorter wavelengths with a slight further broadening of the fwhm compared to the corresponding hydrogel. While the phenomena of shifting to shorter wavelengths and broadening of absorption and emission spectra is not yet perfectly understood, it could be caused by an interplay of partial dissolution of platelets, partial loss of ligands, the change in dielectric constant in combination with tilting, overlaying, and broadening of the NPLs. The broadening might be explained by partial dissolution, removing parts of the CdSe crystallites, which results in slight variations of the thickness of the quantum wells.

At this point, it is interesting to compare the optical properties of the highly porous self-supported network of the same NPLs with those of denser packed NPLs. In order to do so, the optical properties of a NPL film with similar optical density as the aerogel was investigated (1.1 and 1.2 at 300 nm, respectively, measured in scattering free absorption mode at similar areas exposed to the beam). The film was prepared by drying the CdSe/CdS (aq) NPLs solution on a glass slide. The spectra are shown in Figure 4C,D. Here, we observe that the shape of the absorption and the emission spectra of the film and of the aqueous solution are very similar. In the case of aerogel, the CdS absorption onset appears in the same wavelength regime (compared to the film and the solution), while the CdSe absorption band is broadened. Compared to the film, the emission spectrum of the aerogel was also found to be broadened. However, it should be noticed that the PLQY of the film is only 5.5% with a photoluminescence lifetime (τ) of 3.6 ns, whereas the aqueous solution has 18% ($\tau = 11$ ns) and the aerogel has a PLQY of 10.3% ($\tau = 9.5$ ns). This short lifetime and low PLQY of the film is most likely due to the dense packing of the NPLs which increases the occurrence of various nonradiative recombination pathways in the system. Nevertheless, the aerogels from the core/crown NPLs, as shown in the manuscript, have higher PLQY (10.3% for the lowest amount of H_2O_2 used) as well as longer PL decay times compared to the densely packed film. We attribute this to the highly porous morphology, where the NPLs are loosely packed (compared to the film) and the interactions with the neighboring NPLs are limited.

In order to investigate the impact of the H_2O_2 amount used during gelation on the optical properties of the resulting hydrogels and the corresponding aerogels, we have compared the spectra of the samples with four different $[H_2O_2]/[Cd^{2+}]$ molar ratios, namely, 3.0:1, 3.7:1, 4.3:1, and 4.9:1 (Figure 5, black, red, blue, and green lines, respectively). It can be clearly derived that the UV−vis absorption spectra have sharp absorption onsets and have contribution from both CdSe and CdS with band gaps considerably larger than the corresponding bulk semiconductors. In the case of the emission spectra, it should be noticed that there is a small shift of the emission maximum toward the shorter wavelength region with increasing H_2O_2 amount. This can partly be explained by the fact that larger amounts of H_2O_2 can oxidize more thiol ligands (MUA) from the surface of the CdSe/CdS (aq) NPLs leading to a decrease of the exciton probability function in the thickness direction. Furthermore, simultaneously, the dissolution of the CdSe domain occurs. This occurrence of a parallel reaction effecting the CdSe domains is proven by employing a higher
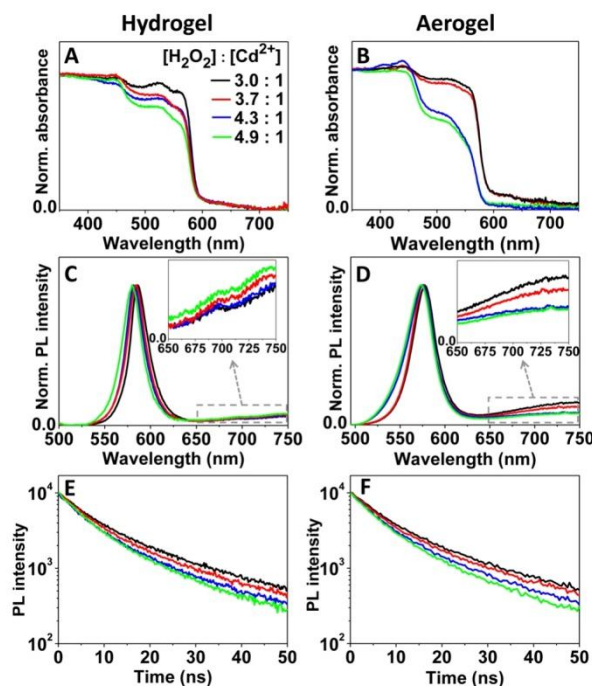

Figure 5. Optical characterization of the hydrogels and the corresponding aerogels with four different $[H_2O_2]/[Cd^{2+}]$ molar ratios of 3.0:1, 3.7:1, 4.3:1, and 4.9:1 (black, red, blue, and green lines, respectively). (A and B) and (C and D) represent UV−vis absorption and emission spectra of the corresponding hydrogels and aerogels, respectively. Insets of (C and D) represent magnified spectra of the selected region. (E and F) represents the PL decay curves of the hydrogels/aerogels.

molar ratio of $[H_2O_2]/[Cd^{2+}] = 17.4:1$. From the TEM images of the corresponding gel shown in Figure 6A,B, it can be
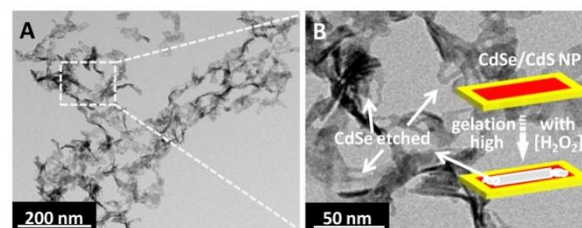

Figure 6. (A and B) TEM micrographs of CdSe/CdS aerogel in two different magnifications with $[H_2O_2]/[Cd^{2+}] = 17.4:1$. A higher amount of H_2O_2 causes etching of CdSe and produces holes inside the rectangular NPLs. Schematic models inside the figures are drawn to guide the eye.

derived that the CdSe is nearly completely vanished from the center of the NPLs leaving holes inside the residual CdS NPL rings. Hence, it is likely that also, with the small amounts of H_2O_2 which we employ in our fluorescent quantum well gelation, we can expect that partial local thinning (not the complete monolayer) of the CdSe platelets occurs, which leads to a slightly reduced (and inhomogeneous) thickness. This results in the shift of the emission peak to shorter wavelengths. In addition, it should be noted that, with higher H_2O_2 concentration, the trap state emission increases, which is in agreement to an increased degree of ligand oxidation and the

creation of, e.g., dangling bonds (imperfect saturation of surface). The lifetime of the (presumably) trap state emission was found to be on the order of tens of microseconds, which is in agreement with previous observations for trap state emission of assembled CdSe nanocrystals (see Figure SI-6).[47]

The measured PLQYs and the corresponding PL lifetimes for both hydrogels and aerogels are shown in Figure 7A,B. The QY
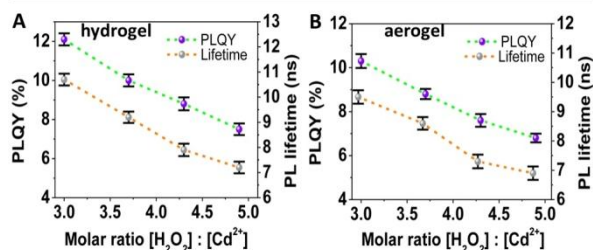

Figure 7. (A and B) PLQY and fluorescence lifetime of CdSe/CdS hydrogels and aerogels with variable molar ratios of $[H_2O_2]/[Cd^{2+}]$.

(in the case of monoexponential PL decay) can be expressed as the ratio of the rate constants of the radiative and nonradiative processes as $QY = k_{rad}/(k_{rad} + \Sigma k_{nonrad})$ where k_{rad} and k_{nonrad} are radiative and nonradiative rate constants, respectively. The PLQY of the CdSe/CdS NPLs in aqueous solution is 18% with a corresponding PL lifetime of 11 ns.

It should be noticed from Figure 7A that the PLQY as well as the measured fluorescence lifetime of the hydrogels decreases with increasing H_2O_2 amount. A similar trend was also observed for the corresponding aerogels (Figure 7B). This decrease in PLQY is most likely due to dissolution of the CdSe with higher amounts of hydrogen peroxide and due to the presence of fewer and fewer ligands on the surface, both effects resulting in the creation of unsaturated surface states and hence nonradiative recombination pathways (or lower-energetic trap state emission).[26] The decay curves can be reasonably fitted with a monoexponential decay, measured with the lifetime

$\tau_{measured} = 1/(k_{rad} + \Sigma k_{nonrad})$. The extent of the decrease in lifetime of the exciton is quite consistent with the decrease in PLQY. Hence, we can conclude that the system undergoes a homogeneous quenching mechanism, which means that all individual fluorescent NPLs of a given ensemble undergo similar quenching upon H_2O_2 addition (for a brief explanation of the terms homogeneous and inhomogeneous quenching, please see the Supporting Information).

In a recent publication of our group, an exceptionally long radiative lifetime (56 ns with a PLQY of 29%) of aerogels from CdSe seeded CdS nanorods has been observed.[26] In that case, according to our interpretations, tip-to-tip connections of the CdSe/CdS nanorod crystallites open up the possibility for the excited electrons to travel to the connected nanoparticles while the holes are confined in the CdSe leading to a delay in the recombination of the exciton and hence longer radiative lifetime. Instead, in the present Article, we do not observe that kind of tip-to-tip connection; rather here, the NPLs are randomly attached with their neighbors. We assume that the connections of the NPLs are not through crystal points and together with that bending of the NPLs reduces the probability of the electron delocalization. In addition, an overall increase in the nonradiative recombination pathways results in shorter PL lifetime. However, also, this work shows similarly to the above-mentioned article that the PLQY can be high in aerogels; in the present case, it is, e.g., approximately two times higher than in the denser packed films of similar optical densities.

Aerogels with very high porosity and large specific surface area are highly promising for catalytic as well as for sensor applications, as the reactant molecules or the analyte can easily diffuse through the pores with minimum hindrance. We analyzed the porosity and the specific surface area of the aerogels obtained from the CdSe NPLs and the CdSe/CdS core/crown NPLs using nitrogen physisorption experiments. The measured isotherms are shown in Figure 8 and analyzed by the Brunauer–Emmett–Teller (BET) method. The isotherms for N_2 gas adsorption and desorption mainly show a multilayer adsorption behavior and can be designated with mixed IUPAC
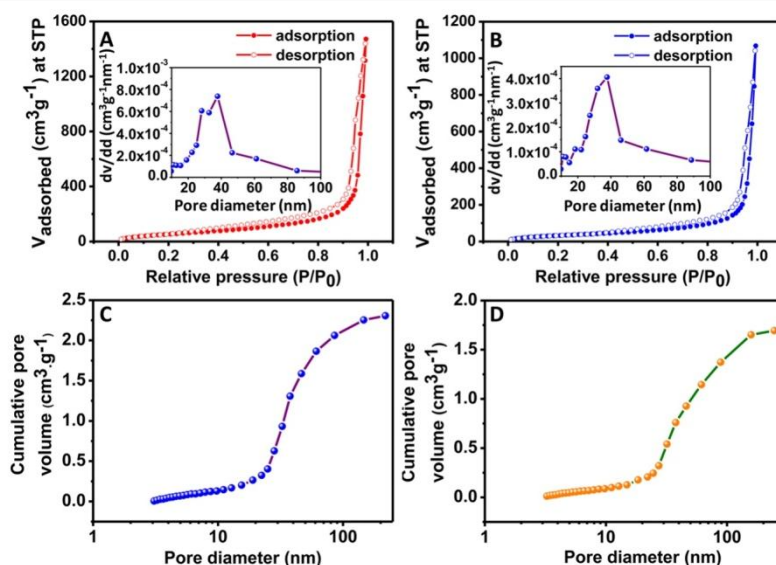

Figure 8. Nitrogen physisorption isotherms for (A) CdSe/CdS core/crown NPL and (B) CdSe NPL aerogels, as well as their pore size distributions derived from these data. (C) and (D) BJH cumulative pore volume distribution of the CdSe/CdS aerogel and of the CdSe aerogel.

type II and type IV behavior. The multipoint BET measurements show very large specific surface areas and high porosities. The aerogels have BET surface areas of 219 and 189 m^2 g^{-1} for the CdSe/CdS NPLs and CdSe NPLs, respectively. These values are comparable with that of previously reported metal chalcogenide aerogels (typically in the range of 90 to 240 m^2 g^{-1}).[20−22] However, care must be taken when comparing mass-specific surface areas of materials of different composition. As noted earlier,[49] such comparisons are biased by the influence of the molar mass of the compounds. For example, a typical silica aerogel with a mass-specific surface area of 500 m^2 g^{-1} has a mole-specific surface area of 30.000 m^2 mol^{-1} for comparison, and a CdSe aerogel with a mass-specific surface area of 200 m^2 g^{-1} has a mole-specific surface area of 29.000 m^2 mol^{-1}.

This comparison shows that the semiconductor NPL aerogels described here have equally high specific surfaces as in classical oxide aerogels. It should be noted that the maximum surface area achievable (from rough geometrical estimations) with this system is ~290 m^2·g^{-1} (considering all the NPLs are present separately). Hence, the specific surface area reported here is around 70% of the maximum possible value. That means roughly 30% of the surface is covered by overlaying of the NPLs surface to form a 3D network. We have also evaluated the pore size distributions from the desorption branch of the isotherms, applying BJH (Barrett−Joyner−Halenda) theory.[42] The broad pore size distributions obtained, ranging from mesopores to macropores, are consistent with a highly porous disordered gel structure, as revealed by the SEM and TEM microscopic analysis. The cumulative pore volumes $V_{3.0-245}$ (lower subscript denotes the pore diameter) calculated for the CdSe/CdS core/crown NPL and CdSe NPL aerogels (at relative pressure $P/P_0 = 0.99$) using BJH theory are 2.27 and 1.65 cm^3·g^{-1}, respectively. The total pore volume V_t can be calculated using the equation $V_t = (1/\rho_a) - (1/\rho_b)$, where V_t is the total pore volume and ρ_a and ρ_b represent the density of aerogel and bulk solid material.[50] The total pore volume for the CdSe/CdS and for the CdSe aerogel are 26.14 and 27.60 cm^{3}g^{-1}, respectively. The average pore diameters estimated using the equation $4 \times V_t/\sigma$ (σ represents the calculated BET specific surface area of the aerogel) are 477 and 584 nm for CdSe/CdS and CdSe aerogel, respectively.[50,51] Thus, the average pore diameters calculated using the equation $V_t = (1/\rho_a) - (1/\rho_b)$ are significantly higher than the average diameters as they were determined from the nitrogen adsorption data. This fact is an indication that the porosity results predominantly from the macropores, which is in accordance with the measured isotherms. The crystallographic characterizations of the CdSe/CdS aerogel and the NPLs in solution (before and after phase transfer) were investigated using powder X-ray diffractometry (XRD) and are shown in the Supporting Information.

4. CONCLUSIONS

In conclusion, we have successfully developed a method to prepare highly porous aerogels from CdSe NPLs and CdSe/CdS core/crown NPLs with high PLQY up to 10.3%. This is the first report on aerogels from colloidal quantum well building blocks. Notably, the aerogels of the NPLs have solely (111) as the exposed facet in the aerogel, which might be of high interest for facet selective catalysis or sensing. The aerogels from the NPLs partially retain the quantum confinement properties of the building blocks and have very large inner specific surface area of 219 m^2/g which is close to the highest

values reported so far for nanocrystal based aerogels. Furthermore, the highly porous character would allow molecules to pass through with minimum hindrance, making them promising candidates, e.g., to detect chemical agents.

■ ASSOCIATED CONTENT

$\circledS$ Supporting Information

The Supporting Information is available free of charge on the ACS Publications website at DOI: 10.1021/acs.chemmater.5b04872.

TEM micrographs of the 5 ML CdSe/CdS core/crown NPLs before and after phase transfer, optical characterizations (UV−vis absorbance, emission, and PL decay) of the CdSe and CdSe/CdS core/crown NPLs in organic and in aqueous medium, SEM micrographs of the aerogels from CdSe (aq) NPLs, SEM micrographs of the xerogel from CdSe/CdS core/crown NPLs, HRTEM of the aerogel from CdSe/CdS core/crown NPLs, XPS spectra of the CdSe/CdS core/crown aerogel, PL decay analysis of the surface trap states, photograph of the film prepared by drying CdSe/CdS NPLs on a glass slide, X-ray diffraction pattern of the CdSe/CdS (aq) NPLs and of the hydrogels and aerogels obtained from CdSe/CdS NPLs. (PDF)

■ AUTHOR INFORMATION

Corresponding Author

*E-mail: nadja.bigall@pci.uni-hannover.de.

Author Contributions

The manuscript was written through contributions of all authors. All authors have given approval to the final version of the manuscript.

Notes

The authors declare no competing financial interest.

■ ACKNOWLEDGMENTS

■ ABBREVIATIONS

NPL, nanoplatelet; MUA, 11-mercaptoundecanoic acid; PLQY, photoluminescence quantum yield; TEM, transmission electron microscopy; SEM, scanning electron microscopy; BET, Brunauer−Emmett−Teller; BJH, Barrett−Joyner−Halenda; XRD, X-ray diffractometry; fwhm, full width at half-maximum; XPS, X-ray photoelectron spectroscopy

■ REFERENCES

(1) Murray, C. B.; Norris, D. J.; Bawendi, M. G. Synthesis and Characterization of Nearly Monodisperse CdE (E = S, Se, Te) Semiconductor Nanocrystallites. *J. Am. Chem. Soc.* **1993**, *115*, 8706−8715.

(2) Manna, L.; Milliron, D. J.; Meisel, A.; Scher, E. C.; Alivisatos, A. P. Controlled growth of tetrapod-branched inorganic nanocrystals. *Nat. Mater.* **2003**, *2*, 382−385.

(3) Deka, S.; Miszta, K.; Dorfs, D.; Genovese, A.; Bertoni, G.; Manna, L. Octapod-Shaped Colloidal Nanocrystals of Cadmium Chalcogenides via "One-Pot" Cation Exchange and Seeded Growth. *Nano Lett.* **2010**, *10*, 3770−3776.

(4) Ithurria, S.; Tessier, M. D.; Mahler, B.; Lobo, R. P. S. M.; Dubertret, B.; Efros, A. L. Colloidal nanoplatelets with two-dimensional electronic structure. *Nat. Mater.* **2011**, *10*, 936−941.

(5) Tessier, M. D.; Spinicelli, P.; Dupont, D.; Patriarche, G.; Ithurria, S.; Dubertret, B. Efficient Exciton Concentrators Built from Colloidal Core/Crown CdSe/CdS Semiconductor Nanoplatelets. *Nano Lett.* **2014**, *14*, 207−213.

(6) Lhuillier, E.; Pedetti, S.; Ithurria, S.; Nadal, B.; Heuclin, H.; Dubertret, B. Two-Dimensional Colloidal Metal Chalcogenides Semiconductors: Synthesis, Spectroscopy, and Applications. *Acc. Chem. Res.* **2015**, *48*, 22−30.

(7) Tessier, M. D.; Javaux, C.; Maksimovic, I.; Loriette, V.; Dubertret, B. Spectroscopy of Single CdSe Nanoplatelets. *ACS Nano* **2012**, *6*, 6751−6758.

(8) Abecassis, B.; Tessier, M. D.; Davidson, P.; Dubertret, B. Self-Assembly of CdSe Nanoplatelets into Giant Micrometer-Scale Needles Emitting Polarized Light. *Nano Lett.* **2014**, *14*, 710−715.

(9) Biadala, L.; Liu, F.; Tessier, M. D.; Yakovlev, D. R.; Dubertret, B.; Bayer, M. Recombination Dynamics of Band Edge Excitons in Quasi-Two-Dimensional CdSe Nanoplatelets. *Nano Lett.* **2014**, *14*, 1134−1139.

(10) Bouet, C.; Mahler, B.; Nadal, B.; Abecassis, B.; Tessier, M. D.; Ithurria, S.; Xu, X.; Dubertret, B. Two-Dimensional Growth of CdSe Nanocrystals, from Nanoplatelets to Nanosheets. *Chem. Mater.* **2013**, *25*, 639−645.

(11) Kunneman, L. T.; Schins, J. M.; Pedetti, S.; Heuclin, H.; Grozema, F. C.; Houtepen, A. J.; Dubertret, B.; Siebbeles, L. D. A. Nature and Decay Pathways of Photoexcited States in CdSe and CdSe/CdS Nanoplatelets. *Nano Lett.* **2014**, *14*, 7039−7045.

(12) Mahler, B.; Nadal, B.; Bouet, C.; Patriarche, G.; Dubertret, B. Core/Shell Colloidal Semiconductor Nanoplatelets. *J. Am. Chem. Soc.* **2012**, *134*, 18591−18598.

(13) Bouet, C.; Laufer, D.; Mahler, B.; Nadal, B.; Heuclin, H.; Pedetti, S.; Patriarche, G.; Dubertret, B. Synthesis of Zinc and Lead Chalcogenide Core and Core/Shell Nanoplatelets Using Sequential Cation Exchange Reactions. *Chem. Mater.* **2014**, *26*, 3002−3008.

(14) Pedetti, S.; Ithurria, S.; Heuclin, H.; Patriarche, G.; Dubertret, B. Type-II CdSe/CdTe Core/Crown Semiconductor Nanoplatelets. *J. Am. Chem. Soc.* **2014**, *136*, 16430−16438.

(15) Guzelturk, B.; Kelestemur, Y.; Olutas, M.; Delikanli, S.; Demir, H. V. Amplified Spontaneous Emission and Lasing in Colloidal Nanoplatelets. *ACS Nano* **2014**, *8*, 6599−6605.

(16) She, C.; Fedin, I.; Dolzhnikov, D. S.; Demortiere, A.; Schaller, R. D.; Pelton, M.; Talapin, D. V. Low-Threshold Stimulated Emission Using Colloidal Quantum Wells. *Nano Lett.* **2014**, *14*, 2772−2777.

(17) Lorenzon, M.; Christodoulou, S.; Vaccaro, G.; Pedrini, J.; Meinardi, F.; Moreels, I.; Brovelli, S. Reversed oxygen sensing using colloidal quantum wells towards highly emissive photoresponsive varnishes. *Nat. Commun.* **2015**, *6*, 6434.

(18) Grim, J. Q.; Christodoulou, S.; Di Stasio, F.; Krahne, R.; Cingolani, R.; Manna, L.; Moreels, I. Continuous-wave biexciton lasing at room temperature using solution-processed quantum wells. *Nat. Nanotechnol.* **2014**, *9*, 891−895.

(19) Mohanan, J. L.; Brock, S. L. A new addition to the aerogel community: unsupported US aerogels with tunable optical properties. *J. Non-Cryst. Solids* **2004**, *350*, 1−8.

(20) Arachchige, I. U.; Brock, S. L. Sol-gel assembly of CdSe nanoparticles to form porous aerogel networks. *J. Am. Chem. Soc.* **2006**, *128*, 7964−7971.

(21) Yao, Q.; Brock, S. L. Optical sensing of triethylamine using CdSe aerogels. *Nanotechnology* **2010**, *21*, 115502.

(22) Yao, Q.; Brock, S. L. Porous CdTe Nanocrystal Assemblies: Ligation Effects on the Gelation Process and the Properties of Resultant Aerogels. *Inorg. Chem.* **2011**, *50*, 9985−9992.

(23) Chen, H.; Lesnyak, V.; Bigall, N. C.; Gaponik, N.; Eychmueller, A. Self-Assembly of TGA-Capped CdTe Nanocrystals into Three-Dimensional Luminescent Nanostructures. *Chem. Mater.* **2010**, *22*, 2309−2314.

(24) Gaponik, N.; Herrmann, A.-K.; Eychmueller, A. Colloidal Nanocrystal-Based Gels and Aerogels: Material Aspects and Application Perspectives. *J. Phys. Chem. Lett.* **2012**, *3*, 8−17.

(25) Korala, L.; Brock, S. L. Aggregation Kinetics of Metal Chalcogenide Nanocrystals: Generation of Transparent CdSe (ZnS) Core (Shell) Gels. *J. Phys. Chem. C* **2012**, *116*, 17110−17117.

(26) Sánchez-Paradinas, S.; Dorfs, D.; Friebe, S.; Freytag, A.; Wolf, A.; Bigall, N. C. Aerogels from CdSe/CdS Nanorods with Ultra-long Exciton Lifetimes and High Fluorescence Quantum Yields. *Adv. Mater.* **2015**, *27*, 6152−6156.

(27) Riley, B. J.; Chun, J.; Um, W.; Lepry, W. C.; Matyas, J.; Olszta, M. J.; Li, X.; Polychronopoulou, K.; Kanatzidis, M. G. Chalcogen-Based Aerogels As Sorbents for Radionuclide Remediation. *Environ. Sci. Technol.* **2013**, *47*, 7540−7547.

(28) Hendel, T.; Lesnyak, V.; Kuehn, L.; Herrmann, A.-K.; Bigall, N. C.; Borchardt, L.; Kaskel, S.; Gaponik, N.; Eychmueller, A. Mixed Aerogels from Au and CdTe Nanoparticles. *Adv. Funct. Mater.* **2013**, *23*, 1903−1911.

(29) Lesnyak, V.; Wolf, A.; Dubavik, A.; Borchardt, L.; Voitekhovich, S. V.; Gaponik, N.; Kaskel, S.; Eychmüller, A. 3D Assembly of Semiconductor and Metal Nanocrystals: Hybrid CdTe/Au Structures with Controlled Content. *J. Am. Chem. Soc.* **2011**, *133*, 13413−13420.

(30) Herrmann, A.-K.; Formanek, P.; Borchardt, L.; Klose, M.; Giebeler, L.; Eckert, J.; Kaskel, S.; Gaponik, N.; Eychmueller, A. Multimetallic Aerogels by Template-Free Self-Assembly of Au, Ag, Pt, and Pd Nanoparticles. *Chem. Mater.* **2014**, *26*, 1074−1083.

(31) Bigall, N. C.; Herrmann, A. K.; Vogel, M.; Rose, M.; Simon, P.; Carrillo-Cabrera, W.; Dorfs, D.; Kaskel, S.; Gaponik, N.; Eychmuller, A. Hydrogels and aerogels from noble metal nanoparticles. *Angew. Chem., Int. Ed.* **2009**, *48*, 9731−9734.

(32) Bigall, N. C.; Eychmüller, A. Synthesis of noble metal nanoparticles and their non-ordered superstructures. *Philos. Trans. R. Soc., A* **2010**, *368*, 1385−1404.

(33) Freytag, A.; Sánchez-Paradinas, S.; Naskar, S.; Wendt, N.; Colombo, M.; Pugliese, G.; Poppe, J.; Demirci, C.; Kretschmer, I.; Bahnemann, D. W.; Behrens, P.; Bigall, N. C. Versatile Aerogel Fabrication by Freezing and Subsequent Freeze-Drying of Colloidal Nanoparticle Solutions. *Angew. Chem., Int. Ed.* **2016**, *55*, 1200.

(34) Liu, W.; Herrmann, A.-K.; Bigall, N. C.; Rodriguez, P.; Wen, D.; Oezaslan, M.; Schmidt, T. J.; Gaponik, N.; Eychmüller, A. Noble Metal Aerogels—Synthesis, Characterization, and Application as Electro-catalysts. *Acc. Chem. Res.* **2015**, *48*, 154−162.

(35) Liu, W.; Herrmann, A.-K.; Geiger, D.; Borchardt, L.; Simon, F.; Kaskel, S.; Gaponik, N.; Eychmueller, A. High-Performance Electro-catalysis on Palladium Aerogels. *Angew. Chem., Int. Ed.* **2012**, *51*, 5743−5747.

(36) Liu, W.; Rodriguez, P.; Borchardt, L.; Foelske, A.; Yuan, J.; Herrmann, A.-K.; Geiger, D.; Zheng, Z.; Kaskel, S.; Gaponik, N.; Koetz, R.; Schmidt, T. J.; Eychmueller, A. Bimetallic Aerogels: High-Performance Electrocatalysts for the Oxygen Reduction Reaction. *Angew. Chem., Int. Ed.* **2013**, *52*, 9849−9852.

(37) Wen, D.; Herrmann, A.-K.; Borchardt, L.; Simon, F.; Liu, W.; Kaskel, S.; Eychmueller, A. Controlling the Growth of Palladium Aerogels with High-Performance toward Bioelectrocatalytic Oxidation of Glucose. *J. Am. Chem. Soc.* **2014**, *136*, 2727−2730.

(38) Lhuillier, E.; Pedetti, S.; Ithurria, S.; Heuclin, H.; Nadal, B.; Robin, A.; Patriarche, G.; Lequeux, N.; Dubertret, B. Electrolyte-Gated Field Effect Transistor to Probe the Surface Defects and Morphology in Films of Thick CdSe Colloidal Nanoplatelets. *ACS Nano* **2014**, *8*, 3813−3820.

(39) Naskar, S.; Schlosser, A.; Miethe, J. F.; Steinbach, F.; Feldhoff, A.; Bigall, N. C. Site-Selective Noble Metal Growth on CdSe Nanoplatelets. *Chem. Mater.* **2015**, *27*, 3159−3166.

(40) Kodanek, T.; Banbela, H. M.; Naskar, S.; Adel, P.; Bigall, N. C.; Dorfs, D. Phase transfer of 1- and 2-dimensional Cd-based nanocrystals. *Nanoscale* **2015**, *7*, 19300−19309.

(41) Brunauer, S.; Emmett, P. H.; Teller, E. Adsorption of Gases in Multimolecular Layers. *J. Am. Chem. Soc.* **1938**, *60*, 309−319.

71

Article

(42) Barrett, E. P.; Joyner, L. G.; Halenda, P. P. The Determination of Pore Volume and Area Distributions in Porous Substances. I. Computations from Nitrogen Isotherms. *J. Am. Chem. Soc.* **1951**, *73*, 373−380.

(43) Arachchige, I. U.; Brock, S. L. Highly luminescent quantum-dot monoliths. *J. Am. Chem. Soc.* **2007**, *129*, 1840−1841.

(44) Arachchige, I. U.; Brock, S. L. Sol-gel methods for the assembly of metal chalcogenide quantum dots. *Acc. Chem. Res.* **2007**, *40*, 801−809.

(45) Brock, S. L.; Arachchige, I. U.; Kalebaila, K. K. Metal chalcogenide gels, xerogels and aerogels. *Comments Inorg. Chem.* **2006**, *27*, 103−126.

(46) Kistler, S. S. Coherent Expanded Aerogels and Jellies. *Nature* **1931**, *127*, 741−741.

(47) Virgili, T.; López, I. S.; Vercelli, B.; Angella, G.; Zotti, G.; Cabanillas-Gonzalez, J.; Granados, D.; Luer, L.; Wannemacher, R.; Tassone, F. Spectroscopic Signature of Trap States in Assembled CdSe Nanocrystal Hybrid Films. *J. Phys. Chem. C* **2012**, *116*, 16259−16263.

(48) Katari, J. E. B.; Colvin, V. L.; Alivisatos, A. P. X-ray Photoelectron Spectroscopy of CdSe Nanocrystals with Applications to Studies of the Nanocrystal Surface. *J. Phys. Chem.* **1994**, *98*, 4109−4117.

(49) Behrens, P. Voids in Variable Chemical Sorroundings: Mesoporous Metal Oxide. *Angew. Chem., Int. Ed. Engl.* **1996**, *35*, 515−518.

(50) Mahadik-Khanolkar, S.; Donthula, S.; Sotiriou-Leventis, C.; Leventis, N. Polybenzoxazine Aerogels. 1. High-Yield Room-Temperature Acid-Catalyzed Synthesis of Robust Monoliths, Oxidative Aromatization, and Conversion to Microporous Carbons. *Chem. Mater.* **2014**, *26*, 1303−1317.

(51) Leventis, N.; Chidambareswarapattar, C.; Bang, A.; Sotiriou-Leventis, C. Cocoon-in-Web-Like Superhydrophobic Aerogels from Hydrophilic Polyurea and Use in Environmental Remediation. *ACS Appl. Mater. Interfaces* **2014**, *6*, 6872−6882.

72

Supporting Information

Photoluminescent Aerogels from Quantum Wells

Suraj Naskar[1,4], Jan. F. Miethe[1, 4], Sara Sánchez-Paradinas[1,4], Nadeschda Schmidt[2,4],

Karthiga Kanthasamy[3,4], Peter Behrens[2, 4], Herbert Pfnür[3,4], Nadja C. Bigall[1,4]*

[1]Institute of Physical Chemistry and Electrochemistry, Leibniz Universität Hannover Callinstraße 3A, D-30167 Hannover, Germany.
[2]Institute of Inorganic Chemistry, Leibniz Universität Hannover, Callinstraße 9, 30167 Hannover, Germany.
[3]Institut für Festkörperphysik, Leibniz Universität Hannover, Appelstr. 2, 30167 Hannover, Germany.
[4]Laboratory for Nano and Quantum Engineering, Schneiderberg 39, 30167 Hannover, Germany.

Content:

1. TEM micrographs of the 5 ML CdSe/CdS core/crown NPLs before and after phase transfer

2. Optical characterizations (UV-Vis absorbance, emission and PL decay) of the CdSe and CdSe/CdS core/crown NPLs in organic and in aqueous medium

3. SEM micrographs of the aerogels from CdSe (aq) NPLs

4. SEM micrographs of the xerogel from CdSe/CdS core/crown NPLs

5. HRTEM of the aerogel from CdSe/CdS core/crown NPLs

6. PL decay analysis of the trap state emissions

7. Explanation of homogeneous quenching and inhomogeneous quenching

8. Photograph of the MUA-CdSe/CdS (aq) NPLs film on a glass slide

9. X-ray diffraction pattern of the aqueous solution, hydrogel and aerogel of CdSe/CdS (aq) NPLs

1. TEM micrographs of the 5 ML CdSe and CdSe/CdS core/crown NPLs before and after phase transfer

A CdSe/CdS core/crown NPL is a system consisting of a CdS crown which has been grown only at the lateral dimension of a CdSe NPL, which means there are no changes in the thickness upon the CdS crown growth (see insets in Figure SI-1).

The CdSe/CdS core/crown NPLs are rectangular in shape and have the average length of 38.1 nm ± 4.3 nm, an average width of 13.64 nm ± 1.5 nm, while the thickness of the NPLs is only 5 monolayer which is ~ 1.5 nm.

There are two kinds of quasi 2D CdSe/CdS NPLs in literature: core/shell NPLs[1] and core/crown NPLs.[2] By optical spectroscopy the two types can be easily distinguished: upon CdS crown growth around the 5 ML CdSe NPLs, a negligible change in the CdSe exciton maxima (lh-e at 515 nm and hh-e at 552 nm) and in addition to that the appearance of CdS exciton maxima at 431 nm can be observed (please refer to figure SI-2). The crown growth induces a slight shift (~6 nm) of the PL emission peak (compared to 5 ML CdSe core NPLs) for the CdSe/CdS NPLs from 551 nm to 557 nm. According to the recent publication of Tessier et al., this observation confirms that the CdS crown growth is only in the lateral dimension and not all around the NPLs, since these authors have shown that if the CdS growth is on the z-direction of the CdSe NPLs, the emission maximum would shift much stronger (~ 100 nm) towards lower energies.[2] For more information regarding the optical properties of the NPLs see section 2.

2
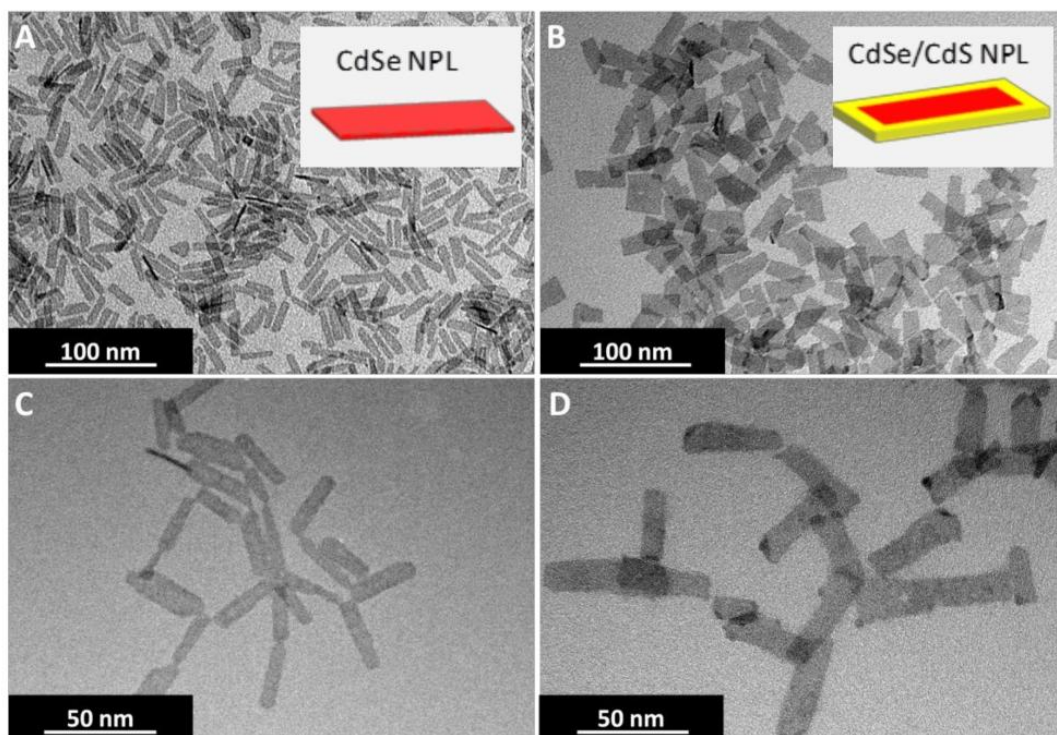
Figure SI-1. TEM micrographs of (A) 5 ML thick CdSe (hex) NPLs, (B) 5 ML thick CdSe/CdS (hex) core/crown NPLs, (C) CdSe (aq) and (D) CdSe/CdS (aq) core/crown NPLs.

3

2. Optical characterizations (UV-Vis absorbance, emission and PL decay) of the CdSe and CdSe/CdS core/crown NPLs in organic and in aqueous medium
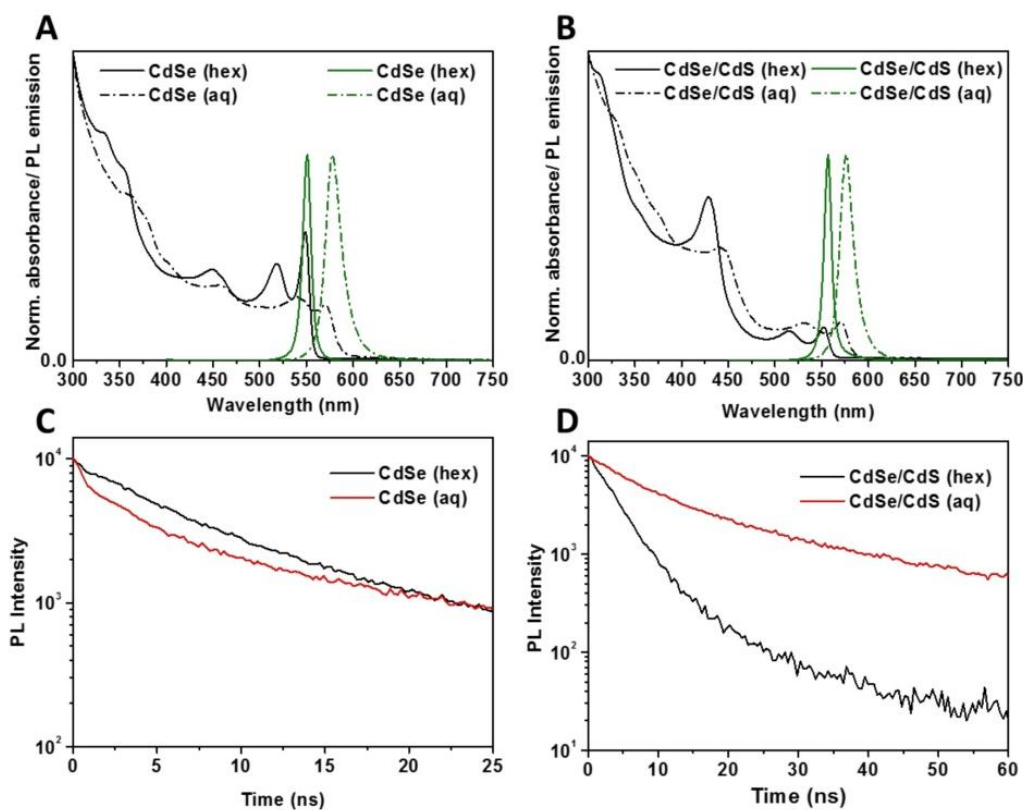
Figure SI-2. Optical characterization of the 5 ML CdSe and CdSe/CdS core/crown NPLs. (A) and (B) UV-Vis absorbance and emission spectra (in organic and in aqueous medium) (C) and (D) room temperature time-resolved PL decay of the CdSe and CdSe/CdS NPLs before and after phase transfer, respectively.

From the UV-Vis absorbance spectra, both of the light-hole electron (lh-e) and the heavy-hole electron (hh-e) transitions at 517 nm and at 550 nm of the CdSe (hex) NPLs can be clearly derived from figure SI-2A. The emission spectra of the CdSe (hex) NPLs shows a sharp peak at 551 nm with a FWHM of 10 nm confirming the thickness to be 5 ML[2, 3] and a strong quantum confinement in the z direction (see figure SI-2A). The CdSe NPLs synthesized have an average length of 31 nm ± 4 nm and a width of 7 nm ± 1.5 nm. The transmission electron microscopy (TEM) images are shown in figure SI-1A. A CdS crown was grown on the CdSe NPLs following a modified procedure of Tessier *et. al.*[2] Upon a CdS crown growth on the

4

5 ML CdSe NPLs, a negligible change in the CdSe absorption onsets (lh-e at 515 nm and hh-e at 552 nm) in addition to that an appearance of CdS absorption band at 431 nm can be observed (see figure SI-2B). The crown growth induces a slight shift (~6 nm) of the emission peak (compared to 5 ML CdSe NPLs) for the CdSe/CdS (hex) NPLs to 557 nm (see figure SI-2B). According to the recent publication,[6] this observation confirms that the CdS crown growth is only in the lateral dimension and not on the flat sides of the NPLs (if the CdS growth is on the z-direction of the CdSe NPLs, one could expect a larger shift of the emission maxima to the lower energy region)[1]. The conduction band offset of the CdSe/CdS system depends on the temperature and is not exactly known.[4] However, the valence band offset is in general at least in the order of 400 meV.[4, 5] Therefore, the holes are rapidly accumulated in the CdSe domain of the CdSe/CdS NPLs.[2, 6] This argument holds well because of the fact that whenever the CdSe/CdS NPLs are excited with photons having energies higher than the CdS band gap, the emission only comes from the CdSe.[1, 2] The CdSe/CdS (hex) NPLs have a PLQY of 37% (measured in absolute mode using an integrating sphere Quanta-φ equipped with DUAL FL spectrophotometer from HORIBA Scientific). In order to do a phase transfer of the NPLs, the non-polar carboxylate ligands were exchanged with 11-mercaptoundecanoic acid (MUA) at a basic pH (pH > 10).[7] The absorbance and emission spectra of the phase transferred CdSe (aq) and CdSe/CdS (aq) NPLs are also shown in figure SI-2A and B respectively. It should be noted that both absorbance and the emission spectra of the CdSe NPLs have shifted to longer wavelength after the phase transfer. Similar results were also obtained by Mahler *et. al.* while using bis-trimethylsilyl sulphide (TMS$_2$S) as the sulphur precursor for the growth of CdS layer over CdSe NPLs.[8] We attribute this observation to the increased degree of exciton mobility in the diretion of the thickness of the NPLs and a broader size distribution after phase transfer. As the zinc blend 100 facet of the 5 ML thick CdSe/CdS NPLs have Cd^{2+} ions on both (top and bottom surface)[9] we could expect the thiol group of the MUA to be attached to the surface of the NPLs while replacing the oleic acid. The PLQY

5

(measured in absolute mode) of the phase transferred CdSe/CdS (aq) NPLs was found to be 18 %. The decrease in the PLQY could be attributed to the increased degree of nonradiative recombination processes. Time correlated single photon count (TCSPC) measurements were employed using a 454 nm, 1.2 ns pulsed LED as the photon source, to estimate the exciton lifetime of the NPLs. The room temperature PL decay curves of the 5 ML CdSe and CdSe/CdS core/crown NPLs, before and after phase transfer are shown in figure SI-2C and D respectively. Similar to the results obtained previously by Tessier *et. al*[2]., the CdSe/CdS (hex) NPLs show an ultrafast PL decay, nevertheless a reasonable biexponential fit of the data aquired suggest 98 % of the excitons have lifetime of 3.74 ns and the rest 2 % have 27 ns. Whereas, a monoexponential fitting of the PL decay curve of the CdSe/CdS (aq) NPLs shows a higher exciton lifetime of 11 ns.[7] The long exciton lifetime after MUA functionalization might be due to increased degree of mobility of the electron in the system after addition of two S layers, as discussed in our earlier work on water transfer of these quantum wells.[7] The CdSe (aq) NPLs show a very low PLQY of 1-2 %, in comparison to the 25 % PLQY obtained for their organic solution. It should also be noticed that the exciton lifetime of the CdSe NPLs in aqueous solution is 4.2 ns, whereas, the NPLs in organic solution have the lifetime of 7.8 ns. This might be due to the imperfect passivation of the surface of the CdSe NPLs after phase transfer. We measured an average length of 38.4 ± 4.1 nm and an average width of 12.42 ± 1.5 nm for the CdSe/CdS (aq) NPLs and the same is 30.8 ± 2.9 nm and 7.6 ± 1.1 nm respectively for the CdSe (aq) NPLs. The TEM micrographs are shown in Figure SI-1C and D.

6

3. SEM micrographs of the aerogels from CdSe (aq) NPLs
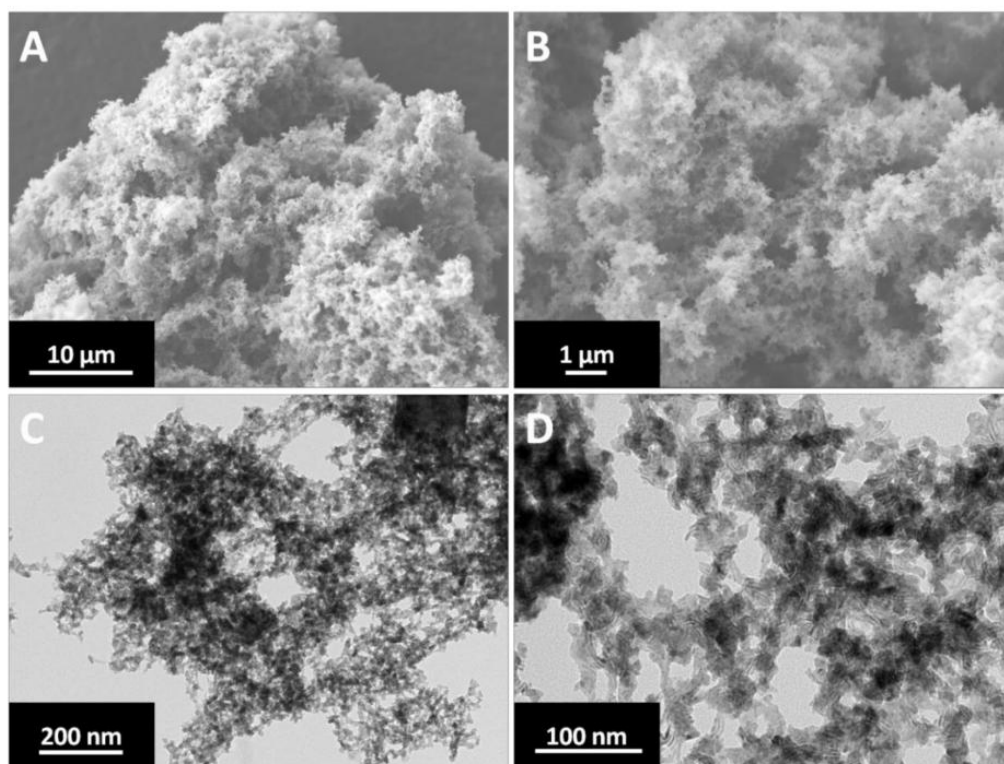
Figure SI-3 (A and B) SEM and (C and D) TEM micrographs of aerogel from CdSe NPLs in two different magnification. The pore distribution ranges from mesopores to macropores.

7

4. SEM micrographs of the xerogel from CdSe/CdS core/crown NPLs
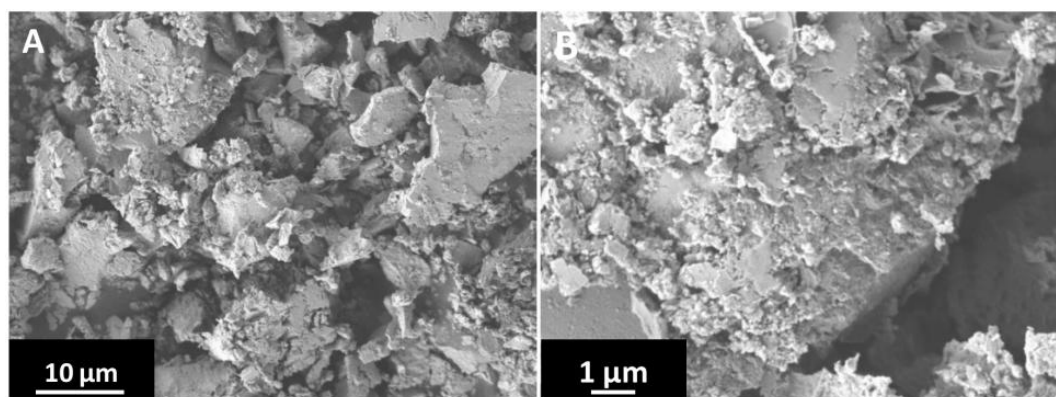
Figure SI-4. (A and B) SEM micrographs of the xerogels obtained after drying the CdSe/CdS NPL hydrogels on bench top under ambient condition.
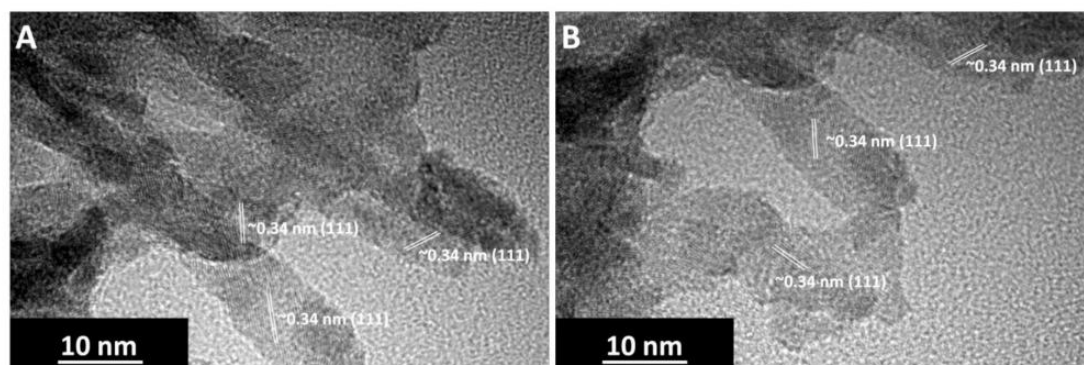
5. HRTEM of the aerogel from CdSe/CdS core/crown NPLs

Figure SI-5. (A and B) HRTEM of the CdSe/CdS (aq) NPLs aerogels. The NPLs are connected in a random way. The lattice distance between the two crystal planes are indicated with vertical white lines.

9

6. PL decay analysis of the trap state emissions

In previous publications it was found that the trap states of CdSe have long lifetime in tens of microseconds to milliseconds regime.[10] In our experimental setup the time correlated single photon counting measurements were carried out up to 26 µs in three different wavelengths: 700 nm, 725 nm and at 750 nm. A reasonable extrapolation of the decay curves shows that in all cases the lifetime of the trap state should be in the microseconds regime, which is in good agreement with the previous observations for the lifetime of the trap states for assembled CdSe nanocrystals (see figure SI-7).
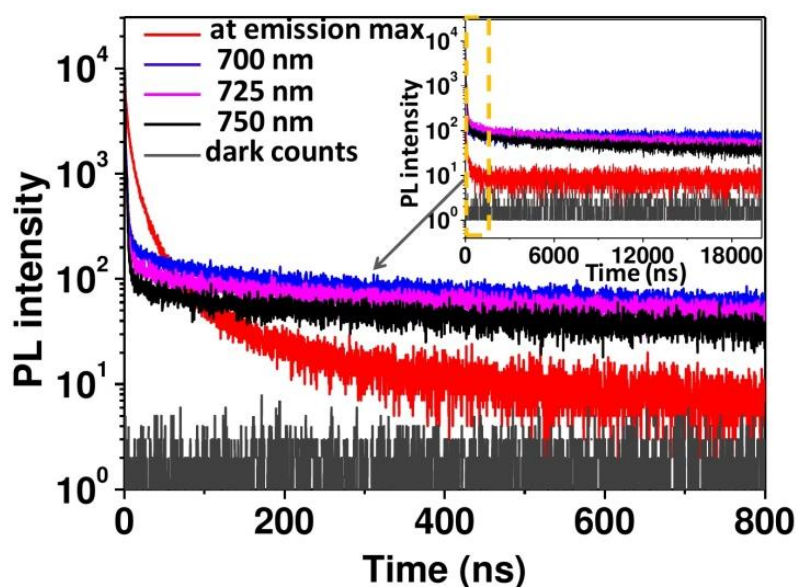
Figure SI-6. PL decay analysis of the trap state emission present on the surface of the aerogel measured at three different wavelengths (namely 700 nm, 725 nm and 750 nm) with molar [H₂O₂] : [Cd²⁺] =4.9:1. Extrapolation of the decay curves represents a long trap state lifetime in tens of micro-seconds regime.

10

7. Explanation of homogeneous quenching and inhomogeneous quenching

Homogeneous quenching means that each individual NPL in an ensemble has a similar PLQY and undergoes quenching upon addition of a quencher to the same extent. Here, in our case with gradual increase of the H_2O_2 concentration in the system, we found that both the PLQY of the gels and the corresponding PL lifetime decrease linearly. Now, one can consider a situation where the individual NPLs do not behave the same way upon the addition of the H_2O_2 e.g. 70 % of the NPLs get completely quenched by the H_2O_2 and the rest 30 % have unaltered fluorescence; in that case the PL lifetime would not change with respect to the starting material while the PLQY would decrease. This case would be described as an inhomogeneous quenching. In our experimental results, the extent of decrease of the PLQY and the PL lifetime is linear (figure 7 in main manuscript) upon gradual increase in the molar ratio of $H_2O_2:Cd^{2+}$, that means all the NPLs present in the gel undergo a similar extent of PLQY quenching upon H_2O_2 addition. This kind of behavior is typical homogeneous quenching.

8. Photograph of the MUA-CdSe/CdS (aq) NPLs film on a glass slide

Figure SI-7. Photograph of the film (size approximately 1 cm) prepared by drying MUA-CdSe/CdS (aq) solution on a glass slide under ambient conditions. The optical density (of the absorption measured in an integrating sphere) is 1.1 at 300 nm wavelength.

11

9. X-ray diffraction pattern of the aqueous solution, hydrogel and aerogel of CdSe/CdS (aq) NPLs

The XRD pattern of the CdSe/CdS NPLs, in organic and in aqueous medium and one of the corresponding aerogels obtained after supercritical drying are shown in figure SI-8. The solid vertical orange and blue lines correspond to the reflections from bulk CdSe and CdS semiconductors, respectively. In case of CdSe/CdS NPLs in organic medium, the main reflections of the face centered cubic (*fcc*) lattice system (such as 111, 200, 220, and 311) can be clearly derived. After the phase transfer with MUA ligands, there are only minor changes in the XRD pattern, assuring the NPLs to retain the same *fcc* crystal lattice structure in aqueous medium.
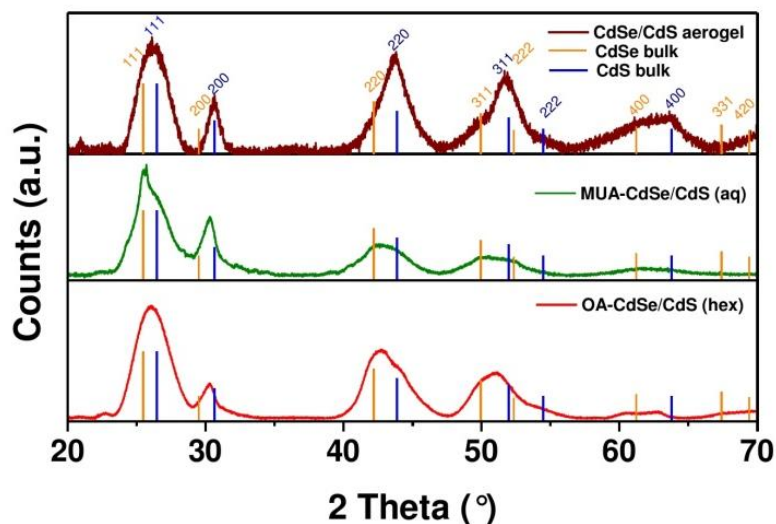
Figure SI-8. PXRD pattern of the CdSe/CdS (hex) NPLs, CdSe/CdS (aq) NPLs and of the CdSe/CdS aerogels.

Similarly, in case of the CdSe/CdS aerogel, the diffraction pattern shows prominent 111 reflections from both CdSe and CdS, while the maxima of the 220, and 311 reflections are more closer to the bulk CdS; however broad reflections at the peak positions of bulk CdSe peak confirms the presence of CdSe crystallites in the material. This broadening is also there in case of 400 reflection. The weakening of the CdSe reflections in the aerogels might be due

12

to the partial oxidation of the CdSe in presence of H_2O_2. This argument is reasonable because dissolution of the CdSe with higher amount of H_2O_2 is evident (see figure-5 in the article).

References:

1.   Tessier, M. D.; Mahler, B.; Nadal, B.; Heuclin, H.; Pedetti, S.; Dubertret, B., Spectroscopy of Colloidal Semiconductor Core/Shell Nanoplatelets with High Quantum Yield. *Nano Lett.* **2013,** 13, 3321-3328.

2.   Tessier, M. D.; Spinicelli, P.; Dupont, D.; Patriarche, G.; Ithurria, S.; Dubertret, B., Efficient Exciton Concentrators Built from Colloidal Core/Crown CdSe/CdS Semiconductor Nanoplatelets. *Nano Lett.* **2014,** 14, 207-213.

3.   Abecassis, B.; Tessier, M. D.; Davidson, P.; Dubertret, B., Self-Assembly of CdSe Nanoplatelets into Giant Micrometer-Scale Needles Emitting Polarized Light. *Nano Lett.* **2014,** 14, 710-715.

4.   Steiner, D.; Dorfs, D.; Banin, U.; Della Sala, F.; Manna, L.; Millo, O., Determination of Band Offsets in Heterostructured Colloidal Nanorods Using Scanning Tunneling Spectroscopy. *Nano Lett.* **2008,** 8, 2954-2958.

5.   Kunneman, L. T.; Schins, J. M.; Pedetti, S.; Heuclin, H.; Grozema, F. C.; Houtepen, A. J.; Dubertret, B.; Siebbeles, L. D. A., Nature and Decay Pathways of Photoexcited States in CdSe and CdSe/CdS Nanoplatelets. *Nano Lett.* **2014,** 14, 7039-7045.

6.   Lorenzon, M.; Christodoulou, S.; Vaccaro, G.; Pedrini, J.; Meinardi, F.; Moreels, I.; Brovelli, S., Reversed oxygen sensing using colloidal quantum wells towards highly emissive photoresponsive varnishes. *Nat. Commun.* **2015,** 6, 6434.

7.   Kodanek, T.; Banbela, H. M.; Naskar, S.; Adel, P.; Bigall, N. C.; Dorfs, D., Phase transfer of 1- and 2-dimensional Cd-based nanocrystals. *Nanoscale* **2015,** 7, 19300-19309.

8.   Mahler, B.; Nadal, B.; Bouet, C.; Patriarche, G.; Dubertret, B., Core/Shell Colloidal Semiconductor Nanoplatelets. *J. Am. Chem. Soc.* **2012,** 134, 18591-18598.

9.   Lim, S. J.; Kim, W.; Shin, S. K., Surface-Dependent, Ligand-Mediated Photochemical Etching of CdSe Nanoplatelets. *J. Am. Chem. Soc.* **2012,** 134, 7576-7579.

10.   Virgili, T.; López, I. S.; Vercelli, B.; Angella, G.; Zotti, G.; Cabanillas-Gonzalez, J.; Granados, D.; Luer, L.; Wannemacher, R.; Tassone, F., Spectroscopic Signature of Trap States in Assembled CdSe Nanocrystal Hybrid Films. *J. Phys. Chem. C* **2012,** 116, 16259-16263.

13

3 Synthesis of Aerogels from Shape Controlled Pt Nanoparticles

3.1 Summary

This section 3.2 demonstrates the first report to synthesize aerogels from shape controlled metal NPs. The procedure developed works in organic colloidal solution. The aerogels are obtained directly from the organic colloidal solution of the Pt NPs. The study represents a unique route of aerogel preparation by alleviating the time consuming ultrafiltration and the phase transfer processes. In this study, the lyogels of Pt nanocubes and nanospheres (in hexane) are prepared by employing hydrazine monohydrate ($N_2H_4 \cdot H_2O$) as the destabilizing agent. The lyogels are then transformed to highly porous macroscopic aerogels by supercritical drying with liquid CO_2. The aerogels are characterized by TEM and SEM microscopy, which proves the 3D self-supported network, is built by the coalescence of the individual Pt NPs. It is also proved with high resolution TEM analysis that the cube aerogels exhibit (100) as the only exposed crystal facets, which could be useful for facet selective catalytic reactions. Moreover, the aerogels exhibit high specific surface areas in the range of 6400-7000 $m^2 \cdot mol^{-1}$. Furthermore, the aerogels derived from the cubes and the spheres are employed as catalyst for the asymmetric hydrogenation of keto-pantolactone. The results illustrate complete conversion of the reactants. An enantiomeric excess of 9% for the 'D' isomer is obtained when Pt nanocube aerogels are used as catalyst. The same is 5% when Pt nanosphere aerogels are employed as catalyst.

3.2 Highly Porous Aerogels from Pt Nanocubes and Nanospheres Directly from Organic Colloidal Medium

Suraj Naskar, Axel Freytag, Jens Deutsch, Natlja Wendt, Angela Köckritz, Peter Behrens and Nadja C. Bigall*

Submitted

Journal Name

ARTICLE

Porous Aerogels from Pt Nanocubes and Nanospheres Directly from Organic Colloidal Solution

S. Naskar,[a] A. Freytag,[a] J. Deutsch,[b] N. Wendt,[c] P. Behrens,[c] A. Köckritz[b] and N. C. Bigall[a*]

Porous architectures of noble metal nanocrystals are promising for many catalytic as well as for fuel cell applications. Here we present the synthesis of porous, extremely light-weight aerogels of self-supported Pt nanocubes and nanospheres, by direct destabilization from organic colloidal solution using hydrazine monohydrate ($N_2H_4.H_2O$) as gelation reagent. The template-free voluminous lyogels of the Pt nanocrystals are converted to macroscopic solid aerogel monoliths by supercritical drying. The aerogels from Pt nanocubes mostly exhibit (100) as the exposed crystal facets throughout the entire monolithic surface, while the aerogels from quasi-quasi-spherical Pt nanocrystals exhibit many crystal facets such as (111) and (100). Furthermore, the aerogels exhibit remarkably low densities of ~ 0.19 g·cm^{-3} ± 0.038 g·cm^{-3} (~0.9 % of bulk Pt) and a specific surface area in the range of ~6400-7000 m^2·mol^{-1}. The nanocube gels show better catalytic performance than the nanosphere gels when employed for asymmetric hydrogenation reaction, which is exemplarily shown for 4,4-dimethyldihydrofuran-2,3-dione to D-/L-pantolactone conversion with an excess of 9% for the D-enantiomer. Owing to their high specific surface area and certain type of exposed crystal facets, Pt aerogels developed here are highly promising for possible future applications in facet selective catalytic reactions.

1. Introduction

Noble metal nanoparticles such as Pt, Pd, Ag and Au have excellent catalytic properties and good electrical conductivities.[1-8] Variation in the reaction parameters such as temperature, types and amounts of metal precursors, organic surfactants, reducing agents have enabled the researchers to fine tune the morphologies of the desired nanoparticles both in dimensions (shape, size) and in the nanoscopic functionalities e.g., surface plasmon resonance, superparamagnetism etc.[1, 3, 4, 9, 10] As a result different shapes of the metallic nanocrystals starting from quasi-spherical[1, 11], cubic[12, 13], octahedral[9], cubo-octahedral[9], tetrahedral[12], rod shaped[14] to nanowires[4] or even more complex structures exist in literature.[9, 15-20] The synthesis of shape controlled noble metal nanoparticles is very useful due to their superior catalytic activity in comparison to non shape-controlled particles.[2, 10, 15] The pioneer work of El-Sayed and co-workers[7, 8, 21] and many other researchers[13, 22, 23] unambiguously indicates that certain exposed crystal facets present on the surface of the nanoparticles play an important role during

the course of catalysis for yielding the selective products.

In spite of the remarkable success in the optimization of the synthesis conditions to obtain highly monodisperse shape controlled nanoparticles, the practical applications of these particles are limited mainly due to their presence in colloidal solution, and also due to organic surfactants present on their surface, which reduce the access of the reactant molecules to the metal surface, and ultimately result in lower catalytic efficiency.[24, 25] Therefore, there is a need to prepare surfactant free, crystalline nanoparticles in solid state while maintaining their excellent electrical conductivity and facet dependent catalytic properties. This can be achieved by porous superstructures of these particles which can be easily separated after the reaction and exhibit a good accessibility of the surface.

In previous attempts, nanosmelting,[26] selective dealloying[27], hydrothermal process[28], pH triggering[29] or combustion synthesis[30] techniques have been utilized for the fabrication of porous superstructures of metal nanoparticles.[31] All these techniques have to deal with time consuming multistep procedures or need nanoscale templates to support the structure. In contemporary reports, the work groups of Brock and Eychmüller have developed a new approach to synthesize template free, highly porous aerogels, which consist of a 3D interconnected network of pure or multi-metallic nanoparticles or quantum dots, *via* the formation of lyogels by controlled destabilization of the colloidal solution followed by supercritical drying with liquid CO_2.[32-39] This excellent technique provides the opportunity to synthesize porous material of the same compounds. Despite of many advantages, the key obstacles here are the time consuming process of concentrating the nanoparticles solution by ultra-filtration before starting the self-assembly process[40] as well as the gelation process can only be started when the nanoparticles are in polar medium or transferred to aqueous

phase *via* ligand exchange reactions.[41] The development of a synthetic route to obtain metal gels by means of direct destabilization of the organic colloidal solution in order to circumvent the time consuming filtration process and complex phase transfer process would be advantageous. Such a route would also open the possibility to fabricate metal aerogels exposing distinct crystal facets, which would be suitable for facet selective catalysis.

In this work, we have developed a new synthesis technique to achieve aerogels from Pt nanocubes and nanospheres, which works directly from organic colloidal solution using $N_2H_4 \cdot H_2O$ as the gelation reagent. The skeletal structures of the aerogels are characterized by scanning and transmission electron microscopy, which prove the presence of porous fractal type networks, created by the random coalescence of the individual nanocrystals. We have also demonstrated a cleaning procedure of the lyogels to remove the excess organic surfactant from the surface of the nanoparticles, which lead to enhancement of the catalytic activity of the ultimate aerogels. This is exemplarily shown by employing the gels as catalyst for asymmetric hydrogenation of keto-pantolactone in presence of cinchonidine as chiral modifier. By this reaction, we furthermore found that the single facet gels are superior in enantiomeric excess in comparison to the multifacet gels.

2. Experimental Section

Reagents. Platinum(II) acetylacetonate Pt(acac)$_2$, (97%), iron(0) pentacarbonyl Fe(CO)$_5$, (99.99%), hydrazine monohydrate $N_2H_4 \cdot H_2O$, (98%), 1-octadecene ODE, (90%), oleic acid (90%), oleylamine (90%), ethanol (99.5%), toluene (99.7%), *n*-hexane (>99%), acetone (>99%), 4,4-dimethyldihydrofuran-2,3-dion, cinchonidine $C_{19}H_{22}N_2O$ (96%) were purchased from Sigma Aldrich. 5% Pt/Al$_2$O$_3$ was purchased from STREM. Pt standard (concentration-1000 mg·L^{-1} ± 4 mg·L^{-1}) was purchased from Fluka Analytical. Nitric acid (>69%) and hydrochloric acid (>37%) were purchased from Fluka.

Synthesis of Pt nanocubes. Pt nanocubes of average side length 7-8 nm were synthesized according to the procedure described by Wang *et al.* with little modifications.[1] Briefly, 0.2 g of Pt(acac)$_2$, 15 mL of ODE, 1 mL of oleic acid and 1 mL of oleylamine were placed in a three neck flask. The mixture was then degassed under vacuum at 80 °C for 1 h at constant stirring condition to remove the dissolved oxygen and the water from the system. Afterwards, the temperature was increased to 120 °C by 20 min under Ar atmosphere. The reagents were kept at this temperature for another 30 min. At this point 120 µL of Fe(CO)$_5$ in ODE (prepared previously by dissolving 0.4 mL of Fe(CO)$_5$ in 4 mL ODE and stored inside a glove box at -25 °C) was swiftly injected into the mixture. After the Fe(CO)$_5$ injection, the temperature of the mixture was slowly increased from 120 °C to 200 °C within 18 min and left under these conditions for another 30 min. The heating mantle was then removed and the mixture was allowed to reach room temperature. To purify the products, 30 mL of isopropanol was added and the whole mixture was then transferred to a 50 mL centrifuge vial and centrifuged at 8000 g (rcf) for 15 min. The black precipitate of Pt nanocubes was then dispersed in 3 mL hexane.

Synthesis of Pt nanospheres. Pt nanospheres of average diameter 4.0 nm were synthesized following the above mentioned synthetic procedure with the difference that only 1 mL oleylamine was added instead of an oleylamine and oleic acid mixture. The purified product of Pt nanospheres was dispersed in 3 mL hexane.

Purification of the Pt nanoparticles before gelation. The excess organic surfactants such as oleic acid and oleylamine present on the surface of the nanocrystals need to be reduced before the gelation experiments. Therefore, 1 mL of ethanol was added to 1 mL of the hexane dispersion of the nanoparticles and the mixture was then centrifuged at 3600 g (rcf) for 10 min. The supernatant was discarded and the precipitate was dispersed in 1 mL hexane. This process was repeated for 2 more times with 1 mL and 0.75 mL ethanol, respectively, and finally the purified product was dispersed in 3 mL hexane. These purified particles were employed as building blocks for the gelation experiments.

Gelation of the Pt nanocubes and Pt nanospheres. The optimum conditions to obtain voluminous gels of the Pt nanoparticles were first experimented by varying the amount of $N_2H_4 \cdot H_2O$, while the amount of Pt (determined from atomic absorption spectroscopy AAS measurements) was kept constant at 12 mg of net Pt contained in 400 µL hexane dispersion. All the gelation experiments were conducted in 2 mL polypropelene micro-centrifuge vials (from Eppendorf). After the addition of $N_2H_4 \cdot H_2O$, a two phase mixture ($N_2H_4 \cdot H_2O$ at the bottom and hexane phase containing the nanoparticles at the top) was observed because of the non-miscibility of hexane and $N_2H_4 \cdot H_2O$. The mixture was shaken manually for 10 seconds to initiate the gelation process. Afterwards, the vials were kept in rest under ambient conditions. It was observed that with high amount of $N_2H_4 \cdot H_2O$ (50 µL of $N_2H_4 \cdot H_2O$, molar ratio $N_2H_4 \cdot H_2O$: Pt = 16 : 1), gelation happens within ~1 h, but the volume of the hydrogel was less in comparison to the lyogels obtained with lower amount of $N_2H_4 \cdot H_2O$ (molar ratios $N_2H_4 \cdot H_2O$: Pt = 3 : 1 to 10 : 1), where gelation was observed after ~2.5 h to 5 h of $N_2H_4 \cdot H_2O$ addition. The highest voluminous gel was obtained with 30 µL of $N_2H_4 \cdot H_2O$, (molar ratio $N_2H_4 \cdot H_2O$: Pt = 10 : 1) where the gelation time was ~2.5 h and these conditions were chosen as the optimum gelation conditions. Further gelation experiments were conducted following these parameters. After obtaining voluminous lyogels, the solvent was exchanged with fresh hexane for 6-7 times to remove the excess $N_2H_4 \cdot H_2O$ and the gelation by-products and the samples were stored for 2 days for aging. In this time the solvent was exchanged gradually with a mixture of acetone/hexane (10% to 90%) and finally the gels were washed 5 times with pure anhydrous acetone and were placed inside a desiccator containing anhydrous CaCl$_2$, to avoid any kind of contaminations with moisture. Following the above mentioned reaction conditions, two sets of samples were prepared; the first set of samples was treated further with Soxhlet extraction (as described in the following section) and the second set of samples was stored without Soxhlet extraction. Both sets of the lyogels were then converted to aerogels *via* supercritical drying. For that the lyogels were transferred to a supercritical dryer (E3100 from Quorum Technologies) in anhydrous acetone environment. The acetone was exchanged with liquid CO$_2$ and the samples were left under these conditions for one day. After flashing the chamber with liquid CO$_2$ for 3 times (to remove residual acetone) the temperature of the chamber was raised above the critical point of CO$_2$ (31.1 °C and 1100 psi). When the critical conditions were reached, the vent valve of the dryer was opened slowly to release

the gaseous CO_2. Supercritical drying helps to maintain the filigree network structure of the lyogels by avoiding capillary forces, which can break down the structural morphology.[42] Aerogels of Pt nanocubes and nanospheres were then collected from the drying boat and stored under ambient conditions. A total volume shrinkage of roughly 25% was observed upon conversion of the lyogels to the aerogels. The aerogels should be handled with care, to keep their monolithic stage intact, since mechanical stress can break them into pieces.

Purification of lyogels via Soxhlet cleaning. The lyogels synthesized above can be further purified from the residual organic surfactants *via* washing with ethanol : acetone = 1 : 1 mixture at 65° C. A Soxhlet glass apparatus was employed for this cleaning purpose where the monoliths of the lyogels were placed inside porous sample holders (Porous Speci Pot with Lid CPD 800A from Quorum Technologies Ltd.) before inserting them in the sample chamber of the Soxhlet apparatus. This special technique was applied to shield the lyogels from the direct hit of the cleaning solvent, which would destroy the gel networks. A total amount of 100 mL of extraction solvent was heated (using an oil bath) in a flask which was mounted at the bottom of the Soxhlet apparatus. This process was continued for 3 h and afterwards the gels were collected from the sample holder and stored in pure anhydrous acetone. Then the cleaned lyogels were converted to aerogels *via* supercritical drying.

FTIR measurements. The FTIR spectra of the samples were collected using a Tensor 27 FT-IR spectrometer from Bruker Optik GmbH equipped with a DLATGS (Deuterated L-alpha-Alanine doped TriGlycine Sulphate) detector in attenuated total reflectance (ATR) mode. The FTIR spectra of the pure oleic acid and pure oleylamine were collected by evaporating one drop of the pure substance on the surface of the ATR cell. The spectra of the aerogels were collected by placing same amount of the solid sample on the ATR cell.

Atomic absorption spectroscopy. The Pt concentration of the hexane dispersion was determined by atomic absorption spectroscopy (AAS) using a Varian AA140 instrument equipped with an air/acetylene flame atomizer. The samples were prepared by digestion with aqua regia. A total of 10 standard Pt solutions (in the range of 0-20 ppm were prepared by diluting 'Pt standard for AAS', were measured to obtain a calibration curve. A 1 % HNO_3 solution was employed in order to correct the background signal.

Scanning electron microscopy. A JEOL JSM 6700F equipped with cold field emission gun electron source was employed for the scanning electron microscopy. For the measurements, small pieces of the Pt aerogels were deposited on adhesive carbon films mounted on the brass sample holder.

Transmission electron microscopy. A FEI Tecnai G2 F20 TMP (C_s = 2 mm, C_C = 2 mm), equipped with a 100 kV field emission gun was employed for transmission electron microscopy (TEM) analysis. The TEM micrographs were collected in bright field mode. Prior to TEM grid preparation, the liquid samples were purified 3 to 4 times by ethanol induced flocculation followed by centrifugation and re-dispersion in hexane. Finally, 10 µL of the purified sample was drop

casted on a 300 mesh carbon coated copper TEM grid, purchased from Quantifoil. In the case of aerogels measurements, the TEM grid was carefully touched on the surface of the aerogel sample.

Powder X-ray diffraction Analysis. The x-ray diffraction (XRD) pattern of the samples was measured using a Bruker D8 Advance in reflection mode. Highly concentrated samples of colloidal Pt nanoparticles were drop casted on a single crystal silicon carrier and were dried in air before measurements. Tiny amount of solid aerogels were placed on solid sample holder for the XRD measurements.

Nitrogen physisorption measurements. A Quantachrome Autosorb-3 instrument operating at 77 K was employed for the nitrogen sorption measurements. Prior to physisorption measurements, the samples were degassed under vacuum at 25° C for 24 h. Brunauer-Emmett-Teller (BET) equation was applied to estimate the specific surface areas.[43] Barrett-Joyner-Halenda (BJH) method was applied to determine the pore size distribution.[44] The total pore volume was estimated using the single point method at $p/p_0 = 0.99$.

Measurement of density of the aerogels. The relative density of the aerogels was estimated by measuring the weight and the approximate volume (the aerogels were inserted inside a cylindrical vial of known diameter and weight, from the filling height measured at least in 20 different positions, the approximate volume was calculated and by measuring the mass of the gels, the density was determined, a maximum of 20% error in measurements were taken into account) for several aerogels. The interconnected porous structure have approximate density of ~ 0.19 g·cm^{-3} ± 0.038 g·cm^{-3} and ~0.2 ± 0.04 g·cm^{-3} for the nanocubes and nanospheres aerogels, respectively. A comparison with the bulk density of the Pt metal (21.45 g·cm^{-3}) implies that the aerogels obtained in our case are approximately 100 times less dense than bulk Pt.

Catalytic hydrogenation. The hydrogenation reaction was followed according to the procedure described in reference 45 with marginal modifications. The reaction mixtures for the autoclave reactions were prepared under dry argon atmosphere. Accordingly, 20 mL toluene containing 5.44 x 10^{-3} mmol (1.6 mg) cinchonidine was added to 4.3 x 10^{-2} mmol (8.4 mg) Pt hydrogel catalyst (same amount of both nanocube and nanosphere lyogels before and after purification with Soxhlet technique was employed) which was placed inside a 100 mL autoclave beaker. Subsequently, 3.68 mmol (472 mg) of 4,4-dimethyldihydrofuran-2,3-dione was added. The mixture was pressurized three times with 20 bar of argon, two times with 20 bar of hydrogen and finally with 50 bar of hydrogen. The hydrogenation was carried out at room temperature and at 100 rpm stirring conditions for 24 hours at 50 bar pressure. After depressurization, the reaction solution was filtered and analyzed with ^{1}H-NMR (analysis of conversion of 4,4-dimethyldihydrofuran-2,3-dione and yield of pantolactone 2D/2L) and gas chromatography (GC) by employing chiral column (ratio of the pantolactone enantiomers). The ^{1}H-NMR analyses of the obtained reaction mixtures were performed in $CDCl_3$ after removal of the solvent toluene using a 300 MHz spectrometer (Fourier). GC analyses were performed with a GC System 6890 (Agilent) with a Lipodex E column. Two sets of catalytic experiments were performed with a reference catalyst:

i) According to reference 45 by employing 20 mL toluene, 2.72×10^{-2} mmol (0.8 mg) cinchonidine, 84 mg 5% Pt/Al_2O_3 [2.15×10^{-2} mmol (4.2 mg) Pt] and 3.68 mmol (472 mg) 4,4-dimethyldihydrofuran-2,3-dione. Reaction conditions: 50 bar H_2, room temperature, 700 rpm, 24 h.

ii) Procedure in reference 45 was adapted according to the experiments of the present paper (marginal modification of Baikers procedure[46] with reduced stirring speed) by using 20 mL toluene, 5.44×10^{-2} mmol (1.6 mg) cinchonidine, 168 mg 5% Pt/Al_2O_3 [4.3×10^{-2} mmol (8.4 mg) Pt] and 3.68 mmol (472 mg) 4,4-dimethyldihydrofuran-2,3-dione. Reaction conditions: 50 bar H_2, room temperature, 100 rpm, 24 h.

3. Results and discussion

At first, Pt nanocubes and nanospheres were synthesized by thermal reduction of platinum acetylacetonate $Pt(acac)_2$ precursor following a procedure as described by Wang *et. al.* with little modifications.[1] A trace amount of $Fe(CO)_5$ was employed as the reducing agent and the shape control of the particles was achieved with slow heating rate (3-5 °C/min) and suitable choice of surfactants such as oleic acid and/or oleylamine. The Pt nanoparticles were characterized with bright field TEM and also by powder XRD. The TEM micrographs of the Pt nanocubes and the Pt nanospheres are shown in Figure SI-1 in the supporting information. The TEM micrographs reveal that the nanocrystals exhibit a narrow standard deviation. The Pt nanocubes have an average side length of 7.7 nm ± 0.47 nm, and the Pt nanospheres have an average diameter of 4.0 nm ± 0.35 nm. From the high resolution TEM (HRTEM) micrograph of a single Pt nanocube (shown in Figure SI-1C), the lattice spacing between two adjacent crystal planes is measured, which is found to be ~ 0.19 nm, confirming (100) as the crystal facets present on the six surfaces of the nanocubes.[1, 20, 47] While in the case of HRTEM of a single Pt sphere, the measured distances between the lattice planes confirm the presence of (100) and (111) crystal planes of an fcc (face centered cubic) lattice system.[1]

Before starting the gelation experiments the nanocrystals as obtained after the synthesis were purified by ethanol induced precipitation and re-dispersion. This treatment helps to remove excess organic surfactants (oleic acid and/or oleylamine). It should be noted that the nanoparticles in hexane were colloidally stable before any gelation experiments. Next, the above purified dispersions of Pt nanospheres and nanocubes were employed as the building blocks for the lyogel formation. The optimum gelation conditions (monolithic voluminous aggregates of the Pt nanocrystals) were investigated by adding variable amounts of $N_2H_4.H_2O$ to the reaction vials containing the same amount of Pt (see experimental section). Photographs of the lyogels obtained are presented in Figure 1. The largest volume achieved for the lyogels was in the case of molar ratio $N_2H_4.H_2O : Pt = 10 : 1$ (as can be seen in the photograph), where the gelation time was ~2.5 h. With lower amounts of $N_2H_4.H_2O$, the appearance of the hydrogel (voluminous aggregates) was observed after ~5 h of $N_2H_4.H_2O$ addition, and the volume of the gel obtained was less. Whereas, in the case of molar ratio $N_2H_4.H_2O : Pt = 16 : 1$, the reaction was fast (~1 h), but the volume of the gel obtained was also less. Presumably, addition of $N_2H_4.H_2O$, leads to two parallel reactions, i) surfactant removal, ii) the degradation of the $N_2H_4.H_2O$ on the surface of Pt.
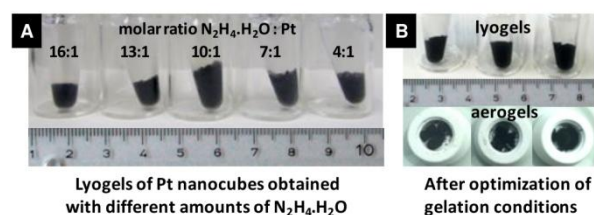

Figure 1. *(A) Photographs of lyogels obtained by adding different amounts of $N_2H_4.H_2O$ in 400 µL hexane dispersion containing 12 mg of Pt nanocubes. Highest volume of the gel is obtained with molar ratio $N_2H_4.H_2O : Pt = 10 : 1$. Lower amount of $N_2H_4.H_2O$ results in less voluminous lyogels, higher amount of $N_2H_4.H_2O$ results in compact aggregates. (B) (top) lyogels of Pt cubes and spheres obtained with optimized gelation conditions, (bottom) corresponding aerogels obtained after supercritical drying with liquid CO_2.*

We presume that, when the $N_2H_4.H_2O$ content is high, the rate of surfactant removal from the surface of the nanoparticles is very fast, generating many active sites on the Pt nanocrystals within short reaction time, which in turn results in the formation of compact aggregates or precipitates and hence the product is less voluminous. On the contrary, with less $N_2H_4.H_2O$ content, the rate of surfactant removal is slow and thus the number of active sites created is less. At the same time, one also has to look at the degradation of $N_2H_4.H_2O$, which takes place at the surface of the Pt nanoparticles. Therefore, after the degradation the amount of $N_2H_4.H_2O$ left to remove the surfactant is much less and hence the gelation takes long time, ultimately resulting lyogels with less volume. In the middle scenario, all these processes happen in a way that the surfactant removal rate, reagent degradation are in optimum state and the gel volume obtained is the highest. We repeated the same reaction conditions for Pt cubes and spheres 8 more times which resulted in similar observations, and each time the highest voluminous gel was obtained with molar ratio $N_2H_4.H_2O : Pt = 10 : 1$. Therefore, we have chosen this to be the optimum gelation conditions and followed to prepare further lyogels from the organic dispersion. The solvent of the gels were exchanged to acetone and the Pt lyogels were then transformed to aerogels following Kistler's method of supercritical drying with liquid CO_2.[42]

The SEM micrographs of the cube aerogel are shown in Figure 2A and B, in two different magnifications. The low resolution image proves the high porosity of the aerogel, with many pores in the macroporous regime, *i.e.*, >50 nm. The high resolution SEM micrograph reveals that the interconnected network has many small pores having diameters in the range of the mesoporous (2-50 nm) regime. Owing to these special physical properties the aerogels could be promising catalysts, as the reagent molecules can diffuse through this porous network with minimum hindrance and also can access the high specific surface area of the aerogel. In order to characterize the connections of the nanocubes and to know how this fractal type network is standing without any
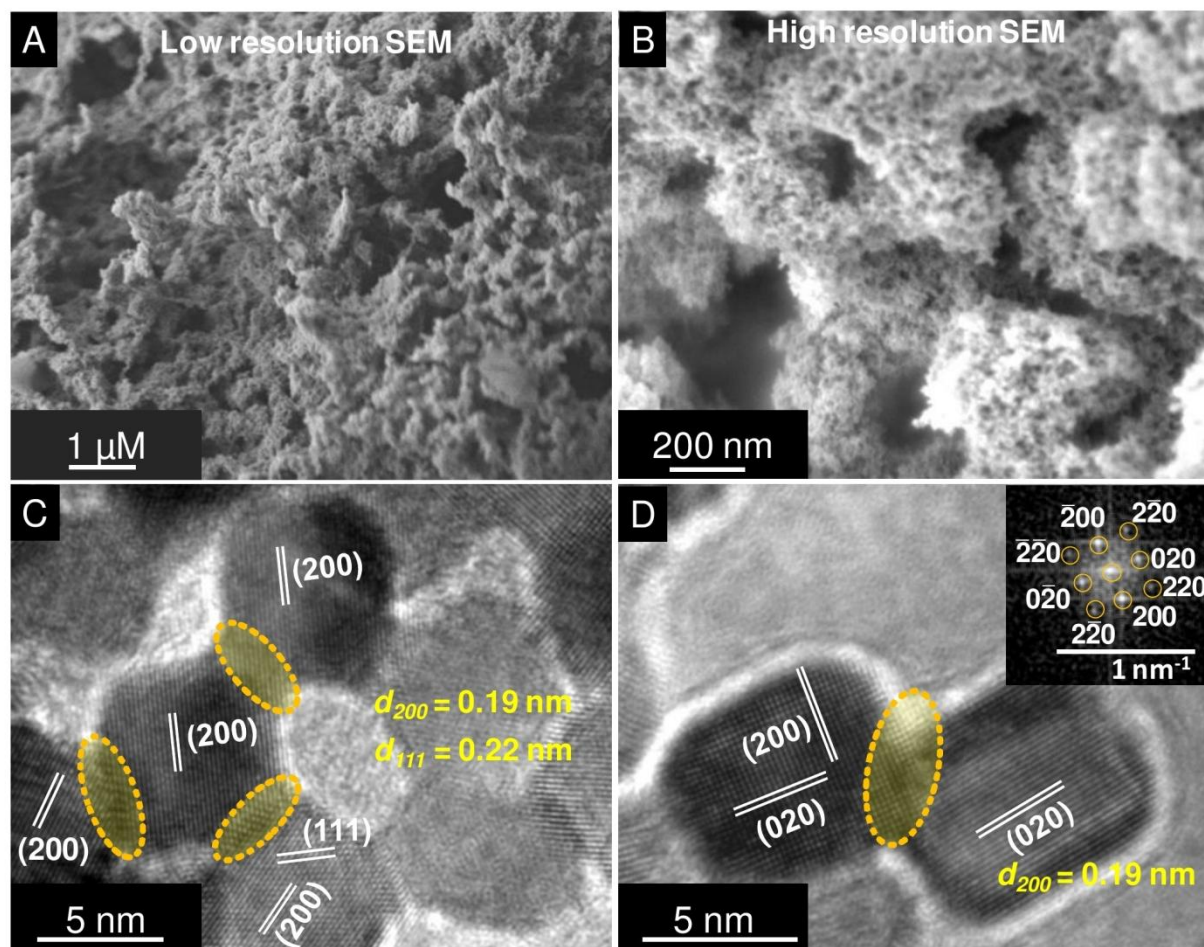
Figure 2. (A) and (B) SEM micrographs of aerogels from Pt nanocubes in two different magnifications. The lower resolution image proves the high porosity of the aerogel with pore diameters in the macroporous regime. High resolution SEM image shows the presence of tunnels inside the skeletal network with pore diameter in the mesoporous regime. (C) and (D) HRTEM images of interconnected Pt nanocubes. Individual nanocubes coalescence to form the 3D network with only (100) as the exposed crystal facet. Inset of Figure (D) is FFT of the connected Pt nanocubes.

template, we have further investigated the aerogels with HRTEM analysis; the images are shown in Figure 2C-D. From the HRTEM micrographs it can be clearly noticed that the Pt nanocubes are interconnected by sharing their lattice points, hence we can expect the Pt-Pt metal bond formation between two nanocrystals. Furthermore, most of the cubes retain their shapes after the treatment with $N_2H_4.H_2O$. By FFT (fast Fourier transformation) analysis, the distance between the lattice fringes among the interconnected Pt cubes is found to be ≈0.19 nm, revealing (100) as the only exposed crystal facets.[1, 19, 20] It can be concluded that even after the aerogel formation where the Pt nanocubes are attached with random orientations, they have (100) facets dominating the entire surface. Therefore, it can be unambiguously said that the cube aerogels will be highly interesting for the facet selective catalytic reactions as is observed for the individual Pt cubes, where

selective reagent molecules are adsorbed on the (100) facets and enhance the reaction rates by several orders of magnitude or yields stereo selective products.[23, 47]

The SEM micrographs of the aerogels from the Pt nanospheres are shown in (Figure SI-2A and 2B). Similar to the observations of the cube aerogels, here also the pore diameters range from meso to macro porous regime. The HRTEM micrographs, shown in Figure SI-2C and 2D, reveal that the self-supported interconnected network has been formed by the coalescence of the individual Pt spheres. A FFT analysis of the lattice fringes present on the surface reveals the presence of different crystal facets e.g., (100) and (111) over the entire surface of the monoliths.

In case the lyogels are dried under ambient conditions (so-called xerogels), the porous networks of the gel collapse due to the capillary forces, ultimately resulting in highly compact structures with much less porosity compared to the aerogels obtained after

supercritical drying. The densities of the xerogels are found to be ~ 3.0 g·cm^{-3} ± 0.6 g·cm^{-3}, which is much higher (~16 times) than the densities of the aerogels. The SEM micrographs of the xerogel of the cubes are shown in Figure SI-4. It should be noted here that the $N_2H_4\cdot H_2O$ triggered gelation was also successful for Pd, Fe_2O_3 and Au-Fe_2O_3 nanoparticles.

Interpretation of the gelation process. A schematic diagram showing the consecutive steps of aerogel formation starting from the organic colloidal solution of Pt nanocubes is depicted in Figure 3 (A). The Pt nanocrystals are stable in colloidal solution due to the interaction of the surfactant present on their surface and the solvent. In case of colloidal Pt nanocubes, oleylammonium oleate which is formed from oleylamine and oleic acid is adsorbed on the surface, and in case of Pt nanosphere oleylamine, is adsorbed on the surface.[1] We presume that $N_2H_4\cdot H_2O$ is strongly adsorbed on the surface of the particles and therefore replaces the existing surfactants. Hence the steric repulsion between the particles is reduced, which results in controlled destabilization, since the particles can get in contact to each other. It should be noted that the highly catalytically active surface of Pt can cause an exothermic decomposition of $N_2H_4\cdot H_2O$ to N_2 which is liberated as a gas, and H_2 which remains partially adsorbed on Pt surface (Figure 3 B and C). In all cases of the gelation experiment, we observed the slow evolution of colorless and non-combustible N_2 gas which was able to quench a burning matchstick.

We presume a gelation mechanism as follows: after partial surfactant removal by replacement with hydrazine, the active facets of the Pt nanocrystals which are in close proximity can form the network structure through sharing of atoms, *via* metal bonding. The edge-to-edge assembly of the particles could be attributed to the crystal defects which are predominantly present at the corners and edges as well as inadequate surfactant binding to these sites,

allowing the particles to form the Pt-Pt bonding at corners and edges. This coalescence of the individual Pt nanoparticles results in the formation of nanoparticle chains which in turn form the 3D porous network.

Specific surface area measurements. Nitrogen gas physisorption measurements were conducted to evaluate the porosity and the specific surface area of the aerogels. The results obtained for the aerogels (both nanocubes and nanospheres) are analyzed by BET method and are presented in Figure 4. The aerogels from Pt nanocubes have inner specific BET surface area of ~7000 m^2·mol^{-1} (~36 m^2·g^{-1}), most of which can be attributed to (100) facets, and the aerogels from nanospheres have the BET surface area of ~6400 m^2·mol^{-1} (~33 m^2·g^{-1}), respectively. Both of these values are in the same order of magnitude of the aerogels obtained from colloidal aqueous solution of noble metal nanoparticle building blocks, reported earlier in literature.[35, 36] It should be noted that the maximum surface areas possible considering all the cubes and the quasispheres are present separately are ~39 m^2·g^{-1} and 70 m^2·g^{-1} (from the rough geometrical estimation), respectively. This means that in the case of a cube aerogel more than 92% of the surfaces are accessible after the aerogel formation. For the quasisphere aerogel only 47% of the theoretically possible surface are accessible, which we attribute to the difference in the building block shapes. Barrett-Joyner-Halenda (BJH) theory was applied to calculate the pore size distribution and the cumulative pore volume from the desorption branch of the isotherm, and the plots are shown in the insets of Figures 4A and 4B for Pt nanocube and nanosphere aerogels, respectively. The isotherms can be ascribed to the type III physisorption isotherm. It can thus be inferred that the porous structures consist of pore diameters mainly in the mesopore (2-50 nm) and macropore (> 50 nm) regimes, which is consistent with the observations from TEM and SEM analysis. The BJH cumulative pore volumes $V_{3.0-242}$ (for pore diameter ranging from 3.0 nm to 242 nm, measured up to a relative pressure p/p$_0$ = 0.99) are 0.29 cm^3·g^{-1} and 0.25 cm^3·g^{-1} for the aerogels derived from cubes and spheres, respectively.

The average pore diameters of the aerogels calculated using the equation 4 x V_t/σ[41, 48] (where σ is BET specific surface area and V_t = 1/ρ_a - 1/ρ_b ; ρ_a = density of aerogel and ρ_b = density of bulk solid Pt), are ~533 nm and ~581 nm for cube and sphere aerogels, respectively. These values are out of range of N_2 physisorption measurements. The porosity of the aerogels thus mainly results from the macropores (>50 nm). Summarizing these results, it can be concluded that both of the Pt aerogels are highly macroporous, exhibiting high BET specific surface areas when related to their mass, but with very low densities due to large open pores and tunnels.
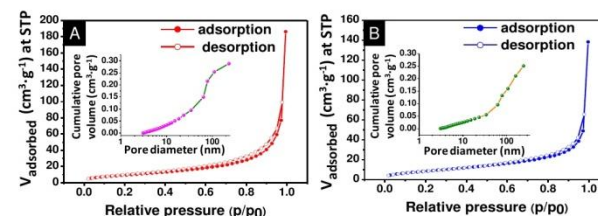

Figure 3. *(A) Schematic diagram of aerogel synthesis from Pt nanocubes directly from organic colloidal solution. First, controlled destabilization is conducted with $N_2H_4.H_2O$ to remove the organic surfactant partially and to obtain voluminous lyogels. Second, the solvent of the lyogels are gradually exchanged from hexane to acetone. Third, the lyogels are converted to monoliths of aerogels by supercritical drying. (B and C) Schematic representation of replacement of the adsorbed stabilizers oleylammonium oleate and oleylamine by hydrazine and subsequent decomposition of hydrazine on the Pt surface into adsorbed hydrogen and liberated nitrogen gas.*

Figure 4. *Nitrogen physisorption measurements of the Pt aerogels. (A) isotherm of nanocube aerogel (B) isotherm of nanosphere aerogel. Inset of (A) and (B) represent BJH cumulative pore volume distribution plots of the respective aerogels.*
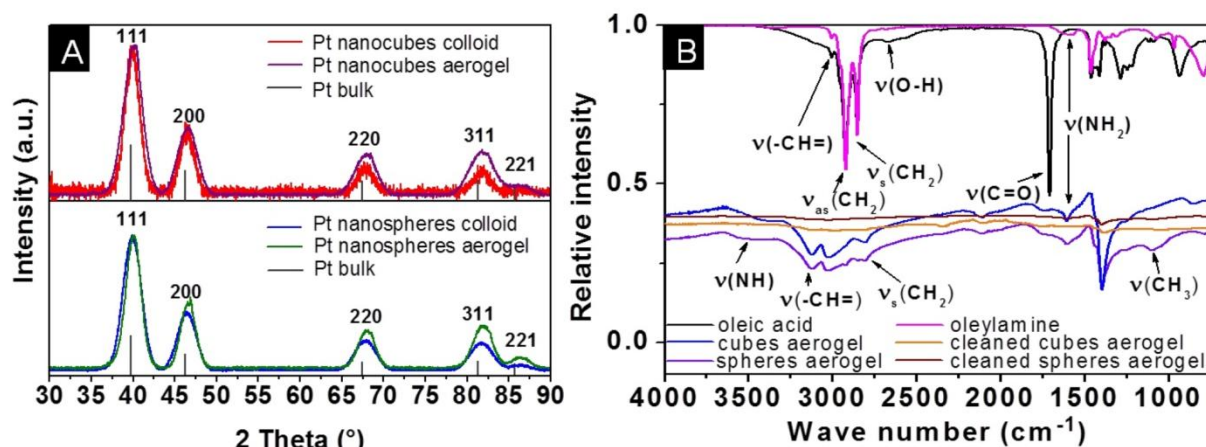
Figure 5. *(A) Comparison of the XRD pattern of the colloidal building blocks of Pt nanocubes and nanospheres and after aerogel formation. Solid vertical grey lines represent bulk Pt. (B) FTIR spectra of the Pt aerogels obtained with and without Soxhlet extraction, FTIR spectra of the pure oleic acid and pure oleylamine are also measured for comparison.*

Therefore, molecules can easily probe the inner surface of the aerogels, which might be suitable for many catalytic reactions or as a sensor.

Characterization of the crystalline structure of the aerogels. Both the Pt nanocubes and the nanospheres were characterized with powder XRD analysis and both are found to exhibit face-centered cubic (fcc) lattice system. Figure 5A shows a comparison between the diffraction pattern of Pt nanocubes and the nanospheres before and after aerogel formation. Solid vertical grey lines are included to mark the positions of reflections from bulk Pt for comparison.[49] The crystallite sizes are calculated from the Scherrer equation $\tau = K*\lambda/\beta cos\theta$ (where, τ = mean crystallite size, K = shape factor or Scherrer constant which depends on integral breadth, shape and crystallite size distribution, λ = X-ray wavelength, β = full width at half maximum, θ = Bragg angle of reflection). The mean crystallite sizes calculated with K = 0.86 (for spheres)[50] and 1.5 (for cubes considering variance slope and variance intercept constant)[50] are 6.9 nm and 3.6 nm for the Pt nanocubes and nanospheres, respectively (calculated from 111 reflection in both cases). These values are only slightly smaller than the average sizes obtained from the TEM analysis (average size of nanocubes and nanospheres estimated from TEM are 7.7 nm ± 0.47 nm and 4.0 nm ± 0.35 nm, respectively). Only minor differences are found in the XRD patterns taken before and after gelation. The positions of the XRD reflections are not altered to any significant extent. A close look reveals that the reflections of the aerogels are slightly broader than those of the dried colloidal nanocrystals, which could be due to slightly smaller crystallite size, stress and strain due to coalescence of the nanocrystals. However, the relative intensities of the higher angle reflections of the aerogels, such as 220, 311 and 221, are higher than those of the pristine nanocrystals, which could be a texture effect due to preferred short range orientation of the cubes/spheres during the assembly of the nanocrystals.[1, 51]

Surfactant removal from the aerogel surface. The aerogels obtained after supercritical drying still contained some residual organic surfactants on their surface. In order to achieve high catalytic activity, the surface of the nanoparticles in the aerogels

must be surfactant free. Therefore, we chose Soxhlet extraction technique for the purification of the Pt lyogels, which had been found to be useful in previous studies to remove excess surfactants from the surface of the nanoparticles.[52]

The aerogels obtained with and without Soxhlet cleaning were then characterized using FTIR spectroscopy. The FTIR spectra of the Pt aerogels and for pure oleic acid and oleylamine are shown in Figure 5B. The IR bands of oleic acid at 1706 cm⁻¹ can be attributed to carboxylic acid C=O stretching, at 2852 cm⁻¹ and 2920 cm⁻¹ can be assigned to symmetric and asymmetric stretching of –CH₂, respectively.[53] The weak band at 2671 cm⁻¹ is due to the stretching of the O-H group of the dimerized oleic acid in solid form. The IR band at 3005 cm⁻¹ can be assigned to *cis* stretching mode of the C–H bond in the –CH= group. In the case of oleylamine, the –NH₂ scissoring mode at 1593 cm⁻¹ and the symmetric and asymmetric stretching of –CH₂ at 2852 cm⁻¹ and 2920 cm⁻¹ can be derived clearly.[54, 55] The IR bands appearing in the range of 800 cm⁻¹ to 1500 cm⁻¹ can be assigned to –C–H rocking in alkyl chain, =C–H bending and C–O stretching, –CH₂ deformation and other complex combinations of different vibration modes. In the aerogels, the broad IR band in the range of 3300 cm⁻¹-3500 cm⁻¹ proves the presence of N-H bonding of the oleylamine with Pt.[54, 55] The strong FTIR bands appearing at 3031 cm⁻¹ and 3110 cm⁻¹ could be due to the stretching mode of the C–H bond adjacent to the –C=C.[54] However, after the Soxhlet cleaning of the lyogels, the amount of the surfactants is reduced, which can be seen from the FTIR spectra of the aerogels (after Soxhlet cleaning), where the intensity of the IR bands of the organic surfactants are much less in comparison to the aerogels without Soxhlet cleaning. It can be inferred that Soxhlet extraction is an effective technique to clean the lyogels from surfactants.

Heterogeneous catalytic activity of the aerogels. The asymmetric catalytic hydrogenation of α-keto esters using supported Pt catalyst modified by cinchona alkaloids, was first described by Orito.[45] This reaction was also found to be shape-sensitive. In our case we chose it as a test reaction for the investigation of catalytic activity and selectivity of the here developed Pt aerogels. A schematic drawing
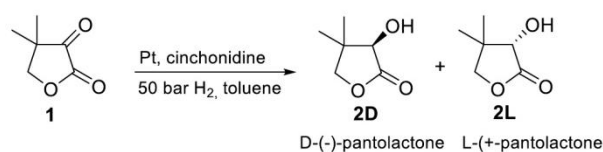
Figure 6. *Enantioselective hydrogenation of 4,4-dimethyldihydrofuran-2,3-dione (keto-pantolactone) to D- and L- pantolactone in presence of Pt as catalyst and cinchonidine as chiral modifier.*

of the catalytic reaction is demonstrated in Figure 6. Recently, the catalytic activity of Pt (100) and Pt (111) facets of specially prepared Pt/SiO₂ catalyst was described in literature, where 4,4-dimethyldihydrofuran-2,3-dione (keto-pantolactone) was employed as a substrate.[46] In the work mentioned in reference 46 an enantiomeric excess of 11-14% was observed in case of Pt (111) facets, which was higher than the result of Pt (100). The stereoselectivity was explained according to the density function theory (DFT) calculations where chinchonidine, employed as a chiral modifier, had a weaker interaction with the Pt (111) crystal facets. As a result, the aromatic ring of the alkaloid was not hydrogenated itself as fast as at the Pt (100) facets. Therefore it did not lose its feasibility for chiral induction. In our experiments, the high stirring speed of 700 rpm required, could not be applied due to the sensitivity of Pt lyogels on mechanical stress. Therefore the reaction mixtures were stirred at 100 rpm and at a pressure of 50 bar. The reaction time was also prolonged to 24 h. For comparison, a commercially available 5% Pt/Al₂O₃ catalyst (available for Orito reaction of ethyl pyruvate) was also investigated (see experimental section). The results of the catalytic experiments are shown in Table 1. All catalysts employed were active in the hydrogenation reactions with > 99**%** conversion of keto-pantolactone to D- and L-pantolactone. The highest enantiomeric excess (for the D isomer) of 9% was observed for the cube aerogels, whereas the same was 5% for the sphere aerogels. Hence, it can be inferred that the cube aerogels with (100) crystal facets are 1.8 fold more efficient in yielding stereo-selective isomers compared to the sphere aerogels. In addition, we have also measured the catalytic activity of the lyogels before Soxhlet cleaning. In that case enantiomeric excess of 3% and 2.5% was observed for the cube and sphere aerogels, respectively.

Catalyst	Conversion of keto-pantolacton [%]	Yield of 2D/L as enantiomer mixture [%]	Enantiomeric excess of 2D [%]
Pt cubes hydrogel	> 99	> 99	9
Pt spheres hydrogel	> 99	> 99	5
5% Pt/Al₂O₃ [i)]	> 99	> 99	41
5% Pt/Al₂O₃ [ii)]	> 99	> 99	38

Table 1. *Results of enantioselective hydrogenation employing Soxhlet cleaned Pt nanocube and nanosphere lyogels ([i)] 700 rpm, according to the procedure given in reference [46]; [ii)] 100 rpm), relative error in measurement 1-2%.*

These results clearly indicate that the Soxhlet cleaning indeed was effective in removing the organic surfactant from the surface of nanoparticles. It is to be noted that the enantiomeric selectivity of the Pt aerogels is comparatively low with respect to the reference catalyst but significantly higher than the measuring error of the method. Possible reasons for low enantiomeric excess values could be that i) the reaction was too slow due to diffusion limitation caused by the stirring speed of 100 rpm, ii) the chiral modifier could be hydrogenated itself to a higher extent in the meantime, iii) it is also known that, the size of the Pt nanoparticles has a decisive influence on the activity and selectivity of the hydrogenation of ethyl pyruvate.[56, 57] Possibly, the individual Pt nanocubes and nanospheres are still a bit too large for the higher selectivity. However, to the best of our knowledge, it is the first time that any enantiomeric excess is observed in a heterogeneous asymmetric catalytic hydrogenation caused by an unsupported, non-colloidal noble metal catalyst. Therefore, in future, it is worth to do further optimization of the catalysis reaction for example by varying the crystallite size of the linked nanoparticles of the aerogel.

4. Conclusions

In conclusion a new approach to obtain gels directly from colloidal organic solution of Pt nanocubes and nanospheres is demonstrated by controlled destabilization with N₂H₄.H₂O. Partial surfactant removal allows the coalescence of the individual nanocrystals to form networks which in turn generate the 3D macroscopic porous monolithic structure. In order to transfer the lyogels to aerogels, solvent exchange with acetone, followed by supercritical drying with liquid CO₂ was performed following Kistler's method. Microscopic characterizations prove the high porosity of the aerogels with pore diameters in meso to macroporous regimes. The aerogels from Pt nanocubes mostly exhibit (100) as the exposed crystals facets whereas the aerogels from Pt quasi-spheres exhibit various facets *e.g.* (100), (111) of fcc lattice systems. The aerogels have high BET specific surface areas which are in the similar order of magnitude as obtained from aqueous building blocks but are lightweight and highly macroporous. Furthermore, the Soxhlet extraction technique is found to be very much effective in removing residual organic surfactant molecules present on the surface of the aerogels. For the first time, an enantiomeric excess was observed in a catalytic hydrogenation using such type of material as catalyst. In addition, N₂H₄.H₂O is found to be effective reagent to obtain lyogels from other nanoparticles such as, Pd, Fe₂O₃ and Au-Fe₂O₃, which indicates the versatility of this gelation process from organic colloidal solution.

Acknowledgements

Notes

The authors declare no competing financial interest. The manuscript was written through contributions of all authors. All authors have given approval to the final version of the manuscript.

References

1   Wang, C.; Daimon, H.; Lee, Y.; Kim, J.; Sun, S., *J. Am. Chem. Soc.* 2007, **129**, 6974.
2   Qi, K.; Wang, Q.; Zheng, W.; Zhang, W.; Cui, X., *Nanoscale* 2014, **6**, 15090.
3   Yu, H.; Chen, M.; Rice, P. M.; Wang, S. X.; White, R. L.; Sun, S. H., *Nano Lett.* 2005, **5**, 379.
4   Garbarino, S.; Ponrouch, A.; Pronovost, S.; Gaudet, J.; Guay, D., *Electrochem. Commun.* 2009, **11**, 1924.
5   Ghosh, S.; Raj, C. R., *Catal. Sci. Technol.* 2013, **3**, 1078.
6   Chen, X.; Jiang, Y.; Sun, J.; Jin, C.; Zhang, Z., *J. Power Sources* 2014, **267**, 212.
7   Narayanan, R.; El-Sayed, M. A., *J. Phys. Chem. B* 2003, **107**, 12416.
8   Narayanan, R.; El-Sayed, M. A., *Nano Lett.* 2004, **4**, 1343.
9   Song, H.; Kim, F.; Connor, S.; Somorjai, G. A.; Yang, P. D., *J. Phys. Chem. B* 2005, **109**, 188.
10 Bratlie, K. M.; Lee, H.; Komvopoulos, K.; Yang, P.; Somorjai, G. A., *Nano Lett.* 2007, **7**, 3097.
11 Bigall, N. C.; Hartling, T.; Klose, M.; Simon, P.; Eng, L. M.; Eychmuller, A., *Nano Lett.* 2008, **8**, 4588.
12 Yin, A.-X.; Min, X.-Q.; Zhang, Y.-W.; Yan, C.-H., *J. Am. Chem. Soc.* 2011, **133**, 3816.
13 Tsung, C. K.; Kuhn, J. N.; Huang, W. Y.; Aliaga, C.; Hung, L. I.; Somorjai, G. A.; Yang, P. D., *J. Am. Chem. Soc.* 2009, **131**, 5816.
14 Lu, Y.; Jiang, Y.; Chen, W., *Nano Energy* 2013, **2**, 836.
15 Kang, Y.; Li, M.; Cai, Y.; Cargnello, M.; Diaz, R. E.; Gordon, T. R.; Wieder, N. L.; Adzic, R. R.; Gorte, R. J.; Stach, E. A.; Murray, C. B., *J. Am. Chem. Soc.* 2013, **135**, 2741.
16 Ren, J.; Tilley, R. D., *Small* 2007, **3**, 1508.
17 Ahmadi, T. S.; Wang, Z. L.; Green, T. C.; Henglein, A.; ElSayed, M. A., *Science* 1996, **272**, 1924.
18 Xia, Y. N.; Xiong, Y. J.; Lim, B.; Skrabalak, S. E., *Angew. Chem. Int. Ed.* 2009, **48**, 60.
19 Cheong, S. S.; Watt, J. D.; Tilley, R. D., *Nanoscale* 2010, **2**, 2045.
20 Chiu, C. Y.; Li, Y. J.; Ruan, L. Y.; Ye, X. C.; Murray, C. B.; Huang, Y., *Nat. Chem.* 2011, **3**, 393.
21 Narayanan, R.; El-Sayed, M. A., *J. Phys. Chem. B* 2005, **109**, 12663.
22 Lee, I.; Morales, R.; Albiter, M. A.; Zaera, F., *Proceedings of the National Academy of Sciences of the United States of America* 2008, **105**, 15241.
23 Cao, M.; Miyabayashi, K.; Shen, Z.; Ebitani, K.; Miyake, M., *J. Nanopart. Res.* 2011, **13**, 5147.
24 Liu, Y.; Jia, C. J.; Yamasaki, J.; Terasaki, O.; Schuth, F., *Angew. Chem. Int. Ed.* 2010, **49**, 5771.
25 Lopez-Sanchez, J. A.; Dimitratos, N.; Hammond, C.; Brett, G. L.; Kesavan, L.; White, S.; Miedziak, P.; Tiruvalam, R.; Jenkins, R. L.; Carley, A. F.; Knight, D.; Kiely, C. J.; Hutchings, G. J., *Nat. Chem.* 2011, **3**, 551.
26 Leventis, N.; Chandrasekaran, N.; Sotiriou-Leventis, C.; Mumtaz, A., *J. Mater. Chem.* 2009, **19**, 63.
27 Wittstock, A.; Neumann, B.; Schaefer, A.; Dumbuya, K.; Kuebel, C.; Biener, M. M.; Zielasek, V.; Steinrueck, H.-P.; Gottfried, J. M.;

Biener, J.; Hamza, A.; Baeumer, M., *J. Phys. Chem. C* 2009, **113**, 5593.
28 Liu, H.; Yang, Q., *J. Mater. Chem.* 2011, **21**, 11961.
29 Qin, G. W.; Liu, J.; Balaji, T.; Xu, X.; Matsunaga, H.; Hakuta, Y.; Zuo, L.; Raveendran, P., *J. Phys. Chem. C* 2008, **112**, 10352.
30 Tappan, B. C.; Steiner, S. A., III; Luther, E. P., *Angew. Chem. Int. Ed.* 2010, **49**, 4544.
31 Armatas, G. S.; Kanatzidis, M. G., *Nature* 2006, **441**, 1122.
32 Bigall, N. C.; Herrmann, A.-K.; Vogel, M.; Rose, M.; Simon, P.; Carrillo-Cabrera, W.; Dorfs, D.; Kaskel, S.; Gaponik, N.; Eychmueller, A., *Angew. Chem. Int. Ed.* 2009, **48**, 9731.
33 Bigall, N. C.; Eychmueller, A., *Philosophical Transactions of the Royal Society a-Mathematical Physical and Engineering Sciences* 2010, **368**, 1385.
34 Liu, W.; Rodriguez, P.; Borchardt, L.; Foelske, A.; Yuan, J.; Herrmann, A.-K.; Geiger, D.; Zheng, Z.; Kaskel, S.; Gaponik, N.; Koetz, R.; Schmidt, T. J.; Eychmueller, A., *Angew. Chem. Int. Ed.* 2013, **52**, 9849.
35 Liu, W.; Herrmann, A.-K.; Geiger, D.; Borchardt, L.; Simon, F.; Kaskel, S.; Gaponik, N.; Eychmueller, A., *Angew. Chem. Int. Ed.* 2012, **51**, 5743.
36 Liu, W.; Herrmann, A.-K.; Bigall, N. C.; Rodriguez, P.; Wen, D.; Oezaslan, M.; Schmidt, T. J.; Gaponik, N.; Eychmüller, A., *Acc. Chem. Res.* 2015.
37 Arachchige, I. U.; Brock, S. L., *J. Am. Chem. Soc.* 2006, **128**, 7964.
38 Mohanan, J. L.; Arachchige, I. U.; Brock, S. L., *Science* 2005, **307**, 397.
39 Sayevich, V.; Cai, B.; Benad, A.; Haubold, D.; Sonntag, L.; Gaponik, N.; Lesnyak, V.; Eychmüller, A., *Angew. Chem. Int. Ed.* 2016, **55**, 6334.
40 Herrmann, A.-K.; Formanek, P.; Borchardt, L.; Klose, M.; Giebeler, L.; Eckert, J.; Kaskel, S.; Gaponik, N.; Eychmueller, A., *Chem. Mater.* 2014, **26**, 1074.
41 Naskar, S.; Miethe, J. F.; Sánchez-Paradinas, S.; Schmidt, N.; Kanthasamy, K.; Behrens, P.; Pfnür, H.; Bigall, N. C., *Chem. Mater.* 2016, **28**, 2089.
42 Kistler, S. S., *Nature* 1931, **127**, 741.
43 Brunauer, S.; Emmett, P. H.; Teller, E., *J. Am. Chem. Soc.* 1938, **60**, 309.
44 Barrett, E. P.; Joyner, L. G.; Halenda, P. P., *J. Am. Chem. Soc.* 1951, **73**, 373.
45 Orito, Y.; Imai, S.; Niwa, S. J., *Synth. Org. Chem.* 1979, **37**, 173.
46 Schmidt, E.; Vargas, A.; Mallat, T.; Baiker, A., *J. Am. Chem. Soc.* 2009, **131**, 12358.
47 Yin, A.-X.; Min, X.-Q.; Zhang, Y.-W.; Yan, C.-H., *J. Am. Chem. Soc.* 2011, **133**, 3816.
48 Mahadik-Khanolkar, S.; Donthula, S.; Sotiriou-Leventis, C.; Leventis, N., *Chem. Mater.* 2014, **26**, 1303.
49 Standard NIST Bulk XRD pdf no Pt (03-068-2868).
50 Langford, J. I.; Wilson, A. J. C., *J. Appl. Crystallogr.* 1978, **11**, 102.
51 Chang, Y.-M.; Lu, I. T.; Chen, C.-Y.; Hsieh, Y.-C.; Wu, P.-W., *J. Alloys Compd.* 2014, **586**, 507.
52 Kozhevnikov, I. V., *Activation of light alkanes: Past and present.* Springer: 1998; Vol. 44, p 75.
53 Zhang, L.; He, R.; Gu, H. C., *Appl. Surf. Sci.* 2006, **253**, 2611.
54 Shukla, N.; Liu, C.; Jones, P. M.; Weller, D., *J. Magn. Magn. Mater.* 2003, **266**, 178.
55 Mourdikoudis, S.; Liz-Marzan, L. M., *Chem. Mater.* 2013, **25**, 1465.
56 Wells, P. B.; Wilkinson, A. G., *Top. Catal.* 1998, **5**, 39.
57 Jackson, S. D., Keegan, M.B.T., McLellan, P G.D., Meheux, A., Moyes, R. B., Webb, G., Wells, P. B., Whyman, R., Wills, J.,

96

Preparation and characterization of Catalysts V in Studies in Surface Science and Catalysis. Elsevier: Amsterdam, 1991; p 135.

97

Supporting Information

Porous Aerogels from Pt Nanocubes and Nanospheres Directly from Organic Colloidal Solution

S. Naskar,[a] A. Freytag,[a] J. Deutsch,[b] N. Wendt,[c] A. Koeckritz,[b] P. Behrens[c] and N. C. Bigall[a*]

[a]Institute of Physical Chemistry and Electrochemistry, Leibniz Universität Hannover Callinstraße 3A, D-30167 Hannover, Germany.

[b]Leibniz-Institut für Katalyse e.V. an der Universität Rostock, Albert-Einstein-Str. 29a, 18059 Rostock, Germany.

[c]Institute for Inorganic Chemistry, Leibniz Universität Hannover, Callinstraße 9, D-30167 Hannover, Germany.

*email: nadja.bigall@pci.uni-hannover.de
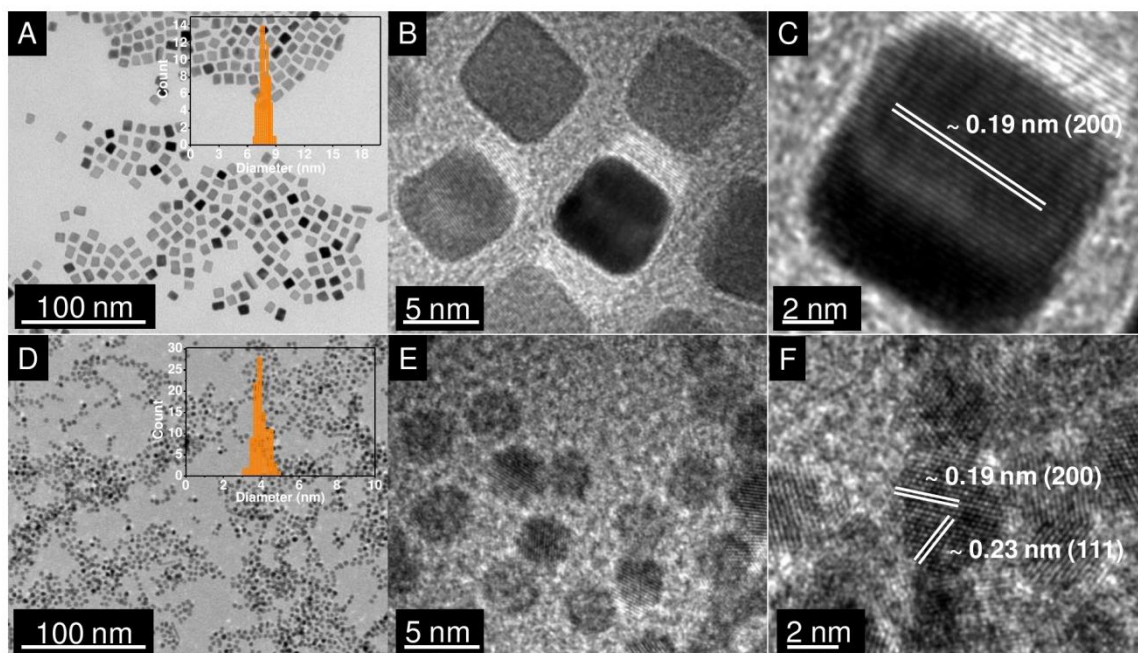
Figure SI-1. *TEM micrographs of the (A-C) Pt nanocubes and (D-F) the nanospheres in different magnifications. Insets of (A) and (D) are the size distribution of the Pt cubes and the spheres, respectively.*
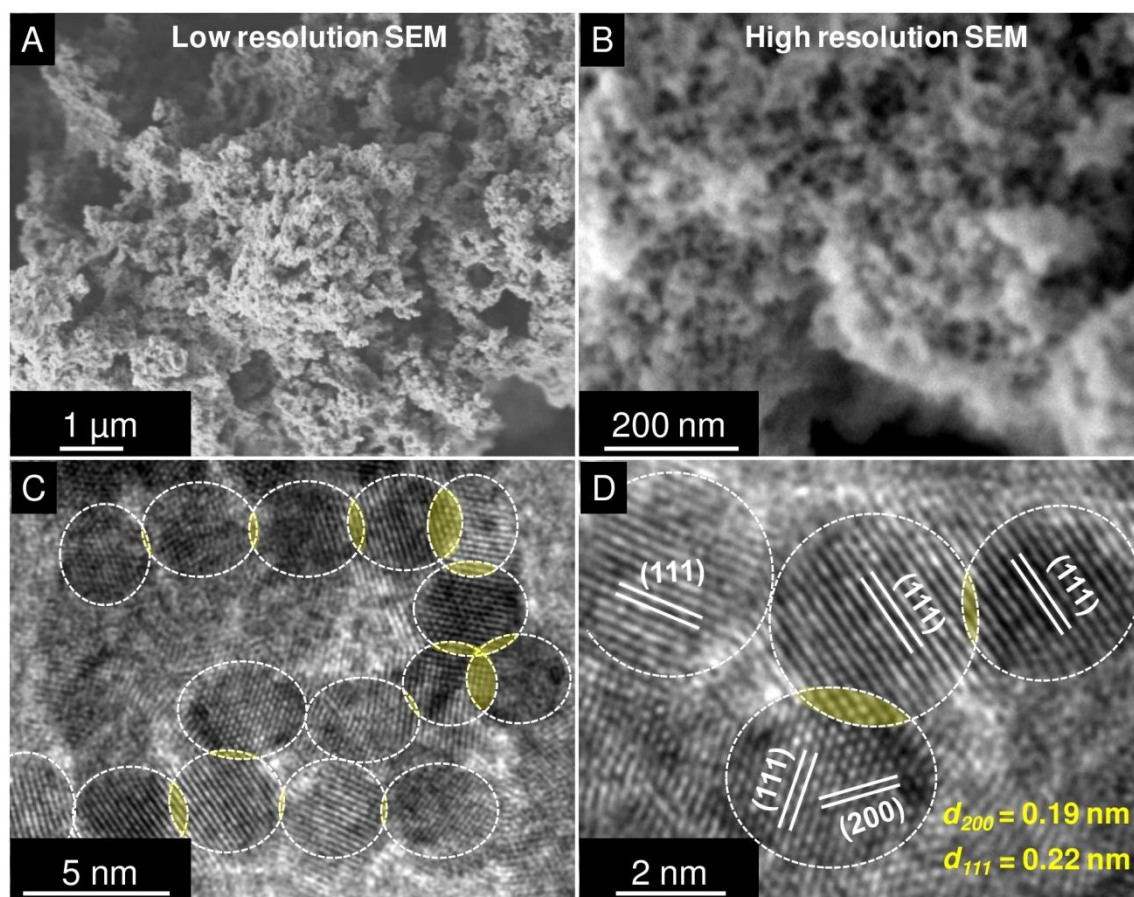
Figure SI-2. *(A) and (B) SEM micrographs of aerogels from Pt nanospheres in two different magnifications. The low resolution image proves the high porosity of the aerogel with pore diameters in the macroporous regime. High resolution SEM image shows the presence of pores inside the skeletal network with pore a diameter in the mesoporous regime. (C) and (D) HRTEM images of Pt nanospheres. Coalescence of the individual nanospheres forms the 3D network with (111), (200) as the exposed crystal facets in the gel network.*
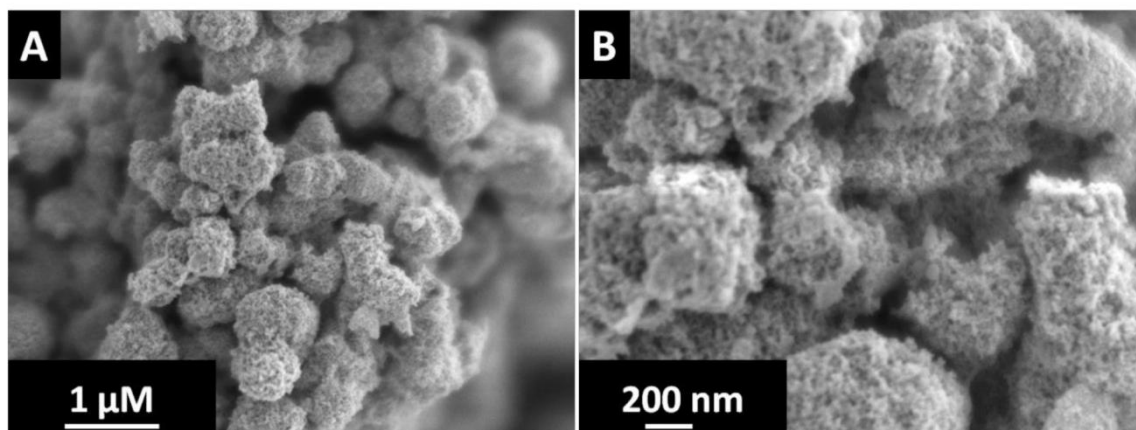
Figure SI-3. *SEM micrographs of the aerogels obtained with lower amount of $N_2H_4.H_2O$ ($N_2H_4.H_2O : Pt = 3 : 1.$)*
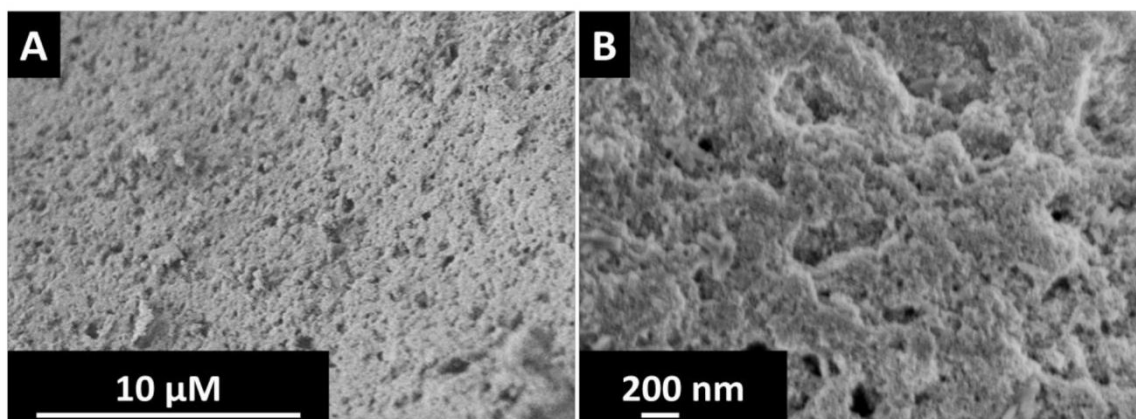
Figure SI-4. SEM micrographs of the xerogels obtained by drying hydrogels ($N_2H_4.H_2O : Pt = 10 : 1$) of Pt nanocube under ambient conditions in two different magnifications. The aerogels are highly compact with much less porosity compared to aerogels.
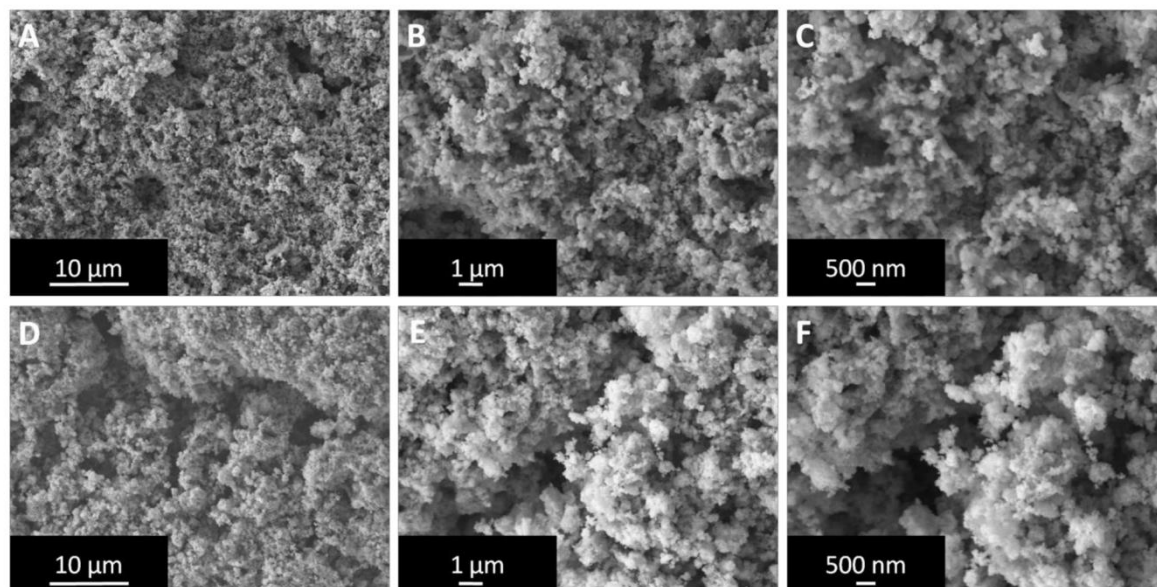
Figure SI-4. *SEM micrographs of the aerogels from (A-C) nanocubes and (D-E) nanospheres obtained after Soxhlet extraction. The aerogels exhibit interconnected cross-linked network structures with high porosity.*

4 Noble Metal Growth on CdSe and CdSe/CdS Nanoplatelets

4.1 Summary

As described earlier in the section 1.3.3, the fabrication of metal-semiconductor hybrid structures by growing Au, Pt, Pd, Ag, Ni or Co metal domains on II-VI semiconductors is well known in literature. However, the study of these nanoheterostructures is limited so far up to 0D (QDs) and 1D (nanorods) materials. Regarding the fabrication of the 2D hybrid structures employing NPLs as the semiconductor, no report was documented. In this context, the synthesis of hybrid NPLs are thought-provoking and of high significance, in terms of metal nucleation behavior, structural morphology, charge carrier separation, colloidal stability and applicability.

In the following two papers (sections 4.2 and 4.3), an in-depth study is dedicated to synthesize and characterize noble metal decorated CdSe and CdSe/CdS hybrid NPLs. Briefly, in section 4.2, the report describes the synthesis of Au, Pt and Pd decorated 5 monolayer (ML) thick CdSe hybrid NPLs with various structural morphologies. Here, site selectivity of noble metal growth is achieved by varying the types of metal precursors and the reaction parameters such as temperature, reaction time and molar precursor ratios. Structural characterizations of the hybrid NPLs by means of TEM prove that three noble metals have completely different growth behavior toward 5 ML thick CdSe NPLs. In the case of Au, when the Au precursor amount is less (with respect to Cd amount), the quasi spherical Au domains are found only at the corners of the NPLs, while with increased Au precursor concentration, the big spherical Au domains are found to be present at the shorter

side edges of the NPLs. In the case of Pt growth, the small quasi spherical Pt domains are found all around the edges of the NPLs, with pearl necklace type morphology. Interestingly, after Pd growth, the metal domains are found in plane of the CdSe NPLs with quasi rectangular morphology and the domains are present only at the shorter side edges of the NPLs. The orientation (in plane or sandwich type) and the morphologies (spherical or quasi rectangular) of the metal domains on the CdSe NPLs are proved by tilting the TEM sample grid under the electron beam of the microscope. The metal growth behavior is also experimented by varying the molar precursor ratios (of Cd and noble metals) and also by performing a time dependent (where samples were collected after regular interval of time and investigated with TEM analysis) study. At the end of this section, a comparative study of the photocatalytic activities of the hybrid NPLs on the degradation of methylene blue dye under visible light illumination is presented. The results clearly indicate that these materials are promising as catalyst for future photocatalytic reactions.

In section 4.3, the noble metal growth has been expanded to CdSe/CdS core/crown NPLs system. It has been shown that the metal nucleation behavior differs significantly when the CdSe core and the CdS crown dimensions are varied. Briefly, when the size of the CdSe core is very small, Au domains are found surrounding the edges of the NPLs, while in the case of NPLs with large CdSe core having small or large CdS crown, large Au islands are found at the middle of the NPLs together with small Au domains at the surrounding edges. Instead, Pt domains are only found at the surrounding edges of the NPLs, irrespective of the size of the CdSe core and CdS crown. The nucleation behavior of Au and Pt metals is also experimented by changing the sequence of the noble metal growth. For instance, Au domain growth on Pt decorated CdSe/CdS NPLs results in the formation of large Au island at the middle of the NPLs. On the contrary, Pt domain growth on Au decorated CdSe/CdS NPLs results in the formation of core/shell or alloy type morphologies. All the

unprecedented ternary and quaternary NPLs obtained are characterized by STEM-EDXS analysis to confirm the local distribution of the elements in the hybrid structures.

In the second part of section 4.3, the hybrid NPLs are transferred to aqueous solution *via* ligand exchange reactions by employing 11-mercaptoundecanoic acid (MUA) and are subsequently tested for photocatalytic H_2 gas generation reactions. Under the white light irradiation all the hybrids NPLs show better performance than the pure NPLs without any metal domains. The highest efficiency observed is ~19.3% in case of the Pt decorated hybrid NPLs with large CdSe core and large CdS crown. Furthermore, a detailed discussion is included to justify the observed differences in the catalytic activities and the possible ways to further improve the current observed efficiency.

4.2 Site-selective noble metal growth on CdSe nanoplatelets

Suraj Naskar, Anja Schlosser, Jan F. Miethe, Frank Steinbach, Armin Feldhoff and Nadja C. Bigall*

Site-Selective Noble Metal Growth on CdSe Nanoplatelets

Suraj Naskar,[‡] Anja Schlosser,[‡] Jan F. Miethe, Frank Steinbach, Armin Feldhoff, and Nadja C. Bigall*

Institute of Physical Chemistry and Electrochemistry, Leibniz Universität Hannover, Callinstraße 3A, D-30167 Hannover, Germany

Ⓢ *Supporting Information*

ABSTRACT: We report on a synthesis procedure to achieve site-selective growth of noble metal domains on CdSe nanoplatelets. The novel morphological properties of the resulting metal–semiconductor nanoheteroplatelets are characterized by transmission electron microscopy, UV–vis absorption, photoluminescence emission, X-ray photoelectron spectroscopy, and by X-ray diffractometry. By variation of the synthesis parameters, several different morphologies can be achieved: depending on the noble metal and the type of precursor, the growth of Au, Pt, and Pd domain takes place at the corners or edges, around or only at the two shorter edges of the rectangular sheet. This novel kind of hybrid nanoheterostructure might find future applications in photocatalysis, chemical sensing, or fabrication of photovoltaic devices.
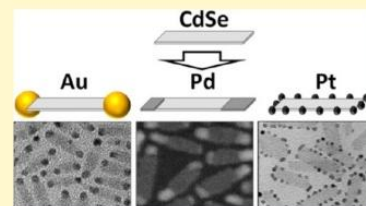
1. INTRODUCTION

Over the past decades, an extensive research effort has been dedicated to the synthesis of hybrid metal–semiconductor nanoheterostructures in order to manipulate the combined properties of metal and semiconductor domains in the same substance. As a result, a large variety of different nanoheterosystems has been reported with many different material combinations ranging from CdSe,[1–14] CdSe/CdS,[15–17] CdS,[3,18,19] PbTe,[20] PbSe[21] to TiO₂,[22] Cu₂ZnSnS₄,[23] and many more for the semiconductor domain,[24–27] and from Au, Ag, Pt, and Pd to Co, Fe, Ni, and so forth, for the metal domain. In-depth kinetic studies were conducted in order to investigate the fluorescence quenching during the Au growth on the CdSe/CdS system.[28] Furthermore, photoinduced versus thermal growth mechanism of Au on semiconductor nanorods were compared by Banin's and Shevchenko's groups.[28,29] Additional investigations focused on the assembly of nanoheterostructures by exploiting the so-called nanowelding approach connecting the structures via the Au domains.[30] The great advantage of metal–semiconductor nanoheterostructures is the ultrafast electron transfer and charge carrier separation at the metal semiconductor interface. Due to these physical properties, a large variety of possible applications exists, such as pollutant degradation, H₂ gas generation, and efficient photocatalysis (e.g., photocatalytic water splitting).[5,7,18,23,31–33] The nanoheterosystems reported include spherical, rod, and multipod geometries for the semiconductor domain by now. The expertise nowadays goes so far that in some cases, the metal domain could be grown site selectively at both ends, one end, or at the side of semiconductor nanorods.[11,15,16,18,27,30]

Recently, quasi 2D anisotropic nanoplatelets (NPLs) from various semiconductor materials, e.g., CdSe, CdSe/CdS/CdZnS, ZnSe/ZnS, PbSe/PbS (core/shell), CdSe/CdS (core/crown), CdSe/CdTe (core/crown), of few monolayer thicknesses have drawn much attention of the scientific world due to their unique optical properties such as extremely narrow

emission band widths (full width at half-maximum: fwhm), ultrafast radiative fluorescence lifetimes, and remarkably high quantum yields.[34–40] Assembled arrangements of such NPLs are discussed for several exciting applications such as polarized light emitters and electroluminescence emitters.[41–43] Furthermore, room-temperature lasing with low energy thresholds has already been reported.[44,45] Regarding nanoheterostructures, however, there is yet a lack of studies about the selective growth of metal compartments on such quasi 2D II–VI semiconductor NPL systems, on which we therefore focus in this work. Here we present simple synthetic strategies for regioselective growth of noble metal domains (Au, Pd, and Pt) on quasi two-dimensional, 5 monolayer (ML) thick CdSe NPLs. Our findings are that these different types of metal exhibit completely different growth behavior. The effect of metal precursors and different reaction temperatures on the morphology and growth behavior is presented. Depending on the reaction conditions and depending on the materials, we are able to fine-tune the morphology in various appearances site selectively: at the corners, at both short edges, and around all edges of the rectangular NPLs (see Scheme 1), with the metal domains being quasi spherical or flat in shape.

2. EXPERIMENTAL SECTION

Reagents. Cadmium nitrate tetrahydrate Cd(NO₃)₂·4H₂O (99.999%), cadmium acetate dihydrate Cd(OAc)₂·2H₂O (98.0%), gold(III) chloride AuCl₃ (99%), platinum(II) acetylacetonate Pt(acac)₂ (97%), platinum tetrachloride PtCl₄ (99%), palladium acetate Pd(OAc)₂ (98%), sodium myristate (>99%), dodecylamine (DDA, 98%), 1-octadecene (90%) (ODE), oleic acid (90%), oleylamine (80–90%), ethanol (99.5%), toluene (99.7%), *n*-hexane (≥99%), and acetone (≥99%) were purchased from Sigma-Aldrich. Selenium powder 200 mesh (99.999%) and palladium acetylacetonate Pd(acac)₂

107

Article

Scheme 1. Morphologies of Noble Metal Domains on 5 ML Thick CdSe NPLs As Presented in This Work
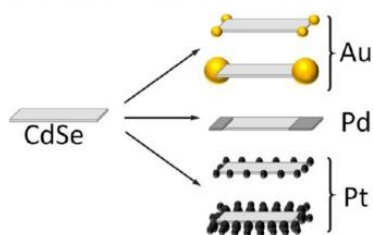
(34.7% Pd) were purchased from Alfa Aesar. Nitric acid (>69%) and hydrochloric acid (>37%) were purchased from Fluka.

Synthesis of 5 ML Thick CdSe NPLs. The 5 ML thick CdSe NPLs were synthesized after minimal modification of the method described by Tessier et al.[39] Briefly, a total amount of 340 mg $Cd(myr)_2$ (0.6 mM) together with 28 mL ODE were mixed in a 50 mL three-neck round-bottom flask and degassed under vacuum in a Schlenk line at 100 °C for 1 h with sustained stirring. This process yielded a clear solution of cadmium myristate dissolved in ODE. Under argon flow, the temperature of the solution was increased to 250 °C. Then 2 mL of 0.30 mM Se (24 mg) from the previously prepared stock solution was quickly injected into the mixture. One minute after the selenium injection, 240 mg (0.9 mM) of $Cd(OAc)_2 \cdot 2H_2O$ was added to the mixture. The reaction was carried out at a constant temperature of 250 °C for 10 min. Finally, 1 mL of oleic acid was injected into the solution, and the reaction mixture was cooled to room temperature by removing the heating mantle. This synthesis produces 5 ML thick CdSe NPLs along with some cubes and spherical CdSe nanoparticles. The whole product was transferred to a centrifuge vial. A 30 mL mixture of n-hexane/ethanol = 3:1 was used to separate the NPLs from the CdSe cubes and spherical nanoparticles. The solution was then centrifuged at 3800g (rcf) for 15 min. The supernatant mostly containing CdSe quantum dots was discarded, and the precipitated 5 ML thick CdSe NPLs were dispersed in 3 mL of toluene.

Room-Temperature Au Growth on 5 ML CdSe NPLs Following a Modified Method As Described by Mokari et al. A stock solution of the Au precursor was prepared by dissolving 10 mg of $AuCl_3$ and 100 mg of DDA in 10 mL of toluene. The mixture was then sonicated in an ultrasonic bath for 5 min. A yellow colored solution of the Au−DDA complex was obtained. CdSe NPLs solution (in toluene) of 22.1 mM Cd ion concentration (calculated from AAS) was used throughout the whole reaction. One hundred microliters of the CdSe NPLs solution, along with 1 mL of toluene, was placed into five separate 8 mL vials. Afterward, a defined amount of Au precursor (20, 40, 70, 100, and 120 μL leading to Cd/Au molar precursor ratios of 21:1, 10.5:1, 6:1, 4.2:1, and 3.5:1, respectively) was added, and the reaction was continued for 30 min under constant stirring; the color of the solution changed to dark brown depending on the amount of Au precursor added. Subsequently, 500 μL of acetone was added to each vial (from 1 to 5) to precipitate the nanoparticles. The products were centrifuged at 3800 rcf for 10 min and finally dispersed in 1 mL of toluene.

In order to see the effect of presence of ambient light irradiation on the Au growth, we did another set of reaction in complete darkness, maintaining all the reaction parameters

exactly the same as before, but we did not observe any morphological difference upon ambient light irradiation or in the dark (not shown).

Generalized Synthesis Route for Metal Domain Growth. The stock solution of 22.1 mM (Cd ion concentration) CdSe NPLs and a calculated amount of metal precursor (for example, for a precursor molar ratio of Cd/M = 1:5, 0.0157 mM of the solid metal precursor and 142 μL of the CdSe NPLs solution, and in the case of Cd/M = 20:1, instead of solid metal precursor, the required amount of a metal precursor solution, prepared by dissolving 0.005 mM of the metal precursor in 2 mL of ODE, was used) were placed together with 50 μL of oleylamine and 7.5 mL of ODE into a reaction flask. The mixture was then degassed for 30 min at 50 °C. After degassing, the temperature of the solution was increased to the reaction temperature (need to be adjusted for each metal) under N_2 flow, and the reaction was kept at this temperature for 2.5 h. The mixture was cooled to room temperature by removing the heating mantle, and 30 mL of isopropanol were added. The solution was centrifuged at a speed of 3800g (rcf) for 15−20 min. The precipitate was dispersed in 2 mL of toluene. If the reaction was carried out at room temperature, the solution was not degassed. In this case, the metal precursor and 50 μL of oleylamine were mixed and sonicated for 20 min before the addition of the 5 ML CdSe NPLs solution. After 1 h, the reaction was quenched by adding 7.5 mL of acetone and precipitating the nanoparticles by centrifugation.

Parameters for Au Domain Growth. For Au growth on the 5 ML CdSe NPLs, $AuCl_3$ was used as the Au precursor. The room-temperature reaction was carried out (described above) with variable molar precursor ratio Cd/Au = 20:1 to 1:30. In this case, the metal precursors could be easily dissolved by ultrasonication producing a yellowish solution. The product solutions in toluene were dark brown and colloidally stable.

Parameters for Pd Domain Growth. For optimum Pd growth on the CdSe NPLs, the generalized synthesis route was followed with $Pd(OAc)_2$ as the metal precursor at a reaction temperature of 90 °C. The reaction procedure was repeated for variable molar precursor ratios of Cd/Pd = 20:1 to 1:20 (however, for molar ratios of 1:20, many Pd nanoparticles formed along with the nanoheteroplatelets (not shown), and therefore, we recommend rather to use ratios of 1:5). The workup procedure was the same as before.

Palladium acetylacetonate was unsuitable for the nanoheterostructure growth at 90 °C because most of the NPLs were found without any Pd domain and additionally results aggregation of the NPLs (not shown). Furthermore, it should be noted that Pd growth at room temperature was not possible using $Pd(OAc)_2$ and $Pd(acac)_2$ as precursors, probably due to a higher activation energy for the Pd reduction.

Parameters for Pt Domain Growth. Pt growth on 5 ML CdSe NPLs was carried out using $Pt(acac)_2$ as the metal precursor at a reaction temperature of 130 °C. The experiment was done with variable precursor molar ratio of Cd/Pt ranging from 20:1 to 1:30, following the synthetic route as described in the section Generalized Synthesis Route for Metal Domain Growth. The product solution was found to be stable for several weeks without any agglomeration.

It should be noted that also $PtCl_4$ was investigated as a Pt precursor. However, during the reaction no Pt growth was observed, even at 130 °C reaction temperature, so that this

108

precisor was found to be unsuitable for growing metal domains on the 5 ML CdSe NPLs.

Room-temperature growth also did not lead to metal growth because neither $PtCl_4$ nor $Pt(acac)_2$ could be dissolved in ODE at this low temperature.

Atomic Absorption Spectroscopy. The Cd ion concentration of the CdSe NPLs solution was determined by atomic absorption spectroscopy (AAS) using a Varian AA140 instrument.

Transmission Electron Microscopy. The morphologies of the nanoheterostructures and NPLs were investigated by transmission electron microscopy using a FEI Tecnai G2 F20 TMP (C_s = 2 mm, C_C = 2 mm), equipped with a 200 kV field-emission gun. Micrographs were taken in bright-field and in high-angle annular dark-field scanning transmission electron mode. The use of a single-tilt specimen holder (FEI, CompuStage Single-Tilt Holder) enabled a tilting of the sample from 0° to 60°. The HAADF micrographs in Supporting Information Figure SI-7D,F were obtained at 200 kV on a JEOL JEM-2100F UHR (C_s = 0.5 mm, C_C = 1.2 mm) with field-emission gun. Prior to TEM grid preparation each sample was purified 5 to 6 times by precipitating with ethanol (CdSe NPLs) or isopropanol (heterostructures) followed by centrifugation and redispersion in toluene. Subsequently, 10 μL of the purified sample were drop-casted on a carbon-coated copper TEM grid.

Spectroscopic Characterization. Absorbance and extinction spectra of the samples were recorded using an Agilent Cary 5000 absorption spectrophotometer. PL emission spectra of the samples were recorded using a Horiba Fluoromax-4 spectrometer. All the absorbance, extinction, and emission spectra of the samples were measured in a 1 cm quartz cuvette using toluene (UV–vis spectroscopy grade) as solvent.

X-ray Diffraction. The X-ray diffraction pattern of the sample was measured out using a Bruker D8 Advance in reflection mode. The samples were prepared by drop-casting 100 μL of a concentrated NPLs solution in toluene on a single crystal silicon carrier.

X-ray Photoelectron Spectroscopy. Concentrated solutions of Pd nanoparticles, 5 ML CdSe NPLs, and Pd decorated CdSe nanoplatelets in toluene are dried on 2 cm × 1 cm silicon wafer before inserting them to the sample holder of Leybold Heraeus XPS analyzer. The samples were incubated in vacuum (10^{-8} mbar) and a Mg $K\alpha$ X-ray beam was used as the excitation source. The raw data from XPS analysis was fitted using XPS 41 software.

3. RESULTS AND DISCUSSION

First, we have synthesized 5 ML thick CdSe NPLs of lateral dimension in length 31 nm ± 3.5 nm and in width 7.9 nm ± 1.3 nm following the synthesis procedure of Tessier et al. with slight modification (see Supporting Information Figure SI-1).[39] On these 5 ML thick CdSe NPLs, we have site selectively grown Au, Pd, and Pt domains. In our growth procedure the Au precursor ($AuCl_3$) in the presence of oleylamine was dissolved in 1-octadecene. A calculated amount of CdSe NPLs was added to this mixture, and the reaction was carried out for 1 h at room temperature. The Cd/Au precursor molar ratio could be changed up to 1:10 in order to yield larger Au domains, without any agglomeration. The exact experimental details together with the findings from more varied parameters are discussed in the Experimental Section. Transmission electron microscope (TEM) micrographs in overview and in higher magnification

are shown in Figure 1A and B, respectively. From these micrographs, it can be derived that under these synthetic
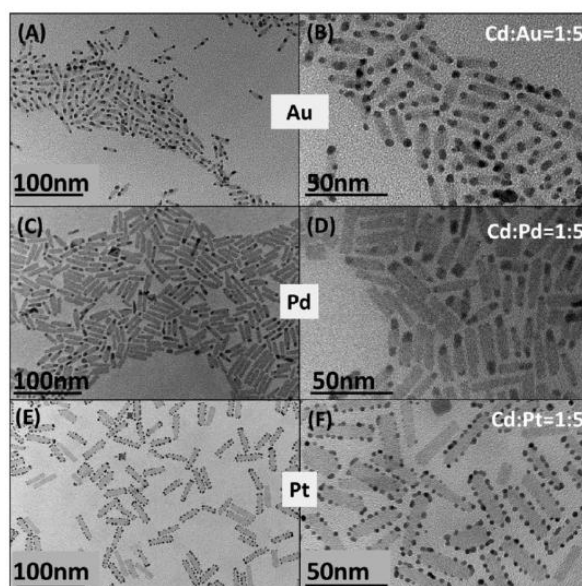

Figure 1. TEM micrographs of Au, Pd, and Pt growth on 5 ML CdSe NPLs in the presence of oleylamine with precursor molar ratios of Cd/M = 1:5 in octadecene.

conditions, the growth takes place quasi spherical at the shorter edges of the NPLs and that the Au domain size is around 5.0 nm ±0.6 nm. Instead, by following Mokari's method[2] with little modification (see Experimental Section), Au growth took place as small domains at the corners of the NPLs. However, by following Mokari's route, the nanoparticles were found to be cross-linked via the Au domain already at quite low Au precursor concentrations, limiting the possibility of higher Cd/Au precursor ratios and hence the Au domain sizes achievable (see Figure SI-2 in the Supporting Information). Interestingly, neither by following Mokari's nor using our new synthesis procedure, were the morphologies of the Au domains similar to the Au domain growth as was observed by Liu et al. on CdSe nanobelt structures (namely, the appearance of gold domain all over the belt surface), which also display colloids with one-dimensional quantization.[46] This group exploited the growth of noble metal domains in order to detect lattice defects in their nanobelt structures with slight differences in the precursor chemicals. If we can adopt their presumption that Au preferably grows at the lattice defect sites, we might conclude that in the case of NPLs, the defect sites are rarely present on the surface and are located mainly at the corners (and edges) of the NPLs which are intrinsic defect points.

Other works (on nanoheterostructures from different semiconductor domain shapes) correlate the appearance of gold domain to the selenium-rich sites of the semiconductor nanoparticles.[2,5,27] This argument also explains the appearance of the gold domains at the edges or corners of the CdSe NPLs. However, both explanations do not entirely explain the growth behavior of Au at the short edges for larger Au precursor amounts, which we observe. It is possible that here also nucleation starts at the corners (in agreement with these previous works), and due to the close proximity of the corners,

the Au domains fuse to form a larger domain at the short edges of the NPLs.

Upon tilting the sample substrate in the electron beam inside the transmission electron microscope (see Figure 2 top), we
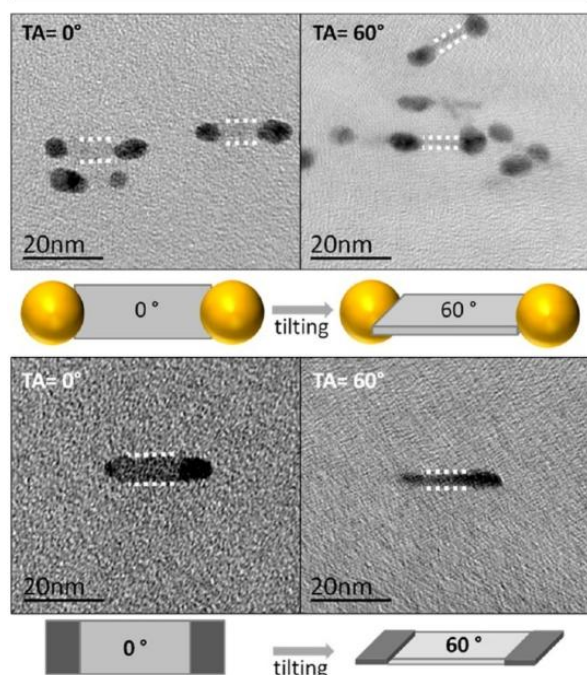

Figure 2. (top) Bright-field TEM micrographs of Au domains on 5 ML CdSe NPLs with different tilt angles (TA) in the electron beam TA: 0° (left) and 60° (right) and (below) schemes derived from the TEM observations. (bottom) TEM micrographs of Pd domains on 5 ML CdSe NPLs with 0° and 60° tilt angles (left and right, respectively) and (below) schemes derived from these observations. The white dotted lines have been included to guide the eye.

observe a narrowing of the CdSe compartment projection, which is in good agreement with the projection of the thin sheet under tilting to higher angle. Regarding the metal compartments, we do not observe significant changes in the quasi spherical appearance of the Au domains. Furthermore, the connection of the NPL to the Au compartments is mainly

found in the center of the Au spheres (see scheme at the top of Figure 2).

The second investigated noble metal was Pd. The Pd domains were grown following our new synthesis route at 90 °C reaction temperature using palladium acetate as precursor. In Figure 1C and D, TEM micrographs of the resulting nanoheterostructures with Cd/Pd = 1:5 molar precursor ratio are shown in two different magnifications. The Pd growth took place apparently on most (≈71%) of the 5 ML CdSe NPLs. Similar to the case of Au growth, large Pd domains were mostly found at the shorter edges of the sheets. The large Pd domains had side lengths of ≈5 to 7 nm, which is almost the same as the width of the NPL. These large domains had quasi rectangular morphologies, which were found to be flat and only marginally thicker than the platelets upon tilting the sample substrate in the electron beam of the TEM to 60° (see Figure 2 bottom). For the CdSe semiconductor NPLs, it is well-known that the presence of acetate ligands is necessary for the lateral extension of the NPLs.[39,47] We assume that the acetate ligands from the palladium acetate precursor might play a similar role and might induce the in-plane Pd domain growth on the shorter edges of the 5 ML CdSe NPLs. Additionally, very small Pd domains were observed both at the longer and shorter edges of the sheets, with diameters around 1 nm (see the high-angle annular dark field (HAADF) scanning transmission electron microscopy (STEM) micrographs in Figure SI-4 in the Supporting Information). A statistical analysis of the TEM micrographs reveals that ≈15% of the NPLs have only one large Pd domain at one short edge, and ≈38% of the NPLs have large Pd domains at both of their short edges; however, ≈18% exhibit very small Pd domains distributed randomly around the NPLs.

The growth behavior was investigated by a time-dependent study of Pd growth on 5 ML CdSe NPLs with a precursor molar ratio of Cd/Pd = 1:5 (TEM micrographs are shown in Figure SI-5 in the Supporting Information). We observed that after 20 min of the reaction, small Pd domains ≈1 to 2.5 nm had formed at the corners and the shorter edges of the NPLs. With increasing time of the reaction, the size of the quasi flat Pd domains had also increased. After 150 min of the reaction, quasi flat Pd domains were observed with average side lengths from 5 to 7 nm, which were located only at the short edges of the NPLs. In order to see the morphology of the nanoheterostructures at significantly lower amounts of the Pd precursor, the synthesis was carried out with a molar precursor ratio of Cd/Pd = 20:1. In appearance, the Pd domains seem similar as in the case of Au (Figure SI-6 in the Supporting
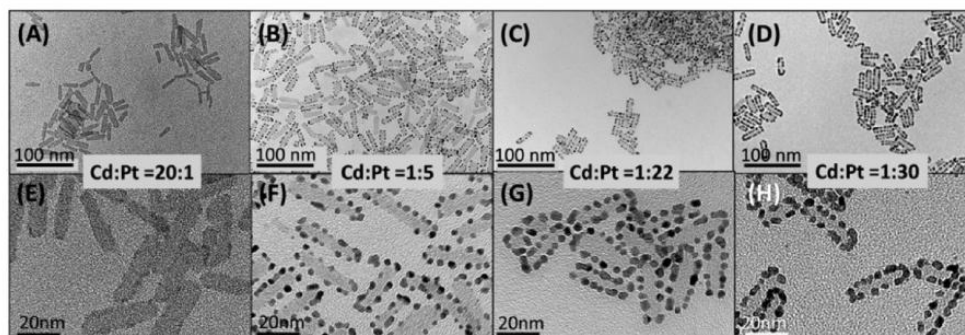

Figure 3. TEM micrographs of Pt domains on 5 ML CdSe NPLs for different Cd/Pt precursor molar ratios ranging from 20:1 to 1:30. (A) to (D) in lower magnification and (E) to (H) in higher magnification.

Information), and the Pd domains were found to grow mainly at the corners of the NPLs.

We furthermore expanded the noble metal growth to Pt by properly adapting the synthetic conditions (details in the Experimental Section). Namely, Pt growth was observed upon changing the precursor to platinum acetylacetonate and raising the reaction temperature to 130 °C. Surprisingly, under these conditions, nanoheteroplatelets formed with the Pt domains being located at all edges around the NPLs (Figure 1 E and F). For a molar precursor ratio of Cd/Pt = 1:5, the Pt domains had an average diameter of 2.8 nm ±0.4 nm. Because this growth behavior around both short and long sides seemed to be in contrast to the observations in the case of Au or Pd, we investigated whether the differences in site-selective growth for Pt also takes place at different noble metal concentrations varying the precursor molar ratio of Cd/Pt from 20:1 to 1:30 (see Figure 3). For the low noble metal precursor content (20:1), Pt domains are very small and hence not so easily distinguishable from the semiconductor material.

By increasing the Pt precursor content up to a Cd/Pt molar ratio of 1:30 (see Figure 3D), the Pt domains can be found at all edges of the NPLs. The average size of the Pt domains for Cd/Pt = 1:30 was 3.5 nm ±0.2 nm. In a previous work, Elmalem et al. have investigated Pt-decorated CdSe nanorods in aqueous solution using $PtCl_4$ as the metal precursor.[9] Here, depending on the pH of the medium, Pt was observed to grow all over the surface of the nanorods. Even at lower pH = 4, the nanorods start to aggregate and produce a porous nanonet structure. Habas et al. and Lawrence et al. have reported the synthesis of one-sided (match stick) and two-sided (dumbbells) Pt-tipped CdSe@CdS nanorods using $Pt(acac)_2$ as the metal precursor and 225 °C as the reaction temperature.[16,18] With increased amount of the same precursor, Pt was observed to grow all over the surface of the CdSe nanowires.[27] However, in our experiments with CdSe NPLs, for all investigated molar ratios, the Pt domains were distributed almost regularly around the NPLs edges and are separately present from each other. We conducted further investigations on the time-dependent growth behavior of Pt on the CdSe NPLs with precursor molar ratio of Cd/Pt = 1:22. In Figure 4, TEM micrographs after different reaction times (from 20 to 210 min) are shown. It can be observed that after 20 min of the reaction, tiny Pt domains have

grown at the corners as well as all around the side edges of the NPLs. Seventy-five min after the reaction starts, many equally sized larger Pt domains have formed. Additionally, still very small Pt domains can be found. We attribute this to a not yet complete growth. Instead, after 150 min, the sizes of the Pt domains are mostly equal. Finally, after 210 min, nearly all of the Pt domains exhibit similar sizes and regular distances. On average, we counted 16 Pt domains per NPL. The shape of the Pt domains has changed from almost spherical at the beginning to dentoid. Surprisingly, also after long reaction times, we did not observe a coagulation of the domains to form larger ones as in the case of Au. Furthermore, all the particles were separately present, and no cross-linking effect via the metal domains was observed. The average distance between the dentoidic domains (Figure 4 D) was measured to be 1.1 nm ±0.5 nm. We presume that Pt has a lower mobility along the edges of the NPLs so that growth takes place at the nucleation sites only. Generally, differences in the growth of noble metal domains from the different materials may be attributed to the different reactivities of the materials and the anionic ligands (anionic part of the metal precursor) present in the respective systems.

In order to see the direct attachment of the metal domain on the CdSe NPLs and to focus on the deeper structural analysis, we have performed HAADF-STEM and HRTEM characterization of the nanoheteroplatelets. However, unfortunately the extremely thin NPLs (≈1.5 nm) turned out to be sensitive to the electron beam under the illumination conditions necessary for HRTEM. Moreover, the situation is complicated by bending of the NPLs, when decorated with Au or Pt and the high contrast difference of the metal domain and CdSe semiconductor part, which did not allow to resolve both the lattice planes (i.e., metal and semiconductor) at the same time (see Figure SI-7 in the Supporting Information). This difficulty of identifying the interface of the metal semiconductor nanoheterostructures in HRTEM due to different orientation and due to the contrast difference have also been faced by previous researchers.[2,5,7,11] However, from the HRTEM and from the HAADF-STEM micrographs, it can be inferred that the metal domains are directly attached to the CdSe semiconductor part.

All nanoheterostructures were characterized also by optical absorbance (see Figure 5A,B) and emission spectroscopy. Upon noble metal growth we observe nearly complete fluorescence quenching in all cases (see Figure SI-8 in the Supporting Information), which is an indication that the noble metal domains grow on nearly all NPLs leading to a fast charge carrier separation from the semiconductor NPLs to the metal domains. This in turn proves that those NPLs, which show no apparent metal domain in TEM analysis, might indeed contain very small metal domains that are not easily detectable by TEM analysis but are able to quench the photoluminescence. Also the absorbance spectra measured at the same Cd concentrations differ significantly for the different metals (see Figure 5B). For Pd- and Pt-decorated CdSe NPLs, the characteristic maxima of CdSe NPLs around 552 nm (heavy hole electron: hh-e) and 518 nm (light hole electron: lh-e) are still present but weaker and broader (especially for Pt) than in the pure CdSe NPLs. Additionally, a background absorption occurs which is probably due to the metal absorption. In case of CdSe/Au NPLs, the characteristic transitions from CdSe NPLs are not recognizable in the absorption spectra. These observations are quite similar to those of Mokari et al. for Au on CdSe rods and tetrapods—namely, that the band structure of the nanoheterostructure is altered in comparison to that of the
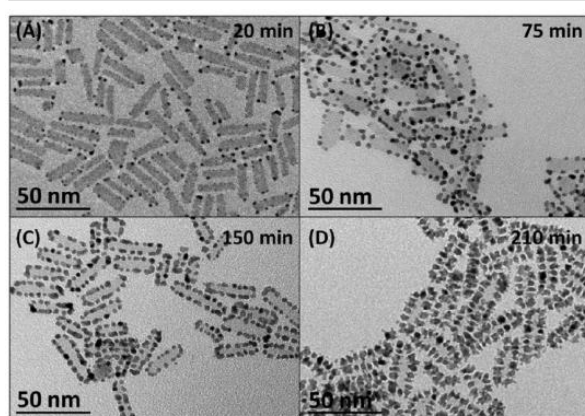

Figure 4. Time-dependent growth of Pt on 5 ML CdSe NPLs: after 20 min (A), 75 min (B), 150 min (C), and 210 min (D) of reaction time, respectively.
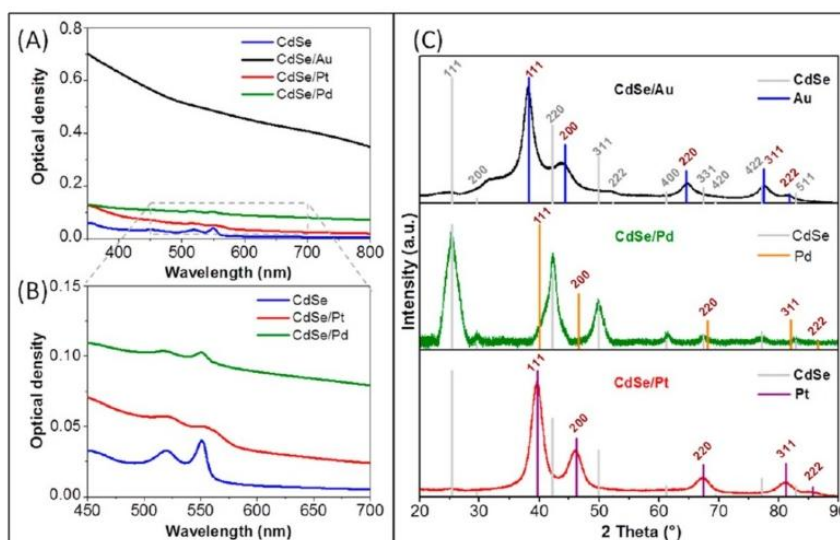
Figure 5. Absorbance spectra of nanoheteroplatelets with the same cadmium ion concentration [0.02 mM] for samples synthesized with a Cd/M (Au/Pd/Pt) molar precursor ratio of 1:5 in all cases. (A) overview and (B) zoom. (C) XRD diffractograms of nanoheteroplatelets from molar precursor ratios of Cd/M = 1:5, (top) CdSe/Au, (center) CdSe/Pd, (bottom) CdSe/Pt NPLs. The gray lines indicate the positions and relative intensities for CdSe, and the colored lines indicate the positions and relative intensities of the respective noble metal in bulk according to the literature.[48]

semiconductor alone.[2] The difference in absorption behavior for the three different metal domain materials can be partly explained by the differences in metal amounts and orientation morphology on the CdSe NPLs. The Au domains are very large so that the optical properties of the corresponding nanoheterostructures exhibit a strong metal absorbance background and the CdSe transitions are not recognizable any more. Instead, the volumes of the Pt domains are smaller, and hence have less effect on the semiconductor compartments, so that here the transitions can still be seen even though they are broadened and reduced in oscillator strength. The smallest metal domain volume is for Pd. For these heterostructures, the transitions caused by the semiconductor are most pronounced and most sharp for all the three heterostructure systems. Here, it can be clearly seen that by increasing the Pd and Pt domain sizes, the semiconductor absorption maxima are more and more broadened and weakened, as described above, which strengthens our hypothesis that the amount of metal influences the electronic structure of the semiconductor domain. The changes in extinction spectra upon Pd and Pt growth on CdSe NPLs after different reaction time are shown in Figure SI-9 and Figure SI-10 in the Supporting Information, respectively.

The crystallographic characterization of the Au, Pd, and Pt on CdSe NPLs heterostructures with precursor molar ratio of Cd/M = 1:5, as obtained from powder X-ray diffractometric (XRD) measurements, is shown in Figure 5C. In the case of CdSe/Pt and CdSe/Au nanoheterostructures, the reflections from CdSe are very weak in intensity in comparison to corresponding Pt and Au reflections. In contrast, the XRD data of the nanoheteroplatelets with Pd shows opposite behavior. Here, the main reflections from the face-centered cubic (fcc) CdSe NPLs such as the 111, 220, and 311 can be clearly derived, while the Pd reflections are not distinguishable. A closer look on the diffraction pattern reveals that the 220 reflection from CdSe is slightly broadened, where the fcc Pd 111 reflection is expected to appear. It might be that the Pd

reflections, which are expected to have weaker intensity at 68.1° and 85.7°, are overlaid by the close-by CdSe reflections. The Pd 200 reflection, indeed, which is not in proximity to any other reflex, can also not be derived with accuracy. These observations might be explained due to the much lower volume of the Pd domains in combination with the expected lower scattering intensity due to the much smaller atomic number of this element in comparison to Au or Pt. Furthermore, because Pd grows in a very thin layer with the platelets, there are only very few crystal planes contributing to the XRD reflexes. Hence, we conclude that we are unable to prove whether the Pd domain growth on the CdSe NPLs takes place epitaxially or not.

In order to investigate whether the Pd-decorated nanoheteroplatelets contain metallic Pd, we have performed X-ray photoelectron spectroscopy (XPS) with the CdSe/Pd nanoheteroplatelets. As reference samples, Pd nanoparticles synthesized following previously reported routes[49] and 5 ML CdSe NPLs were also analyzed, and the results were compared. The XPS spectra of all these samples are shown in Figure SI-11 in the Supporting Information. Notably, CdSe/Pd nanoheteroplatelets contain both the characteristic peaks of Pd as well as of CdSe NPLs. The photoelectron emission peaks at $\approx$405.2 eV and at $\approx$412 eV with a fwhm $\approx$1.8 eV (Figure SI-11A) can be attributed to Cd $3d_{5/2}$ and $3d_{3/2}$ doublets, respectively, confirming the presence of Cd in +2 oxidation state in both cases.[7] A comparison between the Se 3d peaks, appearing at $\approx$54.9 eV (Figure SI-11B), in CdSe NPLs and in CdSe/Pd nanoheteroplatelets reveals that selenium is present as Se^{2-} in both the compounds. The doublets appearing at $\approx$335.7 eV and at $\approx$341.0 eV in Figure SI-11C, can be attributed to Pd $3d_{5/2}$ and $3d_{3/2}$ peaks, respectively. In our measurements, we did not find peaks corresponding to Pd^{2+}, which is expected to appear at $\approx$337 eV (for Pd $3d_{5/2}$) and $\approx$342 to 344 eV (for Pd $3d_{3/2}$).[50,51] Hence, we conclude that Pd is mainly present as Pd^0 in the CdSe/Pd nano-

heteroplatelets. Furthermore, the Pd $3p_{3/2}$ peaks in the Pd nanoparticles and in the CdSe/Pd nanoheteroplatelets (Figure SI-11D) are found to be at $\approx$532 eV, which is in good agreement with the literature value confirming the existence of Pd in zero oxidation state. In addition, photoemission peaks corresponding to C 1s and O 1s can be found at $\approx$531.6 eV and $\approx$285.47 eV, respectively, presumably due to the presence of the organic ligands at the surface of the nanoparticles. Apart from that, no further impurities were detected.

Additionally, we examined the photocatalytic activity of all the nanoheterostructures on the degradation of methylene blue dye, which reveals promising catalytic activity for all the heterostructure in visible light irradiation regime (detailed description of the experimental setup and the results are discussed in the Supporting Information).

4. CONCLUSIONS

In conclusion, we have developed a simple and versatile synthetic strategy to grow noble metal (Au, Pd, and Pt) domains on 5 ML thick CdSe NPLs. Different morphological appearances of the noble metals on the 5 ML CdSe NPLs have been observed depending on the reaction temperature and on the type of the metal precursor, including the site-selective growth at the corners, at the shorter edges, and around all four edges of the NPLs. The metal domains were found to vary in shape from quasi spherical (Au and Pt) and dentoidal (Pt after long reaction time) to quasi rectangular and flat (Pd). The optimum reaction temperatures vary for the different noble metals from room temperature to 130 °C. The introduced novel materials display an important contribution in the development of advanced materials applicable in photocatalysis, chemical sensing, and fabrication of photovoltaic devices.

■ ASSOCIATED CONTENT

⑤ Supporting Information

Structural and optical characterization of the 5 ML CdSe NPLs; TEM and HAADF-STEM micrographs of corner selective Au growth on 5 ML CdSe NPLs and of interconnected CdSe/Au NPLs; TEM micrographs of Au growth on 5 ML CdSe NPLs with our modified method at room temperature and at 130 °C using AuCl$_3$; HAADF-STEM micrographs of Pd growth on 5 ML CdSe NPLs; TEM micrographs of time-dependent Pd growth on 5 ML CdSe NPLs; TEM micrographs of Au and Pd growth on 5 ML CdSe NPLs with molar precursor ratio Cd:Au/Pd = 20:1; HRTEM and HAADF-STEM micrographs of Au, Pd and Pt decorated 5 ML CdSe NPLs; Fluorescence spectroscopy of Au, Pt, Pd decorated 5 ML CdSe NPLs; Photograph and extinction spectra of Pd growth on 5 ML CdSe NPLs: a time-dependent evolution; Photograph and extinction spectra of Pt growth on 5 ML CdSe NPLs: a time-dependent evolution; XPS analysis of Pd nanoparticles, 5 ML CdSe NPLs, CdSe/Pd nanoheteroplatelets; Photocatalytic activity of the nanoheterostructures on the degradation of methylene blue dye. This material is available free of charge via the Internet at http://pubs.acs.org.

■ AUTHOR INFORMATION

Corresponding Author
*E-mail: nadja.bigall@pci.uni-hannover.de.

Author Contributions
‡These authors contributed equally (S.N. and A.S.). The manuscript was written through contributions of all authors. All
authors have given approval to the final version of the manuscript.

Notes
The authors declare no competing financial interest.

■ ACKNOWLEDGMENTS

■ REFERENCES

(1) Meyns, M.; Bastus, N. G.; Cai, Y.; Kornowski, A.; Juarez, B. H.; Weller, H.; Klinke, C. *J. Mater. Chem.* **2010**, *20* (47), 10602.

(2) Mokari, T.; Rothenberg, E.; Popov, I.; Costi, R.; Banin, U. *Science* **2004**, *304* (5678), 1787.

(3) O'Sullivan, C.; Gunning, R. D.; Barrett, C. A.; Singh, A.; Geaney, H.; Sanyal, A.; Ahmed, S.; Bala, T.; Ryan, K. M. In *State-of-the-Art Program on Compound Semiconductors 51*, Stokes, E., Goldhahn, R., Hunter, G., Odwyer, C., Ambacher, O., Huang, J., Kohn, E., Overberg, M. E., Eds.; The Electrochemical Society: Pennington, New Jersey, 2009; Vol. 25, p 17.

(4) Maynadie, J.; Salant, A.; Falqui, A.; Respaud, M.; Shaviv, E.; Banin, U.; Soulantica, K.; Chaudret, B. *Angew. Chem., Int. Ed.* **2009**, *48* (10), 1814.

(5) Soni, U.; Tripathy, P.; Sapra, S. *J. Phys. Chem. Lett.* **2014**, *5* (11), 1909.

(6) Jin, F.; Zhang, M.-L.; Zheng, M.-L.; Liu, Z.-H.; Fan, Y.-M.; Xu, K.; Zhao, Z.-S.; Duan, X.-M. *Phys. Chem. Chem. Phys.* **2012**, *14* (38), 13180.

(7) Haldar, K. K.; Sinha, G.; Lahtinen, J.; Patra, A. *ACS Appl. Mater. Interfaces* **2012**, *4* (11), 6266.

(8) Bala, T.; Ryan, K. M. *Adv. Nanomater. Nanotechnol.* **2013**, *143*, 21.

(9) Elmalem, E.; Saunders, A. E.; Costi, R.; Salant, A.; Banin, U. *Adv. Mater.* **2008**, *20* (22), 4312.

(10) Figuerola, A.; van Huis, M.; Zanella, M.; Genovese, A.; Marras, S.; Falqui, A.; Zandbergen, H. W.; Cingolani, R.; Manna, L. *Nano Lett.* **2010**, *10* (8), 3028.

(11) Mokari, T.; Sztrum, C. G.; Salant, A.; Rabani, E.; Banin, U. *Nat. Mater.* **2005**, *4* (11), 855.

(12) Steiner, D.; Mokari, T.; Banin, U.; Millo, O. *Phys. Rev. Lett.* **2005**, *95* (5), 056805.

(13) Jen-La Plante, I.; Habas, S. E.; Yuhas, B. D.; Gargas, D. J.; Mokari, T. *Chem. Mater.* **2009**, *21* (15), 3662.

(14) Mokari, T.; Costi, R.; Sztrum, C. G.; Rabani, E.; Banin, U. *Phys. Status Solidi B* **2006**, *243* (15), 3952.

(15) Menagen, G.; Mocatta, D.; Salant, A.; Popov, I.; Dorfs, D.; Banin, U. *Chem. Mater.* **2008**, *20* (22), 6900.

(16) Hill, L. J.; Bull, M. M.; Sung, Y.; Simmonds, A. G.; Dirlam, P. T.; Richey, N. E.; DeRosa, S. E.; Shim, I. B.; Guin, D.; Costanzo, P. J.; Pinna, N.; Willinger, M. G.; Vogel, W.; Char, K.; Pyun, J. *ACS Nano* **2012**, *6* (10), 8632.

(17) Li, X.; Lian, J.; Lin, M.; Chan, Y. *J. Am. Chem. Soc.* **2010**, *133* (4), 672.

(18) Habas, S. E.; Yang, P.; Mokari, T. *J. Am. Chem. Soc.* **2008**, *130* (11), 3294.

(19) Saunders, A. E.; Popov, I.; Banin, U. *J. Phys. Chem. B* **2006**, *110* (50), 25421.

113

(20) Franchini, I. R.; Bertoni, G.; Falqui, A.; Giannini, C.; Wang, L. W.; Manna, L. *J. Mater. Chem.* **2010**, *20* (7), 1357.

(21) Yong, K. T.; Sahoo, Y.; Choudhury, K. R.; Swihart, M. T.; Minter, J. R.; Prasad, P. N. *Nano Lett.* **2006**, *6* (4), 709.

(22) Subramanian, V.; Wolf, E. E.; Kamat, P. V. *J. Am. Chem. Soc.* **2004**, *126* (15), 4943.

(23) Yu, X.; Shavel, A.; An, X.; Luo, Z.; Ibanez, M.; Cabot, A. *J. Am. Chem. Soc.* **2014**, *136* (26), 9236.

(24) Costi, R.; Saunders, A. E.; Banin, U. *Angew. Chem., Int. Ed.* **2010**, *49* (29), 4878.

(25) Wu, Y.; Xiang, J.; Yang, C.; Lu, W.; Lieber, C. M. *Nature* **2004**, *430* (6995), 61.

(26) O'Sullivan, C.; Gunning, R. D.; Barrett, C. A.; Singh, A.; Ryan, K. M. *J. Mater. Chem.* **2010**, *20* (36), 7875.

(27) Mokari, T. *Nano Rev.* **2011**, *2*, 5983.

(28) Demortiere, A.; Schaller, R. D.; Li, T.; Chattopadhyay, S.; Krylova, G.; Shibata, T.; Claro, P. C. d. S.; Rowland, C. E.; Miller, J. T.; Cook, R.; Lee, B.; Shevchenko, E. V. *J. Am. Chem. Soc.* **2014**, *136* (6), 2342.

(29) Menagen, G.; Macdonald, J. E.; Shemesh, Y.; Popov, I.; Banin, U. *J. Am. Chem. Soc.* **2009**, *131* (47), 17406.

(30) Figuerola, A.; Franchini, I. R.; Fiore, A.; Mastria, R.; Falqui, A.; Bertoni, G.; Bals, S.; Van Tendeloo, G.; Kudera, S.; Cingolani, R.; Manna, L. *Adv. Mater.* **2009**, *21* (5), 550.

(31) Costi, R.; Saunders, A. E.; Elmalem, E.; Salant, A.; Banin, U. *Nano Lett.* **2008**, *8* (2), 637.

(32) Wu, K.; Chen, Z.; Lv, H.; Zhu, H.; Hill, C. L.; Lian, T. *J. Am. Chem. Soc.* **2014**, *136* (21), 7708.

(33) Dilsaver, P. S.; Reichert, M. D.; Hallmark, B. L.; Thompson, M. J.; Vela, J. *J. Phys. Chem. C* **2014**, *118* (36), 21226.

(34) Ithurria, S.; Tessier, M. D.; Mahler, B.; Lobo, R. P. S. M.; Dubertret, B.; Efros, A. L. *Nat. Mater.* **2011**, *10* (12), 936.

(35) Tessier, M. D.; Javaux, C.; Maksimovic, I.; Loriette, V.; Dubertret, B. *ACS Nano* **2012**, *6* (8), 6751.

(36) Mahler, B.; Nadal, B.; Bouet, C.; Patriarche, G.; Dubertret, B. *J. Am. Chem. Soc.* **2012**, *134* (45), 18591.

(37) Tessier, M. D.; Mahler, B.; Nadal, B.; Heuclin, H.; Pedetti, S.; Dubertret, B. *Nano Lett.* **2013**, *13* (7), 3321.

(38) Bouet, C.; Laufer, D.; Mahler, B.; Nadal, B.; Heuclin, H.; Pedetti, S.; Patriarche, G.; Dubertret, B. *Chem. Mater.* **2014**, *26* (9), 3002.

(39) Tessier, M. D.; Spinicelli, P.; Dupont, D.; Patriarche, G.; Ithurria, S.; Dubertret, B. *Nano Lett.* **2014**, *14* (1), 207.

(40) Pedetti, S.; Ithurria, S.; Heuclin, H.; Patriarche, G.; Dubertret, B. *J. Am. Chem. Soc.* **2014**, *136* (46), 16430.

(41) Abecassis, B.; Tessier, M. D.; Davidson, P.; Dubertret, B. *Nano Lett.* **2014**, *14* (2), 710.

(42) Tessier, M. D.; Biadala, L.; Bouet, C.; Ithurria, S.; Abecassis, B.; Dubertret, B. *ACS Nano* **2013**, *7* (4), 3332.

(43) Chen, Z.; Nadal, B.; Mahler, B.; Aubin, H.; Dubertret, B. *Adv. Funct. Mater.* **2014**, *24* (3), 295.

(44) Guzelturk, B.; Kelestemur, Y.; Olutas, M.; Delikanli, S.; Demir, H. V. *ACS Nano* **2014**, *8* (7), 6599.

(45) She, C.; Fedin, I.; Dolzhnikov, D. S.; Demortiere, A.; Schaller, R. D.; Pelton, M.; Talapin, D. V. *Nano Lett.* **2014**, *14* (5), 2772.

(46) Liu, Y.-H.; Wayman, V. L.; Gibbons, P. C.; Loomis, R. A.; Buhro, W. E. *Nano Lett.* **2009**, *10* (1), 352.

(47) Bouet, C.; Mahler, B.; Nadal, B.; Abecassis, B.; Tessier, M. D.; Ithurria, S.; Xu, X.; Dubertret, B. *Chem. Mater.* **2013**, *25* (4), 639.

(48) Standard NIST bulk XRD pdf no. for CdSe (03-065-2891), for Au (03-065-2870), for Pd (03-065-2867), and for Pt (03-068-2868).

(49) Kwon, S. G.; Hyeon, T. *Acc. Chem. Res.* **2008**, *41* (12), 1696.

(50) Lemke, W. M.; Kaner, R. B.; Diaconescu, P. L. *Inorg. Chem. Front.* **2015**, *2* (1), 35.

(51) Wang, J.; Neoh, K. G.; Kang, E. T. *J. Colloid Interface Sci.* **2001**, *239* (1), 78.

114

Supporting Information

Site-Selective Noble Metal Growth on CdSe Nanoplatelets

Suraj Naskar[‡], Anja Schlosser[‡], Jan F. Miethe, Frank Steinbach, Armin Feldhoff, Nadja C. Bigall*

Institute of Physical Chemistry and Electrochemistry, Leibniz Universität Hannover,

Callinstraße 3A, D-30167 Hannover, Germany

Contents:

(1) Structural and optical characterization of the 5 ML CdSe NPLs

The as-synthesized CdSe NPLs had an initial quantum yield of 23% in toluene at room temperature. The structural and optical properties of the NPLs are shown in Figure SI-1. In a previous work, Lim *et al.* found that cadmium salt and selenium precursors in the molar ratio of 2:1 in presence of oleic acid produce CdSe NPLs with zinc blend cubic crystal lattice structure.[1] The CdSe NPLs had an average length of 31 nm ± 3.5 nm and width of 7.9 nm ± 1.3 nm. The optical spectra are in very good aggrement with the one's reported by Tessier *et al.* for 5 ML NPLs.[2] We therefore, can conclude that the thickness of our NPLs is similar, and hence 1.5 nm.[3] The absorbance (black line), emission (green line) and photoluminescence (PL) excitation spectra (red dotted line) are shown in Figure SI-1C. The absorbance spectra shows two characteristic peaks corresponding to light hole - electron and heavy hole -electron transition at 518 nm and 552 nm respectively. The photoluminescence emission spectra have maxima at 552 nm with full width at half maximum (FWHM) of 13 nm suggesting strong quantum confinement. The normalized photoluminescence excitation spectra and the absorbance spectra are in good agreement, confirming the NPLs are mostly of 5 ML in thickness. The powder x-ray diffraction pattern (XRD) of the NPLs is shown Figure SI-1D. The data is compared with bulk CdSe face centered cubic crystal lattice structure.
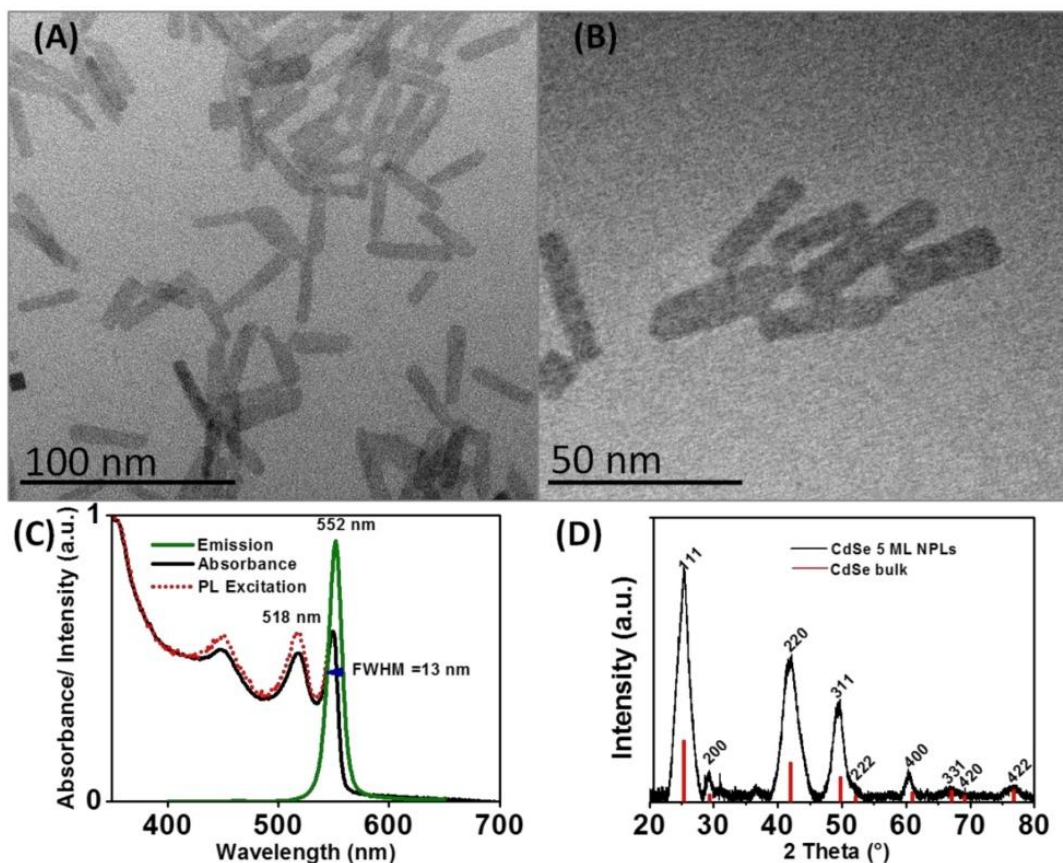
Figure SI-1. *Structural and optical characterization of 5 ML thick CdSe NPLs (A) TEM micrograph of the CdSe NPLs in overview and (B) in high resolution. (C) Normalized absorbance (black line), photoluminescence excitation (red dotted line) and emission spectra (green line) of the colloidal NPLs solution. (D) Powder x-ray diffraction pattern of dried NPLs, compared with bulk CdSe reference (vertical red lines) of zinc blend cubic crystal lattice pdf no.03-065-2891.*

(2) TEM and HAADF-STEM micrographs of corner selective Au growth on 5 ML CdSe NPLs and of interconnected CdSe/Au NPLs
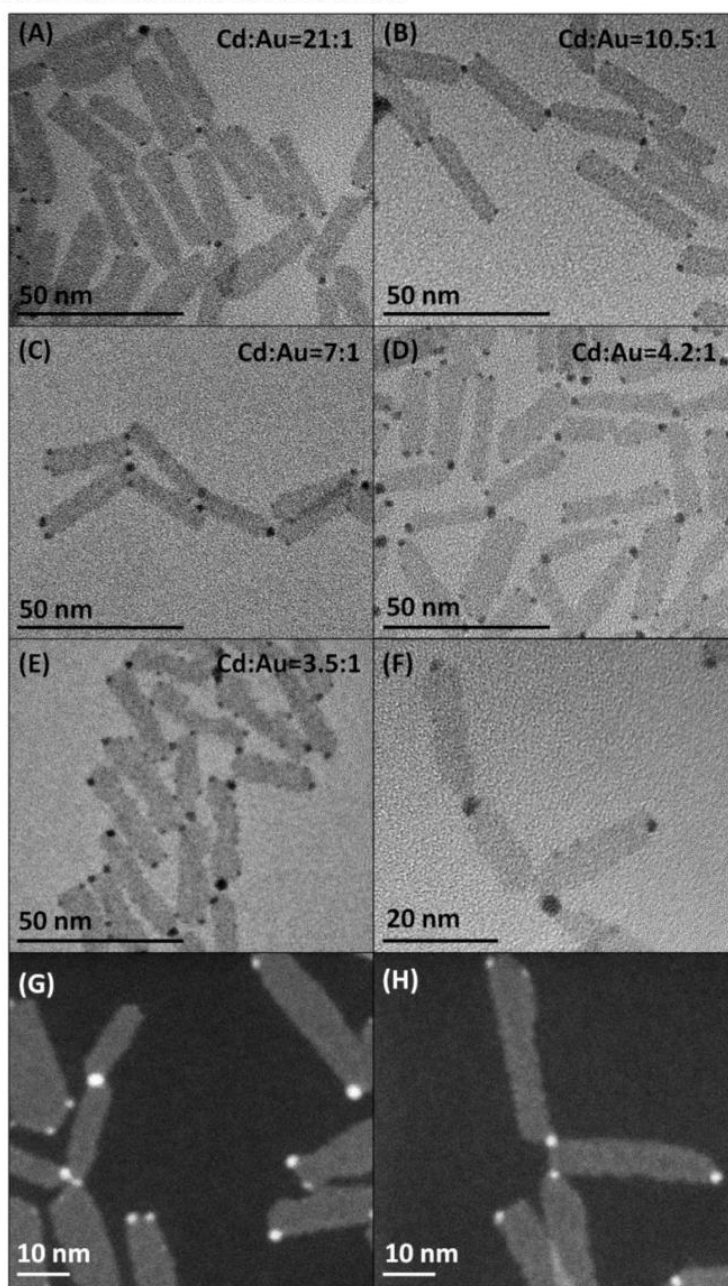

Figure SI-2. *TEM micrographs (A-E) proving Au growth preferentially at the corners of 5 ML CdSe NPLs following the modified synthetic route of Mokari et al. for variable molar precursor ratios ranging from Cd:Au=21:1 to 3.5:1. (F) Higher magnification TEM micrograph of Au on CdSe NPLs molar ratio Cd:Au=4.2:1 showing partial connection of the NPLs via Au domains. (G) & (H) HAADF-STEM micrographs of Au on CdSe NPLs with a molar ratio Cd:Au=10.5:1. Bright spots corresponding to Au domains at the corners of the NPLs are recognizable.*

(3) TEM micrographs of Au growth on 5 ML CdSe NPLs with our modified method at room temperature and at 130 °C using AuCl₃
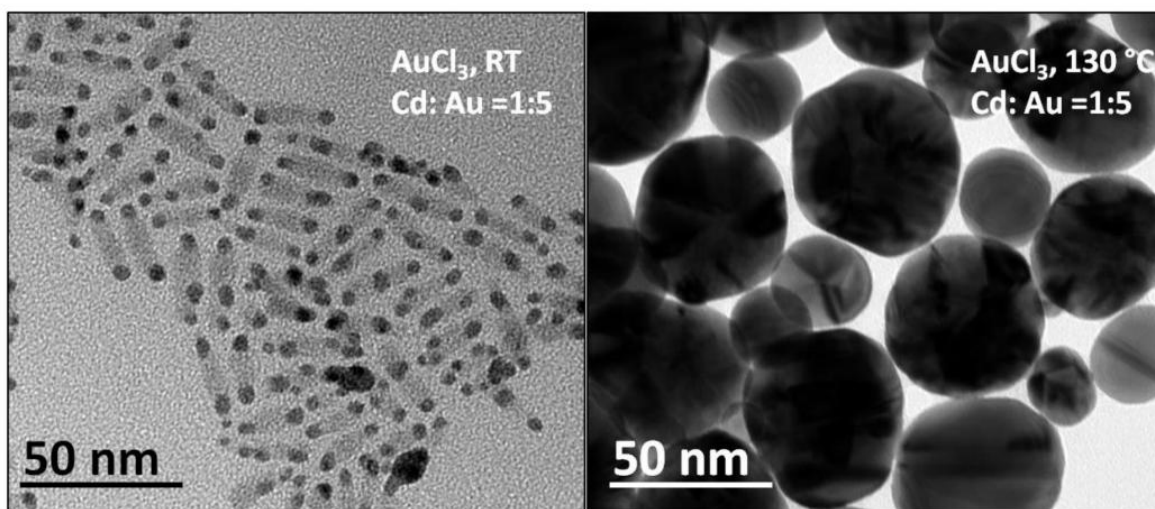

Figure SI-3. *TEM micrographs of Au growth on 5 ML CdSe NPLs with a molar precursor ratio of Cd:Au=1:5, using AuCl₃ as precursor at different reaction temperatures.*
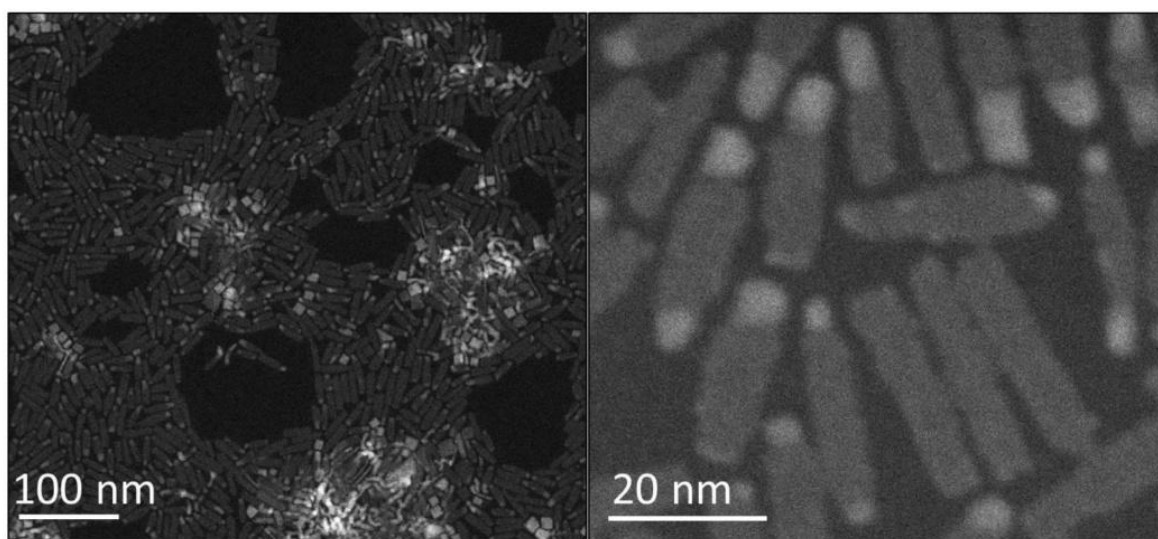
(4) HAADF-STEM micrographs of Pd growth on 5 ML CdSe NPLs

Figure SI-4. *HAADF-STEM micrographs of Pd growth on 5 ML CdSe NPLs with a Cd:Pd molar precursor ratio of 1:5. The bright spots at the shorter edges of the CdSe NPLs indicate the presence of Pd.*
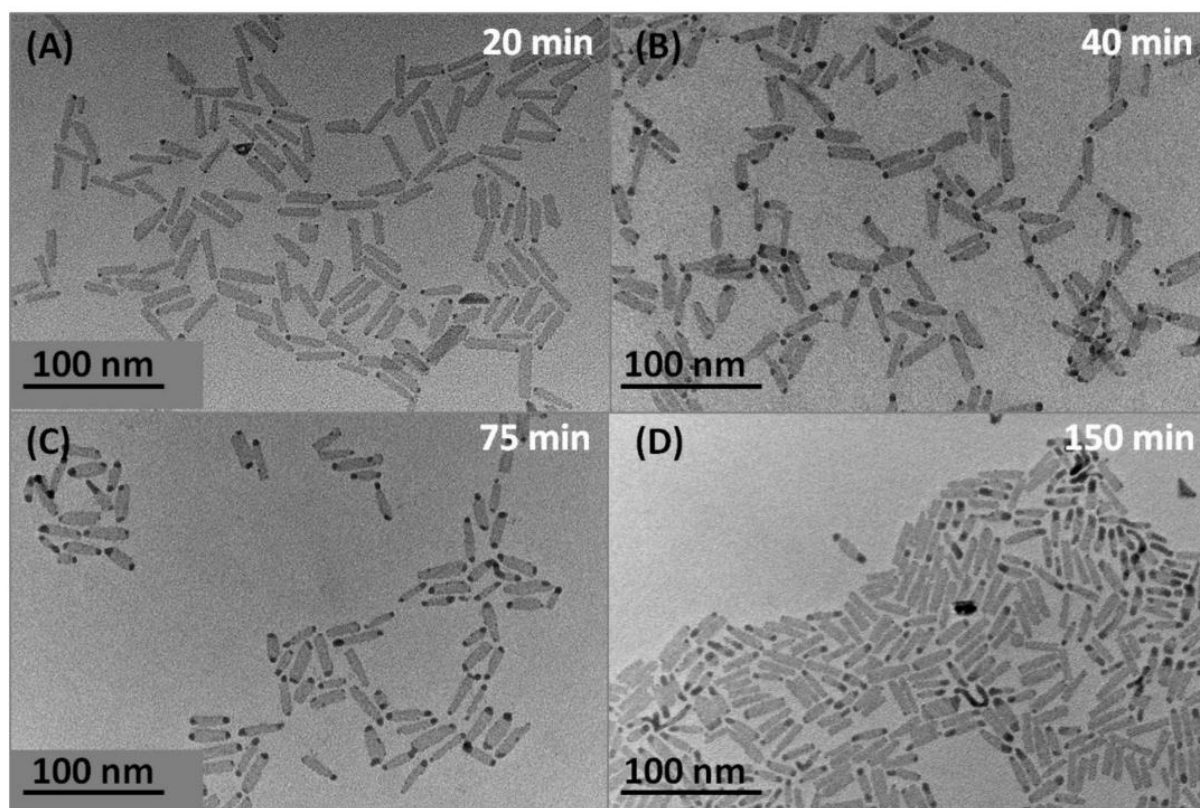
(5) TEM micrographs of time-dependent Pd growth on 5 ML CdSe NPLs

Figure SI-5. TEM micrographs of time dependent Pd growth on 5 ML CdSe NPLs with a Cd:Pd molar precursor ratio of 1:5. The samples were collected after 20 min, 40 min, 75 min and 150 min reaction time, respectively.

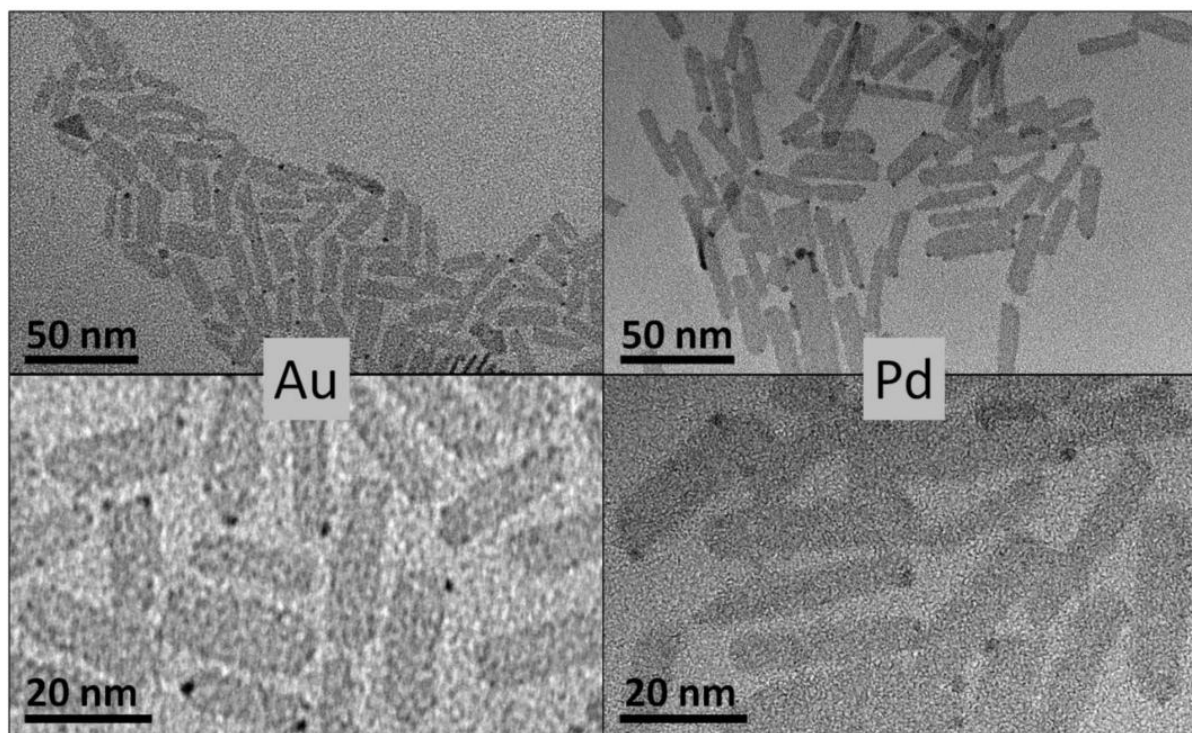**(6) TEM micrographs of Au and Pd growth on 5 ML CdSe NPLs with molar precursor ratio Cd:Au/Pd=20:1**

Figure SI-6. *TEM micrographs of Au and Pd domain growth on 5 ML CdSe NPLs with Cd:Au/Pd precursor molar ratio of 20:1.*
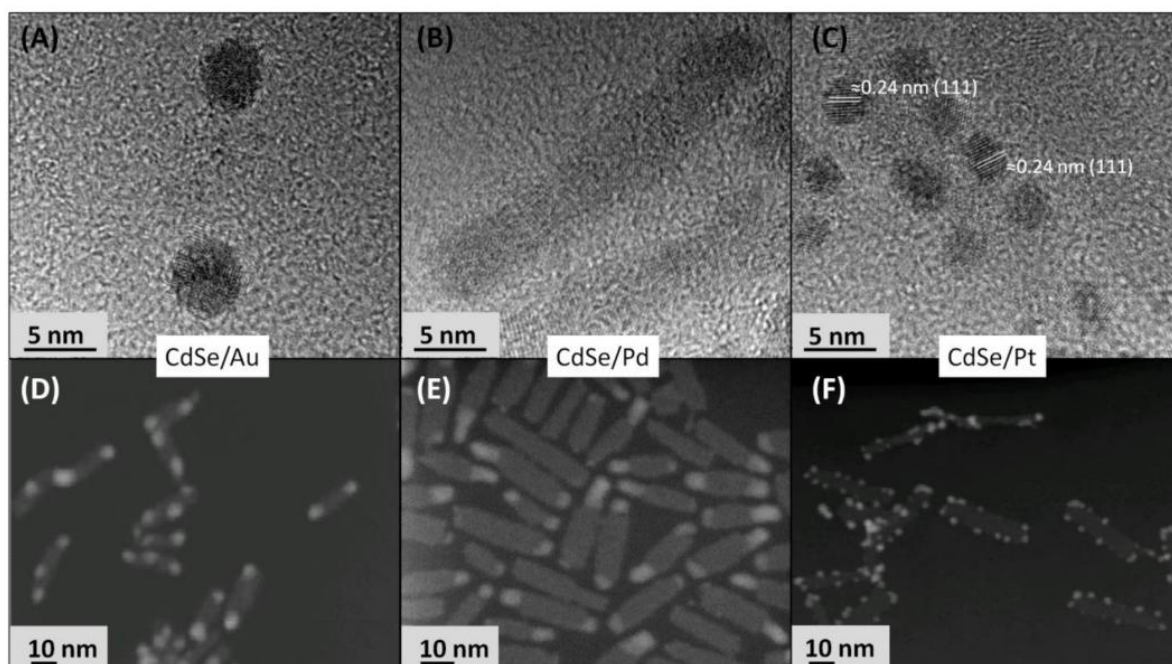
(7) HRTEM and HAADF-STEM micrographs of Au, Pd and Pt decorated 5 ML CdSe NPLs

Figure SI-7. *HRTEM micrographs of Au, Pd, Pt decorated 5 ML CdSe NPLs (A-C). The lattice planes of the CdSe NPLs are not visible due to the thin nature of these sheets being only 5 ML thick. HAADF-STEM micrographs (D-F) of Au, Pd, Pt decorated CdSe NPLs, bright spots are clearly indicating the metal domains are directly attached to the NPLs.*
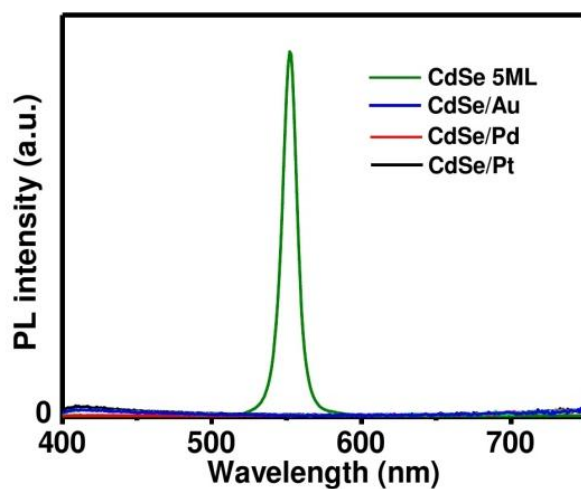
(8) Fluorescence spectroscopy of Au, Pt, Pd decorated 5 ML CdSe NPLs

Figure SI-8. *Photoluminescence emission spectra of the nanoheteroplatelets in comparison to the 5 ML CdSe NPLs, with Cd:M (Pt, Pd or Au) molar precursor ratio of 1:5. The PL emission spectra reveal complete fluorescence quenching upon metal domain growth on the CdSe NPLs.*

(9) Photograph and extinction spectra of Pd growth on 5 ML CdSe NPLs: a time-dependent evolution
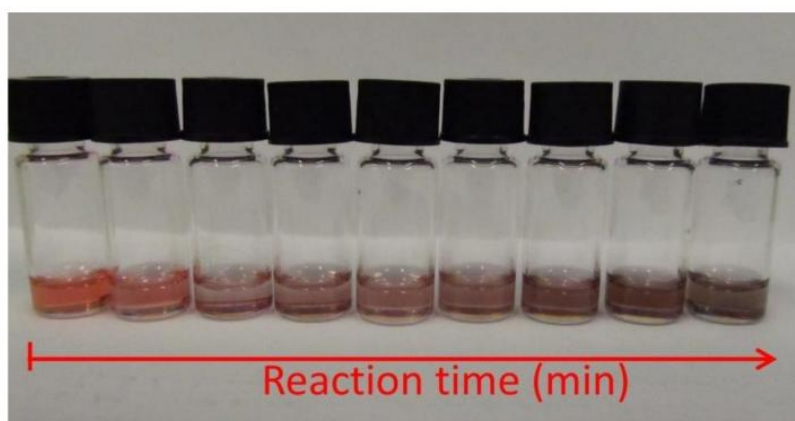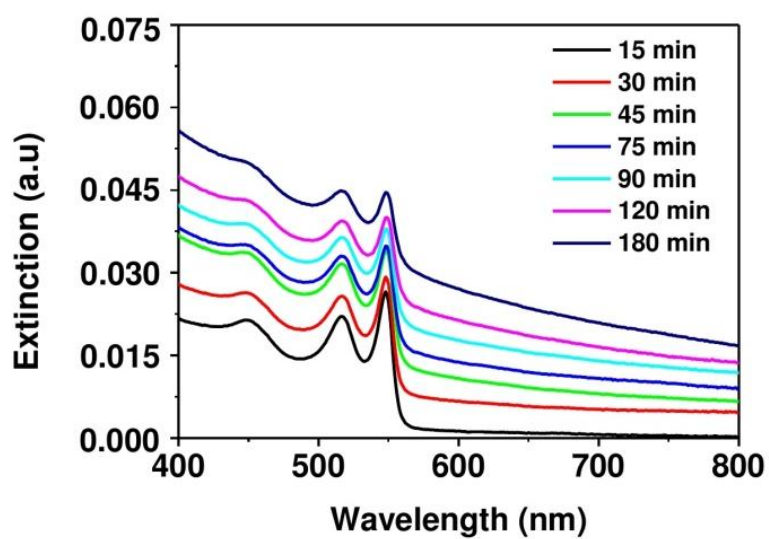

Figure SI-9*. Extinction spectra of time-dependent Pd domain growth on 5 ML CdSe NPLs (top), by photograph (bottom).*

(10)   Photograph and extinction spectra of Pt growth on 5 ML CdSe NPLs: a time-dependent evolution
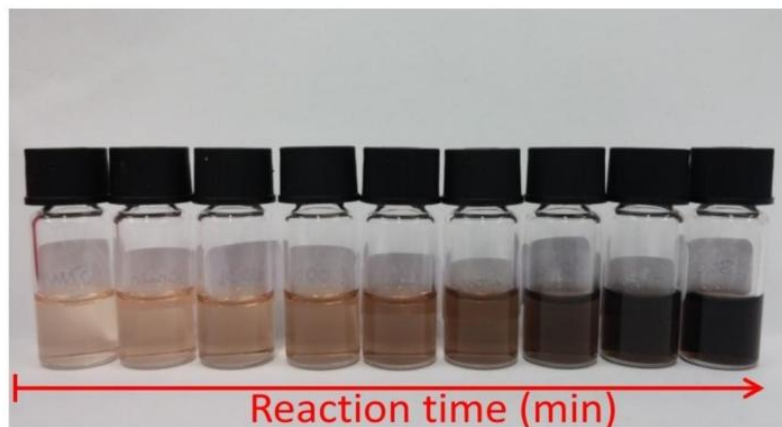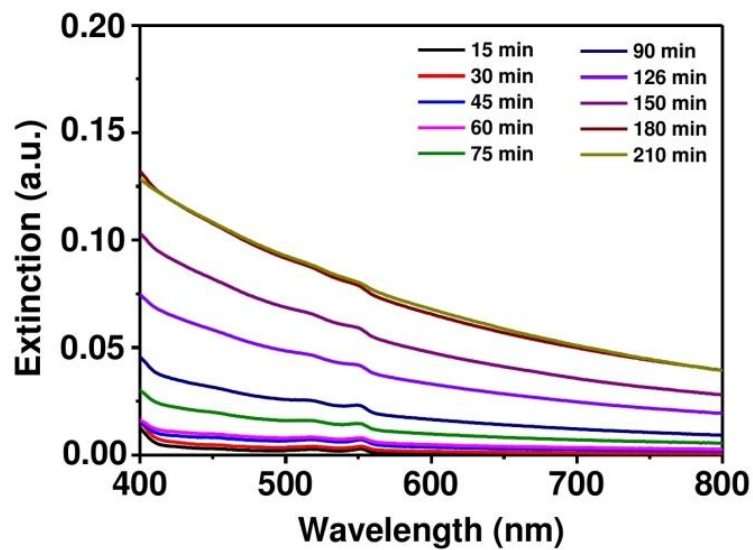
Figure SI-10. Extinction spectra of time-dependent Pt domain growth on 5 ML CdSe NPLs (top), by photograph (bottom).

(11) XPS analysis of Pd nanoparticles, 5 ML CdSe NPLs, CdSe/Pd nanoheteroplatelets
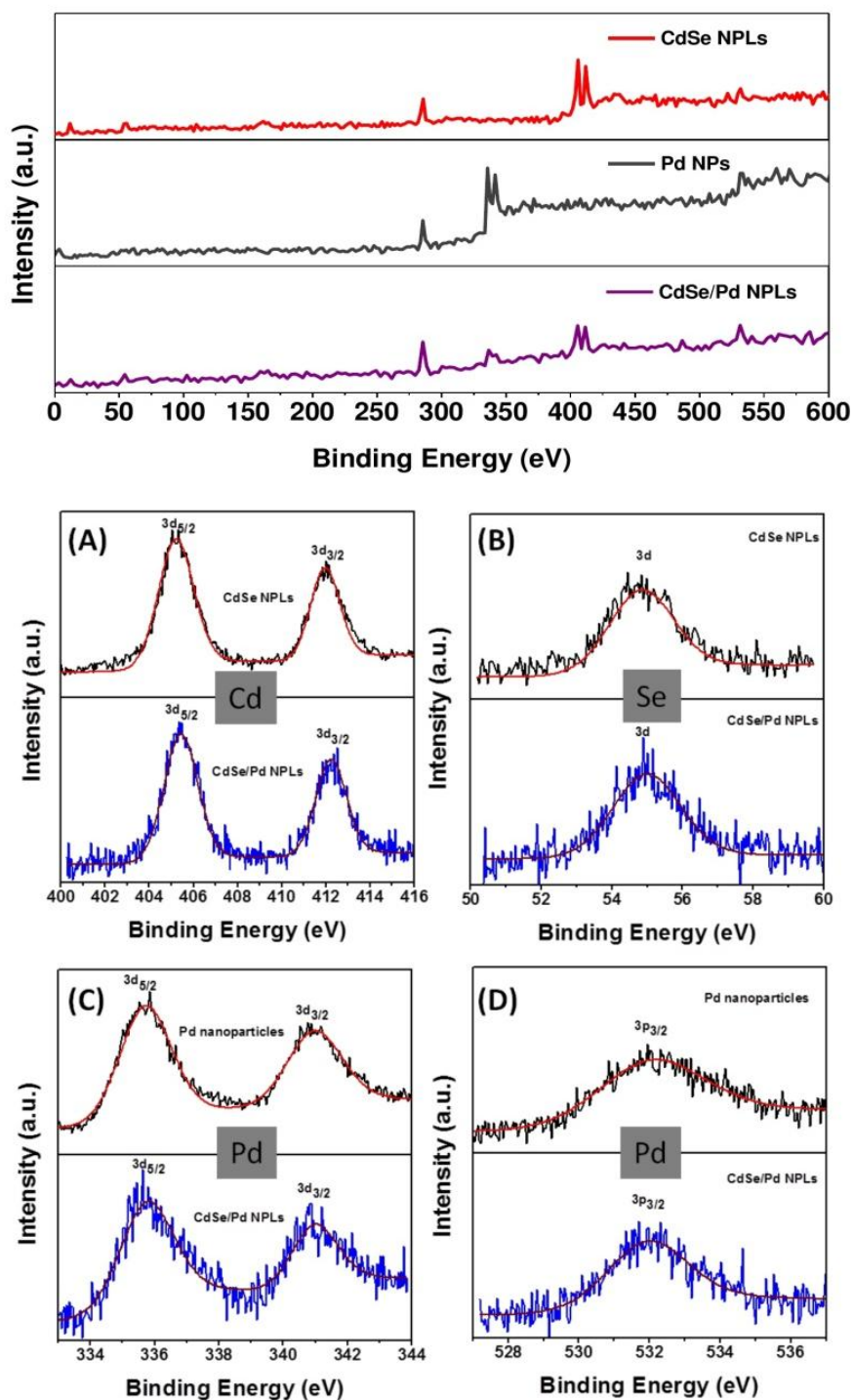
Figure SI-11. *(top) XPS spectra of Pd nanoparticles, 5 ML CdSe NPLs and CdSe/Pd nanoheteroplatelets in overview. (A) & (B) Comparison of X-ray photoelectron peaks of Cd (3d) and Se (3d) between CdSe NPLs and CdSe/Pd nanoheteroplatelets. (C) & (D) Comparison of Pd 3d and 3p peaks between Pd nanoparticles and CdSe/Pd nanoheteroplatelets.*

(12) **Photocatalytic activity of the nanoheterostructures on the degradation of methylene blue dye**

Photocatalytic activity of the metal-semiconductor nanoheteroplatelets: The virtue of charge separation at the metal semiconductor interface has made such kind of material suitable for showing high photocatalytic activity.[3-8] In order to see the photocatalytic activity of our metal decorated semiconductor nanoheterostructures, we have studied the photoreduction of methylene blue (tetramethylthionine chloride $C_{16}H_{18}ClN_3S$) as a model electron acceptor dye. Methylene blue is blue in an oxidizing environment and colorless (leuco methylene blue) if reduced. The absorption spectrum of the dye shows a characteristic maximum at 654 nm. The use of dyes such as methylene blue or rhodamine 6G has been shown to be a reasonable test for proving photocatalytic activities for different shapes and materials of nanoheterostructures in previous works. For example, Costi *et al.* have reported the visible range photocatalytic activity of the Au tipped CdSe nanodumbbels to reduce methylene blue in a mixture of ethanol and aqueous buffer medium.[4] Similarly, Soni *et al.* have reported the degradation of methylene blue with Au tipped CdSe nanocrystals of different diameters using an ethanolic solution of the dye.[5] In order to test the photocatalytic activity of our nanoheterostructures, we followed the experimental route of Soni *et al.,* since it works without a water transfer, and since so far no water transfer route for our sensitive NPLs has been developed. The photocatalytic activity of the catalyst can be evaluated by recording the change in the intensity of the peak at 654 nm upon irradiation with light overtime (see Figure SI-12 A). It was found after one hour of photoirradiation, that for the pristine 5 ML CdSe NPLs as a catalyst only 14 % of the dye was degraded, whereas 17 %, 35 % and 45 % of the dye were degraded for the Au/CdSe, Pt/CdSe and Pd/CdSe nanoheteroplatelets, respectively. From the kinetic profile of the dye degradation, a logarithmic plot of A_0/A versus the photoirradiation time (t) is drawn (see Figure SI-12B), where A_0 and A represent the initial and intermediate extinction intensity

(at time t) at 654 nm, respectively. In each case all the data points can be fitted with a straight line passing through the origin. The slopes of the straight lines give the apparent first order rate constant of the dye degradation reaction. The apparent first order rate constants were found to be $2.7 \cdot 10^{-3}$ min^{-1}, $3.5 \cdot 10^{-3}$ min^{-1}, $7.2 \cdot 10^{-3}$ min^{-1} and $10.2 \cdot 10^{-3}$ min^{-1} for the CdSe NPLs and the Au, Pt and Pd decorated nanoheteroplatelets, respectively. The observed differences in the photo catalytic activity of the nanoheteroplatelets might be due to different agglomeration behavior of the heterostructure in ethanolic medium. Therefore, we can conclude, that our systems have potential for photocatalysis applications, even though an optimization of the arrangements for exploiting the full potential still remains necessary.
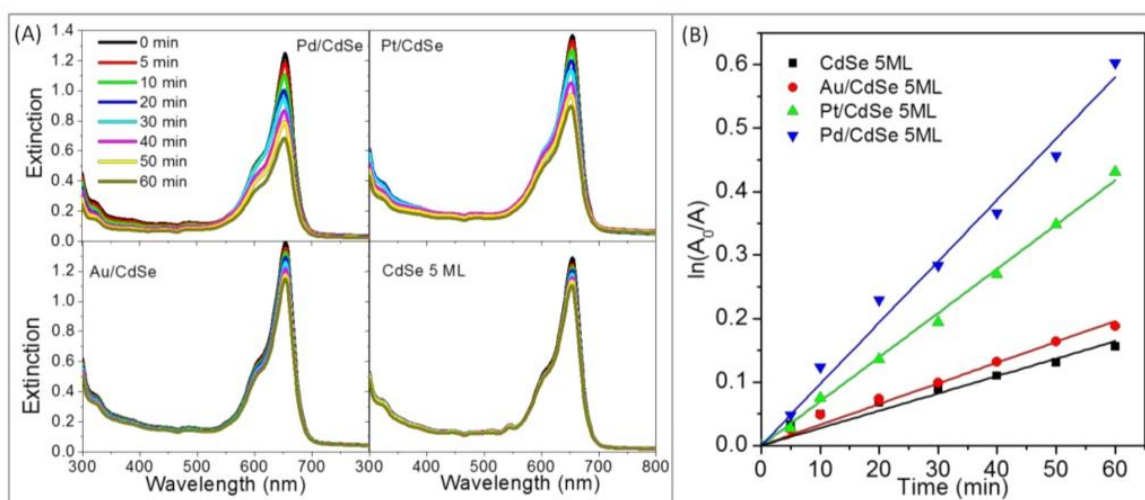
Figure SI-12. Spectroscopic measurement of the photocatalytic reduction of methylene blue by means of nanoheteroplatelets. (A) Extinction spectra after different times of irradiation for 5 ML CdSe NPLs with (top left) Pd, (top right) Pt, (bottom left) Au and (bottom right) without metal domains. (B) Change of extinction intensity at 654 nm in logarithmic plot showing first order reactions.

Experimental set up for photocatalysis tests: We followed the experimental route similar to that described by Soni *et al.*[5] A stock solution of methylene blue was prepared by dissolving 0.0166 g ($4.44 \cdot 10^{-5}$ mol) of methylene blue in 10 mL of ethanol. The photoreduction of methylene blue dye was carried out by diluting 10 µL of this stock solution in a screw cap

4.3 Synthesis of Ternary and Quaternary Au and Pt Decorated CdSe/CdS Heteronanoplatelets with Controllable Morphology

Suraj Naskar, Franziska Lübkemann, Saher Hamid, Axel Freytag, Andreas Wolf, Julian Koch, Irina Ivanova, Herbert Pfnür, Dirk Dorfs, Detlef W. Bahnemann, and Nadja C. Bigall*

FULL PAPER

Synthesis of Ternary and Quaternary Au and Pt Decorated CdSe/CdS Heteronanoplatelets with Controllable Morphology

Suraj Naskar, Franziska Lübkemann, Saher Hamid, Axel Freytag, Andreas Wolf, Julian Koch, Irina Ivanova, Herbert Pfnür, Dirk Dorfs, Detlef W. Bahnemann, and Nadja C. Bigall*

A variety of new ternary and quaternary metal–semiconductor inorganic nanostructures with unprecedented structural morphologies is achieved by the decoration of five monolayer-thick CdSe/CdS core/crown nanoplatelets with Au and Pt domains. Significant differences in metal growth behavior are observed by varying the CdSe core and the CdS crown dimensions. Depending on the core size, Au growth can be directed only to the CdS edges, or both at the edges and at the center of the nanoplatelets. In contrast, the nucleation of Pt domains always happens at the CdS edges independently of the core and crown dimensions. Furthermore, quaternary structures are obtained by additional Au growth on Pt-decorated CdSe/CdS nanoplatelets, where the effect of steric hindrance of the existing Pt domains results in the Au nucleation to occur only at the CdSe core. Instead, a change in the order of growth of the two noble metals results in Pt-Au alloys present only at the surrounding edges of the nanoplatelets. Additionally, the metal-decorated nanoplatelets are found to be efficient catalysts for H_2 fuel generation under white light irradiation. The highest apparent quantum efficiency measured is 19.3% ± 1.4% with a turnover frequency of ≈10^5 molecules of H_2 per hour per nanoplatelet.

1. Introduction

Metal–semiconductor nanoheterostructures are known to be materials with fascinating electronic and electrochemical properties.[1] The nanostructures are currently being researched by investigating the following topics; the extent of charge carrier separation, the mixing of electronic states, and how synergistic properties of metals and the semiconductors occur in the same particle.[1b,2] The great advantage of ultrafast electron transfer and charge carrier (electron–hole) separation at the metal–semiconductor interface has motivated researchers to discuss applications in, e.g., photocatalytic water splitting,[3] pollutant degradation,[4] field effect transistors,[5] CO_2 reduction reactions,[6] etc. The metal-decorated nanostructures are also employed for self-assembling in solutions or on substrates to measure their electrical transport properties.[7] Various synthetic approaches (such as reduction, thermal annealing, photoinduced reactions, nanowelding, and many others) have enabled scientists to produce nano-heteroparticles with many possible combinations of metals (e.g., Au, Pt, Pd, Ni, or Co) and different shapes of metal-chalcogenide semiconductors, starting from spherical dots,[2a,3b,4c,8] nanorods,[1b,2b,9] nanowires,[9a] tetrapods,[1b,10] and pyramids,[11] to cubes[4b,12] and many more.[9g,13] In some cases, selective deposition of the metal domains (Au, Pt, Ag, Ni, Co, or Cu) at one end or both ends of the nanorods, at the tips of tetrapods, or only at the sides of rod-shaped semiconductor domains are shown in literature.[2a,9b,14]

S. Naskar, F. Lübkemann, A. Freytag, A. Wolf,
Dr. D. Dorfs, Dr. N. C. Bigall
Institute of Physical Chemistry and Electrochemistry
Leibniz Universität Hannover
Callinstraße 3A, D-30167 Hannover, Germany
E-mail: nadja.bigall@pci.uni-hannover.de
S. Naskar, F. Lübkemann, S. Hamid, A. Freytag, A. Wolf,
J. Koch, Dr. I. Ivanova, Prof. H. Pfnür, Dr. D. Dorfs,
Prof. D. W. Bahnemann, Dr. N. C. Bigall
Laboratory for Nano and Quantum Engineering
Leibniz Universität Hannover
Schneiderberg 39, 30167 Hannover, Germany

S. Hamid, Dr. I. Ivanova, Prof. D. W. Bahnemann
Institute for Technical Chemistry
Leibniz Universität Hannover
Callinstraße 3, D-30167 Hannover, Germany
Prof. D. W. Bahnemann
Laboratory for Nanocomposite Materials
Department of Photonics
Faculty of Physics
Saint-Petersburg State University
Ulianovskaia street 3, Peterhof, Saint Petersburg 198504, Russia
J. Koch, Prof. H. Pfnür
Institut für Festkörperphysik
Leibniz Universität Hannover
Appelstraße 2, 30167 Hannover, Germany

FULL PAPER

Recently developed quasi-2D metal-chalcogenide nano-platelets (NPLs) of only few monolayer (ML) thicknesses have attracted tremendous attention due to their thickness-dependent optoelectronic properties and large specific surface with only {100} as the exposed crystal facets.[15] Regarding the decoration of such NPLs with noble metal domains, our group has recently developed synthetic strategies to grow Au, Pd, and Pt on 5 ML-thick CdSe NPLs, which exhibit promising photo-catalytic activity toward organic dye (e.g., methylene blue) degradation upon illumination with visible light.[2c] This obser-vation was an indication that metal-decorated NPLs can show efficient charge carrier separation at the metal–semiconductor interface.[2c] The development of nanoheteroplatelets, from synthesis to applications, is still in its infancy. Apart from the above-described site-selective noble metal growth on 5 ML-thick CdSe NPLs, only a few reports have been published regarding the combination of NPLs and metal domains, such as the deco-ration of CdSe quantum belts with Au,[16] CdSe sheets with Pt[17] and Ni domains on CdS nanosheets,[18] and very recently, Au growth on hexagonal CdSe/CdS core/shell NPLs.[13h] Until now, the impacts of the metal decoration on anisotropic CdSe/CdS core/crown NPLs on the structural morphologies, optical prop-erties, electronic structures, charge carrier separation, and the localization of holes and trap states have not been investigated.

Over the last decades, much attention has been paid in search of alternative green energy sources that will release the world from its dependence on fossil fuels. For that matter, H_2 gas is an appealing green energy source, as it has an energy density of 140 kJ g^{-1}, and the combustion of H_2 only produces water as the reaction by-product. The synergistic properties, electronic structure, band gap, and the light harvesting nature of the pure metal oxides, sulfides, or metal oxide loaded with noble metal-based cocatalyst are well known for their photocatalytic performance in H_2 generation by photoreduction of water.[19] These catalysts show promising performance, but the presence of noble metal elements makes them highly expensive, thus limiting their wide-scale production. In contemporary reports, II–VI metal chalcogenide semiconductors such as 0D and 1D CdSe and CdSe/CdS nanocrystals, which have a suitable band gap for visible light absorption, are found to be highly efficient for H_2 gas production,[3b,20] while their 2D counterpart, namely NPLs, the analogues of thin quantum wells with very strong quantum confinement in the z directions, have hardly been investigated. Owing to their large absorption cross-section and large in-plane charge carrier mobility (compared to quantum dots or nanorods), the NPLs could be advantageous over the previous investigated systems.[21] Furthermore, the 2D NPLs are reported to exhibit the strongest electro-optic response than the other shapes like nanorods and quantum dots.[22] The afore-mentioned advantages of the 2D NPLs systems have motivated us to study their photocatalytic H_2 generation ability under white light illumination.

In the present work, a variety of new ternary and quater-nary metal–semiconductor nanostructures is presented, which exhibit unprecedented structural morphologies. Namely, the decoration of five-monolayer thick CdSe/CdS core/crown nano-platelets with Au and Pt domains is investigated. We observe significant differences in the site-selective nucleation of the metal (Pt and/or Au) domains on CdSe/CdS NPLs with variable

CdSe core and CdS crown dimensions, which are proven by structural and morphological characterizations, such as trans-mission electron microscopy (TEM), elemental mapping with scanning TEM-energy dispersive X-ray spectroscopy (STEM-EDXS) and X-ray diffractometry (XRD). The novel ternary and quaternary NPLs synthesized are transferred to aqueous medium by means of ligand exchange reactions. A compara-tive study of photocatalytic H_2 generation activity of the Pt-dec-orated NPLs is performed by varying the lateral dimensions of the CdSe core and the CdS crown, under white-light illumina-tion. The metal-decorated NPLs are found to exhibit compel-ling apparent quantum efficiencies (AQE) up to 19.3% ± 1.4%, which is approximately fivefold higher than the pristine CdSe/CdS NPLs.

2. Results and Discussion

2.1. Synthesis and Characterization of Pt Decorated NPLs

Quasi 2D 5 ML-thick CdSe and CdSe/CdS core/crown NPLs of different core and crown dimensions are synthesized according to previously reported synthetic routes with little modifications (see the Experimental Section in the Supporting Information).[2c,15c] For the sake of simplicity, we introduce the following abbreviations: (1) CdSe(S)/CdS(L) for "small" core/"large" crown NPLs (having average lateral dimensions of 41.4 ± 3.5 nm in length and 13 ± 1.8 nm in width) with a very small CdSe core of only few nanometers in diameter; (2) CdSe(L)/CdS(S) for "large" core/"small" crown NPLs (with total lateral dimensions of 38.1 ± 5.2 nm in length and 13.6 ± 2.1 nm in width) which possess a large rectangular CdSe core (average length of 31 ± 4.5 nm and a width of 7 ± 1.5 nm) and a relatively thin CdS crown; and (3) CdSe(L)/CdS(L) for "large" core/"large" crown NPLs with lateral dimensions of 54.1 ± 7 nm in length and 22.7 ± 4.2 nm in width, with a large rectangular CdSe core of the same size as in the CdSe(L)/CdS(S) NPLs. The average size of the NPLs mentioned above is measured from TEM images. A detailed characterization of the NPLs by means of spectroscopic and structural analysis is presented in Figures S1 and S2 in the Supporting Information.

Based on our previous report, Pt domains are grown on these NPLs by thermal reduction of Pt(acac)$_2$ (molar precursor ratio of Cd/Pt = 1:5) in the presence of oleylamine as the reducing and stabilizing agent (see the Supporting Information).[2c] The bright-field TEM images of the Pt-decorated NPLs are shown in **Figure 1**. Similar to our previous observations,[2c] the small quasi-spherical Pt domains can be found all around the edges of all types of CdSe and CdSe/CdS NPLs. The Pt domains have an average diameter of 2.8 ± 1 nm and are present separately from one another, (see insets of Figure 1) forming pearl necklace-type morphology. The size and shape of the NPLs are retained during the Pt domain growth. We do not observe any presence of Pt domains at the interface of the CdSe core and CdS crown junctions. In our previous work on CdSe NPLs, TEM analysis of the samples collected during the early stage of reactions proved that the nucleation of Pt domains starts at the corner and at the edges of the NPLs, where maximum crystal defects are present.[2c] We presume that the growth of the Pt domains
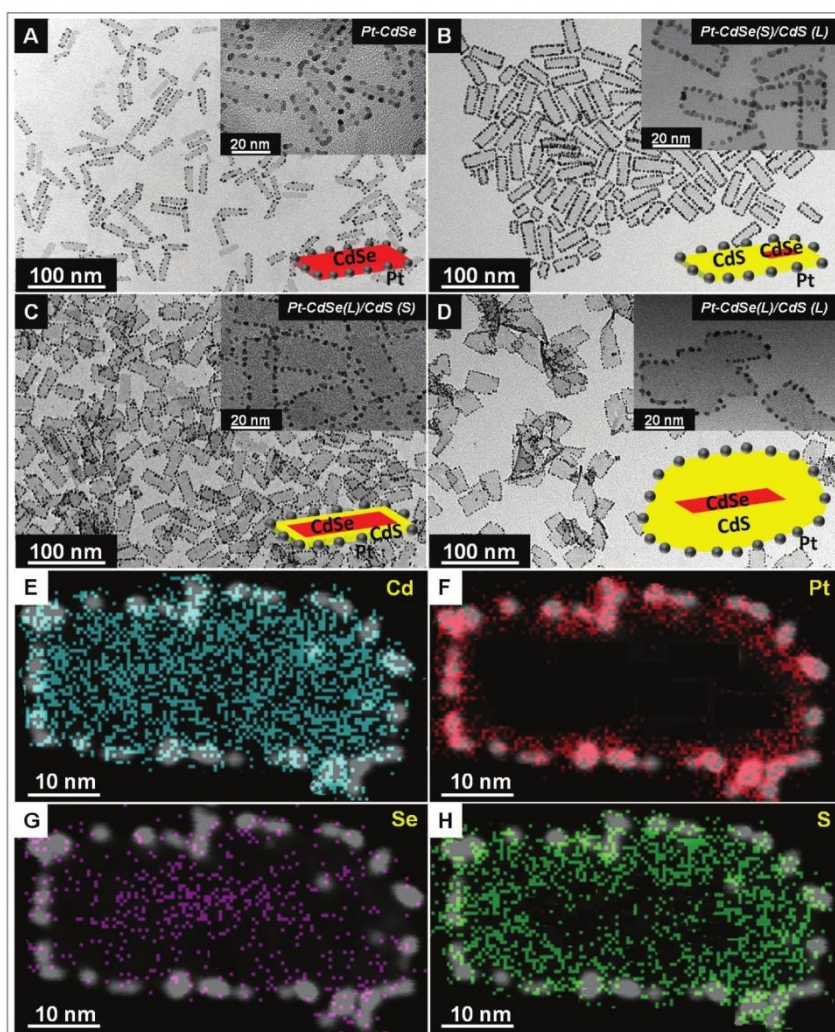
Figure 1. TEM images of Pt-decorated CdSe and CdSe/CdS NPLs with variable CdSe core and CdS crown dimensions. A) Pt on CdSe, B) Pt on CdSe(S)/CdS(L), C) Pt on CdSe(L)/CdS(S), D) Pt on CdSe(L)/CdS(L), respectively, with schematic illustrations of the respective systems. Insets are higher resolution TEM images confirming the presence of quasi-spherical Pt domains around all the edges of the NPLs at regular distances from each other. E–H) HAADF-STEM images averaged with STEM-EDXS mappings for the elements Cd, Pt, Se, and S of Pt-decorated CdSe(L)/CdS(L) NPLs.

on top and bottom surface of the NPLs is restricted because of the zinc blend crystal planes of the CdSe and CdSe/CdS NPLs, which are terminated with Cd ions, as shown by Lim et al.[23] Furthermore, these Cd ion-terminated crystal facets {100} are capped with oleic acid that might hinder the approaching of Pt precursors from these sides. Therefore, the morphologies that we observe for our NPLs is in contrast to previous observations of Elmalem et al.[24] and Habas et al.[9b] where Pt domains were found all over the surface or only at the tips of the CdSe or CdS semiconductors' nanorods. A possible explanation was suggested by the authors considering the wurtzite crystal structure of the nanorods, where the lattice planes are alternatively composed of Cd and S atoms. Apart from that, the tips of the

nanorods along the ⟨001⟩ axis have the maximum amount of crystal defects, which promotes tip-selective metal domain growth.[3b,9b] Moreover, the nanorods are c-axis elongated objects exposing {001} type facets at the apexes and different prismatic facets along longitudinal sidewalls, hence a different seeding behavior toward the accommodation of the metal domains is expected accordingly.

Notably, due to the very low thickness (≈1.5 nm) of the NPLs and the low contrast difference between CdSe and CdS compartments, it is difficult to distinguish these two materials via TEM. Hence, the existence of Pt, CdSe core, and CdS crown cannot be observed simultaneously in the bright field TEM images, as shown in Figure 1A–D. In order to analyze the

FULL PAPER

elemental compositions of the Pt-decorated NPLs, and to prove the presence of a CdSe core inside the NPLs, we have further investigated the structures with high-angle annular dark field scanning transmission electron microscopy (HAADF-STEM) and also with STEM-EDXS mapping. The results for Pt-decorated CdSe(L)/CdS(L) NPLs are presented in Figure 1E–H (for elemental mapping of the Pt-decorated small CdSe core with large CdS crown and Pt decorated large CdSe with small CdS crown, see Figures S3 and S4, in the Supporting Information).

It can be inferred that the Pt domains (bright white spots) are present only at the edges of the NPLs. The elemental mapping of the selected area shows that Cd covers the entire surface of the NPLs, whereas Se and S can be found predominantly at the middle and surroundings of the NPLs, respectively. These observations strongly support our findings, i.e., the existence of rectangular CdSe core at the middle surrounded by a CdS crown with Pt domains present only at the edges of the NPLs. Similar results were also obtained for the other two types of Pt-decorated NPLs. In the case of Pt-decorated CdSe(S)/CdS(L), the presence of Se is not detected with accuracy due to (i) the very small size of the CdSe core as well as (ii) the EDXS signal from Pt and Se overlap, making it more difficult to distinguish between these two elements, especially when only weak signals are detected.

The resulting NPLs solutions were adjusted to have the same Cd ion concentration (measured by atomic absorption spectroscopy) and subsequently characterized by UV–vis absorbance spectroscopy and powder XRD. The results are depicted in Figure S5 (Supporting Information). After the Pt domain growth, the heavy hole–electron (hh–e) and light hole–electron (lh–e) transitions at 556 nm and at 518 nm, characteristics of the CdSe core in a core/crown NPLs, are weaker and broadened in comparison to the pristine NPLs without any metal domains (see Figures S1 and S5A, Supporting Information). In previous reports, similar effects of spectral broadening have also been observed after metal domain growth on CdSe.[2c,24] In the present case, although the CdSe core is insulated laterally by a CdS crown, the electron is expected to still be transferrable to the metal domain since the conduction bands of CdSe and CdS are relatively similar (energy difference of ≈100 meV according to Li et al.).[25] Due to the direct contact of the metallic Pt domains with CdS crown, the excited electrons can travel quickly (typically in the order of picoseconds time range) to the Fermi level of Pt (8.8 eV).[14c] The broadening of the absorbance spectra can be attributed to the change of electron and hole wave functions and overall increased oscillator strength and background absorption by the Pt domains (strong interband d-sp transitions of the Pt domains)[26] throughout the whole UV–vis to near IR wavelength regime.[17,24] The photoluminescence (PL) emission spectra of the nanoheterostructures show a complete quenching of the fluorescence intensity upon Pt domain growth (not shown), which again indicates effective charge transfer from semiconductor to the metal domain.

From the XRD pattern of the Pt-decorated NPLs (see Figure S5, Supporting Information), the main reflections of Pt, such as 111, 200, 220, and 311, and in the case of CdSe and CdS, such as 111, 200, 220, and 311 can be clearly derived. All the reflections belong to a face-centered cubic (fcc) lattice system. A closer look on the XRD pattern reveals a broadening of the

prominent 111 reflection of Pt, which appears at $2\theta = 39.7°$. This effect can be attributed to the overlapping of the 220 reflections from CdSe and CdS crystals and the 111 reflection of the Pt, due to their close proximity. A similar broadening effect is also observed for other reflections of Pt, (e.g., 200, 220, 311, and 222) due to overlap with nearby CdSe and CdS reflections.

2.2. Au Domain Growth on CdSe/CdS Core/Crown Nanoplatelets

At this point, it is interesting to see what happens when we grow only Au domains on the core/crown NPLs. Therefore, we have also investigated Au domain growth on these three different CdSe/CdS core/crown semiconductor NPLs following the same procedure as reported in ref. [2c] (see the Supporting Information for details) and have compared the morphologies by TEM analysis. The TEM images (see Figure S6, Supporting Information) show interesting morphologies. For example, small (1.5–2 nm) spherical gold domains are found at the edges of the NPLs with small CdSe core and large CdS crown (similar to the Pt domain growth), while in the case of large CdSe core with small and large CdS crown, very small (≈1 nm) Au domains along with many larger Au islands (4–6.5 nm) are observed on the surface of the NPLs. In the case of Au-decorated CdSe(L)/CdS(L), we observe sample agglomeration after 2–3 d of synthesis, most likely due to the larger size and interconnections of the NPLs through Au domains (see Figure S6C, Supporting Information). A possible explanation for the absence of Au domains in the center could be that the core in CdSe(S)/CdS(L) NPLs is only a few nanometers in dimension and shielded laterally by a large CdS crown, so that the Au preferably nucleates at the corners and edges of the NPLs with maximum crystal defects, while in most cases the CdSe cores do not come in contact with any Au precursor ions (only 3 out of 25 NPLs have small Au domains ≈1.5 nm at the CdSe core location). Remarkably, the colloidal solution also exhibits low fluorescence emission, which could be due to the presence of very few residual CdSe(S)/CdS(L) NPLs without any metal domain on it, which retains their individual fluorescence emission in the ensemble. In the case of NPLs with large CdSe cores with small or large CdS crown, the CdSe core is more exposed (due to its longer lateral size as mentioned before) to the Au precursors, and as a result we observe relatively large Au domains preferably located at the CdSe/CdS interface or on the CdSe core. In these two cases, complete quenching of the fluorescence emission is observed. The absorbance spectra of the Au-decorated NPLs exhibit CdS onsets around ≈430 nm with long tail at higher wavelength and are similar to the spectra of Au on CdSe NPLs with no distinct plasmon band of Au as observed in Figure S7 (Supporting Information).[2c]

2.3. Synthesis and Characterization of Quaternary Nanoplatelets

Furthermore, we have expanded our synthetic route to grow Au domains on the previously synthesized Pt-decorated CdSe/CdS NPLs. The bright field overview TEM images are shown in **Figure 2**, where we compare the morphologies obtained after the Au domain growth on three different types of CdSe/CdS
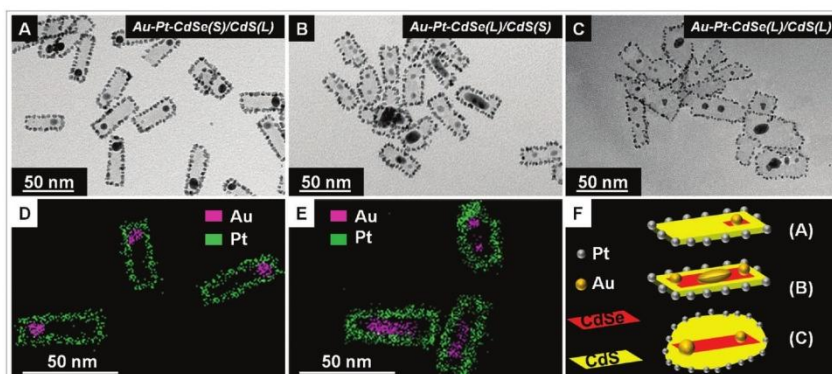
FULL PAPER

Figure 2. TEM images of Au domain growth on Pt decorated NPLs with variable CdSe core and CdS crown dimensions. In all three cases, Au domains are only found at the CdSe core positions and not at the edges of the NPLs. A) Small CdSe cores with large CdS crowns result in a single Au domain near the core. B,C) Large CdSe cores with small and large CdS crowns result in either several Au domains at the CdSe/CdS interface or one single large domain near the CdSe core. D,E) STEM-EDXS mapping of the Au growth on Pt-decorated CdSe(S)/CdS(L) and CdSe(L)/CdS(S) NPLs, respectively. F) Schematic drawings derived for the three different morphologies of the nanoheteroplatelets, following the TEM and STEM-EDXS observations.

NPLs decorated with Pt. Schematic drawings are included for better understanding of the observations. Notably, for all core/crown geometries investigated, we found large Au domains near the CdSe core and no Au domains are found at the edges of the NPLs. In the case of Au growth on Pt-decorated NPLs with small CdSe core, we often observe the presence of only one spherical Au domain (5–7 nm) on the surface, presumably at the site of the very small CdSe core. In the other two cases, e.g., Pt-decorated CdSe(L)/CdS(S) and CdSe(L)/CdS(L), we observe the presence of either one large elongated domain or several (mostly two) medium-sized Au domains near the core of the NPLs. By comparing the CdSe core position as obtained from STEM-EDXS analysis (as shown in Figure 1 and Figure S3 (Supporting Information)), we conclude that in all three cases, gold growth takes place at the interface of the CdSe core and the CdS crown, or solely on the CdSe core. This region-selective nucleation of Au could be due to crystal strain (lattice mismatch between CdSe and CdS),[14a] and the high affinity of stable Au−Se bond formation.[11b,27] Interestingly, the possibility of additional Au growth around the Pt domains or in between two adjacent Pt domains at the interface of CdS–Pt can be ruled out from the observations of the STEM-EDXS mapping, shown in Figure 2D,E. Here, the signals from the Au domains are obtained only from the middle of the NPLs, where the CdSe core is present. The other elements detected are present as per the previous observations from STEM-EDXS mapping. We did not find Au signal around the Pt domains or from the vacant space in between two Pt domains, which is in good agreement with previous observations from bright field TEM analysis.

On the contrary, when growing Pt domains on the Au-decorated CdSe(S)/CdS(L) NPLs, it is noticed (the bright field TEM images, HAADF-STEM images, and the STEM-EDXS mapping are shown in **Figure 3**) that the average metal domain size at the edges of the NPLs has increased from 1.6 to 3.4 nm. Instead, in this order of metal domain growth, there are no Pt domains at the center or at the CdSe core position. The increase in domain size is most likely due to the overgrowth of Pt on the previously present Au domains. In the STEM-EDXS mapping we observe

equal distribution of the Pt and Au surrounding the edges of the NPLs, which could be due to Au–Pt alloy formation or core/shell (Au/Pt)-type geometry. The absence of the Pt domains at the center of the NPLs is most likely due to thermodynamically less favored Pt−Se bond formation as discussed later in this paper. The three different types of quaternary morphologies achieved in this study with small CdSe core and large CdS crown are schematically presented in Figure 3. The absorbance spectra collected after the Au growth on Pt-decorated NPLs show complete smearing of the CdSe excitonic transitions (hh–e and lh–e). This effect was also observed in our previous report when we grew only Au domains on the CdSe NPLs[2c] (see Figure S8 A, Supporting Information) and could be attributed to the strong mixing of the electronic states and changes in the electron and hole wave functions as mentioned earlier.

To attain in-depth characterization of the NPLs, and to see the connections of the metal domains with the NPLs, the structures are characterized with high resolution TEM (HRTEM) analysis. The HRTEM images of the Pt growth on CdSe(S)/CdS(L) and Au growth on Pt-decorated CdSe(S)/CdS(L) NPLs are shown in Figure S9 (Supporting Information). Here, the lattice planes of the crystalline metal domains can be resolved clearly. However, due to the very low thickness (only ≈1.5 nm) of the NPLs, and also due to the high contrast difference between the metal domains and the semiconductor, the lattice planes at the interface of the NPL and the metal domains cannot be resolved simultaneously to gain more information about the hetero junctions. This difficulty was also faced previously by several other researchers while investigating the metal-decorated inorganic structures under the conditions of HRTEM imaging.[2c,4c,15c] Therefore, HRTEM investigations, in this case, do not help revealing the intimate structures at atomic resolution. So, we have investigated the structures and interpreted our observations following the results of STEM-EDXS analysis.

Summarizing our findings on metal growth on CdSe/CdS core/crown NPLs, it can be concluded that Pt domains can only grow at the edges of the NPLs (both CdSe and CdSe/CdS), while Au domains can grow at the edges, as well as at the
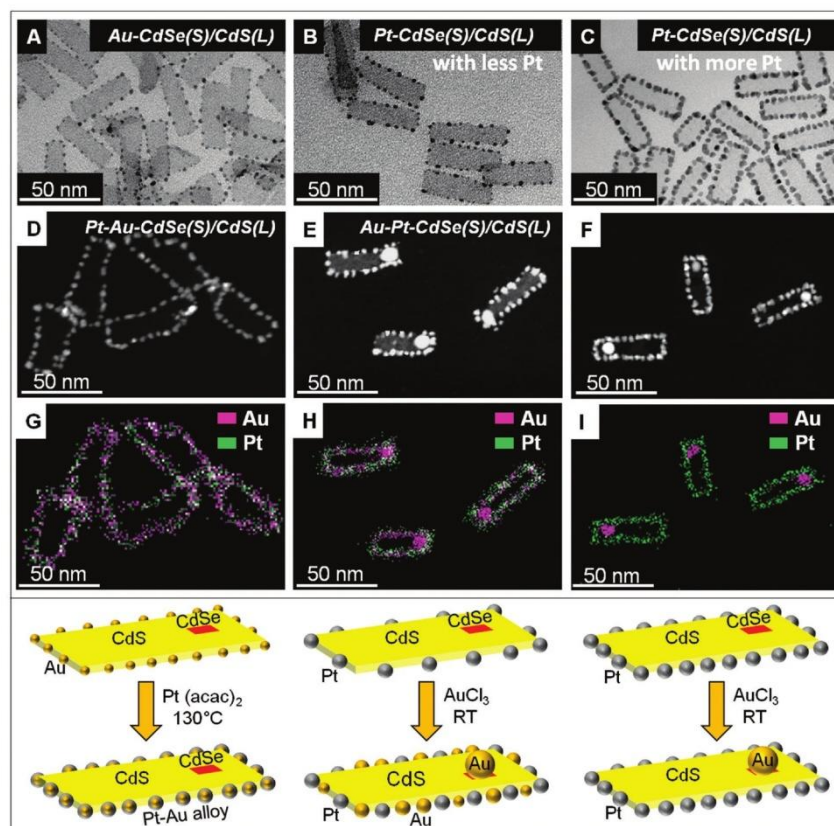
Figure 3. (top) A) TEM image of Au-decorated NPLs with small CdSe core, B,C) TEM images of Pt-decorated CdSe(S)/CdS(L) NPLs with less and more Pt content. HAADF-STEM image of the products obtained after D) Pt overgrowth on Au decorated CdSe(S)/CdS(L) NPLs and E,F) Au overgrowth on Pt-decorated CdSe(S)/CdS(L) NPLs with less and more Pt content. G–I) STEM-EDXS mapping of the respective quaternary NPLs. (bottom) Schematic diagrams of three different types of quaternary NPLs achieved from small CdSe core and large CdS crown NPLs. (Left) Pt domain growth on Au-decorated NPLs results in Pt–Au alloy or core/shell type morphology. (Middle) Au domain growth on Pt-decorated NPLs initially having less Pt islands results in one large domain at the CdSe core position and small domains at the vacant place besides the Pt domains at the CdS edges. (Right) Au domain growth on Pt–decorated NPLs having more Pt islands results in only one large Au domain at the CdSe core position and no Au at the edges. The schematic drawings are presented on the basis of observations from TEM and STEM-EDXS analysis.

interface and/or on the CdSe core. We presume that the edge-selective growth of Pt is favored due to the more stable soft-soft interaction between Pt and S than Pt and Se (according to the Pearson hard-soft acid-base theory, Pt^{2+} is a soft Lewis acid and both Se^{2-} and S^{2-} are soft Lewis bases).[28] Moreover, previous studies prove that platinum–sulfur complexes are more stable than platinum–selenium complexes due to the formation of a stronger π-bond with S than Se.[29] Therefore, the slow nucleation of Pt always happens at the edges of the NPLs, most likely via the formation of tiny Pt clusters at the beginning, which enlarges during the course of reactions, and the size of the NPLs remains almost invariant.[2c,14d] While growing only Au on the CdSe/CdS NPLs, we observe small Au domains surrounding all edges of all three types of NPLs, which indicates that defects present at the edges of CdS crown could induce Au growth at these sites. Specifically, in the case of NPLs with small core, most of the time the tiny CdSe cores do not come in contact with the Au precursor, hence the Au

precursor ions present in the medium are reduced only at the edges. The NPLs with a large CdSe core have large Au islands on the surface, which could be due to the better availability of the exposed CdSe core and the higher affinity of relatively more stable Au–Se bond formation (though Se and S both belong to the same group, the atomic radius and electronegativity of Se is closer to Au than S, hence the Au—Se bond is covalently more stronger than the Au—S bond).[27a,b] Most possibly a parallel reaction occurs: one is the nucleation at the CdSe core position and the other is the nucleation at the CdS edges. In order for the metal precursors (Au or Pt) to access the Se atoms present at the core surface, the surface Cd atoms from the top layers (as both layers are terminated with Cd ions)[23] need to be replaced, which is achieved with Au due to the high affinity of relatively stable Au–Se bond formation.

In previous studies regarding the formation of complex nanoheterostructures, for example, growth of Au, Ag, Ni, and Pd on Pt-decorated Fe_2O_3 or Co deposition on Pt tipped

137

Noble Metal Growth on Nanoplatelets

**ADVANCED
SCIENCE NEWS**
www.advancedsciencenews.com

*ADVANCED
FUNCTIONAL
MATERIALS*
www.afm-journal.de

FULL PAPER

CdSe/CdS nanorods, the second metal was promptly found to grow on the existing Pt domains.[14c,20a] It was anticipated that the Pt domains present on the semiconductor act as a sink of electrons to reduce the second metal domain on it, although in our experimental conditions (room temperature) of Au growth on Pt decorated NPLs with variable CdSe core and CdS crown size, we observe large Au domains to be present at the middle of the NPLs only and not on the Pt domains (proved with STEM-EDXS mapping, see Figure 2D,E). The possible reasons could be (i) the NPLs edges are already surrounded by small Pt domains, hence the nucleation of Au at these sites is not preferred due to steric hindrance as well as (ii) due to nonavailability of unsaturated S atoms (which are already occupied by Pt). Presumably, due to the crystal strain present at the interface of CdSe/CdS (caused by lattice mismatch) and high tendency of stable Au—Se bond formation, larger Au domains are formed at CdSe core positions.[30] To check the selectivity of the Au growth and also to prove the effect of steric hindrance, additional experiments were conducted with less Pt-containing CdSe(S)/CdS(L) NPLs: in that case, we observe small Au domains at the CdS edges besides the Pt domains and also one large Au domain at the CdSe core position (confirmed by STEM-EDXS analysis shown in Figure 3). This observation indicates that when the NPLs edges are heavily crowded with Pt domains, Au prefers to nucleate at the CdSe core position, and when the edges are less crowded, Au domains are formed both at the edges and at the core position.

2.4. X-Ray Photoelectron Spectroscopy of the Heteronanoplatelets

In order to investigate the oxidation state of the metal domains present on the NPLs, we have studied X-ray photoelectron spectroscopy (XPS) of the pristine and metal-decorated ternary and quaternary NPLs. The results of the XPS analysis are shown in **Figure 4**. In pure NPLs, the binding energy peaks at ≈405.7 and ≈412.5 eV can be attributed to Cd $3d_{5/2}$ and $3d_{3/2}$ doublets (appear due to spin-orbit splitting), and confirm the presence of Cd in the +2 oxidation state.[2c,31] Notably, in the overview

spectra, it can be noticed that the binding energy peaks of Cd do not shift after the metal decoration, which proves that the metal domain growth does not change the chemistry of the CdSe/CdS NPLs. After the Au deposition on the NPLs, distinct peaks can be observed at ≈84.1 and ≈87.7 eV, which correspond to $4f_{7/2}$ and $4f_{5/2}$ binding energy peaks of Au in its zero oxidation state.[32] Similarly, in the case of Pt-decorated NPLs the $4f_{7/2}$ and $4f_{5/2}$ peaks of Pt appear at ≈70.9 and ≈74.1 eV, respectively. The metallic Pt (zero oxidation state) has $4f_{7/2}$ and $4f_{5/2}$ binding energy peaks at ≈71.0 and ≈74.3 eV.[33] Hence, it can be concluded that Pt is also present in its zero oxidation state.[33] In the other two quaternary systems, the presence of binding energy peaks of Au and the Pt can be distinguished at the same time. Here, the $4f_{7/2}$ and $4f_{5/2}$ signals appear at the same position as of the ternary systems; the only difference observed here is the signal intensity. After the Au domain growth on Pt-decorated NPLs, the 4f peaks of Au and Pt have almost similar intensity, whereas when the growth order is reversed, the Au 4f signal intensity is lower than Pt. This could be due to the formation of core/shell (Au/Pt) type geometry as predicted earlier. Here, it is possible that the electrons emitted by the Au atoms are scattered by the Pt atoms on top, resulting in a lower Au 4f signal. The NPLs also exhibit a sharp binding energy peak centered at ≈285.3 eV, which can be attributed to the 1s signal of carbon, corresponding to the surfactant or long alkyl chain present on the surface of the NPLs.[11b] The peaks appearing at ≈333.7 and ≈353.1 eV can be assigned to Au $4d_{5/2}$ and Au $4d_{3/2}$, respectively. Also, the binding energy peaks at ≈315.6 and ≈332.1 eV correspond to Pt $4d_{5/2}$ and Au $4d_{3/2}$, respectively. Apart from that, no other elements or impurities are detected.

2.5. Metal-Decorated NPLs as Catalyst for Photocatalytic H$_2$ Generation

In order to see the photocatalytic activity of the metal-decorated NPLs in steady state H$_2$ gas generation through the photoreduction of water, a phase transfer from organic to aqueous medium is conducted with 11-mercaptoundecanoic acid (MUA) as the phase transfer reagent, following a procedure reported
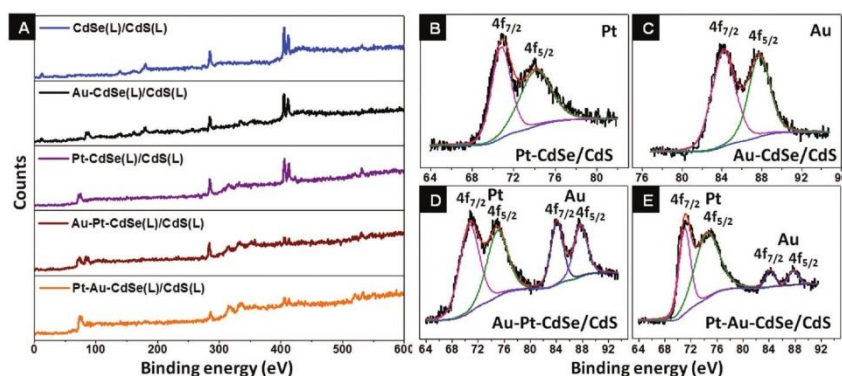

Figure 4. A) Overview XPS spectra of the pure and metal-decorated CdSe(L)/CdS(L) NPLs. B) Binding energy peak of Pt 4f, and C) Au 4f for Pt- CdSe(L)/CdS(L) and Au- CdSe(L)/CdS(L) NPLs, respectively. D) Binding energy peak of combined Pt and Au 4f for Au growth on Pt-decorated CdSe(L)/CdS(L) NPLs. E) Binding energy peak of combined Pt and Au 4f for Pt growth on Au-decorated CdSe(L)/CdS(L) NPLs.
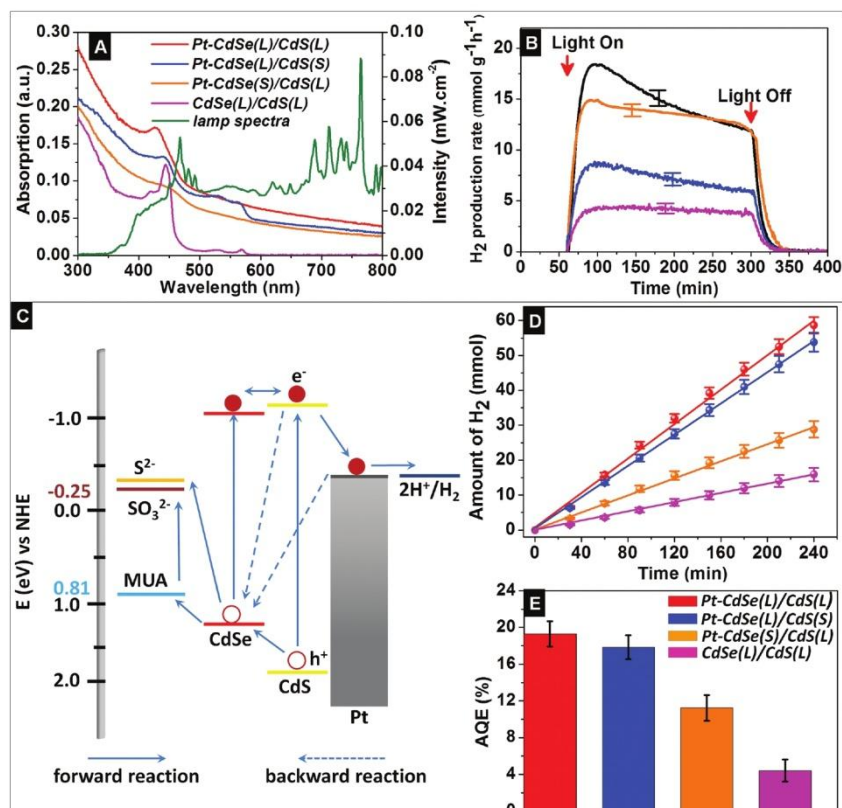
Figure 5. A) UV–vis absorption spectra of the Pt-decorated CdSe/CdS core/crown NPLs in aqueous medium and the xenon-arc lamp spectrum measured in front of the glass reactor. B) Photocatalytic H_2 gas generation through water reduction half reactions using Pt-decorated CdSe/CdS NPLs and CdSe(L)/CdS(L) NPLs without Pt domains. "Light On" and "Light Off" signify the illumination on and off, respectively. C) Schematic diagram of the energy transfer processes involved in H_2 generation (upper panel) and (below) processes of charge carrier separation and H_2 generation, exemplarily shown for Pt-decorated CdSe(L)/CdS(S) NPLs. D) Total amount of H_2 generation in the course of reaction. E) Comparison of the AQE of the catalyst.

by Kodanek et al.[23c,31] The absorption spectra (measured in an integrating sphere due to the scattering nature of the samples) of the Pt-decorated NPLs after the phase transfer to aqueous solution are shown in **Figure 5**. Notably, here the whole absorption spectra of the Pt-decorated NPLs is shifted to a longer wavelength by 13–14 nm. The shift of the absorption spectra was observed previously during the phase transition of CdSe/CdS core/crown NPLs,[23c] and can be attributed to the addition of two additional S layers on the top and bottom surface, i.e., {100} lattice planes of the NPLs. In previous reports,[15a,b] it was observed that the absorption or the emission peak positions of the NPLs strongly depend on their thickness. Presumably, the increase in thickness by the addition of two S layers (≈0.5 nm) reduces the quantum confinement in the z direction of the NPLs and hence an overall shift of the absorption spectra is observed.[23c,31] A comparison of the absorption spectra, before and after the phase transfer, is presented in Figure S8C,D in the Supporting Information. The TEM images of the Pt-decorated CdSe/CdS NPLs after phase transfer are shown in Figure S10 (Supporting Information). It should be noted that after the phase transfer, the aqueous solution of Pt decorated CdSe

core NPLs is found to be highly unstable; aggregation of the particles can be observed within 2–3 h of phase transfer, while the Pt decorated core/crown systems are found to be relatively stable, and hence the core/crown based nanoheteroplatelets are chosen as catalyst for further investigation of photocatalytic H_2 gas generation, as discussed later in this paper.

The II–VI metal-chalcogenide semiconductors, such as CdSe or CdS or the combination of both, are highly promising for photocatalytic reactions because of their suitable band gap, which allows visible light absorption, long-term stability, and fast redox chemical reactions on their surface.[3b,6b,9e,34] In recent reports, the nanoheterostructures, e.g., Pt-tipped CdSe/CdS nanorods or Ni-decorated CdS nanosheets are found to be highly advantageous with very high AQE (up to near unity) upon photoexcitation with monochromatic light sources, e.g., by light emitting diodes or lasers.[3a,8,9c,35] These results have motivated us to investigate the photocatalytic H_2 generation efficiency of our nanoheteroplatelets using a white light Xe-arc lamp as the light irradiation source. The impact of both the metal domains (Pt and Au-Pt) and the semiconductor compartments (CdSe and CdS domain sizes) on the

rate of H_2 gas generation is investigated. The results are compared with pure NPLs without any metal domains and also with Pt-decorated CdSe/CdS nanorods. The colloidal synthesis, phase transfer, and the morphological and spectroscopic characterizations of Pt-decorated CdSe/CdS nanorods are presented in detail in Figures S10D and S11 (Supporting Information).

The results for the H_2 gas generation for pure and Pt-decorated CdSe/CdS NPLs are shown in Figure 5B. The same measurements for Au on Pt decorated NPLs and Pt decorated CdSe/CdS nanorods are shown in Figures S7B and S10D (Supporting Information), respectively. Notably, the rates of H_2 generation reach a maximum value after a few minutes of the light illumination and thereafter a gradual decrease ($\approx$0.2–2 mmol h^{-1}, depending on the type of the NPLs) in the production rate can be observed during the course of the reaction. This effect could be attributed to the consumptions of the hole scavengers or the formation of reaction intermediates that block the active surface of the catalyst.[9e,36] The removal of MUA ligands from the surface due to the formation of disulfide bonds by the photoexcited holes can also lead to aggregation of the NPLs in the system and can cause a reduction of the H_2 generation rate.[3a,37] After a total time of 4 h of illumination, the light source was turned off and the H_2 production rates decreased to the value of the baseline. The total amount of H_2 generation over the period of light illumination is shown in Figure 5D. The slope of the straight line obtained from the graphs denotes the average H_2 production rate. The average H_2 production rates per gram of Cd ion concentration are 15.5, 13.8, 7.55, and 8.3 mmol h^{-1} for the Pt-decorated CdSe(L)/CdS(L), CdSe(L)/CdS(S), CdSe(S)/CdS(L), and Au on Pt-decorated CdSe(L)/CdS(L) NPLs, respectively. The pure CdSe(L)/CdS(L) NPLs show H_2 generation rate of 4.40 mmol h^{-1}, which means that under the same reaction conditions the rate of H_2 production is much higher in all cases of Pt-decorated NPLs than in the case of NPL without any Pt domain. The higher H_2 production rates of the nanoheteroplatelets can be attributed to the fast charge carrier separation at the metal–semiconductor interface.[3a]

A schematic drawing concerning the band alignments (the band edge energy positions corresponds to pH = 7) and the electron–hole transport processes are presented in Figure 5C.[3a,9c] Upon photoirradiation, the electrons are excited from the valence band (VB) to the conduction band (CB) of the semiconductor and subsequently transferred to the metal domains, where the reduction of the H$^+$ ions takes place. The photoexcited holes (h$^+$) are confined in the CdSe core (due to the energy difference of around 500 meV between the VB of CdSe and CdS, which has a type I band gap alignment).[25,38] The MUA ligands present on the surface of the NPLs play an important role by accepting the photoexcited holes and at the same time preventing the degradation of the semiconductor domains.[37] It should be noted that the electron transfer from the CB of the semiconductor to the Pt tips is much faster (in the picoseconds regime)[9c,17] than the hole transfer from the surface of the semiconductor to the electron donors (in the couple of nanosecond regime).[9c] In previous reports of photocatalytic H_2 generation with Pt decorated CdSe/CdS nanorods as catalyst, the removal of holes from the surface of the nanocrystals to the electron donor has been illustrated as the key rate limiting step or the driving force of photocatalytic H_2 generation.[3a,9c]

Hence, in this study we have also compared the holes removal rates using PL decay analysis of the NPLs in the presence and absence of the electron donor.

The AQE calculated at the maximum rate of H_2 evolution are 19.3% ± 1.4%, 17.8% ± 1.3%, 13.2% ± 1.4%, 10.2% ± 1.6%, and 4.4% ± 1.2% for the Pt-decorated CdSe(L)/CdS(L), CdSe(L)/CdS(S), CdSe(S)/CdS(L), Au on Pt-decorated CdSe(L)/CdS(L), and pure CdSe(L)/CdS(L), respectively. Notably, the AQE obtained for Pt-decorated CdSe/CdS nanorods is 27.8% ± 1.1% under the same reaction conditions. Hence, clearly the Pt-decorated NPLs with large CdSe core and large CdS crown show better performance than other NPLs but compared to Pt-decorated nanorods, the performance is less. A probable explanation for this could be the higher colloidal stability of the aqueous nanorods over the NPLs under the same reaction conditions. However, in this regard one has to consider that the nanorod synthesis is much better established in literature than NPL synthesis, with at least 10 years more development time. Having this in mind, it is surely not completely speculative that the NPL-based heterostructures might become more efficient in the near future by optimizing synthesis and phase transfer protocols. The observed differences in the H_2 generation of the nanoheteroplatelets under consideration are discussed in detail in the Supporting Information. Our findings in these studies clearly indicate that the Pt-decorated NPLs are promising catalysts for future photocatalytic reactions, as they show effective charge carrier separation at the metal–semiconductor interface.

The possible ways to improve the hydrogen generation performance need another study and probably could be achieved by optimizing the type and the amount of the surface capping ligands to improve the overall colloidal stability of the catalyst in the reaction medium or by using hydrogels of these NPLs, where precipitation can be avoided effectively.[31,37,39] It could also be achieved by controlling the cluster size, number of metal domains present (less number of Pt domains results in higher efficiency),[40] pH of the medium, or by utilizing a suitable redox couple, e.g., hydroxyl anion/radical as suggested by Simon et al.[3a]

3. Conclusion

We have successfully synthesized unprecedented multicomponent metal–semiconductor nanostructures by growing Pt and Au domains on CdSe/CdS NPLs of variable core and crown dimensions. In all cases, independent of the CdSe core and CdS crown size, Pt domains are found only at the edges of the NPLs with closed pearl necklace morphology. In the case of decoration of the NPLs only with Au, we observed morphologies with small quasi-spherical Au domains surrounding the edges, and single or multiple bigger Au islands on the surface of the NPLs, depending on the CdSe core and CdS crown dimensions. Furthermore, quaternary systems are obtained by additional Au/Pt growth on the Au/Pt decorated CdSe/CdS NPLs, where the sequence of the metal domain growth controls the final morphologies. The systems developed here represent the combination of three or more disparate materials on the same nanostructure and also is an innovative contribution to

FULL PAPER

the class of advanced materials with multiple functionalities. Self-assembly of these structures, e.g., tip-to-tip or side-by-side by means of postchemical modification, solvent exchange, or by nanowelding could provide a bottom-up approach for the fabrication of photovoltaic, electronic, or sensing devices. As an application, the metal-decorated NPLs are employed as catalyst for the photocatalytic H_2 generation through water reduction reaction. The Pt-decorated CdSe/CdS system with larger CdSe core and larger CdS crown dimensions exhibit the highest apparent quantum efficiency of 19.3% ± 1.4% under UV–vis light irradiation. This performance could even be improved in future research, focusing on the variation of size and number of noble metal domains present on the NPLs, and also by increasing the colloidal stability of the system.

Supporting Information

Supporting Information is available from the Wiley Online Library or from the author.

Acknowledgements

[1] a) U. Banin, Y. Ben-Shahar, K. Vinokurov, *Chem. Mater.* **2014**, *26*, 97; b) T. Mokari, E. Rothenberg, I. Popov, R. Costi, U. Banin, *Science* **2004**, *304*, 1787.

[2] a) T. Mokari, C. G. Sztrum, A. Salant, E. Rabani, U. Banin, *Nat. Mater.* **2005**, *4*, 855; b) A. Figuerola, M. van Huis, M. Zanella, A. Genovese, S. Marras, A. Falqui, H. W. Zandbergen, R. Cingolani, L. Manna, *Nano Lett.* **2010**, *10*, 3028; c) S. Naskar, A. Schlosser, J. F. Miethe, F. Steinbach, A. Feldhoff, N. C. Bigall, *Chem. Mater.* **2015**, *27*, 3159.

[3] a) T. Simon, N. Bouchonville, M. J. Berr, A. Vaneski, A. Adrović, D. Volbers, R. Wyrwich, M. Döblinger, A. S. Susha, A. L. Rogach, F. Jäckel, J. K. Stolarczyk, J. Feldmann, *Nat. Mater.* **2014**, *13*, 1013; b) L. Amirav, A. P. Alivisatos, *J. Phys. Chem. Lett.* **2010**, *1*, 1051.

[4] a) R. Costi, A. E. Saunders, E. Elmalem, A. Salant, U. Banin, *Nano Lett.* **2008**, *8*, 637; b) S. K. Dutta, S. K. Mehetor, N. Pradhan, *J. Phys. Chem. Lett.* **2015**, *6*, 936; c) U. Soni, P. Tripathy, S. Sapra, *J. Phys. Chem. Lett.* **2014**, *5*, 1909.

[5] Y. Wu, J. Xiang, C. Yang, W. Lu, C. M. Lieber, *Nature* **2004**, *430*, 61.

[6] a) S. N. Habisreutinger, L. Schmidt-Mende, J. K. Stolarczyk, *Angew. Chem., Int. Ed.* **2013**, *52*, 7372; b) N. Razgoniaeva, P. Moroz, S. Lambright, M. Zamkov, *J. Phys. Chem. Lett.* **2015**, *6*, 4352.

[7] a) A. Figuerola, I. R. Franchini, A. Fiore, R. Mastria, A. Falqui, G. Bertoni, S. Bals, G. Van Tendeloo, S. Kudera, R. Cingolani, L. Manna, *Adv. Mater.* **2009**, *21*, 550; b) A. Salant, E. Amitay-Sadovsky, U. Banin, *J. Am. Chem. Soc.* **2006**, *128*, 10006; c) M. Meyns, S. Willing, H. Lehmann, C. Klinke, *ACS Nano* **2015**, *9*, 6077.

[8] X. Yu, A. Shavel, X. An, Z. Luo, M. Ibáñez, A. Cabot, *J. Am. Chem. Soc.* **2014**, *136*, 9236.

[9] a) T. Mokari, *Nano Rev.* **2011**, *2*, 5983; b) S. E. Habas, P. Yang, T. Mokari, *J. Am. Chem. Soc.* **2008**, *130*, 3294; c) K. Wu, Z. Chen, H. Lv, H. Zhu, C. L. Hill, T. Lian, *J. Am. Chem. Soc.* **2014**, *136*, 7708; d) K. Wu, W. Rodriguez-Cordoba, T. Lian, *J. Phys. Chem. B* **2014**, *118*, 14062; e) P. Kalisman, Y. Nakibli, L. Amirav, *Nano Lett.* **2016**, *16*, 1776; f) M. G. Alemseghed, T. P. A. Ruberu, J. Vela, *Chem. Mater.* **2011**, *23*, 3571; g) J. W. Ha, T. P. A. Ruberu, R. Han, B. Dong, J. Vela, N. Fang, *J. Am. Chem. Soc.* **2014**, *136*, 1398.

[10] Y. Sung, J. Lim, J. H. Koh, L. J. Hill, B. K. Min, J. Pyun, K. Char, *Cryst. Eng. Commun.* **2015**, *17*, 8423.

[11] a) W. D. Kim, S. Lee, C. Pak, J. Y. Woo, K. Lee, F. Baum, J. Won, D. C. Lee, *Chem. Commun.* **2014**, *50*, 1719; b) L. de la Cueva, M. Meyns, N. G. Bastús, J. Rodríguez-Fernández, R. Otero, J. M. Gallego, C. Alonso, C. Klinke, B. H. Juárez, *Chem. Mater.* **2016**, *28*, 2704.

[12] B. K. Patra, A. K. Guria, A. Dutta, A. Shit, N. Pradhan, *Chem. Mater.* **2014**, *26*, 7194.

[13] a) Z. Sun, Z. Yang, J. Zhou, M. H. Yeung, W. Ni, H. Wu, J. Wang, *Angew. Chem., Int. Ed.* **2009**, *48*, 2881; b) J.-S. Lee, E. V. Shevchenko, D. V. Talapin, *J. Am. Chem. Soc.* **2008**, *130*, 9673; c) A. Wolf, T. Kodanek, D. Dorfs, *Nanoscale* **2015**, *7*, 19519; d) M. Casavola, V. Grillo, E. Carlino, C. Giannini, F. Gozzo, E. Fernandez Pinel, M. A. Garcia, L. Manna, R. Cingolani, P. D. Cozzoli, *Nano Lett.* **2007**, *7*, 1386; e) J. Yang, L. Levina, E. H. Sargent, S. O. Kelley, *J. Mater. Chem.* **2006**, *16*, 4025; f) J. Yang, H. I. Elim, Q. Zhang, J. Y. Lee, W. Ji, *J. Am. Chem. Soc.* **2006**, *128*, 11921; g) R. Costi, A. E. Saunders, U. Banin, *Angew. Chem., Int. Ed.* **2010**, *49*, 4878; h) H. Chauhan, Y. Kumar, J. Dana, B. Satpati, H. N. Ghosh, S. Deka, *Nanoscale* **2016**, *8*, 15802; i) S. Das, B. Satpati, H. Chauhan, S. Deka, M. K. Ghosalya, C. S. Gopinath, T. Bala, *RSC Adv.* **2016**, *6*, 14658.

[14] a) G. Menagen, D. Mocatta, A. Salant, I. Popov, D. Dorfs, U. Banin, *Chem. Mater.* **2008**, *20*, 6900; b) H. Schlicke, D. Ghosh, L.-K. Fong, H. L. Xin, H. Zheng, A. P. Alivisatos, *Angew. Chem., Int. Ed.* **2013**, *52*, 980; c) M. R. Buck, J. F. Bondi, R. E. Schaak, *Nat. Chem.* **2012**, *4*, 37; d) S. Deka, A. Falqui, G. Bertoni, C. Sangregorio, G. Poneti, G. Morello, M. D. Giorgi, C. Giannini, R. Cingolani, L. Manna, P. D. Cozzoli, *J. Am. Chem. Soc.* **2009**, *131*, 12817; e) X. Li, J. Lian, M. Lin, Y. Chan, *J. Am. Chem. Soc.* **2011**, *133*, 672; f) E. Aronovitch, P. Kalisman, L. Houben, L. Amirav, M. Bar-Sadan, *Chem. Mater.* **2016**, *28*, 1546.

[15] a) S. Ithurria, B. Dubertret, *J. Am. Chem. Soc.* **2008**, *130*, 16504; b) S. Ithurria, M. D. Tessier, B. Mahler, R. P. S. M. Lobo, B. Dubertret, A. L. Efros, *Nat. Mater.* **2011**, *10*, 936; c) M. D. Tessier, P. Spinicelli, D. Dupont, G. Patriarche, S. Ithurria, B. Dubertret, *Nano Lett.* **2014**, *14*, 207; d) M. D. Tessier, B. Mahler, B. Nadal, H. Heuclin, S. Pedetti, B. Dubertret, *Nano Lett.* **2013**, *13*, 3321; e) E. Lhuillier, S. Pedetti, S. Ithurria, B. Nadal, H. Heuclin, B. Dubertret, *Acc. Chem. Res.* **2015**, *48*, 22.

[16] Y.-H. Liu, V. L. Wayman, P. C. Gibbons, R. A. Loomis, W. E. Buhro, *Nano Lett.* **2009**, *10*, 352.

[17] K. Wu, Q. Li, Y. Du, Z. Chen, T. Lian, *Chem. Sci.* **2015**, *6*, 1049.

[18] M. Zhukovskyi, P. Tongying, H. Yashan, Y. Wang, M. Kuno, *ACS Catal.* **2015**, *5*, 6615.

[19] a) G. Carraro, D. Barreca, D. Bekermann, T. Montini, A. Gasparotto, V. Gombac, C. Maccato, P. Fornasiero, *J. Nanosci. Nanotechnol.* **2013**, *13*, 4962; b) Q. Simon, D. Barreca, D. Bekermann,

FULL PAPER

A. Gasparotto, C. Maccato, E. Comini, V. Gombac, P. Fornasiero, O. I. Lebedev, S. Turner, A. Devi, R. A. Fischer, G. Van Tendeloo, *Int. J. Hydrogen Energy* **2011**, *36*, 15527; c) M. Cargnello, A. Gasparotto, V. Gombac, T. Montini, D. Barreca, P. Fornasiero, *Eur. J. Inorg. Chem.* **2011**, 4309; d) C. Maccato, D. Barreca, G. Carraro, A. Gasparotto, V. Gombac, P. Fornasiero, *Surf. Coat. Technol.* **2013**, *230*, 219; e) X. Li, J. Yu, J. Low, Y. Fang, J. Xiao, X. Chen, *J. Mater. Chem. A* **2015**, *3*, 2485.

[20] a) L. J. Hill, M. M. Bull, Y. Sung, A. G. Simmonds, P. T. Dirlam, N. E. Richey, S. E. DeRosa, I.-B. Shim, D. Guin, P. J. Costanzo, N. Pinna, M.-G. Willinger, W. Vogel, K. Char, J. Pyun, *ACS Nano* **2012**, *6*, 8632; b) H. Park, W. Choi, M. R. Hoffmann, *J. Mater. Chem.* **2008**, *18*, 2379; c) K. Wu, Y. Du, H. Tang, Z. Chen, T. Lian, *J. Am. Chem. Soc.* **2015**, *137*, 10224; d) P. Wang, J. Zhang, H. L. He, X. T. Xua, Y. D. Jin, *Nanoscale* **2014**, *6*, 13470; e) J.-J. Wang, Z.-J. Li, X.-B. Li, X.-B. Fan, Q.-Y. Meng, S. Yu, C.-B. Li, J.-X. Li, C.-H. Tung, L.-Z. Wu, *ChemSusChem* **2014**, *7*, 1468; f) P. Tongying, V. V. Plashnitsa, N. Petchsang, F. Vietmeyer, G. J. Ferraudi, G. Krylova, M. Kuno, *J. Phys. Chem. Lett.* **2012**, *3*, 3234.

[21] D. O. Sigle, L. Zhang, S. Ithurria, B. Dubertret, J. J. Baumberg, *J. Phys. Chem. Lett.* **2015**, *6*, 1099.

[22] A. W. Achtstein, A. V. Prudnikau, M. V. Ermolenko, L. I. Gurinovich, S. V. Gaponenko, U. Woggon, A. V. Baranov, M. Y. Leonov, I. D. Rukhlenko, A. V. Fedorov, M. V. Artemyev, *ACS Nano* **2014**, *8*, 7678.

[23] a) C. She, I. Fedin, D. S. Dolzhnikov, A. Demortière, R. D. Schaller, M. Pelton, D. V. Talapin, *Nano Lett.* **2014**, *14*, 2772; b) S. J. Lim, W. Kim, S. K. Shin, *J. Am. Chem. Soc.* **2012**, *134*, 7576; c) T. Kodanek, H. M. Banbela, S. Naskar, P. Adel, N. C. Bigall, D. Dorfs, *Nanoscale* **2015**, *7*, 19300.

[24] E. Elmalem, A. E. Saunders, R. Costi, A. Salant, U. Banin, *Adv. Mater.* **2008**, *20*, 4312.

[25] Q. Li, K. Wu, J. Chen, Z. Chen, J. R. McBride, T. Lian, *ACS Nano* **2016**, *10*, 3843.

[26] R. C. Johnson, J. T. Li, J. T. Hupp, G. C. Schatz, *Chem. Phys. Lett.* **2002**, *356*, 534.

[27] a) M. Mingos, in *Gold Clusters, Colloids and Nanoparticles* (Ed: D. M. P. Mingos), Springer, Oxford, UK **2014**; b) S. Mankefors, A. Grigoriev, G. Wendin, *Nanotechnology* **2003**, *14*, 849; c) R. de Paiva, R. Di Felice, *ACS Nano* **2008**, *2*, 2225.

[28] a) R. G. Pearson, *J. Am. Chem. Soc.* **1963**, *85*, 3533; b) R. G. Pearson, *Inorg. Chem.* **1966**, *27*, 734.

[29] J. Pluscec, A. D. Westland, *J. Chem. Soc.* **1965**, 5371.

[30] B. J. Beberwyck, Y. Surendranath, A. P. Alivisatos, *J. Phys. Chem. C* **2013**, *117*, 19759.

[31] S. Naskar, J. F. Miethe, S. Sánchez-Paradinas, N. Schmidt, K. Kanthasamy, P. Behrens, H. Pfnür, N. C. Bigall, *Chem. Mater.* **2016**, *28*, 2089.

[32] a) B. Mahler, L. Guillemot, L. Bossard-Giannesini, S. Ithurria, D. Pierucci, A. Ouerghi, G. Patriarche, R. Benbalagh, E. Lacaze, F. Rochet, E. Lhuillier, *J. Phys. Chem. C* **2016**, *120*, 12351; b) M. Brust, M. Walker, D. Bethell, D. J. Schiffrin, R. Whyman, *J. Chem. Soc., Chem. Commun.* **1994**, 801.

[33] A. S. Arico, A. K. Shukla, H. Kim, S. Park, M. Min, V. Antonucci, *Appl. Surf. Sci.* **2001**, *172*, 33.

[34] H. Zhu, N. Song, H. Lv, C. L. Hill, T. Lian, *J. Am. Chem. Soc.* **2012**, *134*, 11701.

[35] K. Wu, H. Zhu, T. Lian, *Acc. Chem. Res.* **2015**, *48*, 851.

[36] T. A. Kandiel, I. Ivanova, D. W. Bahnemann, *Energy Environ. Sci.* **2014**, *7*, 1420.

[37] K. P. Acharya, R. S. Khnayzer, T. O'Connor, G. Diederich, M. Kirsanova, A. Klinkova, D. Roth, E. Kinder, M. Imboden, M. Zamkov, *Nano Lett.* **2011**, *11*, 2919.

[38] a) L. T. Kunneman, J. M. Schins, S. Pedetti, H. Heuclin, F. C. Grozema, A. J. Houtepen, B. Dubertret, L. D. A. Siebbeles, *Nano Lett.* **2014**, *14*, 7039; b) D. Steiner, D. Dorfs, U. Banin, F. Della Sala, L. Manna, O. Millo, *Nano Lett.* **2008**, *8*, 2954.

[39] S. Sanchez-Paradinas, D. Dorfs, S. Friebe, A. Freytag, A. Wolf, N. C. Bigall, *Adv. Mater.* **2015**, *27*, 6152.

[40] a) F. F. Schweinberger, M. J. Berr, M. Doeblinger, C. Wolff, K. E. Sanwald, A. S. Crampton, C. J. Ridge, F. Jaeckel, J. Feldmann, M. Tschurl, U. Heiz, *J. Am. Chem. Soc.* **2013**, *135*, 13262; b) Y. Nakibli, P. Kalisman, L. Amirav, *J. Phys. Chem. Lett.* **2015**, *6*, 2265.

ADVANCED FUNCTIONAL MATERIALS

Supporting Information

Synthesis of Ternary and Quaternary Au and Pt Decorated CdSe/CdS Heteronanoplatelets with Controllable Morphology

Suraj Naskar, Franziska Lübkemann, Saher Hamid, Axel Freytag, Andreas Wolf, Julian Koch, Irina Ivanova, Herbert Pfnür, Dirk Dorfs, Detlef W. Bahnemann, and Nadja C. Bigall*

Supporting Information

Synthesis of Ternary and Quaternary Au and Pt Decorated CdSe/CdS Heteronanoplatelets with Controllable Morphology

Suraj Naskar, Franziska Lübkemann, Saher Hamid, Axel Freytag, Andreas Wolf, Julian Koch, Irina Ivanova, Herbert Pfnür, Dirk Dorfs, Detlef W. Bahnemann and Nadja C. Bigall*

S. Naskar, F. Lübkemann, A. Freytag, A. Wolf, Dr. D. Dorfs, Dr. N. C. Bigall
Institute of Physical Chemistry and Electrochemistry, Leibniz Universität Hannover, Callinstraße 3A, D-30167 Hannover, Germany
Laboratory for Nano and Quantum Engineering, Schneiderberg 39, 30167 Hannover, Germany

S. Hamid, Dr. I. Ivanova, Prof. D. W. Bahnemann
Institute for Technical Chemistry, Leibniz Universität Hannover, Callinstraße 3, D-30167 Hannover, Germany
Laboratory for Nano and Quantum Engineering, Schneiderberg 39, 30167 Hannover, Germany
Laboratory for Nanocomposite Materials, Department of Photonics, Faculty of Physics, Saint-Petersburg State University, Ulianovskaia street 3, Peterhof, 198504 Saint Petersburg, Russia

J. Koch, Prof. H. Pfnür
Institut für Festkörperphysik, Leibniz Universität Hannover, Appelstr. 2, 30167 Hannover, Germany
Laboratory for Nano and Quantum Engineering, Schneiderberg 39, 30167 Hannover, Germany

E-mail: nadja.bigall@pci.uni-hannover.de

Content

1. Experimental Section

2. Characteristics of 5ML thick *CdSe* and *CdSe/CdS* core/crown NPLs

3. Elemental mapping (STEM-EDXS) of Pt decorated *CdSe(L)/CdS(S)* and *CdSe(S)/CdS(L)*

NPLs

4. Optical and structural characterizations Pt decorated *CdSe/CdS* NPLs.

5. TEM characterizations of Au decorated *CdSe/CdS* NPLs

6. Optical characterizations of Au decorated *CdSe/CdS* NPLs

7. Optical characterizations and H_2 gas generation ability of Au on Pt decorated NPLs. Absorption spectra of the Pt decorated *CdSe/CdS* NPLs after phase transfer

8. HRTEM images of Pt and Au-Pt decorated NPLs

9. TEM micrographs of the Pt decorated *CdSe/CdS* NPLs and *CdSe/CdS* nanorods in aqueous solution

10. Characteristics of Pt decorated CdSe/CdS nanorods and its H_2 gas generation ability

11. Determination of AQE and TOF of hydrogen generation

12. Discussions of the observed differences in TOF and AQE of the catalyst for photocatalytic H_2 generation

13. PL decay analysis of the aqueous NPLs in presence and absence of S^{2-}/SO_3^{2-} electrolyte

1. Experimental Section.

Reagents. Cadmium nitrate tetrahydrate $Cd(NO_3)_2 \cdot 4H_2O$ (99.999%), cadmium acetate dihydrate $Cd(OAc)_2.2H_2O$ (98.0%), sulfur powder S (99.98%), gold(III) chloride $AuCl_3$ (99%), platinum(II) acetylacetonate $Pt(acac)_2$ (97%), sodium myristate (>99%), dodecylamine (DDA) (98%), 1-octadecene ODE (90%), oleic acid (90%), oleylamine (80-90%), 11-mercaptoundecanoic acid MUA (95%), sodium sulfide Na_2S (98 %), potassium hydroxide KOH (> 85%), ethanol (99.5%), toluene (99.7%), n-hexane (>=99%), acetone (>=99%) were purchased from Sigma Aldrich. Sodium sulfite Na_2SO_3 (97%) was purchased from Fisher Chemicals. Cadmium oxide CdO (99.99%), selenium powder 200 mesh (99.999%) were purchased from Alfa Aesar. Tri-n-octylphosphine oxide TOPO (99%) and Tri-n-octylphosphine TOP (97%) were purchased from ABCR. Octadecylphosphonic acid ODPA (99%) and hexylphosphonic acid HPA (99%) were purchased from PCI Synthesis. Nitric acid (>69%) and hydrochloric acid (>37%) were purchased from Fluka. All chemicals were used as purchased without further purification.

Synthesis of 5 ML Thick CdSe and CdSe/CdS Core/Crown NPLs. The 5 ML thick CdSe NPLs were synthesized following a synthesis route as described in previous reports.[1] After the synthesis, the products were purified by centrifugation with a mixture of hexane/ethanol = 3: 1, and finally the dark red precipitate of CdSe NPLs were dispersed in 3 mL of hexane. The synthesis was repeated several times to obtain a stock solution of Cd ion concentration 22 mM (determined from atomic absorption spectroscopy, AAS analysis). These NPLs were used as "seed" for the synthesis of *CdSe(L)/CdS(S)* and *CdSe(L)/CdS(L)* core/crown NPLs, following a procedure described in literature.[1b, 2]. Briefly, a mixture of 3 mL of CdSe NPLs (in hexane) together with 7.5 mL of ODE was degassed for 30 min at 100°C. Thereafter, under Ar flow, the temperature was raised to 240°C and a CdS crown growth mixture (prepared previously by heating 480 mg of $Cd(OAc)_2$, 340 µL of oleic acid and 2 mL of ODE at 150 C for 15 min, after cooling down to room temperature 3 mL of a 0.1 M sulfur precursor solution in ODE were added) was injected continuously at a rate of 8 mL/h for 9 min, to obtain *CdSe(L)/CdS(S)* core/crown NPLs, and for 25 min, to obtain *CdSe(L)/CdS(L)* core/crown NPLs. The whole product was then centrifuged at 3800 g (rcf) with 10 mL ethanol and the precipitate was dispersed in 3 mL of hexane. For the synthesis of *CdSe(S)/CdS(*L) core/crown NPLs, a total amount of 85 mg of cadmium myristate and 7.5 mL of ODE were degassed for 1 h at 100°C. Thereafter, under Ar flow the temperature of the mixture was raised to 250°C and a

selenium precursor solution (prepared by dispersing 12 mg of Se powder in 1 mL of ODE) was quickly injected. After exactly 30 seconds of selenium injection, the anisotropic CdS growth mixture (previously prepared as mentioned above) was continuously injected at a rate of 30 mL/h for 20 min. After the synthesis, the temperature was lowered down to room temperature and 20 mL of ethanol was added. The NPLs were precipitated by centrifugation at 3800 g (rcf) and dispersed in 3 mL of hexane.

Growth of Pt Domains on 5 ML Thick CdSe and CdSe/CdS Core/Crown NPLs. In a three neck round bottom flask, a mixture of 24 mg of Pt(acac)$_2$, 120 µL of oleylamine, 8 mL of ODE and required amount of the NPLs solution in hexane (so that the molar precursor ratio Cd/Pt = 1 : 5) were degassed at 50°C for 30 min. Under Ar flow, the temperature was raised to 130°C, and the reaction was continued for 2.5 h. The temperature was lowered down to room temperature and a 15 mL mixture of isopropanol/acetone = 1:1 was added. The whole product was centrifuged at 3800 g (rcf) for 15 min, the supernatant was discarded and the precipitate of the NPLs was dispersed in 3 mL hexane.

Growth of Au Domains on 5 ML Thick CdSe/CdS Core/Crown NPLs. The pre-synthesized NPLs dispersed in hexane are precipitated using ethanol and re-dispersed in toluene. In an 8 mL vial, 12 mg of AuCl$_3$ together with 80 mg of DDA and 4 mL of toluene were sonicated for 5 min to obtain a light yellow color mixture of Au precursor. Thereafter, 200 µL of the Pt decorated *CdSe/CdS* NPLs were taken inside a vial with 2 mL toluene and a magnetic stirring bar. A definite amount of the above Au precursor (so that the molar precursor ratio Cd/Au = 1:5) was added to this mixture. After the Au precursor addition, the mixture was stirred for 30 min at room temperature and normal day light condition. Subsequently, 500 µL of acetone was added and the products were centrifuged at 3800 g (rcf) for 5 min and finally dispersed in 2 mL of toluene.

Growth of Au Domains on 5 ML Thick Pt Decorated CdSe/CdS Core/Crown NPLs. Au domains were grown on Pt decorated *CdSe/CdS* NPLs at room temperature, using AuCl$_3$ as the gold precursor in toluene medium.[1a] For that, the NPLs were precipitated from hexane using ethanol and re-dispersed in toluene. Thereafter, Au precursor solution was prepared by dissolving AuCl$_3$, DDA in toluene as mentioned above. A total amount of 200 µL of the Pt decorated *CdSe/CdS* NPLs were taken inside a vial with 2 mL toluene and a magnetic stirring bar. A definite amount of the above Au precursor (so that the molar precursor ratio Cd/Au = 1:5) was added to this mixture. After the Au precursor addition, the mixture was stirred for 30 min at room temperature and normal day light condition. Subsequently,

500 μL of acetone was added and the products were centrifuged at 3800 g (rcf) for 5 min and finally dispersed in 3 mL of hexane.

Growth of Pt Domains on 5 ML Thick Au Decorated CdSe(S)/CdS(L) NPLs. Pt domains are grown on Au decorated *CdSe(S)/CdS(L)* NPLs following the same reaction procedure as mentioned above for "*Growth of Pt Domains on 5 ML Thick CdSe and CdSe/CdS Core/Crown NPLs.*" After the centrifugation the product was dispersed in 3 mL hexane.

Phase Transfer of CdSe/CdS and Pt Decorated CdSe/CdS NPLs. The *CdSe/CdS* core/crown NPLs and the metal decorated (Pt or Au on Pt) NPLs were transferred to aqueous medium following a procedure as described by Kodanek *et.al.*[2-3] Briefly, 3 mL of the NPLs in hexane and a phase transfer reagent, prepared by dissolving 100 mg of MUA and 0.1 g of KOH in 4 mL of MeOH, were placed in a 20 mL vial and shaken overnight. The NPLs came to the MeOH phase leaving hexane. The MeOH phase, containing the NPLs, were separated from hexane using a phase separation flask, and centrifuged for 5 min at 3800 g (rcf). The precipitate was dispersed in 0.1 M KOH. The solution was washed 2 times with distilled water to remove excess KOH.

Synthesis of Pt Decorated CdSe/CdS Nanorods. *CdSe/CdS* core/shell nanorods of average length 23.2 nm ± 1.8 nm and average diameter of 5.7 nm ± 0.6 nm were prepared according to the procedure described in literature.[4] The CdSe seeds used in the rod synthesis had an average diameter of 4.2 nm ± 0.4 nm. The nanorods are optically characterized with UV-vis absorption and also by emission spectroscopy (shown in Figure S10). Thereafter, growth of Pt domains and phase transfer to aqueous medium were performed, following the same procedure and reaction conditions as described above for the Pt decorated NPLs.

Atomic Absorption Spectroscopy. The Cd ion concentration of CdSe NPLs and the metal decorated *CdSe/CdS* NPLs solution were determined by atomic absorption spectroscopy (AAS) using a Varian AA140 instrument. A series of Cd ion (0 to 2.5 ppm) solutions of known concentrations were prepared to obtain a calibration curve.

Transmission Electron Microscopy. The morphologies of the NPLs, metal decorated NPLs and the nanorods were investigated by transmission electron microscopy using a FEI Tecnai G2 F20 TMP ($C_{s=}$ 2 mm, C_C = 2 mm), and a JEOL JEM-2100F UHR (C_s= 0.5 mm, C_C = 1.2 mm), equipped with a 200 kV field-emission gun. Micrographs were taken in bright-field and in high-angle annular dark-field scanning transmission electron mode. Prior to TEM grid preparation the samples were precipitated by ethanol (CdSe and *CdSe/CdS*

NPLs) or isopropanol (metal decorated CdSe or *CdSe/CdS* NPLs) followed by centrifugation and re-dispersion in hexane (2 times). Subsequently, 10 µL of the purified sample were drop-casted on a carbon coated copper TEM grid.

STEM-EDXS measurements were conducted in scanning transmission electron microscopy mode. A JEOL JEM-2100F, equipped with a field emission gun and operated at 200 kV was used for this analysis.

Optical Characterizations. Absorption spectra of the samples were recorded using an Agilent Cary 5000 absorption spectrophotometer equipped with an integrating sphere. Absorbance spectra are collected in transmission mode. PL emission spectra of the samples were recorded using a Horiba Fluoromax-4 spectrometer. The PL quantum yield (QY) (in absolute mode) of the samples in solution was measured with a Horiba-DUAL FL spectrophotometer equipped with a Quanta-φ integrating sphere (Horiba). Time-correlated single photon counting (TCSPC) measurements were performed using a Fluorohub TCSPC unit (Horiba) combined with Fluoromax-4 spectrometer. A nanosecond pulsed LED (454 nm) with FWHM of 1.2 ns was used as the excitation source for the TCSPC measurements. All the absorption, absorbance and emission spectra of the samples were measured in a 1 cm quartz cuvette using hexane, toluene (UV-vis spectroscopy grade) or water as solvent.

Powder X-ray Diffraction Analysis. The x-ray diffraction pattern of the samples was measured using a Bruker D8 Advance in reflection mode. Highly concentrated samples of *CdSe/CdS* NPLs and of the Pt decorated *CdSe/CdS* NPLs were drop casted on a single crystal silicon carrier and were dried in air before measurements.

X-ray photoelectron spectroscopy (XPS). A Leybold Heraeus XPS analyzer with aluminium Kα x-ray beam was used as the excitation source to analyze the oxidation state of the metal domains. The concentrated colloidal solution of the pure CdSe/CdS and metal decorated CdSe/CdS NPLs were drop casted and dried under ambient conditions on silicon wafer (1 cm X 1.8 cm). The samples were then inserted into the XPS chamber and incubated in vacuum (10^{-8} mbar) for 18 h prior to the measurements. The binding energy

peaks are calibrated with carbon 1s peak. Gaussian/Lorentzian curve fitting was applied on the raw data using XPS 4.1 software.

Photocatalytic Hydrogen Generation Experiment. The photocatalysts in aqueous medium (Pt decorated *CdSe/CdS* core/crown NPLs, Au on Pt decorated *CdSe/CdS* core/crown NPLs, *CdSe(L)/CdS(L)* NPLs and the Pt decorated *CdSe/CdS* nanorods) containing 1 mg of Cd ion concentration (measured by AAS) was dispersed in 50 mL deionized water with 0.1 M Na_2S and Na_2SO_3 as the sacrificial hole scavengers. The whole suspension was placed inside a 50 mL double jacket Duran quartz glass reactor with inlets and outlets for temperature control. The suspension was purged with Ar gas for 20 min to remove the dissolved O_2 present in the system. Thereafter, the reactor was connected to the mass flow controller and to the Q/C capillary sampling inlet of a quadrupol Mass Spectrometer (QMS) for gas analysis (Hiden HPR-20) by the help of metal flanges and adapters. To remove the air completely from the headspace of the reactor, and to obtain a stable baseline, Ar gas stream was continuously flown through the reactor before irradiation, until no traces of molecular oxygen or nitrogen could be detected by the QMS. A constant Ar gas flow rate of $10 \ cm^3 \cdot min^{-1}$ was maintained through the reactor during the whole experiment. The inlet consumption by the QMS was $1 \ cm^3 \cdot min^{-1}$ and the excess gas were allowed to pass through the exhaust. The sampling rate of the QMS was in the millisecond time range, allowing a fast tracking of the H_2 production. After the background stabilization of the system (1 h), the reactor was illuminated using a 1000 W Xenon-arc lamp. The irradiation intensity measured before the glass reactor was $55 \ mW \cdot cm^{-2}$. The H_2 generation reaction was carried out for 4 h (light on to light off) under the same illumination conditions. For quantitative analysis of H_2, the QMS was previously calibrated employing standard diluted H_2, in Ar (Linde Gas, Germany).

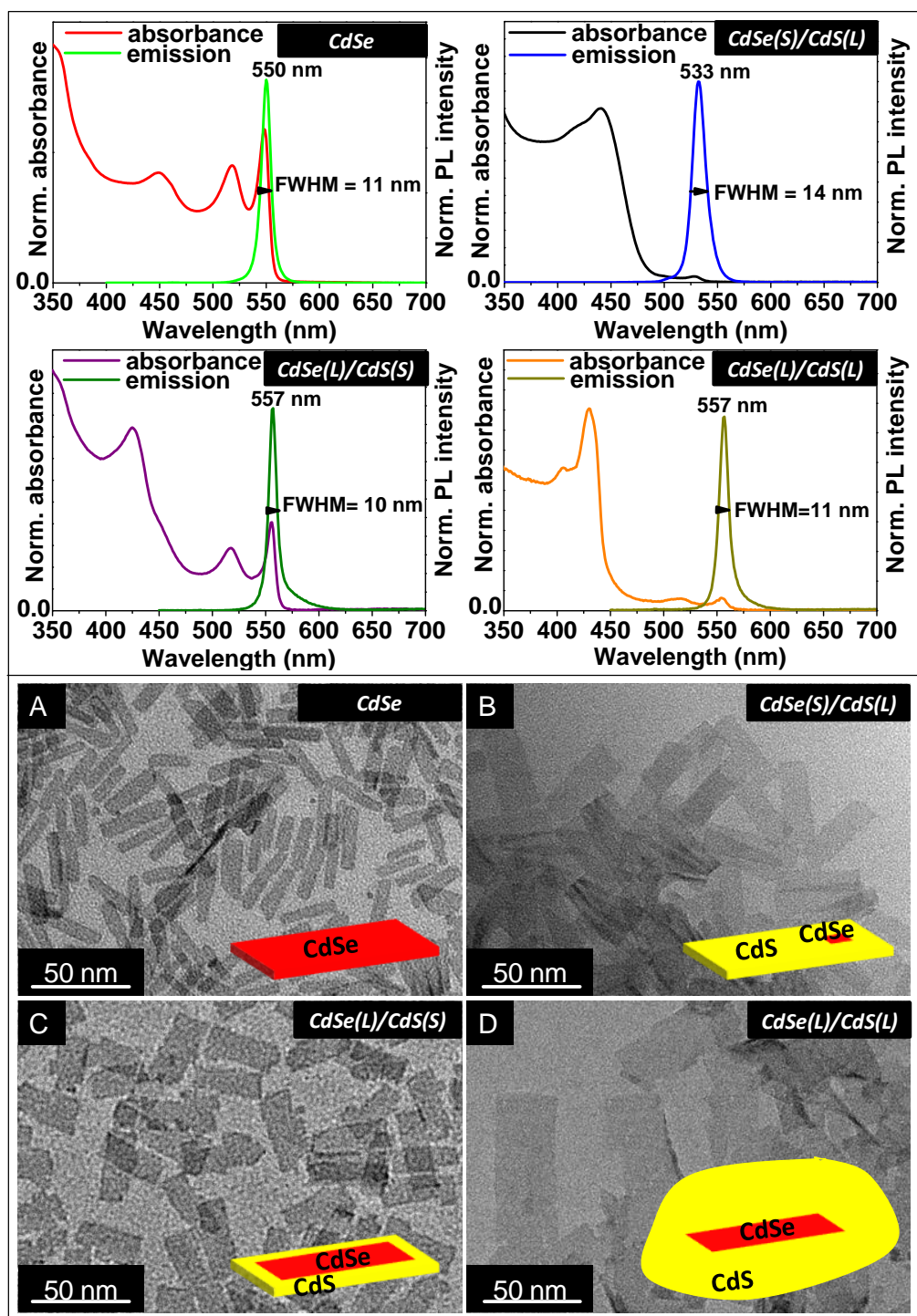## 2. Characteristics of 5ML thick *CdSe* and *CdSe/CdS* core/crown NPLs

Figure S1. (upper panel) UV-vis absorbance and emission spectra of the 5 ML thick CdSe, *CdSe(S)/CdS(L)*, *CdSe(L)/CdS(S)*, and *CdSe(L)/CdS(L)* core/crown NPLs. (lower panel A-D) TEM micrographs of the 5 ML thick CdSe and *CdSe/CdS* core/crown NPLs.

The absorbance spectra of the 5 ML thick CdSe NPLs show the characteristics bands at 518 nm and at 550 nm, which corresponds to the lh-e (lighthole- electron) and hh-e (heavyhole- electron) transitions, respectively.[1] The emission peak appears at 550 nm with a full width at half maximum (FWHM) of 11 nm, confirming the strong quantum confinement in the z direction. The absorbance spectra of *CdSe(S)/CdS(L)* core/crown NPLs exhibit characteristic transitions at 533 nm and at 430 nm for the very small CdSe core and the CdS crown, respectively. The emission spectra of the *CdSe(S)/CdS(L)* NPLs show a sharp peak at 533 nm with a FWHM of 14 nm. In the case of *CdSe(L)/CdS(S)* and *CdSe(L)/CdS(L)* NPLs, the anisotropic CdS crown has been grown on previously synthesized 5 ML thick CdSe NPLs. The absorbance spectra in both cases shows characteristics of the CdSe core and CdS crown. The emission maximum of *CdSe(L)/CdS(S)* and *CdSe(L)/CdS(L)* NPLs appear at 557 nm. Notably, the excitonic feature from CdS crown of the *CdSe(L)/CdS(L)* NPLs is much more pronounced than that of the *CdSe(L)/CdS(S)* NPLs, which is due to the larger CdS crown size on the same CdSe core NPLs. All the NPLs with different core/crown dimensions are characterized with bright field TEM analysis and are shown in the lower panel of Figure S1. The average size obtained for CdSe core NPLs is 31 nm ± 4.5 nm (in length) and 7 nm ± 1.5 nm (in width). The *CdSe(S)/CdS(L)* core/crown NPLs have an average side length of 41.4 nm ± 3.5 nm and a width of 13 nm ± 1.8 nm. The average size obtained for *CdSe(L)/CdS(S)* core/crown NPLs is 38.1 nm ± 5.2 nm (in length) and 13.6 nm ± 2.1 nm (in width); and for *CdSe(L)/CdS(L)* core/crown NPLs the average dimensions are 54.1 nm ± 7 nm (in length) and 22.7 nm ± 4.2 nm (in width). Due to the large crown size of the *CdSe(L)/CdS(L)* NPLs, some broken parts of the CdS crown (possibly due to the high strain) could be found on the TEM grid.
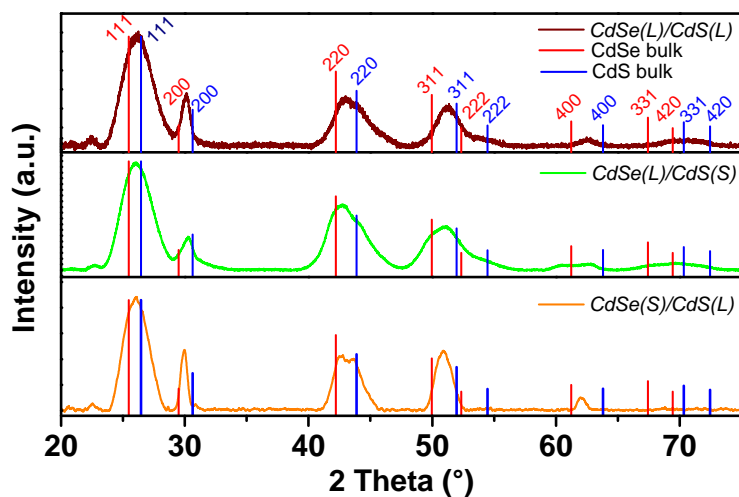
Figure S2. XRD pattern of three different types of *CdSe/CdS* core/crown NPLs. Red and blue vertical lines correspond to the reflections from the bulk CdSe and CdS semiconductor respectively.[5]

3. Elemental mapping (STEM-EDXS) of Pt decorated *CdSe(L)/CdS(S)* and *CdSe(S)/CdS(L)* NPLs
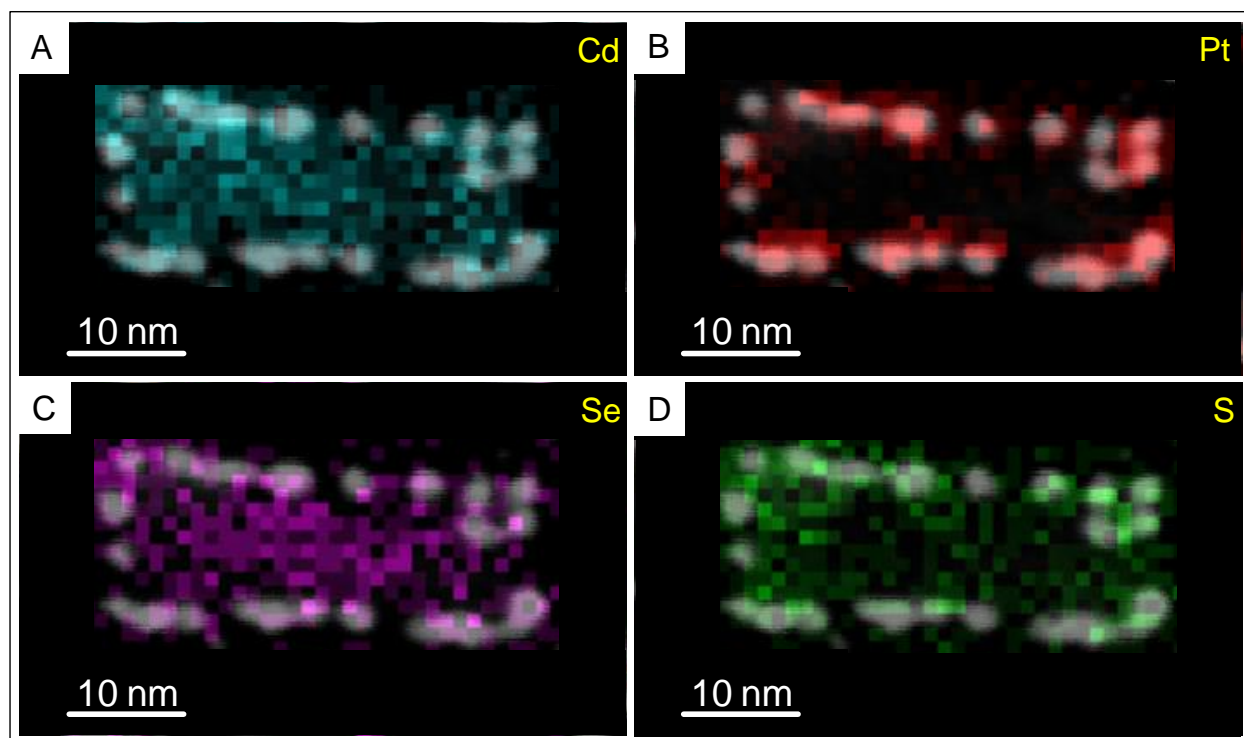

Figure S3. HAADF-STEM images averaged with STEM-EDXS mappings for the elements Cd, Pt, Se and S (A-D, respectively) for Pt decorated *CdSe(L)/CdS(S)* core/crown NPLs.
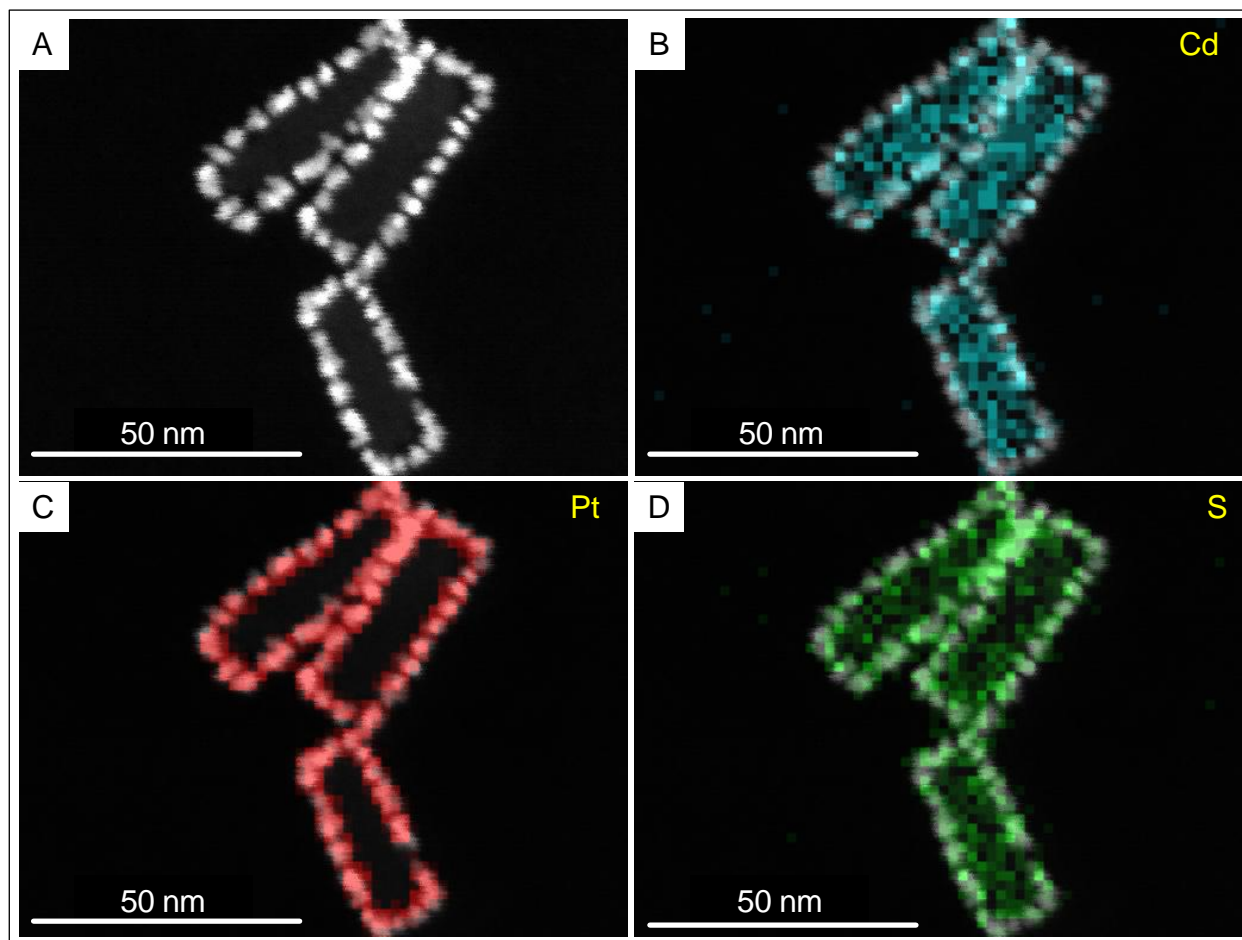
Figure S4. (A) HAADF-STEM micrograph showing the bright white spots of Pt domains, (B-D) HAADF-STEM images averaged with STEM-EDXS mappings for the elements Cd, Pt, and S (A-D, respectively) for Pt decorated *CdSe(S)/CdS(L)* core/crown NPLs.

4. Optical and structural characterizations of Pt decorated *CdSe/CdS* NPLs
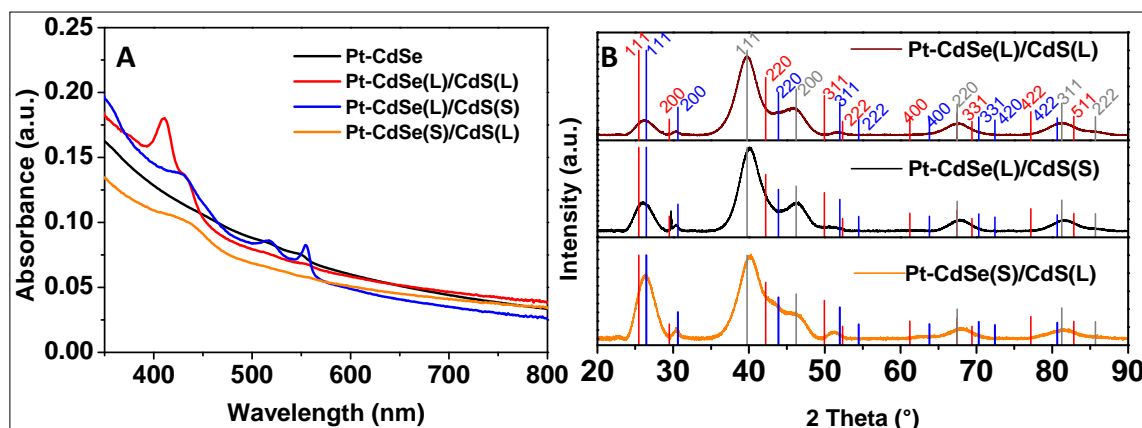

Figure S5. (A) UV-vis absorbance spectra of the Pt decorated CdSe and *CdSe/CdS* core/crown NPLs with the same Cd ion concentration. (B) XRD pattern of the Pt decorated *CdSe/CdS* core/crown NPLs. Red, blue and grey vertical lines correspond to the reflexes from the bulk CdSe, CdS semiconductor and Pt metal respectively.[5]

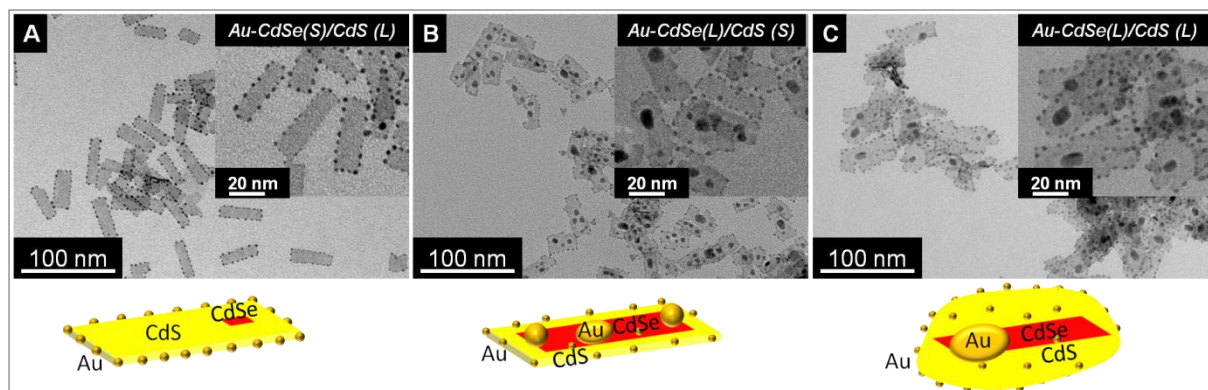**5. TEM characterizations of Au decorated *CdSe/CdS* NPLs**

Figure S6. TEM micrographs of Au domain growth on *CdSe/CdS* core/crown NPLs. (A) Small Au domains surrounding the edges of the NPLs are observed in the case of small CdSe core with large CdS crown. (B and C) Larger Au islands on the surface (near the CdSe core) together with very small Au domains surrounding the edges of the NPLs are observed for large CdSe core with small and large CdS crown, respectively. Insets are higher resolution TEM micrographs of the corresponding Au decorated NPLs. Schematic diagrams, included under the images are drawn following the TEM observations.

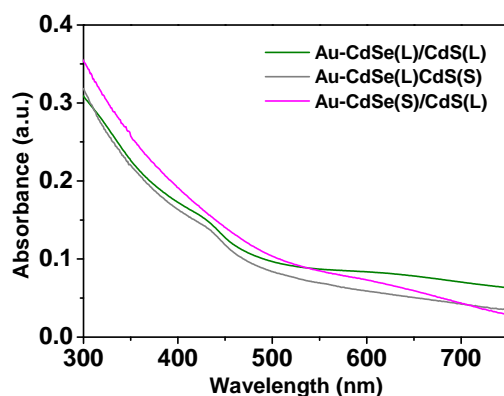## 6. Optical characterizations of Au decorated *CdSe/CdS* NPLs

Figure S7. (A) UV-vis absorbance spectra of the Au decorated CdSe and *CdSe/CdS* core/crown NPLs with the same Cd ion concentration.

7. Optical characterizations and H$_2$ gas generation ability of Au on Pt decorated NPLs. Absorption spectra of the Pt decorated *CdSe/CdS* NPLs after phase transfer
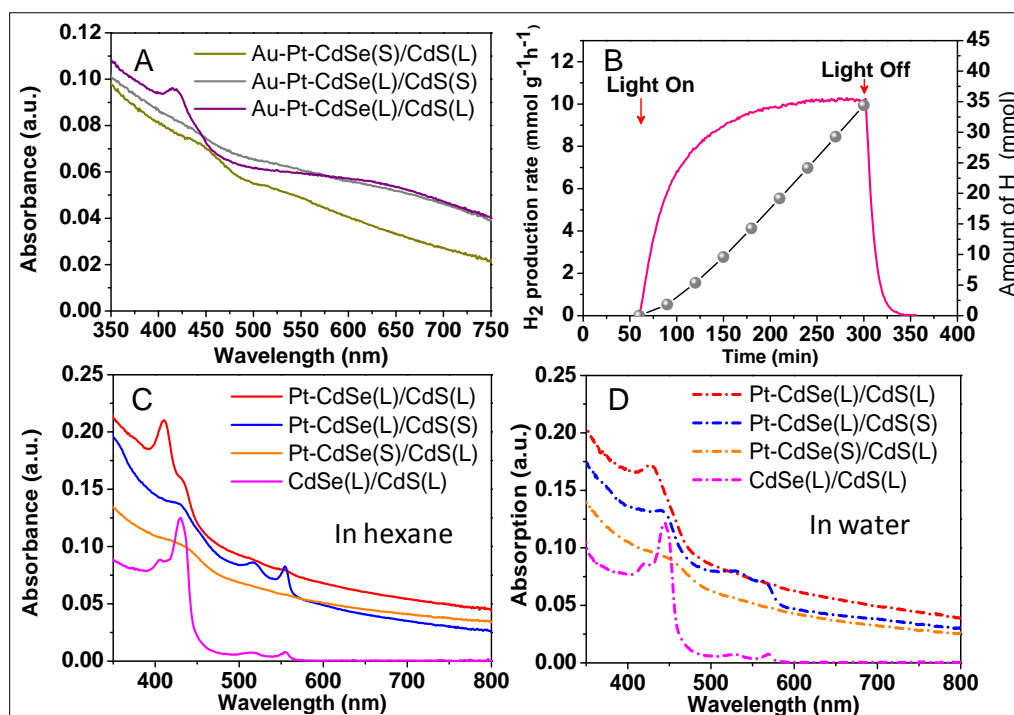

Figure S8. (A) Absorbance spectra of the samples after Au growth on Pt decorated NPLs in organic medium. (B) H$_2$ production rate using Au on Pt decorated *CdSe(L)/CdS(L)* NPLs as catalyst. (C) Absorbance spectra of the NPLs in hexane medium. (D) Absorption spectra of the NPLs in aqueous solution after phase transfer with MUA ligands.

8. HRTEM images of Pt and Au-Pt decorated NPLs
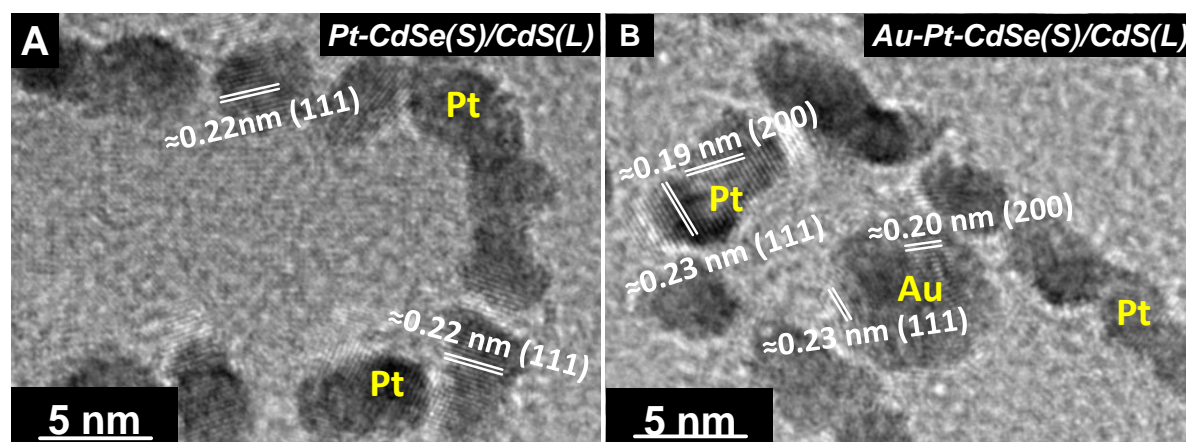
Figure S9. HRTEM images of (A) Pt decorated *CdSe(S)/CdS(L)* NPLs and (B) Au growth on Pt decorated *CdSe(S)/CdS(L)* NPLs. The crystal lattice planes of the metal domains can be distinguished easily. Due to the very thin nature of the NPLs and also due to the high contrast difference between the metal and the *CdSe/CdS* segment, the lattice planes of both cannot be distinguished simultaneously.

9. TEM micrographs of the Pt decorated *CdSe/CdS* NPLs and *CdSe/CdS* nanorods in aqueous solution
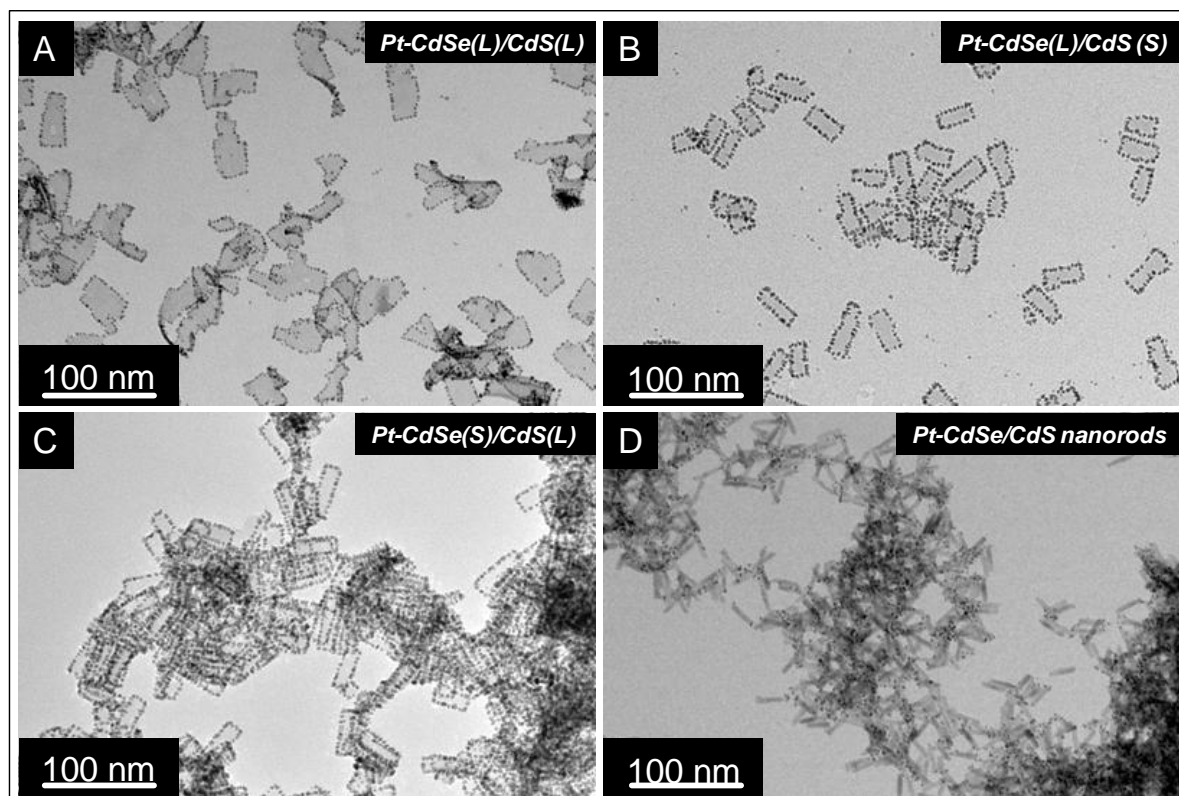
Figure S10. (A-C) TEM micrographs of Pt decorated *CdSe/CdS* core/crown NPLs and (D) Pt decorated *CdSe/CdS* nanorods in aqueous solution.

10. Characteristics of Pt decorated CdSe/CdS nanorods and its H$_2$ gas generation ability
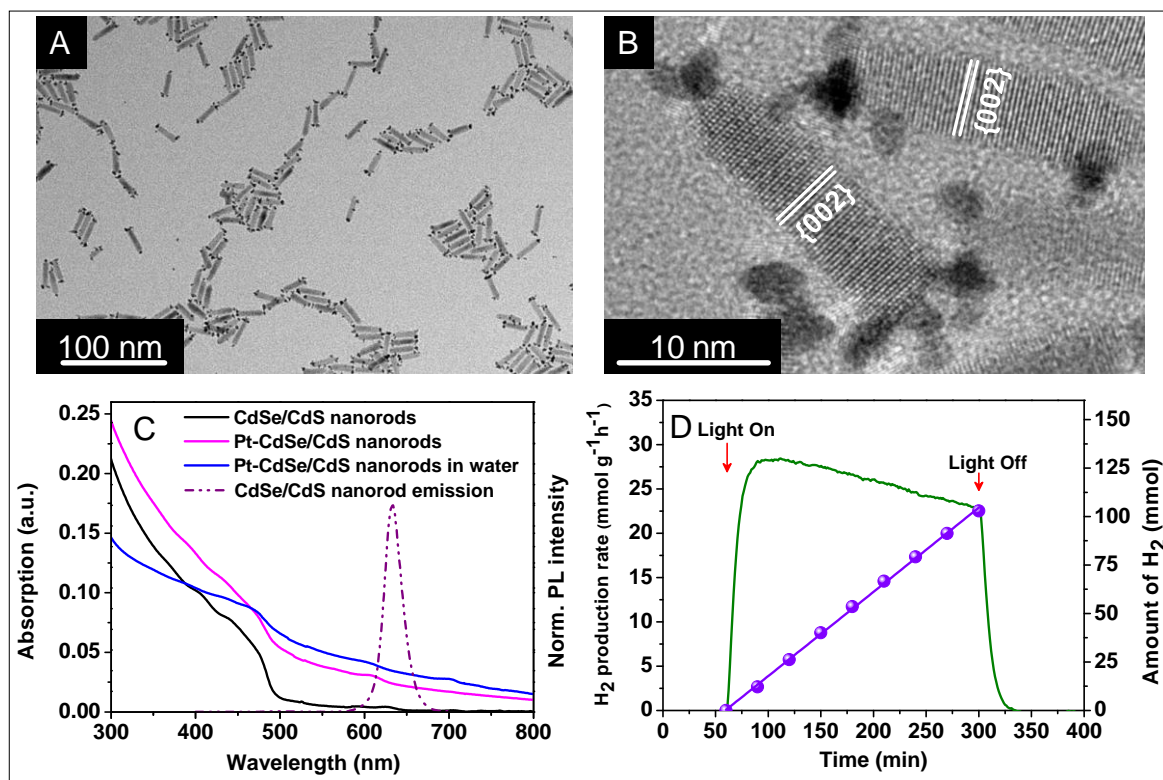
Figure S11. (A) Overview and (B) Higher resolution TEM micrographs of Pt domain growth on *CdSe/CdS* core/shell nanorods. (C) UV-vis absorption (solid lines) of *CdSe/CdS* nanorods, with Pt decoration and after phase transfer with MUA ligands, emission spectra (dotted line) of *CdSe/CdS* nanorods in hexane. (D) Photocatalytic H$_2$ generation rate (green line) and the total amount of H$_2$ produced (violet line) during the course of reaction with aqueous Pt decorated *CdSe/CdS* nanorods (containing 1 mg of Cd ion) as the photocatalyst.

11. Determination of AQE and TOF of hydrogen generation

The AQE of the system can be evaluated by using the equation $AQE = 2N_{H2}/N_{hv}$, where, N_{H2} = number of hydrogen molecules generated per second; can be easily calculated from the rate of hydrogen generation (N_{H2} = rate (mol/s)), whereas the number of absorbed photon by the system can be calculated from the equations (1) and (2) as mentioned below.

$$Nhv = \frac{Ia \cdot \lambda}{Nahc} \ (1)$$

$$\text{again, Ia} = Io \cdot Fs; \text{ and } Fs = \frac{\int_{\lambda 1}^{\lambda 2} I \cdot (1 - 10^A) \cdot d\lambda}{\int_{\lambda 1}^{\lambda 2} I \cdot d\lambda} \ (2)$$

where, Ia = intensity of the absorbed light, λ = wavelength of absorption maximum, Na = Avogadro number, h = Planck's constant, c = speed of light, Io = intensity of incident light, Fs = fraction of light absorbed, λ_1- λ_2 = range of wavelength where the sample absorbs light, A= absorption of the sample at wavelength λ (measured in integrating sphere).

The highest rate of H_2 generation by Pt decorated *CdSe(L)/CdS(L)* observed is 18.34 µmol/h (per mg of Cd ion concentration)

$$\text{Hence } N_{H2} = (18.34 \text{ x } 10^{-6})/3600 = 5.1 \text{x} 10^{-9} \text{ mol/s}$$

Again, considering the area under the curve, (from λ_1 = 300 nm and λ_2 = 800 nm)

$$Io = \int_{\lambda 1}^{\lambda 2} I \cdot d\lambda = 53.1 \text{ mW} \cdot \text{cm}^{-2}.\text{and}$$

$$\int_{\lambda 1}^{\lambda 2} I \cdot (1 - 10^A) \cdot d\lambda = 14.23 \text{ mW} \cdot \text{cm}^{-2},$$

Hence, Fs is equal to 0.2680.

Now, Ia = Io $\cdot$ Fs = 14.228 mW$\cdot$cm^{-2}, so Nhv = $\frac{Ia \cdot \lambda}{Na \ hc}$ = 52.77 x 10^{-9} mol/s

So AQE = {(2 x 5.1 x 10^{-9}) / (52.77 x 10^{-9})} x 100% = 19.31%

Volume of a single Pt decorated *CdSe(L)/CdS(L)* core/crown NPLs = (L x W x H) = 54.1 x 22.7 x 2 nm^3 = 2456.14 nm^3 (the actual thickness of the NPLs changes from 1.5 to ~2 nm upon 2 layers of S from MUA top and bottom).

Mass of a single NPL

$$= 2456.14 \text{ nm}^3 \text{ x } 4.82 \text{ (density of CdS 4.82 g/cc)}$$

$$= 2456.14 \text{ x } 10^{-27} \text{ x } 10^6 \text{ x } 4.82 \text{ g (after unit conversion)}$$

$$= 11.838 \text{ x } 10^{-18} \text{ g}$$

We have used 1 mg of Cd ion concentration which leads to sample weight of 1.28×10^{-3} g (considering one Cd atom is attached with one Se or S atom, here mass of S is considered).

Hence number of NPLs present in the system

$$= (1.28 \text{ x } 10^{-3}) / (11.838 \text{ x } 10^{-18})$$

$$= 1.08 \text{ x } 10^{14}$$

Now, the maximum rate of H_2 generation in the case of Pt decorated *CdSe(L)/CdS(L)* is 18.34 µmol/h (per mg of Cd ion concentration).

Hence, number of H_2 molecules produced per second

$$= (18.34 \text{ x } 10^{-6} \text{ x } 6.023 \text{ x } 10^{23}) / 3600$$

$$= 3.07 \text{ x } 10^{15} \text{ molecules of } H_2/s$$

So, a single NPL can generate

$$= (3.07 \text{ x } 10^{15}) / (1.08 \text{ x } 10^{14}) \text{ molecules of } H_2/s$$

$$= 28.42 \text{ molecules of } H_2/s$$

Hence TOF would be $\quad = (28.42 \text{ x } 3600)$

$$= 102312 \text{ molecules of } H_2/h/NPL$$

$$\sim 10^5 \text{ molecules of } H_2/h/NPL$$

12. Discussions of the observed differences in TOF and AQE of the catalyst for photocatalytic H₂ generation

In order to explain the observed differences in H_2 production rate, AQE and TOF, the interplay of the following factors can be taken into account: (a) charge carrier separation (b) rate of hole removal by the hole scavenger, and (c) overall stability of the catalyst during the course of reaction. In the case of *CdSe(L)/CdS(L)* without any metal domain, the charge carrier separation is ineffective (due to absence of the metal domains), owing to higher degree of charge carrier recombination and hence less number of electrons are available to reduce the H^+ ions, which ultimately results in lower efficiency. In the presence of the metal domains electrons are immediately transferred to the metal tips and due to this effective charge carrier separation, a higher number of electrons is available to reduce H^+ ions, and hence higher efficiency of H_2 production is observed for the Pt decorated NPLs than *CdSe(L)/CdS (L)* without any metal domain.

In order to explain the observed differences of AQE among the metal decorated NPLs, we need to consider the hole removal rate from the surface of the semiconductor to the sacrificial electron donor, which was suggested previously as one of the major rate limiting steps in photocatalytic H_2 generation reactions, where Pt decorated *CdSe/CdS* nanorods are used as the catalyst.[6] In this regard, the study of photoluminescence (PL) quenching and the change of PL decay time in presence of the hole scavenger were found to be helpful in literature.[6] Therefore, we have conducted steady state emission (PL emission) and time resolved PL decay measurements by time correlated single photon counting (TCSPC measurements). The experiments were performed in aqueous solution of the *CdSe/CdS* NPLs (without any metal domain) in the presence and absence of the hole scavengers (a mixture of Na₂S and Na₂SO₃), maintaining the same concentration of the reagents in the cuvette as used for the photocatalytic water reduction reactions. The excitation intensity and the sample absorption were the same (454 nm) for the samples (with and without hole scavengers) so that the quantum yield (measured in absolute mode using an integrating sphere) and the PL decay times can be directly related.

The PL intensity of the initial NPLs after the phase transfer is reduced by ~50%, in contrast to the NPLs in hexane medium,[2-3] due to the increased degree of non-radiative

recombination processes and due to the different ligands (MUA) employed in the phase transfer, since thiol ligands can also act as effective hole acceptors.[7] Upon the addition of the hole scavengers in all cases the PL quantum yield decreases accompanied by a decrease in the PL decay time. The apparent hole transfer rate can be determined from the PL decay times measured (here only mono-exponential decay is considered for the ease of calculations), by using the equations $k_{ht} = [k_{(MUA+ED)} - k_{MUA}]$ (with $\tau_{ht} = 1/k_{ht}$), so $\tau_{(MUA+ED)} = 1/k_{(MUA+ED)}$, $\tau_{MUA} = 1/k_{(MUA)}$.[6a] Here, k_{ht}, represents the apparent hole transfer rate from the surface of the NPLs to the electron donor (ED $i.e.$ S^{2-}/SO_3^{2-}), independent from the holes accepting effect of MUA, whereas, $k_{(MUA+ED)}$ and k_{MUA} represent the same in the presence and absence of S^{2-}/SO_3^{2-}, respectively. τ_{ht}, $\tau_{(MUA+ED)}$ and τ_{MUA} represent the observed PL decay time of the system, in the presence and absence of S^{2-}/SO_3^{2-}, respectively. The PL decay of the NPLs and the nanorods before and after addition of S^{2-}/SO_3^{2-} are presented in Figure S11. The PL quantum yield (absolute) and the mono-exponential PL decay times are summarized in Table 1. The hole removal rates are found to be 0.085 ns^{-1}, 0.055 ns^{-1}, 0.031 ns^{-1} and 0.028 ns^{-1} for *CdSe(L)/CdS(L)*, *CdSe(L)/CdS(S)*, *CdSe(S)/CdS(L)* and *CdSe/CdS* nanorods, respectively. This means that in the case of *CdSe(L)/CdS(L)*, the holes are removed faster than all other systems, or in other words, the S^{2-}/SO_3^{2-} electrolyte can donate the electron faster to the holes. This is most likely due to the larger exposed surface of the *CdSe(L)/CdS(L)* NPLs, which come in contact of the S^{2-}/SO_3^{2-} ions. The hole transfer rates in turn explain the observed differences of the H_2 production rate of the Pt decorated NPLs. It should also be noted that the Pt decorated *CdSe/CdS* nanorods have the lowest hole removal rate among all investigated systems, under similar conditions, most likely due to the shielding of the CdSe core inside the CdS rods, the electron donor cannot reach the core effectively. Hence, the parallel relationship of the hole removal rates and the AQE is in contrary for the Pt decorated *CdSe/CdS* nanorods. The overall stability of the catalyst under the reaction conditions could explain these observations. Sometimes the large CdS crown of the Pt decorated *CdSe(L)/CdS(L)* might break due to its thin nature,[1b] local strain[1b] and the stirring reaction conditions, causing a decrease in the effective surface area responsible for the light absorption and hence lower efficiency. Moreover, after the photocatalytic reactions, sample aggregation was observed in all cases of metal decorated NPLs, whereas the sample with nanorods was found to be relatively stable after the reactions. In the case of Au-Pt-*CdSe(S)/CdS(L)* NPLs, the photo excited electron can be transferred to Au or Pt (Fermi

level energy of Pt is 8.8 eV and for Au 5.53 eV),[8] which could lead to a competition between the two noble metal domains to receive the electron. In summary, the differences in H_2 production rate and the AQE of the catalyst can be explained through the interplay of all the above mentioned factors such as, effects of metal domains, holes scavenging rate, and overall stability of the catalyst in the reaction medium.

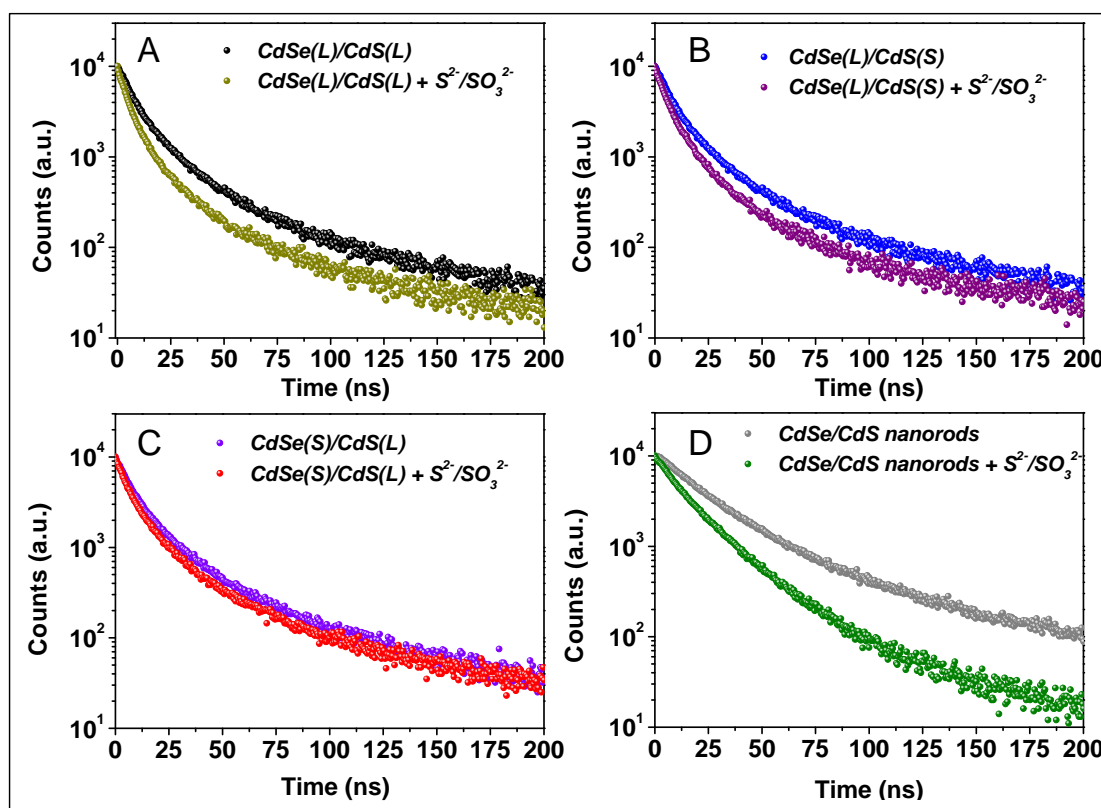## 13. PL decay analysis of the aqueous NPLs in presence and absence of S^{2-}/SO_3^{2-} electrolyte

Figure S11. (A-C) PL decay analysis of the aqueous *CdSe/CdS* core/crown NPLs and of (D) *CdSe/CdS* nanorods, before and after addition of S^{2-}/SO_3^{2-} electron donor.

Table 1. Quantum Yield (QY) and PL decay time (τ) of the NPLs and nanorods with and without electron donor.

Sample	QY (%)	τ (ns)	Sample (aqueous)	QY (%)	τ (ns)
CdSe(L)/CdS(L)	15.4	11.1	*CdSe(L)/CdS(L)* $+ S^{2-}/SO_3^{2-}$	7.4	5.7
CdSe(L)/CdS(S)	18.1	10.9	*CdSe(L)/CdS(S)* $+ S^{2-}/SO_3^{2}$	9.8	6.8
CdSe(S)/CdS(L)	10.4	9.8	*CdSe(S)/CdS(L)* $+ S^{2-}/SO_3^{2}$	7.4	7.5
CdSe/CdS nanorods	16.2	24.6	*CdSe/CdS* nanorods $+ S^{2-}/SO_3^{2}$	10.1	14.5

References:

[1]   a) Naskar, S.; Schlosser, A.; Miethe, J. F.; Steinbach, F.; Feldhoff, A.; Bigall, N. C., *Chem. Mater.* **2015,** *27,* 8, 3159; b) Tessier, M. D.; Spinicelli, P.; Dupont, D.; Patriarche, G.; Ithurria, S.; Dubertret, B., *Nano Lett.* **2014,** *14,* 1, 207.

[2]   Naskar, S.; Miethe, J. F.; Sánchez-Paradinas, S.; Schmidt, N.; Kanthasamy, K.; Behrens, P.; Pfnür, H.; Bigall, N. C., *Chem. Mater.* **2016,** *28*, 2089.

[3]   Kodanek, T.; Banbela, H. M.; Naskar, S.; Adel, P.; Bigall, N. C.; Dorfs, D., *Nanoscale* **2015,** *7,* 45, 19300.

[4]   a) Sanchez-Paradinas, S.; Dorfs, D.; Friebe, S.; Freytag, A.; Wolf, A.; Bigall, N. C., *Adv. Mater.* **2015,** *27,* 40, 6152; b) Carbone, L.; Nobile, C.; De Giorgi, M.; Sala, F. D.; Morello, G.; Pompa, P.; Hytch, M.; Snoeck, E.; Fiore, A.; Franchini, I. R.; Nadasan, M.; Silvestre, A. F.; Chiodo, L.; Kudera, S.; Cingolani, R.; Krahne, R.; Manna, L., *Nano Lett.* **2007,** *7,* 10, 2942.

[5]   *Standard NIST Bulk XRD pdf no for CdSe (03-065-2891), for CdS (01-089-0440), for Pt (03-068-2868).*

[6]   a) Wu, K.; Chen, Z.; Lv, H.; Zhu, H.; Hill, C. L.; Lian, T., *J. Am. Chem. Soc.* **2014,** *136,* 21, 7708; b) Wang, P.; Zhang, J.; He, H.; Xu, X.; Jin, Y., *Nanoscale* **2015,** *7,* 13, 5767.

[7]   a) Gaponik, N.; Wolf, A.; Marx, R.; Lesnyak, V.; Schilling, K.; Eychmueller, A., *Adv. Mater.* **2008,** *20,* 22, 4257; b) Hendel, T.; Lesnyak, V.; Kuehn, L.; Herrmann, A.-K.; Bigall, N. C.; Borchardt, L.; Kaskel, S.; Gaponik, N.; Eychmueller, A., *Adv. Funct. Mater.* **2013,** *23,* 15, 1903. [8]   Buck, M. R.; Bondi, J. F.; Schaak, R. E., *Nat Chem* **2012,** *4,* 1, 37.

5 What is next?

The quasi 2D metal decorated nanoheteroplatelets reported here could be a starting monomer for the fabrication of multicomponent aerogel with homogeneous metal distribution and controlled interfaces. Therefore, the direct next step would be the synthesis of aerogels from metal-semiconductor heteroplatelets. The macroscopic porous multicomponent aerogels will exhibit the synergistic properties of both the metal and the semiconductor in solid state, which might be beneficial for catalytic reactions and sensor based applications.

Initial experiments were performed successfully for the fabrication of the Au decorated CdSe/CdS core/crown NPLs in aqueous solution. In this case, the NPLs synthesized in organic solution were phase transferred to aqueous solution and the Au domains were grown on the NPLs by reducing $HAuCl_4$. $3H_2O$. Ascorbic acid and citric acid-Na-citrate mixture were employed as reducing agents. However Au domains were found to be present all over the surface of the NPLs in both cases. It should be noted, that the phase transfer of the Au decorated CdSe/CdS NPLs from organic to aqueous solution was not successful (aggregation of the particles were observed). Therefore, in future modifications of the present synthetic routes are needed to achieve heterostructures with selective metal nucleation in aqueous solution.

The site selective growth of Pt domains on the CdSe or CdSe/CdS NPLs in aqueous solution is hardly reported in literature. One example reported by Elmalem *et al.* shows the growth of CdSe-Pt hybrid structure at different pH values, where CdSe nanorods, synthesized in organic solution were transferred to aqueous solution and then $PtCl_4$ was reacted with it.[112] The hybrid system contained Pt domains all over the surface of the

nanorods and ultimately formed nanonet type geometry. The similar synthesis route when adopted for the NPLs results in aggregate formation, which could be due to the high sensitivity of the NPLs toward the reaction conditions. Hence, in future to develop the porous 3D aerogels from selective Pt decorated NPLs, a new route need to be developed to grow Pt domains site selectively on the CdSe and CdSe/CdS NPLs in aqueous solution, which could act as the building blocks for the aerogel formation. Polymer coating of the heteronanoplatelets could be another option to bring them into water. The gelation can be also achieved by adding suitable metal ions to the aqueous solution which will bind with the anionic end of the ligands to form the network structure.[182] The present problem of colloidal instability (as discussed in section 4.3) of the catalyst in the glass reactor could be circumvented by employing these multicomponent aerogels. Moreover, in the aerogels, the interconnected NPLs will also have (100) as the exposed crystal facets, which will be helpful for future facet selective catalytic as well as photocatalytic reactions. Therefore, it can be said that in near future it will be possible to make aerogels from selectively metal decorated NPLs by suitable variation of the reaction conditions.

The aerogels from CdSe/CdS NPLs employed in the gelation experiments are core/crown type, where the CdSe part is more exposed and found to be sensitive to external environment. Therefore, in future, one could think of core/shell type of NPLs as the building blocks for the gelation experiments, where, the CdSe core NPL is shielded by CdSe shell, both at the top and bottom surface. Hence these types of NPLs might overcome the dissolution effect of the H_2O_2 and would exhibit even higher PLQY. The hydrogels and the aerogels from semiconductor NPLs could possibly be employed as a material for photo-electrochemical sensor by coating them on transparent conductive glass electrode (*e.g.*, FTO or ITO) by using suitable linker molecules or by using 3D printing. Recently, it is known that the fluorescence of the NPLs coated film strongly depends on the O_2 content of

the external environment thus help in fabrication of biosensors for oxygen detection. This process is reversible in nature, *i.e.* with decreasing concentration of the O_2 molecule, the fluorescence intensity decreases and vice versa. The aerogels developed here therefore in principle would be able to serve this purpose even better due to the presence of enormous number of pores where, the O_2 or other reactant molecules can diffuse easily.

In section 3.2, the gelation of the Pt nanocubes and nanospheres, from organic solution is presented. Therefore, it would be of high interest in future to prepare gels of different shapes of Pt as well as from other noble metal NPs. It would be also interesting in future to prepare multimetallic aerogels from shape controlled metal NPs with certain exposed crystal facets and to compare their catalytic activities. The light weight, porous aerogels from Pt NPs developed here with such high specific surface area with distinct crystal facets could be advantageous for example in making stimulation electrodes, fuel cells, sensors, mechanical actuator and catalysis, in general. For all these applications aerogels need to be connected with a current collector. This purpose might be solved by placing the aerogels on glassy carbon electrode or other conductive electrode followed by a thin layer of Nafion for fixation purpose.

The heteronanoplatelets reported in this thesis are formed by growing noble metal such as Au, Pt and Pd domains on the CdSe/CdS NPLs. These noble metals are expensive and are limited in resources. Therefore, alternative pathways need to be developed in future *e.g.*, Ni or Co could be of preferred choice. Hence, the reaction conditions of nanoheteroplatelets synthesis should be modified accordingly. Also the different nucleation behavior of the metal domains on CdSe NPLs, should be realized by further experiments employing metal salts with same cation and different anions, to see the effects of the anionic part on the nucleation behavior and also on the final morphologies.

The photochemical instability of the II-VI semiconductors under reaction conditions are found to affect the catalytic activity. This problem might be circumvented by employing second co-catalyst such as IrO_2 or Ru, or using suitable redox couple, which can scavenge the holes (these holes are responsible for the corrosion) from the semiconductor to water very fast and would provide desired photochemical stability of the cadmium based structure. The modification of the structural morphologies by varying the amounts of noble metal co-catalyst could also increase the photo-catalytic efficiency.

It should be also noted that the cadmium based NPs employed are toxic in nature, even consumptions of low amount of cadmium can be carcinogenic, and hence alternative pathways should be developed to prepare NPs with less or no toxic effects.

Therefore it can be unambiguously said that the work presented in this thesis will definitely contribute to the broader aspects of the materials science mainly in catalysis and sensor fabrication and will bridge the laboratory inventions and the commercial market.

6 Final Remarks

This thesis in overall describes the development of new synthetic routes to produce highly porous, light weight macroscopic aerogels from shape controlled metal, and semiconductor NPs. The fabrication techniques of hydrogels and aerogels from cubic and quasispherical Pt NPs overcome the existing methodological drawbacks of time consuming phase transfer and ultrafiltration processes. The gels from semiconductor NPLs as well as from Pt nanocubes exhibit high inner specific surface with enriched (100) crystal facets. This thesis also presents new types of metal-semiconductor hybrid nanoheterostructures with tunable morphology. The synthesis of heteroplatelets is a contribution to the class of hybrid materials with advanced functionalities. The photocatalytic activity of the hybrid structures is promising for applications in *e.g.*, H_2 gas generation through water reduction.

In details, the synthesis of luminescent aerogels from CdSe and CdSe/CdS core/crown NPLs is presented in section 2. The hydrogels are formed from the aqueous solution of the building blocks using H_2O_2 assisted destabilization, which is converted to aerogels by supercritical drying. Aerogels acquire a remarkably high specific surface area in the range of 189-219 $m^2 \cdot g^{-1}$ (27000-34000 $m^2 \cdot mol^{-1}$) and densities of 0.038 $g \cdot cm^{-3}$, which is only 0.8% of bulk CdS and 0.69% of bulk CdSe densities. The optical properties of the aerogels are found to be similar with the pristine NPLs in aqueous solution. A comparison of the optical properties between the dense packed films and the porous aerogels proves that the aerogels acquire roughly 2 times higher PLQY and longer PL lifetime. Advantageously, the entire surface of the aerogels consist of only (100) crystal facets suitable for facet selective catalytic reactions.

Section 3 of the thesis, represents the development of new synthetic strategies to prepare aerogels from shape controlled Pt NPs. The procedure works in colloidal organic solution. In this method, time consuming phase transfer, and ultrafiltration processes for concentrating the NPs solution can be effectively avoided. The entire template free aerogels consist of crystalline connections of the individual Pt NPs. The highly voluminous and porous structure of the aerogels from Pt nanocubes and nanospheres exhibits specific surface area in the range of 33-36 $m^2 \cdot g^{-1}$ (6400-7000 $m^2 \cdot mol^{-1}$) which is in the same order of magnitude with the specific surface area of the aerogels obtained from traditional methods. More interestingly, the cube aerogels exhibit (100) as the only exposed crystal facets. The catalytic activity of the cube aerogels are found to be better than the sphere aerogels in asymmetric hydrogenation of 4,4-dimethyldihydrofuran-2,3-dione (keto-pantolactone) with an enantiomeric excess of 9% for the D-isomer.

Section 4 represents the very first report to combine the synergistic properties of quasi 2D NPLs and noble metal domains (Au, Pd and Pt) in the same material with controlled morphologies. Metal domains such as Au, Pt and Pd have been grown site-selectively on the 5 ML thick CdSe NPLs. It has been shown that the metal nucleation behavior and the final morphologies of the hybrid structure strongly depends on the types and amount of precursors and other reaction parameters, such as temperature, reaction time and ligands present in the solution. Additionally, the charge carrier separation in this new hybrid structure is investigated by the degradation of methylene blue as model electron acceptor dye. All hybrid structures show catalytic activities superior to the pristine CdSe NPLs without any metal domains.

Furthermore, section 4 demonstrates the expansion of the metal domain growth on anisotropic CdSe/CdS core/crown NPLs with variable dimensions. Significant differences

in the metal nucleation behavior are observed, when the size of the CdSe core and the CdS crown is varied. It is also proved that the reaction order of the metal domain growth also controls the final morphologies of the hybrid structure. The local distribution and elemental compositions of the ternary and quaternary hybrid NPLs are thoroughly investigated with elemental analysis. Moreover, the hybrid structures synthesized in organic solution are transferred to aqueous solution by ligand exchange reactions and employed as catalyst for photo assisted water reduction reaction to produce H_2 gas. An apparent quantum efficiency of ~19.3% is observed for the Pt decorated CdSe/CdS NPLs with a large CdSe core and large CdS crown.

Keeping the above advantages of metal-semiconductor hybrid structures in mind, the next step would be the synthesis of gels from noble metal decorated semiconductor NPLs. Preliminary experiments of growing Au domains on CdSe/CdS NPLs in aqueous solution by means of citric acid/Na-citrate and ascorbic acid induced reduction of chloroauric acid have already been successful, but the gelation of the heteroplatelets is still under development.

Summarizing, this thesis includes new invention of the metal-semiconductor nanoheteroplatelets with variable morphologies. It also demonstrates an efficient way to transform shape controlled Pt NPs and CdSe, CdSe/CdS NPLs to highly porous, light weight, macroscopic aerogels. Model systems of catalytic applications are also experimented by employing the hybrid structures as catalyst. The results are promising in the controlled environment of the research laboratory. In order to bring the advantages of these particles in our day-to-day life, or in commercial level, further improvements regarding the processibility of the materials is required, which is beyond the scope of this thesis.

Appendix

Publications included in this thesis

(1) Naskar, S.; Schlosser, A.; Miethe, J. F.; Steinbach, F.; Feldhoff, A.; Bigall, N. C., Site-selective Noble Metal Growth on CdSe Nanoplatelets, *Chemistry of Materials* **2015,** *27* (8), 3159-3166.

(2) Naskar, S.; Miethe, J. F.; Sánchez-Paradinas, S.; Schmidt, N.; Kanthasamy, K.; Behrens, P.; Pfnür, H.; Bigall, N. C., Photoluminescent Aerogels from Quantum Wells, *Chemistry of Materials* **2016,** *28*, 2089-2099.

(3) Naskar, S.; Lübkemann, F.; Hamid, S.; Freytag, A.; Wolf, A.; Koch, J.; Ivanova, I.; Pfnür, H.; Dorfs, D.; Bahnemann, D. W.; Bigall, N. C. *Advanced Functional Materials* **2017**, 27, 1604685.

(4) Naskar, S.; Freytag, A.; Deutsch, J.; Wendt, N.; Köckritz, A.; Behrens, P.; Bigall, N. C. **Submitted.**

Publications not included in this thesis

(1) Kodanek, T.; Banbela, H. M.; Naskar, S.; Adel, P.; Bigall, N. C.; Dorfs, D., Phase transfer of 1- and 2-dimensional Cd-based nanocrystals, *Nanoscale* **2015,** *7* , 19300-19309.

(2) Freytag, A.; Sánchez-Paradinas, S.; Naskar, S.; Wendt, N.; Colombo, M.; Pugliese, G.; Poppe, J.; Demirci, C.; Kretschmer, I.; Bahnemann, D. W.; Behrens, P.; Bigall, N. C., Versatile Aerogel Fabrication by Freezing and Subsequent Freeze-Drying of Colloidal Nanoparticle Solutions, *Angewandte Chemie International Edition* **2015,** *55*, 1200-1203.

(3) Hinrichs, D. Galchenko, M.; Kodanek, T.; Naskar, S.; Bigall, N. C.; Dorfs, D. Chloride Ion Mediated Synthesis of Metal/Semiconductor Hybrid Nanocrystals, *Small* **2016,** *12* (19), 2588.

Contribution to conferences

<u>Oral</u>

(1) Suraj Naskar, Nadja. C. Bigall, 'Synthesis and Optical Properties of Aerogels from Tailored Nanocrystals' *Photonic Colloidal Nanostructures: Synthesis, Properties, and Applications, (PCNSPA) Conference 2016*, St. Petersburg, Russia.

(2) Suraj Naskar, Nadja. C. Bigall, **'**Synthesis and Optical Properties of Aerogels from Tailored Nanocrystals' *European Materials Research Society, EMRS-Fall 2016*, Lille, France.

(3) Suraj Naskar, Nadja. C. Bigall, 'Synthesis of Nanoheterostructures from CdSe Nanoplatelets and Noble Metals' *European Materials Research Society, EMRS-Spring 2015*, Warsaw, Poland.

<u>Poster</u>

(1) Suraj Naskar, Nadja. C. Bigall, 'Aerogel from CdSe and CdSe/CdS nanoplatelets' *115th General Assembly of the German Bunsen Society for Physical Chemistry – Bunsentagung* 2016, Rostock, Germany.

(2) Suraj Naskar, Anja Schlosser, Jan. F. Miethe, Nadja C. Bigall, 'Site-Selective Noble Metal Growth on CdSe Nanoplatelets' *LNQE Nanoday* 2015, Hannover, Germany.

(3) Suraj Naskar, Anja Schlosser, Nadja C. Bigall, 'Site selective metal domain growth on CdSe nanoplatelets' *114th General Assembly of the German Bunsen Society for Physical Chemistry – Bunsentagung* 2015, (<u>PCCP "Hot Topics" Poster prize</u>), Bochum, Germany.

(4) Anja Schlosser, Suraj Naskar, Nadja C. Bigall, 'Growth of Noble Metal Domains on CdSe Nanoplatelets' *LNQE Nanoday* 2014, Hannover, Germany.

(5) Suraj Naskar, Nadja C. Bigall, 'Superstructures from Metal and Semiconductor Nanoparticles for Sensing Applications' *113*th *General Assembly of the German Bunsen Society for Physical Chemistry – Bunsentagung* 2014, Hamburg, Germany.

<u>Curriculum Vitae</u>

Mr. Suraj Naskar

Date of birth: 05.04.1991

Place of birth: Kolkata, India

Education

11/2013-03/2017   Ph.D. in Chemistry

Leibniz University of Hannover, Institute for Physical Chemistry and Electrochemistry

07/2011-07/2013   M.Sc. in Chemistry

Indian Institute of Technology Delhi (IIT Delhi)

06/2008-06/2011   B.Sc. (Honours) in Chemistry

University of Calcutta